Microstructure and Properties of (Rare Earth) Doped Oxide Ceramics.

by

James M Perkins MPhys AMinstP

Thesis

Submitted to the University of Warwick

for the degree of

Doctor of Philosophy

Department of Physics

April 2006

THE UNIVERSITY OF
WARWICK

Contents

List of Tables

List of Figures

Acknowledgments

The writing of a thesis seems like a very long and winding road, I have learned a great deal and have recieved much help, input and encouragement.

I would like to thank, in particular, Meg for her support throughout my time as a PhD student. My parents for the motivation and encouragement they have given me, and G&G for understanding why I didn't go and get a real job!

Specific thanks must go to Professor Mike Lewis and Dr. Geoff West, my supervisor and collegue, respectively. They have made the postgraduate experience an enjoyable, interesting and challenging one.

I also wish to acknowledge Dr. Andrew Bleloch and the other on-site staff at the SuperSTEM for making me feel welcome during my sessions at the facility.

Acknowledgments must also be paid to a number of people who have contributed in terms of lunch, microscopy training, mechanical testing, powder processing, fixing equipment etc. etc. (in no particular order!); Dr. Nick Goold, Dave Hammond, Steve York, Dr. Ian Gee, Dr. Geoff Diamond and Keith Briggs (whose songs and wittisisms have made for an entertaining lab), finally Dr. Richard Dobedoe, Dr. Niel Wilson and Steve Carpenter for maintaining the microscopy suite banter.

Declarations

This thesis is submitted to the University of Warwick in suport of my application for admission to the degree of Doctor of Philosophy. It is an account of my work carried out over the period October 2002 to November 2005, and except where specifically acknowledged in the text, is a result of my own research. No part of this thesis has been submitted in respect of a degree to this or any other university. Some parts of this thesis have been published as detailed below.

1). **J. M. Perkins.**, G. D. West and M. H. Lewis., "Analysis and spectroscopy of rare earth doped magnesuim aluminate spinel"., *Advances in Applied Ceramics.*, **104** 3 (2005) p131 - 134.

2). G. D. West., **J. M .Perkins** and M. H. Lewis., "Characterisation of fine-grained oxide ceramics.", *Journal of Materials Science.*, **39** (2004) p6687 - 6704.

3). G. D. West., **J. M. Perkins** and M. H. Lewis., "Transparent fine-grained oxide ceramics.",*Key Engineering Materials.*, **264-268** (2004) p801 - 804.

4). G. D. West., **J. M. Perkins** and M. H. Lewis., "The effect of rare earth dopants on grain boundary cohesion in alumina.", *J. Eur. Ceram. Soc.* in press.

James M. Perkins. March 2006.

Abstract

A study of alumina (Al_2O_3) and magnesium aluminate spinel ($MgAl_2O_4$) was undertaken with the aim of investigating the changes in properties and microstructural characteristics upon doping with specific rare earth elements.

Microscopic imaging and analysis of RE doped polycrystalline oxide ceramics has shown convincing evidence for monolayer segregation of RE cations to grain boundaries. State of the art aberration corrected scanning transmission electron microscopy (SuperSTEM, Daresbury Laboratories) has shown monolayer segregation to grain boundaries, and atomic resolution parallel electron energy loss spectroscopy has confirmed the presence of the RE cation at the grain boundary position. The region affected by segregation has been shown to extend no further than one monolayer from the centre of the grain boundary with RE cations occupying matrix cation boundary sites.

The effect of RE dopants on the powder processing and sintering of high purity commercial grade precursor powders was investigated. Differences were found between doped alumina and spinel in the sintering whereby the alumina grain growth was restricted by grain boundary mobility such that the grain size was reduced for a given sintering temperature. The grain size of spinel was unaffected by sintering temperature.

Differences in the fracture behaviour between doped alumina and spinel was found. The alumina samples manifested a change from trans-granular fracture to inter-granular fracture due to the addition of RE dopants. Spinel did not show such an effect. Alumina was shown to posess an approximate Hall-Petch relationship between hardness and grain size for both doped and undoped samples, such that sub-micron grain size samples posessed high hardness.

Optical characterisation has shown the potential for the use of fine grained RE doped alumina and spinel samples for hard window applications. A reduction in the grain size of alumina to below 1 μm leads to a change in the scattering mechanism, thus reducing low angle scatter and birefringence due to the refractive index mismatch. The benefits

to optical properties are in addition to the benefits in mechanical properties of a sub-micron grain structure.

Abbreviations

ADF   Annular Dark Field

ALON   Aluminium Oxy-Nitride

BF   Bright Field

BN   Boron Nitride

CCD   Charge Coupled Device

CIP   Cold Isostatic Press

CSL   Coincident Site Lattice

CTEM   Conventional Transmission Electron Microscopy

DF   Dark Field

EBSD   Electron Back Scatter Diffraction

EDS   Energy Dispersive Spectroscopy

EELS   Electron Energy Loss Spectroscopy

ELNES   Energy Loss Near Edge Structure

Eu   Europium

FEG   Field Emission Gun

FP Filter Press

FWHM Full Width at Half Maximum

HAADF High Angle Annular Dark Field

HIP Hot Isostatic Press

HP Hot Press

HRTEM High Resolution Transmission Electron Microscopy

IPA Isopropyl-Alcohol

IR Infra Red

PCA Polycrystalline Alumina

PEELS Parallel Electron Energy Loss Spectroscopy

PTF Percentage Transgranular Fracture

PVA Poly Vinyl Alcohol

RE Rare Earth

RIT Real In-line Transmission

SEM Scanning Electron Microscope or Scanning Electron Microscopy

SIMS Secondary Ion Mass Spectroscopy

SPS Spark Plasma Sintering

STEM Scanning Transmission Electron Microscope or Scanning Transmission Electron Microscopy

TEM Transmission Electron Microscope or Transmission Electron Microscopy

TFT Total Forward Transmission

TIA Technical Imaging and Analysis software

Tm Thulium

UMIST University of Manchester Institute of Science and Technology

YAG Yttrium Aluminium Garnet

Y Yttrium

Yb Ytterbium

Chapter 1

Introduction

1.1 Project Background

This project is a continuation of work broadly associated with a European program on advanced ceramics for industrial and biomedical applications. Aspects of this project that were succesful were continued for this PhD program under the supervision of Prof. M. H. Lewis.

The broad aim was to produce and characterise advanced ceramics with enhanced characteristics, both optical and mechanical arising from microstructural changes due to doping, and/or simple processing improvements.

The project has evolved as various techniques have become available for use by the author. The SuperSTEM facility at Daresbury Laboratory is a a world-leading centre for the development of aberration corrected scanning transmission electron microscopy (STEM) and analysis. The collaboration with SuperSTEM (specific thanks to Dr. Andrew Bleloch, technical director) has yielded, what are considerd to be, state of the art STEM images of grain boundary segregation. The initial SuperSTEM work has been published and further work, found in chapter 5.3, has been submitted for publication.

1.2 A Brief History of Alumina Based Oxide Ceramics

Alumina has a wide and varied use as an industrial ceramic; from cutting tools to hip implants. Its hardness, resistance to corrosive environments and ease of processing have led to a large number of products, uses and applications for the material. There exists a large number of publications centered on alumina, however there are still improvements that can be made. Magnesium aluminate spinel is a very similar material to alumina, however it has a different crystal structure and mechanical properties. The appearance of spinel in the literature has followed research trends more than alumina and is currently being revived as a potential 'nano-material'[1].

Polycrystalline ceramics, in general, have favourable mechanical properties compared to single crystals for many applications. While polycrystalline ceramic manufacturing is often complex and difficult, the cost of the final products are often less than their single crystal alternatives, such as sapphire.

As is often the case in research, a processing accident led to one of the most important breakthroughs in polycrystalline ceramic technology. The addition of MgO to alumina by contamination from a furnace led to the widespread production of translucent poly-crystalline alumina. This initial work by Coble[2] led to the development of Lucalox$^{(tm)}$, used in high pressure sodium lamps found in streeetlamps across the globe. This dis-covery in the 1960s began the story of translucent, then transparent, oxide ceramics on which part of this thesis is based.

1.2.1 Applications of Polycrystalline Oxide Ceramics

The variety of applications for oxide ceramics is wide. Below are some examples that may directly benefit from the property improvements indicated in this thesis.

Cutting tools

Ceramics have been used in the cutting tool industry for over 60 years. More recently, however, ceramic tool inserts have dominated the cutting processes for the turning and milling of cast iron, nickel based superalloys and the finishing of hardened steels. Alumina and silicon carbide ceramics are the most widely used, and currently constitute $\sim$5% of the indexible tool market[3]. One of the main properties of ceramic tools is the 'hot hardness' such that the components can maintain hardness at high temperatures without significant wear. This leads to the possibility of increased spindle speeds and thus reduced cutting times and longer component lifetimes compared with cemented carbide coated materials[4].

Concerns regarding thermal shock, structural defects and fracture toughness of ceramics has restricted the growth of the market share. Improvements of these properties, however, coupled with concerns for health and safety, and the cost of disposal for cooling fluid (not required for dry cutting using ceramic tools), is expected to fuel an increase in demand for ceramic tool inserts in the near future[3].

Biomedical materials

Existing ceramic technologies have been implemented for biomechanical implants, most succesfully hip replacements. The high hardness and low wear rates ($<$5 μm per year compared with up to 150 μm per year with steel against high molecular weight polyethene ball and socket[5]) lead to increased lifetimes of implants minimising the need for repeat operations where the initial replacement was required at a young age. Thus while component costs are higher, the saving in terms of repeat total hip replacement operations is significant[6].

Future concerns are centred on emerging nano devices in several areas of treatment and medicine. Opportunities include controlled release delivery of bioactive agents; ma-

terials that can be 'bioactive' responding both to healing processes and combatting infection, development of intelligent nano-scale devices that remove debris or stop fluid flow, simple, low cost, disposable instruments such as scalpel blades and other types of prosthesis including dental ceramics, articulating surfaces (joints) and bone spacers[7].

Hard window materials

This is an area in which the potential applications are large and varied. The anticipated improvements and new applications for materials that are truly transparent as opposed to translucent include replacement of single crystals with harder polycrystalline components[8]. Examples include missile domes, watch glass and improvements in non-corrosive lamp envelopes for lighting. Conventionally popular polycrystalline ceramics such as alumina and aluminium oxynitride (ALON) have demonstrated translucency but not transparency. The US army have programs investigating such materials[9].

A demonstration of the importance of grain growth control is from the long term tests carried out on polycrystalline alumina used in lamp envelopes. Long term anneal tests (to simulate the long operational lifetime of commercial products) has shown that there is a large amount of grain growth for the undoped fine grained polycrystalline materials and that grain size instability may reduce the working lifetime of the product[10]

Armour

Ceramic armour technology has become increasingly important for both artillary (tank and armoured vehicle) and personal protection (bullet/shrapnel proof jackets). There is specific interest in the improvement of properties for alumina sheets[11] for personal protection and transparent hard window materials for visors and vehicle windows[12]. The ceramic industry is currently benefitting from a large investment in this area, an example of which is a further contract, awarded to Ceradyne by the US military (November 2005) worth $60.1 million, which increases the total contracts awarded since August

2004 to \$292 million[13].

1.3 Thesis Objectives

The aim of the project is to study the effects of RE doping on the sintering, microstructure, mechanical and optical properties of two oxide ceramics; alumina (Al_2O_3) and magnesium aluminate 'spinel' ($MgAl_2O_4$). The effect of RE on these properties are investigated by systematically studying each topic and relating the sintering and microstructure to the emergent properties.

Chapter four compares two manufacturing methods used to produce samples and investigates the effect of RE doping on the sinterability, specifically the grain size evolution with temperature.

Chapters five and six investigate the microstructure of the oxides, with emphesis on investigating suggested grain boundary segregation. It is believed that the RE segregates to the grain boundary region in both alumina and spinel, important since the emergent properties of polycrystalline ceramics are closely related to their grain size and boundary structure. The microstructure investigation aims to investigate both the compositional and the structural components of the grain boundaries using a variety of modern microscopy-based techniques. Chapter six focuses on a recent advancement in microscopy, the aberration corrected STEM, used to probe the composition and structure of RE-containing boundaries at an atomic scale.

From the control of grain size and grain boundary characteristics, the mechanical and optical properties may be understood. Chapter seven highlights the effect of RE segregation to grain boundaries on mechanical properties such as hardness, grain boundary cohesion, fracture toughness and wear, and indicates the major differences between alumina and spinel. Chapter eight investigates whether RE doping of alumina and spinel

5

adversely affects their potential for hard window applications, relating the microstructure to the optical properties.

Chapter 2

Doped oxide ceramics; properties and microstructural analysis

2.1 Structure of Alumina and Spinel

The crystal structures of alpha alumina and spinel are shown schematically in figures 2.1 and 2.2. Magnesium aluminate is the crystal after which all spinels are named. Spinel is constructed of a face centred cubic array of oxygen ions, and has general formula XY_2O_4 where X = divalent cation, Y = trivalent cation and O = oxygen. The cations are positioned in half the tetrahedral and one eighth of the octahedral sites respectively. Other examples of spinels include gahnite, franklinite, chromite and magnetite, all having various combinations of cations. The lattice parameter of the unit cell, a = 8.08 Å[14].

Alpha alumina has a rhombohedral structure, which is often approximated to an hexagonal close packed structure with the aluminium occupying octahedral sites. The cation sites of this close packed structure are $\frac{2}{3}$ occupied by aluminium ions, by virtue of the

7

chemical formula. Gamma alumina has a cubic structure but will transform to alpha at higher temperatures. Alpha alumina is used throughout so the gamma structure will not be considered further. The lattice parameters of alpha alumina are a = 4.7 Å and c = 13.0 Å at room temperature [15].
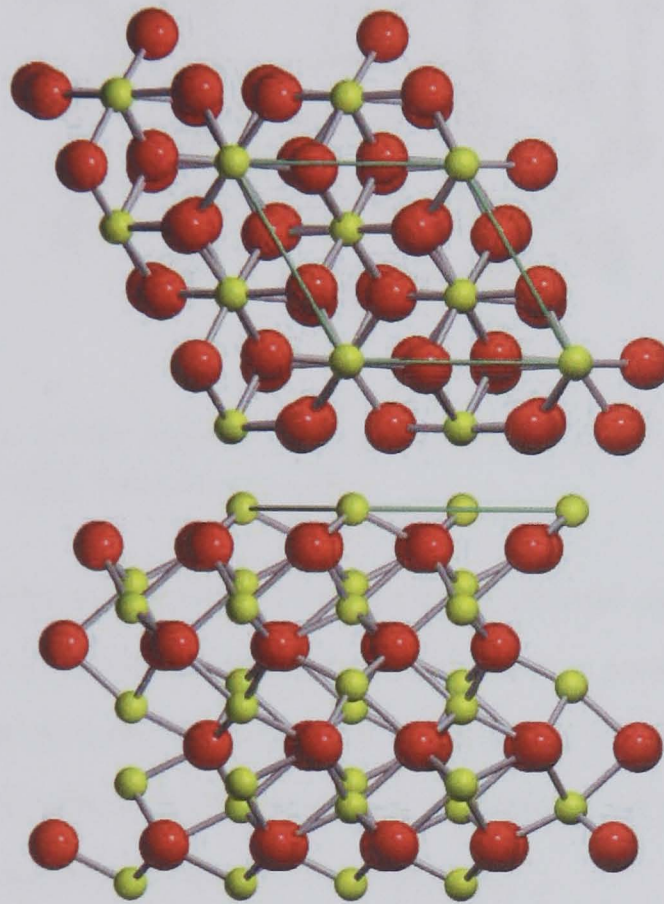
Figure 2.1: *Schematic of the crystal structure of alumina, looking down on the 001 planes and (bottom) along the 001 plane. Atom colours; yellow = Al ions in octahedral sites, red = oxygen.*

2.2 Doping of Oxide Ceramics, an Overview

As mentioned in the previous chapter, the uses of oxide ceramics are wide and varied. An important consideration in their use is the application of dopants to change various properties. For oxide ceramics the most well known application of dopants is the use of
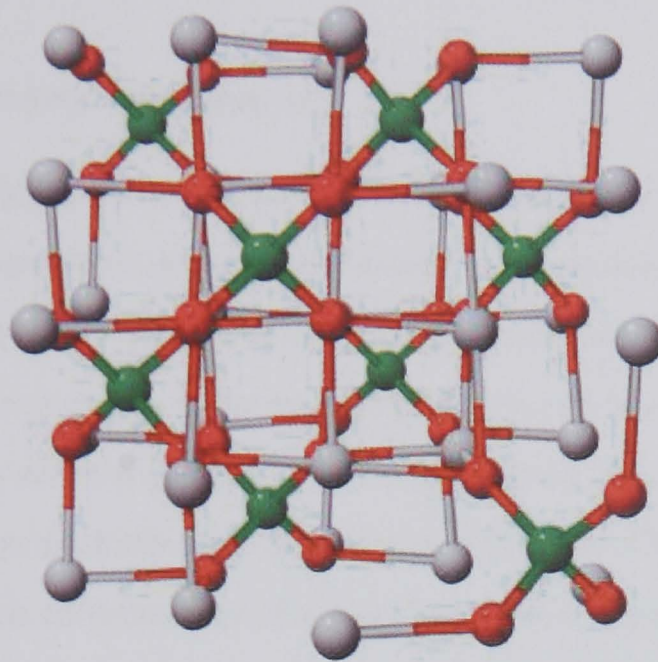
Figure 2.2: *Schematic of the crystal structure of magnesium aluminate spinel; grey atoms = Al, green = Mg, red atoms = O.*

MgO to aid densification in alumina. This was an accidental discovery, made possible by the contamination of alumina with residual MgO from a previous process remaining in a furnace. This demonstrates one aspect of doping, the sensitivity. Throughout this thesis the doped oxides have only 500 ppm level of doping, and yet this level of dopant is enough to provoke significant changes in properties.

The accidental discovery of the MgO densification aid in alumina has led to the widespread use of polycrystalline alumina sodium lamp envelopes. Since this discovery, the doping of ceramics has been a key element in improving properties and shall be discussed throughout this review chapter. Importantly, many dopants segregate to grain boundaries affecting the densification and/or sintering mechanisms as well as the grain growth processes. It is important to understand the nature of the segregation in order to further understand the sintering process itself. As will be seen in the following discussion, the use of segregating dopants to control grain size has implications not just on processing

(sintering, grain growth etc.) but on mechanical and optical properties.

2.2.1 Grain Boundary Segregation

It is important to understand that polycrystalline materials are not simply macroscopic representations of a combined set of single crystals with random orientations. The very existence of grain boundaries contributes to the bulk properties of a polycrystalline material even when no second phase, impurity or pore structure is present. With the addition of such second phases etc. the properties of a material may alter dramatically, for example phenomena such as embrittlement or increased diffusivity. Other effects are due only to the fact that crystals on either side of a boundary have a degree of misorientation[16].

Grain boundaries are distinct, just as the surface of a liquid or solid posesses properties unique to the region, grain boundaries, pores, defects etc. have a different structure to the bulk material. A surface is not nessesarily a grain boundary, however, a contaminated surface may contribute to a change in mechanical behaviour[16].

Segregation to either surfaces or grain boundaries must be energetically favourable, hence the supposition that if a solute reduces the surface tension then it must segregate to the surface, or if a solute increases the surface tension then it must avoid the surface[17]. This may not be directly applicable to boundaries[16], but a similar argument can be made regarding the energy of distortion around a solute atom. The amount of distortion around a solute atom will depend on the size of the solute atom compared with the given position. In a polycrystalline material there will be regions within grain boundaries where solute atoms may be accomodated with minimal change in local lattice energy, indeed, smaller atoms may 'fit' into holes. The energy required to alter a lattice so it may accommodate a solute atom is extremely large but if the segregant may find an already distorted region (such as a dislocation or grain boundary) then it will more favourably exist there. This may be described as equilibrium segre-

gation. In terms of driving force for segregation, assuming the distortion energy of a segregant at a boundary is small, the whole energy of distortion caused by a solute atom existing within a grain may be saved. Other driving forces may include electronic interactions, whereby a solute atom also relieves some strain energy via electronic means[16].

The extent of segregation in terms of 'boundary size' is non trivial and is limited by definitions of extent, either the physical width of a region containing solute atoms or the scale at which such segregation has some amount of influence over its locality. Phenomena contributing to grain boundary models include; the existence of a range of segregation sites that have a number of solute binding energies, interactions between solute atoms within a segregate region, co-segregation of two or more elements that may enhance/reduce segregation, and the formation of further structures within the segregant region that produce greater than one monolayer segregation[18].

The theory of grain boundary segregation is based on thermodynamic principles proposed by Gibbs[17], with important contributions from Mclean[16] and Seah[19] (mainly with regards to metals).

2.2.2 Impurities, Dopants and Segregation in Alumina.

It is well known that impurities in ceramic powders contribute significantly to the properties of the sintered products. Low-level impurities can be used to control the microstructure, however, the initial powder must be of ultra-high purity and the processing steps undertaken must minimise the risk of any unwanted contamination. The purity of industrial powders is one of the major considerations of the main suppliers.

There are still contradictions in the literature regarding certain properties, this is often due to the impurity content[20, 21]. There are a number of ways impurities can manifest themselves within a polycrystalline sample. In the case of alumina, if the ionic

11

Cation	Al^{3+}	Si^{4+}	Cr^{3+}	Fe^{3+}	Fe^{2+}	Mg^{2+}	Y^{3+}	La^{3+}	Tm^{2+}	Tm^{3+}	Ti^{4+}	O^{2-}	S^{2-}
Ionic radii / A	0.54	0.40	0.62	0.65	0.78	0.72	0.9	1.03	1.09	1.05	0.61	0.140	1.84

Table 2.1: *Ionic radii of selected cations.*

radius of the cation is similar to that of the matrix ion (aluminium, $Al^{3-} = 0.0675$ nm), the impurity may be soluble within the grains themselves. This is significant with ions such as Fe^{3-}, Cr^{3+} and Ti^{4+}, indeed, these are the main dopants required to create the colours in ruby and blue sapphire respectively (the Fe and Ti must both be present in the correct valence state to achieve this)[22, 23, 24, 25]. In general, the solubility of cations with a large mismatch in ionic radius with Al^{3+} is low (with the exception of aliovalent cation inclusion, eg. Ti^{4+}, where co-solubility of charge compensating impurities are known to increase[26]).

The ionic radii of various dopants used in this thesis are shown in table 2.1[27], along with sulphur (anion impurity discussed in chapter 4.2), chromium, titanium and iron as mentioned above. The impurities/dopants tend to segregate to defect structures (which include grain boundaries and surfaces) or, at higher concentrations, appear as a precipitate. [28].

The doping of heavier elements in alumina is well documented, a good example being that of yttria in alumina. For Y doping, the creep resistance is increased by two orders of magnitude[29]. Y is also used as a model system and is the most widely studied of all alumina dopants[30]. Part of the problem in identifying the reasons behind the property changes is that the Y (and similar size ions) segregate strongly to the grain boundaries as the solubility level is <10 ppm[31]. It has been suggested that the presence of such dopants at grain boundaries may increase the number of special boundaries present in a specimen[32], thus altering the mechanical properties. Cho et al[33], however, have shown that there is no change in the number of special boundaries or grain misorientation. The suggested difference in segregation depending on special boundary type has

also been investigated, and here the segregation was found to be lower in certain types of special boundaries[1], with $\Sigma 3$ and $\Sigma 7$ containing zero segregation[35]. In general, the number of special boundaries is a small percentage of the total number of boundaries, thus the actual distribution of segregates to grain boundaries is uniform.

For any given dopant concentration, the structure of the segregated region at the boundary will be dependent on the local grain boundary concentration. With smaller grain size, the relative amount of segregate at the boundary will be relatively lower than that of a sample with larger grain size due to the grain boundary area present. It has been argued that segregation at boundaries falls into three distinct types i) dilute or below saturation, ii) between saturation and supersaturation and iii) at equilibrium with the presence of precipitates at boundary triple points, such that the boundary structure is that of the pre-saturation type. There is certainly a suggestion, for Y at least, that there is no amorphous second phase running through the boundary region.

Figures 2.4 and 2.3 show the potential distribution of Y^{3+} for any given boundary (except those special boundaries mentioned earlier). Initially a linear dependence of Y^{3+} at grain boundaries with concentration increase is shown until the grain boundary sites are saturated with low energy sites suitable for large ion occupancy. As the concentration rises further, however, the Y^{3+} may begin to occupy near boundary sites, this is when the boundary becomes 'supersaturated' and a reduction in the excess Y^{3+} occurs. This supersaturation is a more disordered stucture, but thought to be only one or two monolayers wide[29]. With further increase in RE concentration, precipitation occurs and any further addition of the large ion simply increases the size of the precipitate phase particle while maintaining a saturated boundary. This is known as equilibrium saturation, and is indicated by the levelling out of the graph. The difference in local

---

[1]Special boundaries are defined either as boundaries with coincident lattice sites, i.e. lattice sites occupied by atoms in both adjacent grains or a boundary along which dense lattice planes of each grain lie. Both types are low energy boundaries[34]
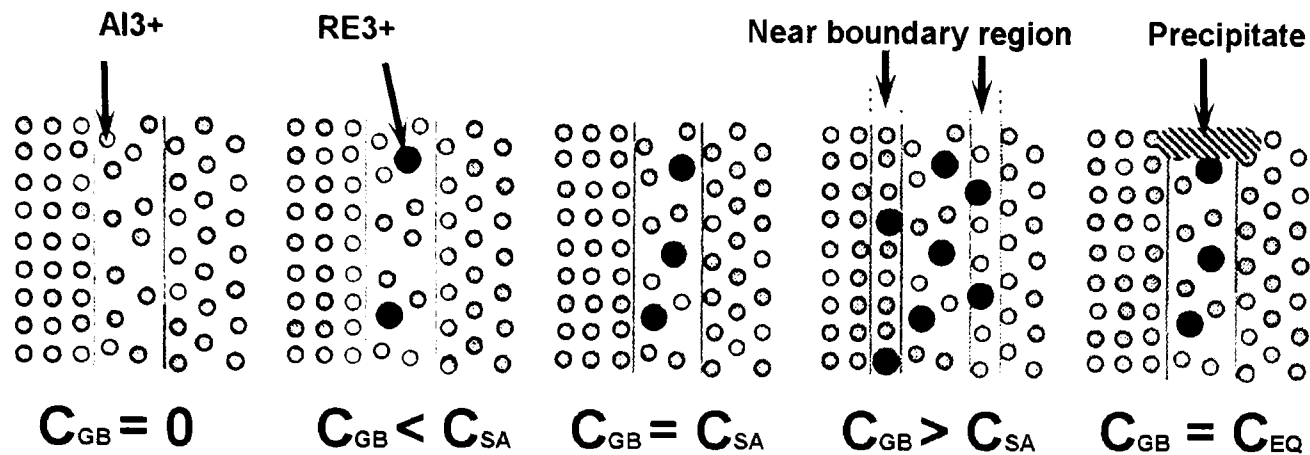
Figure 2.3: *Diagram showing the proposed boundary occupancies for different concentrations of dopant ion.* C_{GB} = *concentration at grain boundary,* C_{SA} = *dopant grain boundary saturation concentration and* C_{EQ} = *dopant grain boundary equilibrium concentration[29].*

concentration between the supersaturated state and the equilibrium state is dependent on the nucleation barrier for the precipitate formed (in this case, yttrium aluminium garnet, YAG)[29].

Aside from dopant ions there is still the problem with impurity ions that do not necessarily behave in the same way. Other important impurities are, for example, silica and calcia. Both are glass-forming and have very different effects on the grain boundaries, and thus the properties. It is important to maintain tight control on the Si/Ca content in order to prevent amorphous glassy phases forming[20].

2.2.3 Microscopic Effects of Segregation in Alumina

Sintering of ceramics relies heavily on the mass transport pathways provided by the grain boundaries, therefore densification is sensitive to the presence of dopants that affect mass transport directly by being present as a segregant. Various studies have looked
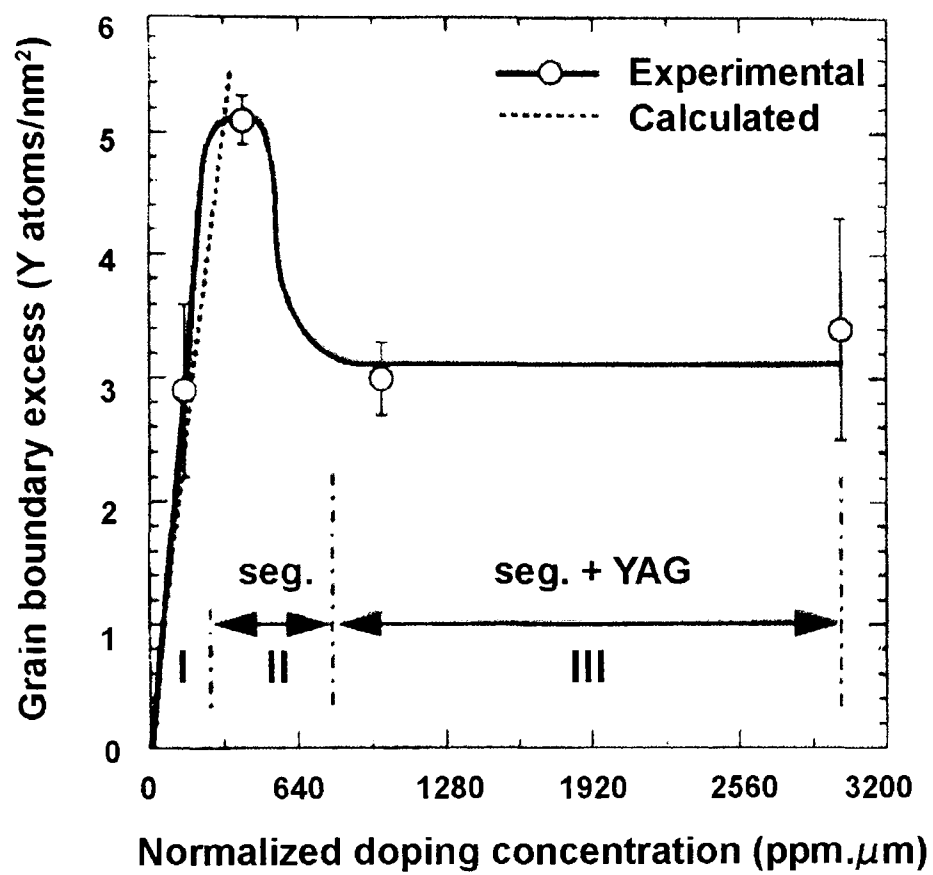
Figure 2.4: *Grain boundary dopant excess (in this case Yttrium $^{3+}$) measured by STEM as a function of grain size-normalised doping concentration. There are three distinct regions in the graph, (I) dilute, (II) supersaturated, and (III) equilibrium[29].*

at the underlying effects that the dopants have, including a systematic investigation by Rossi and Burke[36]. While it has been important to understand the processes, the key material studied has continued to pose important questions, including why the addition of MgO to alumina aids the densification process.

Proposed mechanisms of densification involving the grain boundary region are summarised below.

Particle pinning

This is effectively the creation of a composite material with the second phase precipitates, formed when grain boundary concentration passes through the supersaturation criteria. While there is still a saturated grain boundary the precipitation forms at defect sites, mainly along triple points. These particles block mass transport, thereby 'pinnning' the grain and preventing abnormal grain growth. However, studies have shown that the existence of precipitates is not a requirement for full densification, and therefore must be in addition to other processes[37].

Solute drag

Before the advent of modern analysis techniques, the idea that MgO segregated to grain boundaries was supported by auger electron analysis and X-ray photoelectron spectroscopy of fracture sections[38, 39]. This demonstrates that the concentration of dopants was highest within the top tens of angstroms of the fracture surface. This work cited Jorgenson and Westbrook's[40] solute segregation theory, whereby the dopant segregated to the grain boundary, lowering grain boundary mobility and preventing pore detatchment (thus remaining within the grain) during boundary migration. By keeping pores at grain boundaries, shrinkage will occur as densification progresses by grain boundary diffusion. However, the auger and xps results could have arisen due to second

16

phase MgO based particles. Modern techniques (discussed in chapters 5.3 and 6) have supported the theory of segregation to the grain boundary region, thus solute drag has become a favoured theory, especially with respect to the reduced grain growth kinetics in RE doped alumina. The magnitude of the drag is proportional to grain boundary concentration.

Grain boundary and surface energy

Where pores are sitting at grain boundary or triple point interfaces, there exists a gas-solid dihedral angle which is altered by any change in the grain boundary and surface energies. For a pore of given volume, the larger the surface area exposed to the gas (i.e. smaller dihedral angle), the greater the extent of drag and reduction of boundary mobility. The dihedral angles of MgO doped alumina have been shown to narrow (measured at free surfaces), therefore reducing the possibility of abnormal grain growth[41].

Solid solution

Studies have shown that co-doping MgO with SiO_2 increases the solid solubility of both ions, thus reducing the propensity to segregate at boundaries[42]. Low levels of SiO_2 impurity will, therefore, not appear at grain boundaries but disperse into the bulk, reducing the risk of glassy phases along boundaries. However, this mechanism is not applicable for large isovalent dopants/impurities, such as RE ions.

Surface diffusion

In the situation where surface diffusion occurs readily, pores would have increased mobility, keeping up with boundary movement. To achieve this, Mg ions must segregate to the surface, i.e. the pore surface.

2.2.4 Rare Earth Doping of Alumina

The development of MgO doped alumina took a step forward in 1968 when Y was added to aid sintering[43]. Compared with sintered undoped alumina, the addition of Y increased creep resistance by 2 - 3 orders of magnitude. The effect of Y addition on sintering behaviour and high temperature creep is well documented and has been the subject of a comprehensive review[44]. Further to this, the improvements in creep resistance due to other RE dopants have been widely reported[45, 46, 47]. Improvements in high temperature creep resistance have been reported at similar level to Y doped samples. The mechanism of creep resistance has not been resolved, however two theories have been put forward by groups in the US and Japan. The Lehigh group (US) stated that the size of the dopant ion plays a significant role whereby the blocking of diffusion pathways is increased as the size of the ion increases[46]. This is related to the smaller strain rates for larger ions which corresponds to a larger creep activation energy (this size effect is reported to saturate as ionic radius becomes large than 0.9 Å). The Japanese group studied the effect systematically and found a poor relationship with ion size[48]. Their approach was to study the ionic bonding state. Their first principles molecular orbital calculations correlate well with observed creep results[49].

The effect of rare earth dopants on creep is clear from the literature, however, comparing methods of study between different groups is often difficult and indeed unwise due to their sample preparation techniques. The differences in opinion regarding the mechanisms behind the high temperature creep resistance may stem from grain size, porosity content and level of dopant, all of which are not always similar or indeed defined adequately in the literature. For example, a reduction in grain size will reduce the relative grain boundary concentration therefore reducing apparent creep activation energy. Where the intrinsic grain size effect may be taken into consideration[50] for 'grain size normalisation', the concentration change is not. Creep is an important property, however, it is only described here as an indication of the importance of RE doping. The

18

2002 review of segregation is a useful review to provide further information[50].

The embrittlement of metals due to grain boundary segregation has been known for over 100 years[51] and the relationship of segregation with respect to oxide ceramics is relatively recent. The effects on boundary bonding should be directly related to sintering and grain growth retardation, however, most studies have concentrated on grain size effects[52] and/or stoichiometry[53]. Some studies examining the direct effect of RE segregation on fracture energy and strength have reported an increase in grain boundary cohesion[54]. It is difficult to isolate the effects of microstructural evolution of RE doped samples (grain growth, sintering, pore structure etc.) from the effect of grain boundary chemistry[55]. This will be discussed further in chapter 7.4.

2.2.5 Optical Properties

The optical properties have been briefly mentioned within the context of the project background. The importance of these materials cannot be overstated in terms of their potential wide-ranging applications. More generally, the improvements in processing and the understanding of the scattering mechanisms for fine-grained oxides has implications for other ceramic systems. The understanding of the optical properties should also be considered in parallel to the changes in mechanical properties due to microstructural control. The theory of light scatter within these materials is presented in chapter 8.3 and the measured quantities in section 3.6.

Candidate ceramics for hard window applications

Alumina Alumina is one of the most versatile and well known of all commercial ceramics. Its uses in optical industries are equally varied. In single crystal (sapphire) form, it is widely used in the electronics sector. Large single crystals of sapphire have been produced (at great cost) for hard window applications. The required complex shapes

19

limit its use, due to the extremely high cost of grinding and polishing (due to exceptional hardness) and its non cubic structure which leads to mechanical properties that vary depending on crystal orientation.

Polycrystalline alumina (PCA) is a cheaper alternative to single crystal sapphire, however, its optical properties suffer both due to the non-cubic structure leading to a refractive index mismatch for different crystallographic orientations[56], and the scattering at grain boundaries from impurities. This view led many groups to increase the grain size of alumina to minimise the number of grain boundaries for a given thickness of material[57, 58, 59].

Other groups have taken a different approach and have published work suggesting that fine grain size (1 - 2 μm) alumina should have a higher transmission than coarse grained[60], and more significantly transparent (as opposed to high transmission yet translucent) alumina has been reported[61, 62]. This idea is based on a traditional light scattering model presented by Apetz and van Bruggen[63] (considered in detail in chapter 8.3), where the mechanism of scatter changes as the grain size approaches the wavelength of light. In this model the major scattering centres are the pores, however, pore reduction is generally achieved at high sintering temperatures where grain growth occurs. The relatively low sintering temperatures required to maintain a fine grain size must be combined with high pressure to minimise residual porosity.

Recent research involving methods to improve the density of green bodies prior to sintering include colloidal processing[8, 64] and precursor powder size and size distribution studies [65, 66], or a combination of the above[67]. These methods form an approach to minimise residual porosity in the final sintered body such that truly transparent materials can be manufactured.

20

Magnesium aluminate spinel

As a hard window material, spinel is an excellent candidate. With a cubic structure and good mechanical properties, it features highly in the recent literature ([1, 68, 9]). Again, the arguments regarding the scattering at grain boundaries have led to the increase in grain size to minimise the number of boundaries. Microcracking[69] within large grains and microstructural inhomogeneities [70] create scattering centers visible as opaque regions. A very high optical quality is required for some spinel applications, for example, the IR transparent domes in guided missile nose cones. This quality of material is currently produced using both liquid phase sintering aids and two stage sintering processes, however several processing stages mean the unit cost remains high. The emergent material has very large grains ($\sim$750 μm) and maintains a level of impurity that manifests itself as a 'haze'. It is advantageous to produce a fine grained spinel so that better mechanical properties can be achieved.

While the mechanical properties are not as good as alumina, they are within the regimen required for most hard window uses. Combined with the cubic structure, this makes spinel an excellent choice for such applications.

Other optical ceramic candidates

The most significant other candidate materials are ALON[71] and YAG[72]. Similar materials such as Yttria (Y_2O_3) and MgALON as well as more recently, α-sialons[73, 74] are further candidates. The SiALONS are similar to alumina in that they have non cubic structures, however, YAG and ALON are useful materials with high transparency, YAG has a hardness approximately half that of spinel and ALON powders are difficult to manufacture in industrial quantities.

2.3 Imaging and Analysis of Doped Oxide Ceramics

There are many imaging and analysis techniques that have been used to image and measure properties of doped ceramics. Initially, auger electron spectroscopy from fracture surfaces indicated that MgO was segregating to grain boundaries[38, 39]. Segregation to grain boundaries has since been confirmed using other imaging methods, and higher resolution microscopy techniques have begun to probe the boundary structure.

2.3.1 Grain Boundary Analysis by Electron Microscopy

Electron beam-specimen interactions

The high energy electrons in the electron microscope are an ionising radiation source. Figure 2.5 shows the various secondary signals produced when an electron beam is incident on a sample. There has been the use of both Scanning electron microscopy (SEM) and Transmission electron microscopy (TEM) to gather data. SEM images are produced using only the secondary or backscattered electrons (signals generated above the sample in figure 2.5)[75].

When high energy electrons pass through a TEM sample they interact with the atoms in the sample via electrostatic forces. Such interactions are divided between elastic and inelastic scattering.

Elastic scattering is the Coulomb interaction between the incident fast electron and the atomic nucleus. For electrons that pass close to the sample atomic nuclei the interaction may be described by Rutherford scattering and is detected using the high angle annular dark field detector below the sample in the TEM. Most electrons interact at a further distance from the atomic nuclei and are under the influence of the weaker shielded (screened by inner atomic electrons) field. This interaction is governed by the

inverse square law and incident electrons are typically scattered by small angles. In a crystalline specimen the electrons interact in a wave-like nature with the lattice. The interference between such electron waves leads to what is known as Bragg diffraction, where the angular intensity of scattered electrons is related to the lattice spacing[76].

Inelastic scattering arises as a result of the coulomb interaction between the incident fast electron and the atomic electrons within the sample. This interaction may be understood either in single electron terms where the excitation is from an atomic electron to a higher quantum number Bohr orbital or as a transition between energy levels. For inner shell excitations, i.e. where a core electron is excited to a level above the Fermi level (below the Fermi level all energy states are occupied), the electron must acquire at least its binding energy from the incident high energy electron to make the transition. The incident electron loses its energy and is scattered. Further emission of an Auger electron or x-ray occurs as a result of the highly excited atom returning to its initial state with the excited electron returning to its ground state. The outer shell electrons may also be excited. In this case electrons may make transitions between or within bands. If such an electron gains enough energy (energy of vacuum) it may be fully expelled from the atom and emitted as a secondary electron. A further description of inelastic scattering involves the situation where outer shell scattering involves several atoms. This is represented as an oscillation of the valence electron density, otherwise known as plasmon oscillation[76].

For all of the above interactions there are methods of detection that provide different imaging contrast features or analytical information. Bragg diffraction in crystalline samples leads to diffraction contrast (simply strongly diffracting crystals/orientations appear dark). Atomic number contrast can be obtained from Rutherford scattering of the incident electron by the atomic nuclei. Compositional analysis may be performed using x-ray/auger spectroscopy (photons/electrons emitted when ionised atom returns to ground state) and electron energy loss spectroscopy (measuring the energy of forward

scattered electrons with small scattering angles). The techniques relevant to this project are outlined below, however, a more complete description of the electron interactions and their detection can be found in Williams and Carter[77] and Egerton[76].

High Energy electron beam

Backscattered electrons

Secondary electrons

Auger electrons

Characteristic x-rays

Visible light

Absorbed electrons

Thin sample

Electron-hole pairs

Bremstrahlung x-rays

Elastically scattered electrons

Inelastically scattered electrons

Direct beam
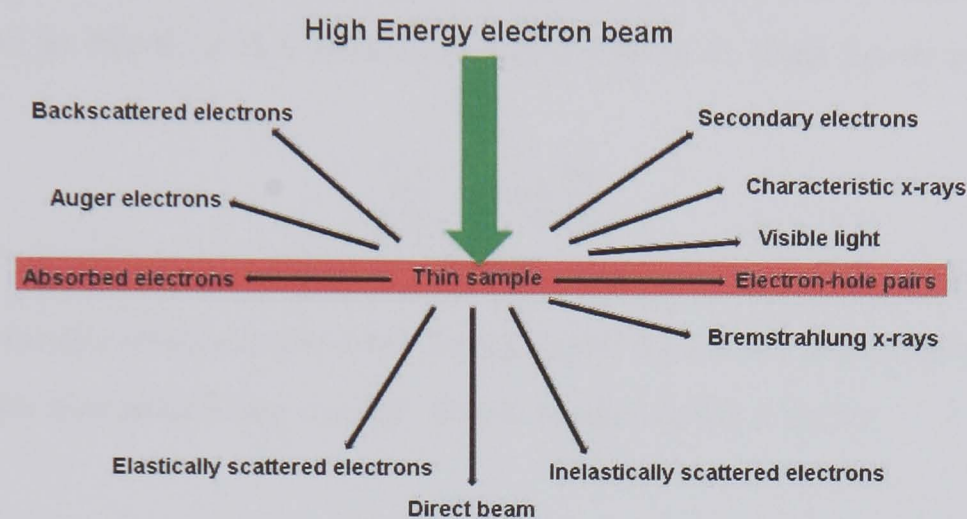
Figure 2.5: *Schematic of the signals generated when a high-energy electron beam interacts with a thin sample.*

Important interactions that are relevant here are Bragg diffraction, Rutherford scattering and the Coulomb interaction. Simplistically, they are responsible for the signals leading to imaging/analysis in bright field TEM imaging, atomic number contrast in STEM HAADF imaging, chemical/bonding/electronic structure analysis using EELS.

Improvements in electron microscopy have enabled groups imaging and analysing grain boundaries to obtain progressively more useful information about grain boundaries. The two most common (often combined) techniques are high angle annular dark field imaging (HAADF, in the STEM) and energy dispersive x-ray spectroscopy (EDS). Both techniques are described in more detail in section 3.7.1 and 3.7.2. Relevent uses of HAADF and EDS include imaging and analysis of grain boundaries in Y, Nd and La oxide doped microstructures [78, 79]. Here, the imaging using HAADF clearly shows the segregation of RE ions to grain boundaries because of large differences in atomic number between

the dopant and matrix elements due to atomic number contrast. From this, further analysis of grain boundaries using EDS either as a spot on the boundary or a line scan (or indeed an area map) over the boundary can be employed to gain further information about concentration levels of dopant. EDS spectra can be quantified for a specific region using the Cliff-Lorimer equation[80] (equation 2.1), provided adequate calibration standards can be found (it is possible to use precipitates at triple points to find this).

$$\frac{C_A}{C_B} = k_{AB}\frac{I_A}{I_B} \tag{2.1}$$

C_A and C_B are the concentrations in the interaction volume of the incident beam and I are the intensities of signal above the background, k_{AB} is the expected ratio of intensities from two elements being studied, this is known as the *k-factor*.

It follows that the grain boundary dopant excess can be defined by equation 2.2 where Γ represents the amount of solute present per unit area of grain boundry in excess of the amount of solute that would be present if there were no grain boundary[81].

$$\Gamma_x = dn_y k_{x/y} \left[\left(\frac{I_x}{I_y}\right)_{gb} - \left(\frac{I_x}{I_y}\right)_{m} \right] \tag{2.2}$$

Where d = width of the electron beam probe size, n_y = the atomic density of the matrix, gb and m refer to grain boundary and matrix respectively. EDS has the advantage over SIMS in terms of any quantitative analysis. Its spatial resolution is higher and can be focussed on well oriented boundaries without averaging over a large number of grains[78].

Electron Energy Loss Spectroscopy

To complement EDS, EELS is a further analytical technique that provides compositional data. However, the spectrum can provide much more information in terms of electronic structure, local environment and bonding. The energy loss spectrum is acquired by collecting the inelastically scattered electrons that emerge from the specimen. Electrons are

selected by an entrance aperture, they then pass through a 90° magnetic-prism which produces an energy separation in the dispersion plane, the resultant spectrum is brought to focus on the detector (CCD)[77].

A schematic of a typical EELS spectrum is shown in figure 2.6. The spectrum can be divided into a number of sections: zero loss, low loss and high loss.

(A) Zero loss peak: The zero loss peak represents electrons passing through a specimen without any appreciable (relative to the energy resolution of the equipment) loss in energy and minimal scattering. Most electrons will pass through having suffered zero energy loss and zero scatter, this makes the peak large with respect to the other spectrum features.

(B) Low Loss: This is the section of the spectrum that describes energy losses up to $\sim$ 50 eV. These arise from plasmon oscillations and inter/intra-band transitions (weakly bound electrons). It is most dominant in materials with a free electron structure, however, it occurs with variable intensity in all materials. In thicker samples there may be multiple plasmon peaks with decreasing intensity at $n\times$ the initial peak energy due to multiple scattering events, this causes problems as it dominates higher energy spectrum features but may be removed by deconvolution. The excitation of core electrons to an unoccupied energy level, these are characteristic of the particular specimen and can therefore be compared with spectra from known compositions.

(C) High Loss: The high loss part of the spectrum provides information arising from inelastic interactions between the incident electron and inner (core) shell. If ionisation takes place the energy loss of the incident electron must be at least the binding energy of the core shell electron. The spectrum appears as a sharp 'edge' with a rapidly decreas-
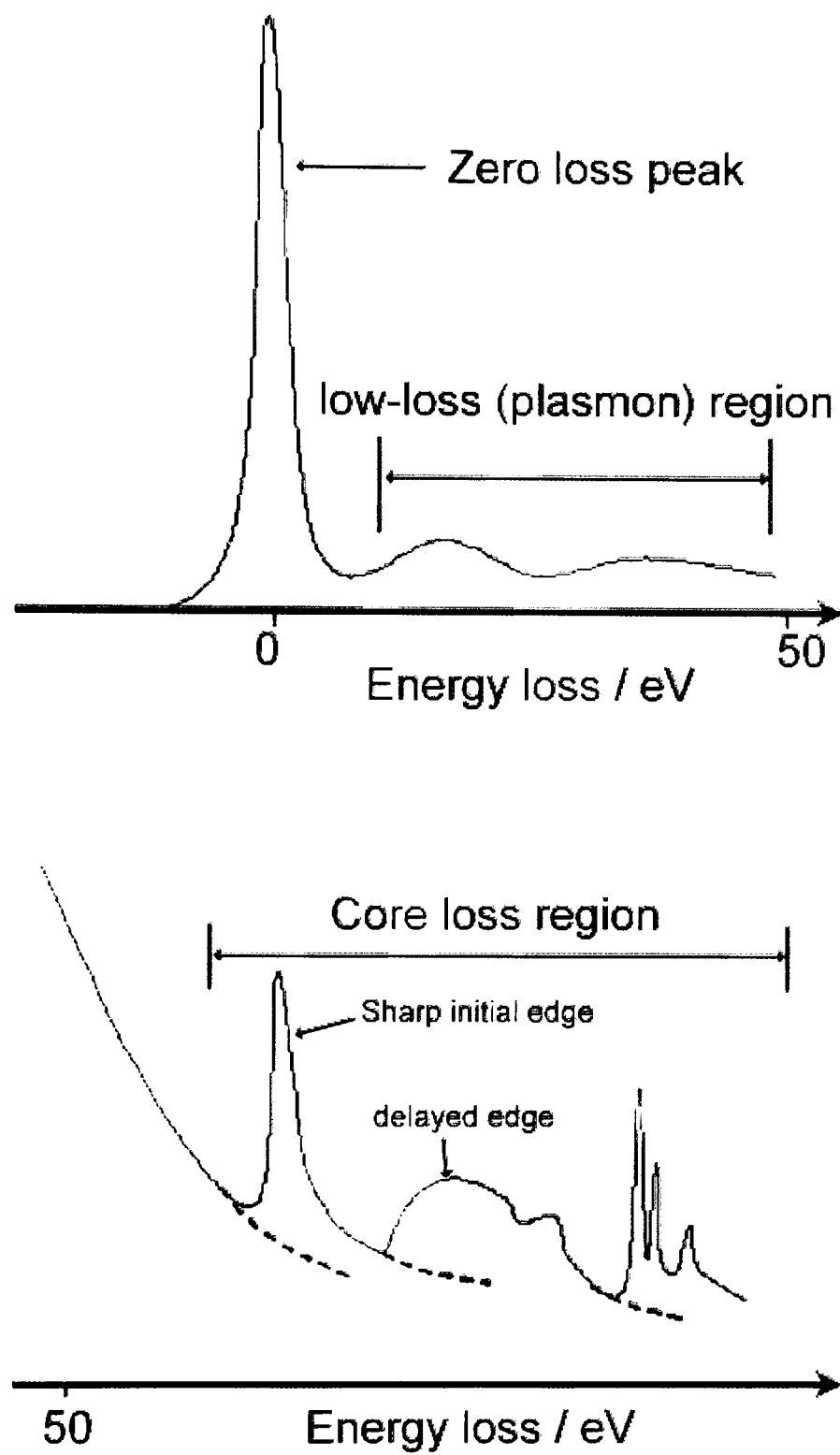
Figure 2.6: *Schematic showing the main features of an EELS spectrum.*

ing tail with the onset of the edge representing the binding energy of the core electron. There is fine structure within the tail due to bonding effects, this is known as the energy loss near edge structure (ELNES), and further fine oscillations known as extended energy loss fine structure (EXELFS). The edges are denoted K, L, M etc. where each represents a core shell ionisation. Thus, K = 1s electrons, L = 2s, 2p, M = 3s, 3p, 3d etc. with increasing energy. These edges are characteristic of the atom present, as the atomic number increases the more energy is required to remove an electron from a specific shell.

Conventional TEM has been used to image boundary regions at high resolution (HRTEM). While there are some limitations to this technique, such as rapid sample damage in oxide ceramics and non-trivial imaging artefacts, it is applicable to grain boundary analysis by identifying possible second phases and amorphous/disordered areas[82]. More recently, aberration corrected STEM has improved the resolution of scanning probes such that HAADF imaging resolution can match, if not better, that of conventional HRTEM. This new development is discussed in detail in chapter 6.1.1.

2.3.2   Grain Boundary Analysis by SIMS

The dopant distribution of rare earth doped alumina has been mapped using imaging secondary ion mass spectrometry (SIMS)[83, 84, 85]. This technique involves sputtering of highly polished alumina surfaces with ions from a liquid ion source and analysing the charged fragments in a modified magnetic sector mass spectrometer. The ion is raster scanned across a small region of the sample with each pixel $\sim$ 20 nm in size. The yield of RE containing compounds is compared at each point so that a map of relative concentration between grain boundaries and grain interiors can be seen. The limitation of this technique is the spatial resolution which, in the above mentioned papers, is limited to $\sim$ 1 μm. SIMS can provide excellent depth resolution and highly sensitive compositional analysis.

Chapter 3

Experimental Procedures

3.1 Introduction

This chapter provides a description of all the techniques used from the powder processing and sintering, to the microscopy and other analytical techniques.

3.2 Oxide Ceramic Powders.

This project deals with two oxide ceramics, alumina (Al_2O_3), and magnesium aluminate spinel ($MgAl_2O_4$). All powders used were sourced from commercial suppliers and are listed in table 3.1. The batches were produced by various methods leading to differences in powder size, impurity content and agglomeration. The highest grade powders are the Taimicron alumina and Baikowski spinel, and from these powder bases, various processed, doped and mixed powders were produced. In all cases, the eventual microstructure of the sintered specimens was highly dependent on the starting powder.

In the case of spinel, the powder selection was easy as only two manufacturers produce commercially available fine, high purity, highly stoichiometric powder. Batches of Baikowski S30CR powder were used throughout, except where specifically stated. For

alumina, Taimicron Tm-DAR was the powder of choice for its high purity and fine particle size. One notable difference between the S30 and Tm-Dar powders is the sulphur content in the S30. Such a large impurity content relative to the other impurities (and indeed the dopant level, typically 500 ppm) is an important consideration.

	Purity	Mean particle size (μm)	Surface area ($\frac{m^2}{g}$)	Trace impurities (ppm)					
Alumina				Na	Si	Fe	Ca	K	Mg
Ceralox APA-0.5*	99.97	0.4	8	5	95	110	5	-	-
Taimicron TM-DAR (Taimei CHBS Chemicals, Tokyo, Japan)	99.99	0.2	13.4	2	4	4	1	1	1
Magnesium aluminate spinel				Na	Si	Fe	Ca	K	S
Spinel DBM AF (Condea Vista Co., Ceralox division, Arizona, USA.)	>99	0.82	10.9	<4	52	10	19	-	-
S30CR Spinel (Baikowski Chimie, France.)	99.9	0.16	30	6.6	14	6	2.3	21	800

Table 3.1: *Summary of the commercial oxide powders used to manufacture ceramic samples.*

3.2.1 Powder Processing

Initial sample preparation showed how sensitive the powders were to contamination. A regimen of minimum intervention was employed such that the number of processing steps was kept to a minimum and care was taken during handling powders and cleaning apparatus.

Much of this thesis deals with the effects of RE and other element doping on the sintering behaviour and properties of the ceramic. In the case of RE doping, RE-nitrate compounds were used exclusively (listed in table 3.2), where 'RE' represents the specific rare earth element, as they are readily soluble in solvents (propan-2-ol used here). These compounds decompose well below the ceramic sintering temperature and the decomposed elements do not interfere with the sintering process. Unless otherwise specified, the level of doping was 500 ppm by cation weight.

Cation	Precursor compound	FW / amu	Z(Cation)	Atomic weight (Cation)
Eu	Europium (III) Nitrate Pentahydrate	428.05	63	151.95
Yb	Ytterbium (III) Nitrate Pentahydrate	449.13	70	173.04
Tm	Thulium (III) Nitrate Pentahydrate	445.03	69	168.93
La	Lanthanum (III) Nitrate Hydrate	415.01	57	138.91
Gd	Gadolinium (III) Nitrate Hexahydrate	451.36	64	157.25
S	Flowers of Sulphur	32.066	16	32.07*

Table 3.2: *Summary of the RE dopant cations and their precursor compounds. *atomic weight*

Accepted methods of doping powders usually involve dissolving the dopant in solvent and adding it to a suspension of the powder in the same solvent, ball milling the slurry, drying (by evaporation) and finally calcining (heat treatment to remove organic compounds). It was found in earlier work by West[86] that the number of processing steps led to an increase in contamination and the production of hard agglomerates in the calcining step, both of which led to problems (described later). Replacing the milling stage with a mixing stage, whereby the milling balls are removed and the slurry is mixed in a clean container for a long period (typically 24 hours), led to a reduction in contamination. The simple mixing provided a satisfactory homogeneous dispersion of the dopant. The removal of the calcining step was compensated by the addition of the burn-out phase in the sintering run.

The final processing stage for a doped powder consisted of suspending the high purity powder in propan-2-ol at approx 10 - 20% solids loading, followed by mixing for 30 mins to fully wet the powder. The required amount of RE-nitrate was then added to a measured quantity of the appropriate solvent and mixed for 30 mins until fully dissolved. The nitrate solution was then poured into the powder slurry and mixed for a further 24 hours. Once fully mixed, the slurry was poured into an evaporating dish, covered with a breathable membrane to prevent contamination and dried at room temparature for 12 hours. To maintain consistency, the undoped samples followed exactly the same procedure, without the addition of the nitrate solution.

Prior to sintering, various procedures can be used to prepare a green body, these are pressed compacts formed either via simple dry pressing or colloidal filter pressing. Dry pressing can be achieved either uniaxially or isostatically. A number of samples were cold isostatically pressed (CIP) by encasing the powder or a uniaxially pressed pellet in a non permeable membrane, then submerging in water and subjecting to a pressure of 100 MPa. The green bodies were removed from the membrane prior to sintering. Uniaxially

pressed pellets were formed in a 10 mm diameter steel die subjected to a pressure of 50 MPa, stearic acid/acetone solution was used for die wall lubrication.

3.2.2 The Filter Press

Pressure filtration (or filter press, FP) was conducted by producing a powder plus solvent slurry then filtering the solvent by the application of an external pressure. The advantages are that the choice of solvent and additives are such that there is maximum dispersion of powder, thus reducing the viscosity and agglomerate formation. For some samples a PVA binder was added (approximately 1% in solution) to increase the green strength of the body. Highly dense green bodies were produced by this method. The powder was prepared similarly to the initial processing, once the slurry had been made it was left to mix for 24 hours. Before each filter press run the slurry was mixed again for 30 mins.

The filter press consisted of a steel die with a removable steel sleeve. O-rings on the underside seal against a lower assembly into which the die was placed. Between the die and the assembly sat a layer of filter paper, beneath that a porous spacer made of $\sim$0.5 mm diameter brass spheres. The whole assembly sat on a tripod within which stood a container for the filtered solvent from the pressed slurry. This whole apparatus was set within an Instron 1120 testing rig such that the load could be precisely controlled. A stainless steel spacer was inserted above the slurry within the die sleeve, then a steel rod with an O-ring around the bottom was pushed on to the spacer. To maintain the pressure a maximum load was set to cycle such that the pressure was removed when the load reached the set maximum then reapplied as the slurry relaxed. This was typically left cycling overnight. A typical cycling schedule is shown in figure 3.1 from the pen chart recorder on the testing rig.
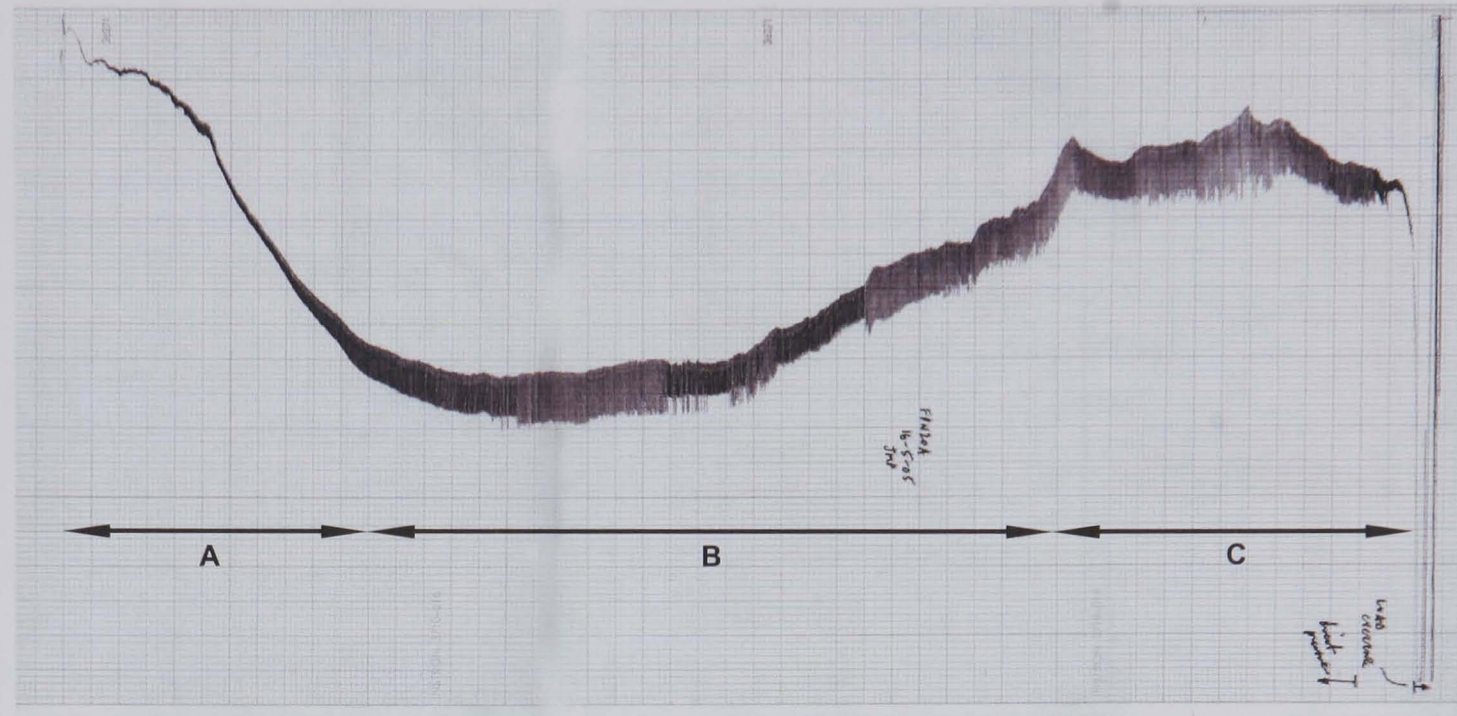
Figure 3.1: *Example of load against time for a typical filter pressed sample. Section A) Initial press, low resistance, B) Cyclic loading as particles within slurry redistribute, C) Final press with cyclic loading until further compression ceases (500 N max pressure).*

Figure 3.2 is a schematic of a pressure filtration apparatus. It is important that the die material is appropriate to the powder used. Throughout this project a 2.5 cm hardened steel die insert with hardened steel spacer was used with an Instron (Model 1122) mechanical test rig to produce filter press samples.
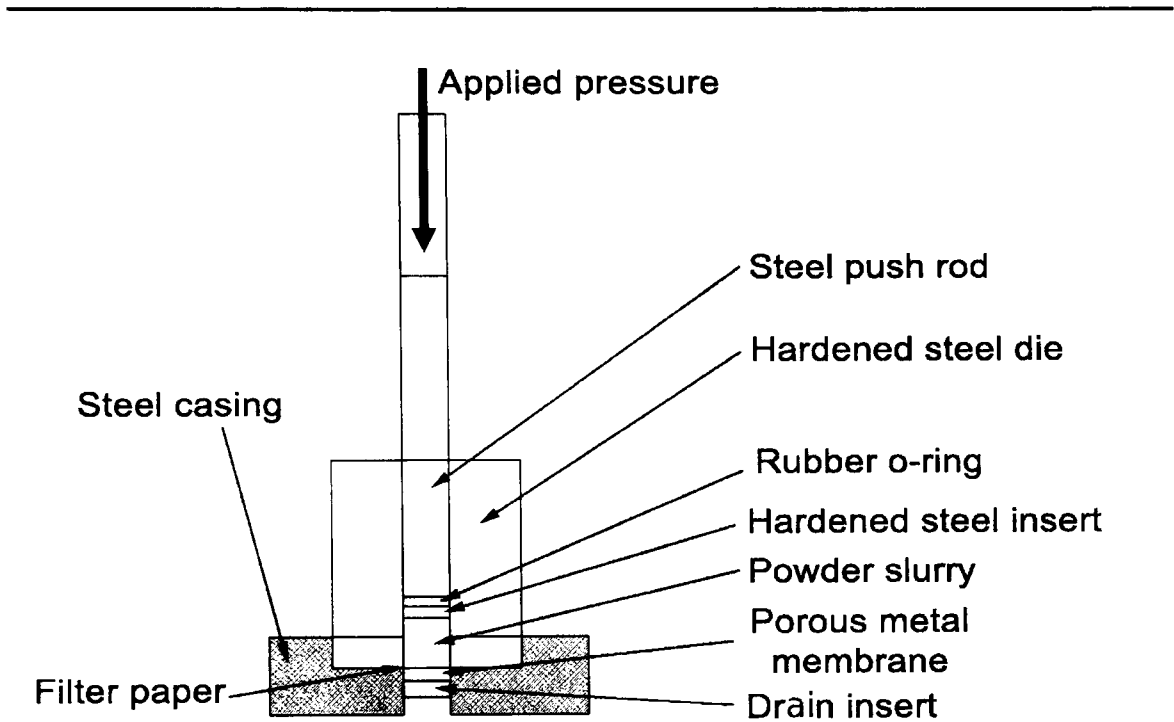
Figure 3.2: *Schematic of the University of Warwick filter press.*

3.3 Sintering

For the sintering stage there are three options; pressureless sintering, Hot Isostatic Pressing (Sinter HIP) and Hot (uniaxial) Pressing (HP).

3.3.1 Pressureless Sintering

The most simple of the three is pressureless sintering where the green body is placed within a furnace (this can be under vacuum) in an inert gas or simply in air. Uniaxially pressed and filter pressed samples were pressurelessly sintered either in an alumina tube

furnace in air, or in a vacuum furnace. In both instances the body was encased in a bed of the appropriate precursor powder to minimise contamination. Samples were typically sintered at temperatures between 1400 and 1600°C and held for 2 hours at the sintering temperature. Uniaxially and cold isostatically pressed pellets mostly did not reach full density so pressure assisted sintering was adopted as the favoured technique.

3.3.2 The Hot Press

The majority of samples studied were sintered using a hot press of standard design (figure 3.3) built at the University of Warwick.
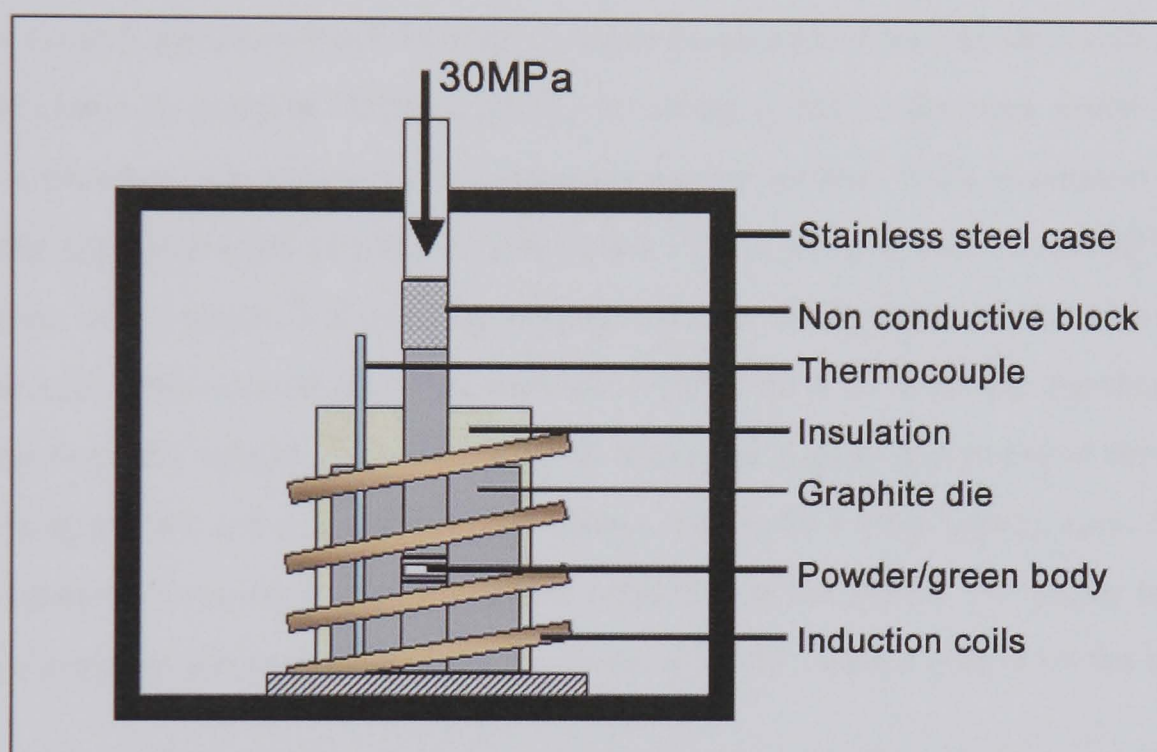
Figure 3.3: *Schematic of the University of Warwick hot press.*

Doped or undoped powder was poured directly into a 25 mm diameter graphite die. The inside surface of the die was coated with hexagonal boron nitride (BN in acetone slurry) to lubricate the die walls and to help prevent contact between the powder and the graphite. The powder was positioned between carbon (graphite) disks, molybdenum foil (0.125 mm thickness) or spacers previously sintered from the sample material

as shown in figure 3.3. The choice of spacer was dependent on the sample required as molybdenum could not be used with RE doped samples due to a reaction between the metal and the rare earth. For "model samples", a polished single crystal of the precursor powder material was carefully positioned on the spacer, the powder was then poured onto the polished side, thus creating a boundary between the single crystal of a known orientation and the polycrystalline region.

Temperatures between 1400 and 1600°C were obtained through inductive heating, whereby a current is passed through water-cooled copper coils at a frequency of 450kHz which surround a susceptor (the 25 mm graphite die). The temperature was measured with a Code C platinum/rhenium thermocouple positioned within the die as close to the sample space as possible. With graphite, hot pressing must take place under vacuum or in a nitrogen atmosphere as the susceptor readily oxidises if O_2 is present. Arcing between susceptor (die) and the rf coils occurs in low pressure environment[87]. Some problems with vacuum hot pressing occurred due to arcing between the turns of the copper coil. This occured if the vacuum was insufficient or if there was significant outgassing from the sample. The likelihood of arcing for a given gas pressure depends on both temperature and voltage, thus providing a restriction on the heating rate. Samples were produced in vacuum with reasonable reliability up to 1550°C. For higher temperatures a nitrogen atmosphere was used with no apparent adverse effects on the samples.

Both the heating and the applied load was controlled remotely via a computer with temperature, applied load and shrinkage plotted against time. Figure 3.4 shows data from a typical hot press run. To maintain consistency, the same hot press run (with variation only in temperature) was used throughout. Six sintering stages were applied. Firstly the prepress; maximum pressure was applied to remove agglomeration and homogenise the powder. This pressure was then removed and samples were rapidly heated to 800°C (below the sintering temperature) where any outgassing occurs. The tem-

40

perature was held at 800°C such that the vacuum could recover after any outgassing etc. During this initial hold the pressure is reapplied (pressure is commonly applied at roughly 60% of the sintering temperature). The samples were then heated up to sintering temperature and held for an appropriate length of time (10 minutes for all samples studied here) followed by rapid cooling once the power was removed.
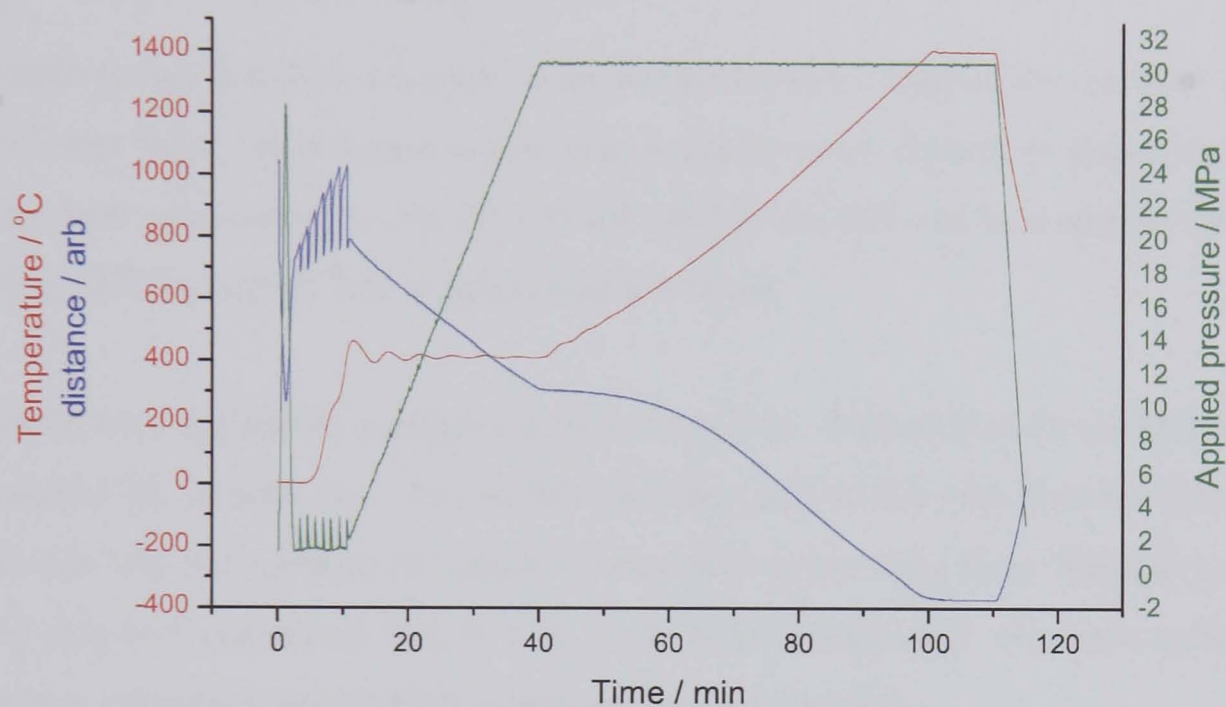
Figure 3.4: *Example runfile of a typical hot press sintering process.*

3.4 Sample Preparation

All the characterisation techniques, analytical or mechanical, require extremely high quality samples such that the results are truly representitive of the material. A brief description is given of the methods of preparation for the main techniques used.

41

The hot pressed billets were cut into several sections for the various techniques. The alumina samples proved more difficult to cut than the magnesium aluminate. A metal-bonded-diamond cutting wheel (1.2 mm thickness blade attatched to a Capco high precision cutting machine) was therefore employed in contrast to the low speed diamond wheel saw (0.3 mm thickness blade on Model 650, South Bay Technology cutting wheel rig) used for the spinel.

3.4.1 Electron Microscopy Samples

The most simple sample is a fracture cross section for SEM. Cleaned thin sections (typically 1 mm thick) were broken in half and mounted on an aluminium stub. Silver or carbon paint was applied to the sides to aid conduction, followed by a sputter coating (Polaron sputter coater) with a gold/palladium target.

For most other techniques, a polished surface is required. Cleaned sections were mounted on bakelite blocks with wax. The surface was then ground flat with a coarse diamond grinding wheel and polished on various chemo-textile pads using water based polycrystalline diamond suspensions (15, 9, 6, 3, 1 μm respectively) using automatic polishing apparatus (Buehler Phoenix 4000 sample praparation system).

For TEM samples, one side of a thin section was polished, as above, then turned over and ground until appoximately 60 μm thick before a final polish was applied until thickness approached 30 μm. Further thinning of TEM sections was performed with an ion beam milling machine (5 keV argon, slow rotation double beam, Gatan 691 Precision Ion Milling unit PIPS) to electron transparency. Beaming took place with a beam incidence angle of 10° until a small hole was observed, then a lower angle (typically between 2 - 4° was selected for a final 10 - 20 minutes beam time. The milled samples were then mounted on standard 3 mm diameter copper foil rings using an epoxy resin. Some more fragile samples were mounted on the copper ring prior to milling. The milling process

must be closely monitored for hard and brittle materials as extensive beaming can lead to a degradation in the sample quality. Samples were plasma cleaned prior to analysis (25% O_2, 75% He Fischione 1020 Plasma cleaner). Treatment time varied between 30 seconds and 5 minutes depending on the cleanliness of the sample, however, in most cases the plasma cleaner removed all traces of contamination. Plasma cleaning did not adversely affect the samples.

For EBSD, a very high surface quality was required, therefore a final polish with colloidal silica (0.06 μm) was applied, followed by careful cleaning and sputter coating where appropriate. The surface finish is especially important for EBSD, the cutting/grinding/polishing processes cause subsurface damage that extends well below the polished surface. It has been quoted that the damage reaches down to three times the last polishing media size (for example 45 μm after a 15 μm diamond paste stage). Thus the final stages require that finer polishing paste and long polishing times were used. In general gold/palladium sputter coating was applied, at approximately 15 mA for 30 seconds. Coating tests using a glass slide were conducted before any sample was placed in the coater.

For SIMS, samples were prepared similarly to EBSD samples, with a highly polished surface. However further cleaning culminating in a wash with high purity IPA was neccesary to remove as much organic residue as possible as a result of the extreme sensitivity of the instrument.

Wear samples were prepared in a similar manner to the EBSD samples, however, they were mounted within bakelite to provide a more solid base to sit within the wear test apparatus.

For grain size determination and specific SIMS experiments, thermal etching was per-

formed. EBSD quality surface finish samples were placed on clean alumina sheets within a furnace and heated to etching temperature 1100°C with hold time of 1 hour for spinel and 3 hours for alumina.

3.4.2 Mechanical and Optical Samples

For hardness, fracture toughness, a small section was encased towards the surface of a bakelite block. The surface was then ground to reveal a portion of the sample and polished to a 1 μm mirror finish. The polished surface was used for diamond indentation as explained in section 3.5.2.

Optical samples required that the faces be parallel and polished on both sides. To achieve this, a large metal block (figure 3.5) was used and several samples were prepared simultaneously. Samples were polished to a 1 μm mirror finish then turned over to repeat the process. A small section of the mounting wax was chipped away (as shown in figure 3.5) such that a micrometer could be used to measure the thickness of the sample and ensure that it remained parallel.

3.5 Mechanical Properties

3.5.1 Density

Density was measured using the Archimedes principle of immersion in water except where green body density was required. In that instance, accurate measurements of volume were taken to find an approximate density. A balance with a below stage arm attatched was used, the arm was submerged in water in a bath below the balance. All hot pressed samples reached near theoretical density (<99.5%) so no comparison could be made within experimental error and, therefore, no conclusions could be made regarding pore content by this method.

Figure 3.5: *Metal blocks on which samples are mounted in wax then polished using automatic polishing machine. Blocks large enough to ensure parallel top and bottom surfaces.*

3.5.2 Hardness and Fracture Toughness

Hardness and fracture toughness were measured using the Vickers indentation technique with a 50 N indentation force applied normal to the polished surface using the Instron testing rig. Samples were placed on a stage and the applied load plotted against time on a chart recorder (example shown in figure 3.6).
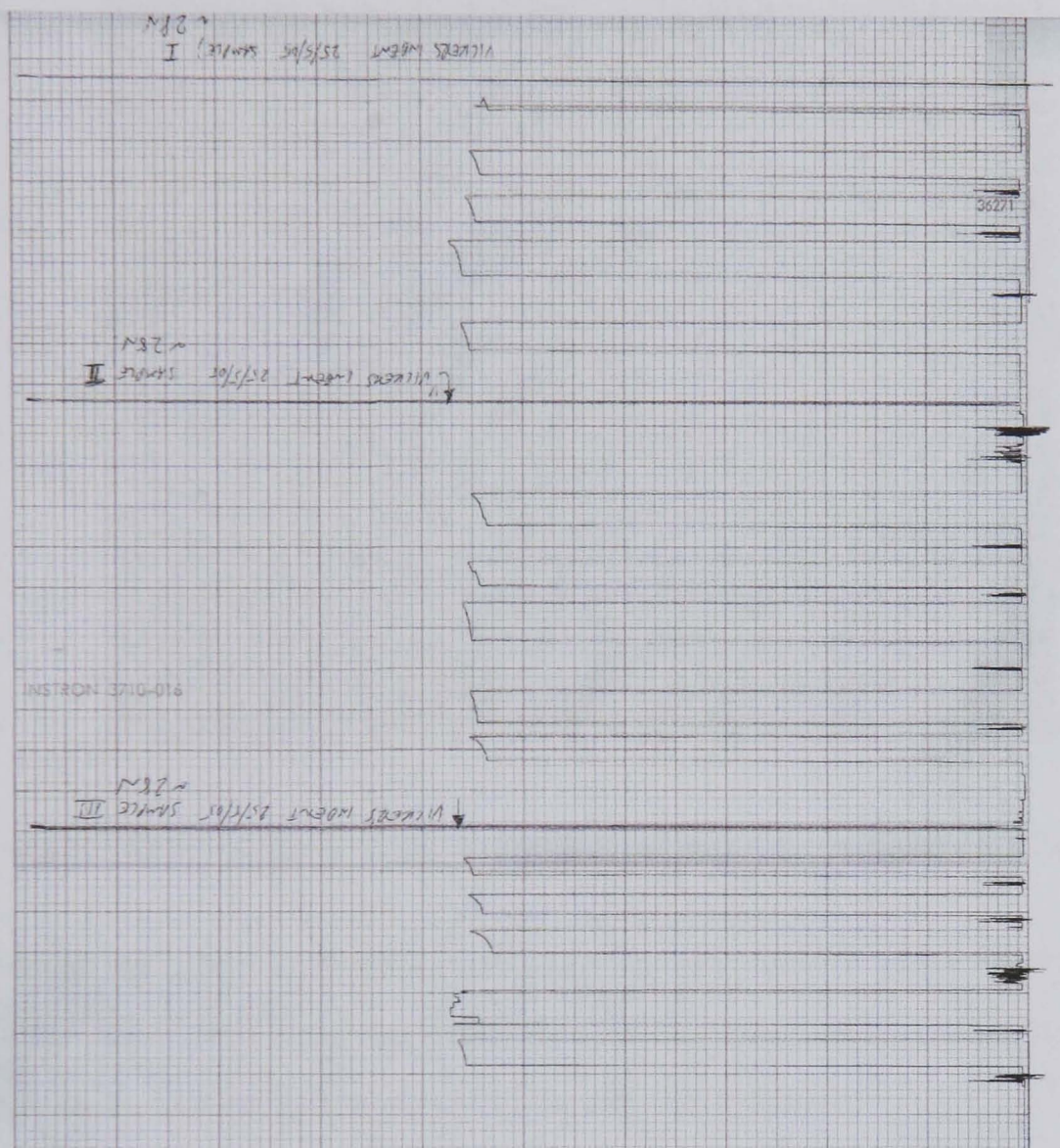
Figure 3.6: *Example of load against time for a typical set of Vickers indents. Shown are three sets of five indents.*

47

Observations and measurements of the indentation were made using an optical micro-scope (Reichert MeF2). The indentation generates a localized stress, exceeding the high yield strength of ceramics without destroying the structure, it leaves a permanent indent and a series of radial subsurface cracks above a critical load.
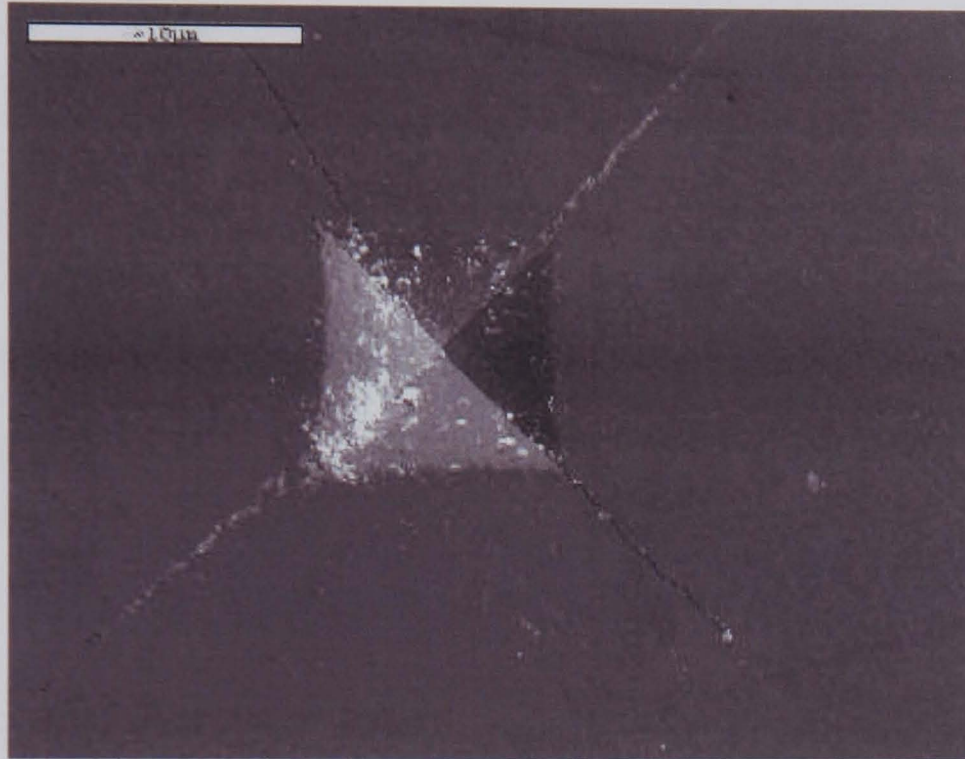
Figure 3.7: *SEM image of a Vickers indent in a polycrystalline alumina sample.*

The size of the indent is directly related to the yield strength of the bulk material, i.e. the further the indent sinks the lower the yield strength. The true hardness is defined as the load, F, divided by the projected area of the indent, A.

Fracture toughness is related to the length of the cracks propagating from the cor-ners of the indent. Both indent size and crack length are measured using an optical microscope. Values for hardness (H_V) and fracture toughness (K_{1C}) were obtained from the following equations:

$$H_V = \frac{1.8544P}{(2a)^2} \qquad (3.1)$$

Vickers hardness (H_V). Where (P) = applied indentation load (N), ($2a$) = average length of indentation diagonal (m).

Indentation fracture toughness (from Anstis [88])

$$K_{1C} = \left(\frac{E}{H_V}\right)^{0.5} P(c')^{-1.5} \qquad (3.2)$$

Where E = Young's modulus of material and c = average propagating crack length.

3.5.3 Secondary Ion Mass Spectroscopy

SIMS was employed both to examine impurity content and compare surface concentrations of elements with a high depth resolution. The analyses were performed with an Atomika 4500 SIMS instrument (University of Warwick) equipped with ultra low energy ion guns delivering Cs+ and O_2- beams [89]. Positive secondary ion data was obtained with 10 or 20 nA of 500 eV O_2- incident at 60° to the surface plane, whilst negative ions were sputtered using 11nA of 500 eV Cs+ incident at 40°. The beams were scanned over a 1 mm square to reduce the erosion rate and enhance the sampling of the surface. For all of the spectra, the mass range 0-250 Da was scanned at a rate of 10 Da/min, where 1 Da = 1 amu.

3.6 Optical Properties

The optical samples were prepared as described earlier such that a study of the optical transmission characteristics could be performed. In choosing the type of experiments it was important to consider the potential applications of such materials. All the tiles produced for optical work were made as parallel as possible and were polished to a 1 μm

mirror finish. Care was taken to thoroughly clean the optical samples before analysis as any dirt or grease on the surface would reduce transmission.

There are several ways to define the optical qualities of a material; Total Forward Transmission (TFT). Real in-line transmission (RIT) and wavelength dependent transmission (WDT). As possible candidate materials for hard window applications, the materials must be transparent. Transparency is defined as having the property of transmitting light, so as to render bodies lying beyond completely visible[90]. The TFT simply represents the total transmitted light, regardless of angle, i.e. the translucency. While it is useful in determining the translucency, it cannot be used as a measure of transparency. The RIT is defined as the amount of light transmitted within a small angle, i.e. direct, unscattered light. A more detailed explanation is given in section 8.3.

To measure RIT an optical bench was set up as in figure 3.8. A class 3B 4 mW He-Ne (λ = 633.5 nm) laser beam was directed at a 100 mm^2 photodiode detector set 1 m from the laser. The sample was positioned 1 cm from the end of the laser so that the beam entered normal to the surface. This is repeated with a more powerful, high quality 300 mW frequency doubled YAG (class IV) laser (λ = 532 nm). The YAG laser required attenuating blocks to be positioned between the beam and the sample such that the detector did not become saturated. All experiments were calibrated using a polished single crystal sapphire standard.

This set-up was also used to measure the transmission at different collection angles. For each sample, the detector was moved to four different positions between the maximum (1 m) and minimum (0 m, effectively the TFT of the sample). This quality of the YAG laser meant that without a sample present there were negligible losses so it was straightforward to compare the divergence due to scatter from the various samples.
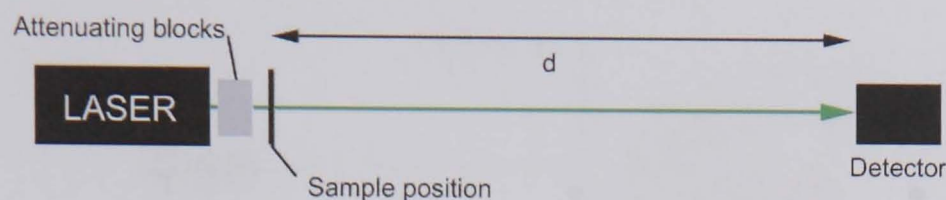
Figure 3.8: *Schematic of the apparatus used for measuring RIT.*

Percentage RIT is given by:

$$\frac{(S-T)}{(X-T)} \times 100 = \%transmission \tag{3.3}$$

Where S = voltage detected with sample, X = voltage detected with laser only (background), T = zero offset, voltage detected without laser.

The scattering profile, representing the angular dependence on intensity, was measured by two methods; an optical bench with the He-Ne laser directed at the sample approximately 1 m away; and a green YAG laser shone through a sample onto a CCD.

In the first method, the sample was positioned in the centre of a goniometer. A 25 mm^2 detector was placed on an arm with angular adjustment with 1/3 degree precision, and 'as the arm moved around' the intensity at a given angle could be measured. At high angles, however, the detector efficiency was poor and produced a noisy signal.

The second method consisted of a green YAG laser shone through a sample on to a simple CCD arrayconnected directly to a computer. The scattering profile was captured as an image and analysed using "Image J" processing software[91]. This method was simpler and gave a clearer profile of the angular dependence, however, it could only compare the profile shapes. This was because it could not provide a quantitative measure of intensity as the camera automatically corrected the gain.
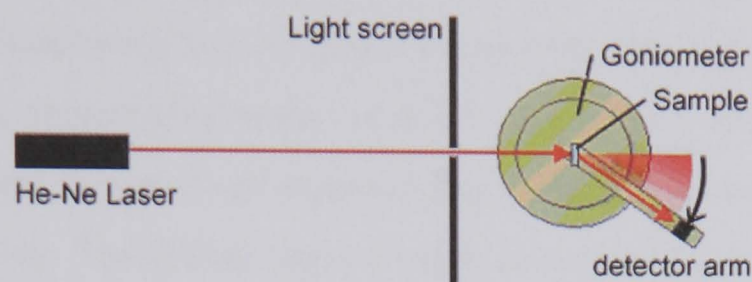
Figure 3.9: *Schematic of the apparatus used for measuring light scatter.*

3.7   Microstructural Studies

3.7.1   Transmission Electron Microscopy.

Transmission electron microscopy was performed using a JEOL 2000FX (University of Warwick) and an FEI F20 Tecnai field emmission (FEG) TEM (Midlands shared facility - Warwick, Birmingham and Loughborough). Both instruments are 200 kV but have different sources. The JEOL 2000FX employs a conventional tungsten filament source whereas the Tecnai contains a Schottky field emission source. The FEG is a tungsten needle, rather than a filament, coated with ZrO_2 to reduce the work function for electron emission. It produces a thermally assisted field emission ($\sim$1000 times brighter than standard filament source) beam that can be focused to a highly coherent fine probe ($<$ 1 nm) with a high current density.

Scanning Transmission Electron Microscopy

The Tecnai is a versatile instrument, with the ability to image conventionally and in scanning mode (STEM). In STEM, there is a choice of detection mode, bright field (BF), dark field (DF) or HAADF (model 3000, Fischione Instruments). The HAADF detector is an annular ring set at a distance (camera length) from the sample above

the projection screen. The HAADF detector provides atomic number (Z) contrast. The atomic number contrast arises from electrons interacting with atomic nuclei, strongly scattering the beam necessitating large collection angles. To collect these scattered electrons a short camera length is set, however, there is usually some element of diffraction contrast remaining. The shorter camera length decreases the overal intensity of the image (increasing noise). It also requires a uniformly thin sample since thicker regions increase scatter and lead to added thickness contrast in the image.

The Tecnai is controlled remotely via its computer, STEM imaging is performed using the Tecnical imaging and analysis (TIA) software as part of the microscope control software. In STEM, the microscope is operated in diffraction mode with a nano probe beam, this is automatically optimised for STEM and only minor adjustments are necessary. Spot size, camera length and detector type are selected within the software and only sample movement, tilt and the beam alignments are controlled manually. Adjustments in spot size and stigmation were made to optimise the results. The STEM was also used for compositonal analysis as described below.

High Resolution TEM

The narrow electron beam of the Tecnai allows high resolution phase contrast imaging, used here to image grain boundaries. With polycrystalline samples it is possible to find boundaries that are well aligned with respect to the incident beam. Fine adjustments are made such that the boundary is aligned parallel, and lattice fringes are observed either side of the boundary. Boundaries were imaged using a Gatan Multiscan CCD camera. To reduce noise, the camera was cooled with a Peltier cooling system. The high beam current and the susceptibility of the materials to damage (specifically alumina) resulted in a restriction on imaging time for a given region.
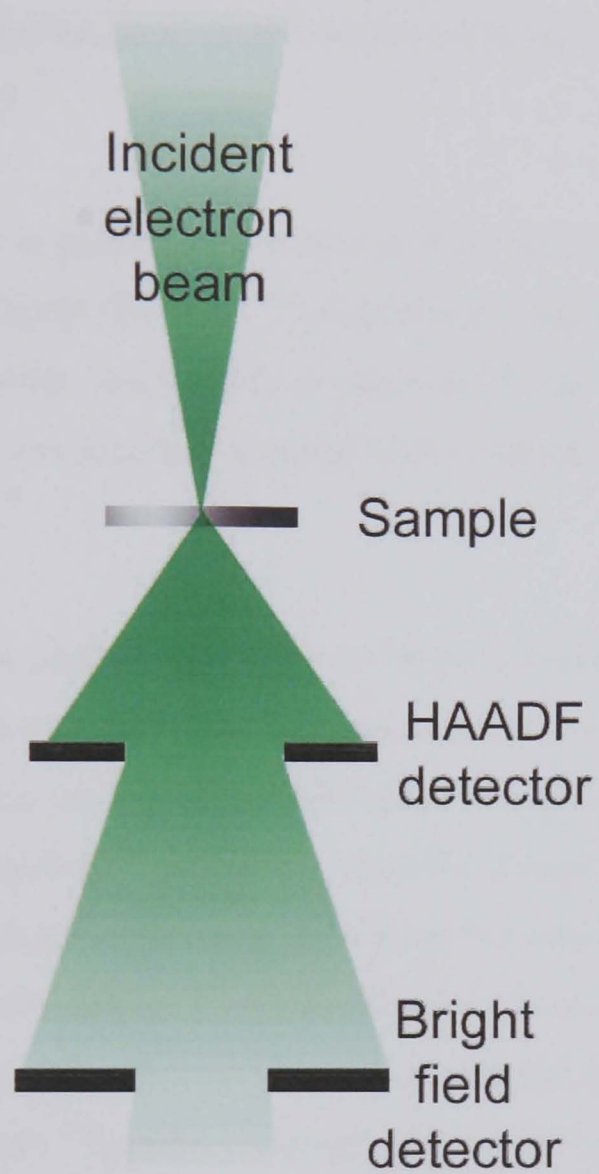
Figure 3.10: *Schematic of the detectors within a TEM/STEM column and their position relative to a sample.*

3.7.2 Energy Dispersive X-ray Spectroscopy

In both TEMs, EDS can be used to find the elemental composition of a specific region of the sample. In the Tecnai, the high beam current with relatively smaller spot size mean that good quantitative line scans with high resolution can be performed. It uses an Oxford Link ISIS windowless detector system controlled via a microprocessor separate to the microscope control.

The Tecnai EDS detector is positioned such that samples must be tilted 18° towards the detector for optimum collector efficiency. To maximise the signal at the detector a large aperture is inserted, however, this leads to a reduction in spatial resolution. Optimisation of the counts/resolution issue was essential when analysing the grain boundaries of the materials.

Simple spot analysis was used to determine elemental composition of specific points or to verify the presence of a particular element, however, for most analyses the line scan mode was used. Line scans provide information about the image intensity across the line as well as the elemental composition. Specific elements can be chosen for the line scan and individual plots can be made. The image intensity scan can verify the position of certain artefacts with respect to the composition, for example heavy elements at grain boundaries appear as a bright peak on the line scan and can be directly compared with the elemental line scan. Typically, a background scan for an element known not to be present in the sample was captured to measure any variation in background across the boundary.

Problems with EDS included the drift of samples that are charging, which led to the broadening of features, notably grain boundaries. Also, if boundaries were not perfectly aligned (parallel to the incident beam), a broader feature will be plotted rather than an accurate representation of the boundary. With a known probe size, the full width at half

maximum (FWHM) of a peak can provide the maximum width of the grain boundary region.

3.7.3 The SuperSTEM

The SuperSTEM facility at Daresbury Laboratories was used for high resolution STEM imaging and parallel electron energy loss spectrosopy (PEELS) analysis. A review of the principles and practice of aberration corrected imaging will be presented in chapter 6.

The SuperSTEM consists of a VG 100kV dedicated STEM equipped with a Nion Co. spherical aberration corrector. The column is situated within a specially designed building where possible vibration sources are eliminated using a selection of techniques. Acoustic shielding on two walls and the ceiling, removes any sound vibrations around the column. The air conditioning is set so that the airflow does not present even a slight pressure on the instrument and the microscope room is built such that it is isolated from the rest of the building.

The FEG sits at the bottom of the column with the aberration corrector above the first condenser lens. The remaining optics and sample holder are positioned above with the (PEELS) at the top of the column. Images were acquired using the HAADF detector with a collection angle between 70 and 210 mrads. More recently[1] a bright field detector has been added to the column in addition to the HAADF detector such that both BF and HAADF images could be aquired simulaneously. The focus was slightly different for each detector, however it was useful to have the BF scan to ensure the correct region was being imaged. The PEELS data was gathered as line scans across boundaries, similarly to EDS in the Tecnai. A PEELS probe of $\sim$0.2 nm was used, with each point having an acquisition time of $\sim$1 s.

---

[1]Chapter 6 includes images aquired before and after the BF detector was installed such that later results include BF and HAADF images, wheras earlier results contain only HAADF images.

3.7.4 Scanning Electron Microscopy

Two SEMs were used, the Jeol 6100 and the Zeiss Supra 55VP. The 6100 was mainly used for routine imaging to check the quality of surface finish or for topographic images of samples with large grain size. The Zeiss has a FEG source and was, therefore, used to image samples with sub micron grains. Both instruments were equipped with EDS (TSL EDAX). The FEG SEM was fundamental for unambiguously differentiating between fracture type in fracture section analysis (section 7.4). The resolution was high enough such that subtle fracture elements such as intergranular pores could be identified. The Zeiss routinely used three detection modes; backscatter, in-lens secondary and conventional secondary. While conventional secondary electron imaging was useful, the in-lens detector was used for the highest resolution work as an extremely small working distance could be used so that a small probe still has high signal. The limitation to the in-lens detector is the reduced depth of field, however, for thermally etched surfaces and most fracture surfaces this was unimportant.

Thermally etched samples were used for grain size measurements, SEM images were analysed using the Image-J image processing software package [91]. The image was adjusted to provide maximum contrast at grain boundaries. By assuming the grains are spheres, the average cross sectional surface of a sphere of diameter g is given by $(1/6)\pi g^2$ thus approximating the grains as circles with an average radius, G, the true grain size $g \simeq 1.225G$. For consistency, images were chosen with a large number of grains present. Average grain diameter was measured by marking a line acrosss a large number of grains and counting the number of boundaries intersected by the line (linear intercept method).

3.7.5 Electron Backscatter Diffraction

The use of EBSD allows the measurement of crystal orientation with respect to a given plane. This information can be used for various purposes including phase recognition,

texture analysis, grain misorientation and grain size/size distribution statistics. Here, two instruments were used; firstly the Philips XL30 FEG SEM (University of Manchester Institute of Science and Technology, UMIST), and the Zeiss Leo FEG SEM (University of Warwick) operating at various voltages up to 20 kV depending on sample surface finish and quality/thickness of conductive coatings.

The sample is tilted such that the polished surface is ~70° to the electron beam and facing a camera that is brought into the chamber and positioned adjacent to the sample. Backscattered (elastically scattered) electrons are emitted from the sample surface (to a depth of ~10 - 50 nm depending on the atomic number of the sample) having diffracted through the top few planes of the crystal lattice. The backscattered electrons form a Kikuchi pattern on a phosphor screen positioned in front of the camera lens. To succesfully index (i.e. identify the characteristic pattern due to a particular crystal), the surface must be strain free so that damage from sample preparation and polishing is removed. The non-conductive oxides studied here required a thin (~0.5 nm) coating of either Au/Pd or Pt. It was essential that the coating was not too thick otherwise the signal was poor, and not too thin otherwise charging would occur.

The EBSD software (HKL technology at UMIST and TSL-OEM at the University of Warwick) identified each band on the Kikuchi pattern and was able to calculate the orientation of the grain that was illuminated. The beam was scanned across a large area containing several grains to produce maps of grain orientation, boundary misorientation, existance of coincident site lattice (CSL) boundaries or image quality (or indeed many other representations of the aquired data).

Figure 3.11 shows a schematic of the EBSD apparatus within a conventional SEM; the incident electron beam is rastered across a selected region of the sample. A Kikuchi pattern from a spinel sample, both imaged by the camera and with overlaid information

showing the lattice orientation information generated by the software, is shown in figure 3.12.
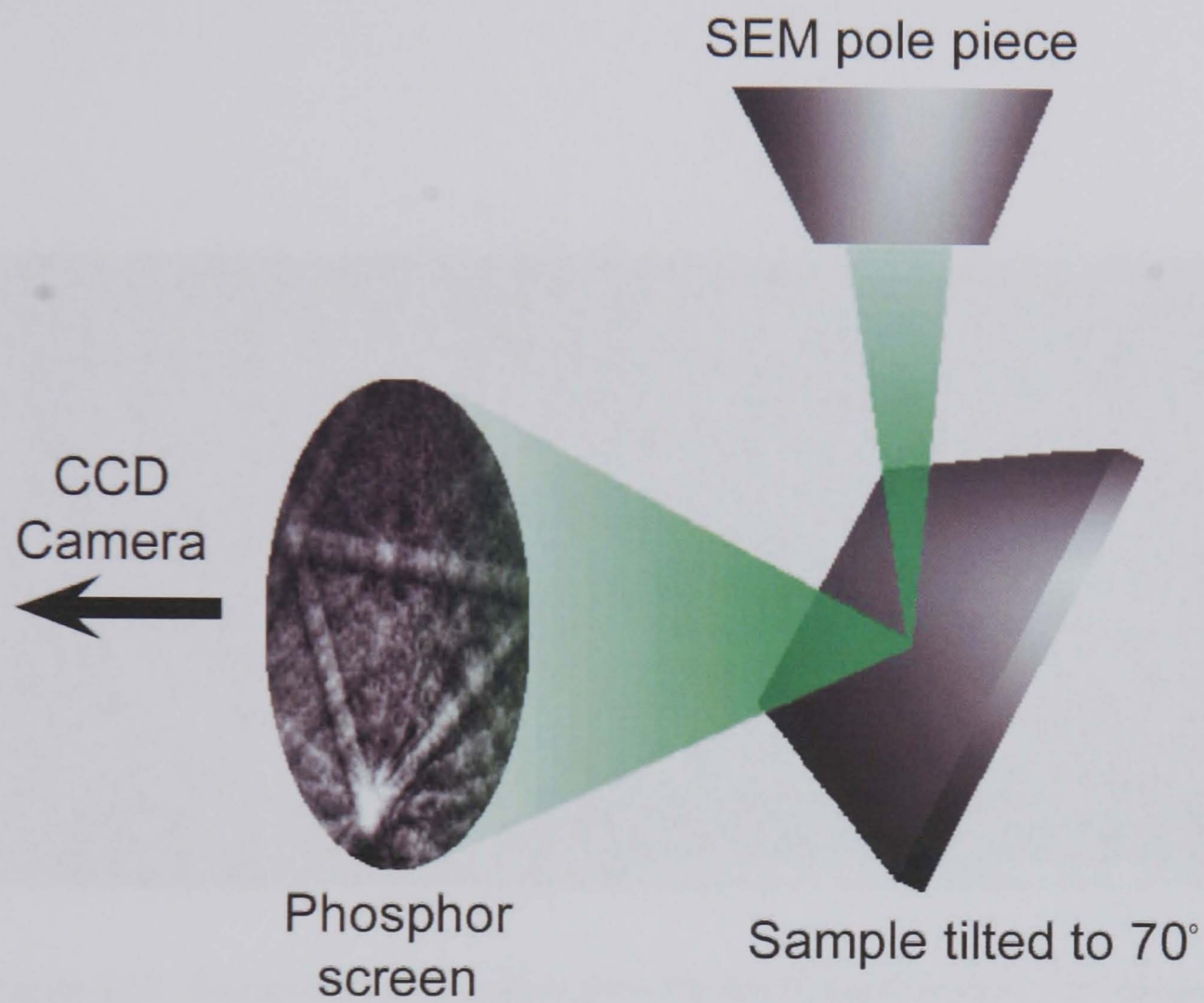
Figure 3.11: *Schematic of the main features of an EBSD system within a SEM.*

Further EBSD maps were aquired of TEM thin films for grain orientation mapping prior to analysis in the TEM. This required careful manipulation of the TEM sample so that it could be subsequently imaged in the TEM. Further details of this technique can be found in section 4.1.7.
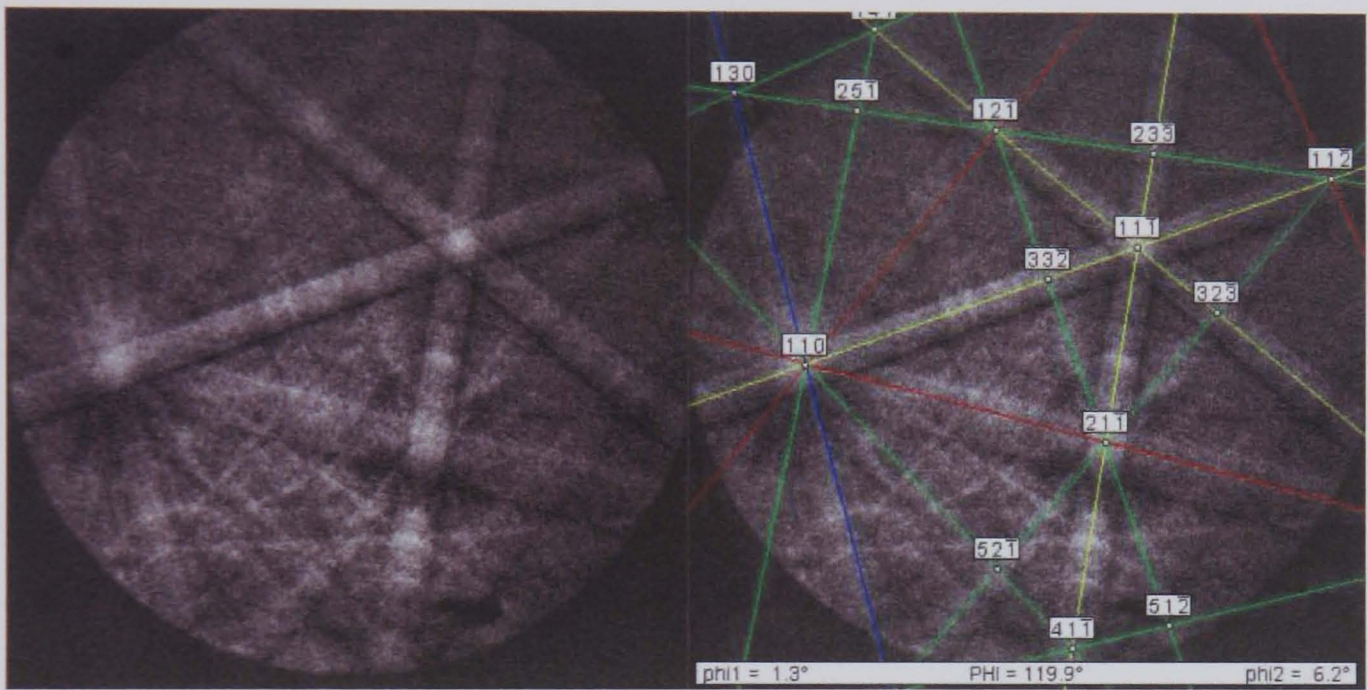
Figure 3.12: *Example Kikuchi pattern from Eu doped spinel sample. The image on the right shows succesfully indexed bands.*

Chapter 4

Processing and Sinterability of Oxide Ceramics

4.1 Introduction

The processing of ceramics from powder to final shaped product has a number of steps and much research has been undertaken over the years to improve both the final products in terms of their properties but also the processing methods to reduce the time and cost of production.

In order to study the effect of rare earth dopants on the properties of oxide ceramics it is important to produce comparable samples. For example, density has an effect on each of the properties that are studied here; hardness, fracture toughness, light scattering etc. The methods of microanalysis that have been used also rely on the homogeneity of samples. Electron microscopy, specifically TEM, will only probe very small sections of the samples so there must be confidence that these sections are representitive of the whole sample. The microstructure study is detailed in later chapters.

The focus of this chapter is the effect of RE elements on the processing of the ox-

61

ide ceramics.

4.1.1 Hot Pressed Ceramics

It has been mentioned in the experimental procedures that the number of processing steps have been minimised. The most important step in the comparison with similar studies is the removal of the calcining process. Calcining is the process of heating a powder so that any residual organic component may be burned out. The 'burn out' was added as a component of the hot press run rather than as a separate step. It was found[92] that the decomposition of the RE containing compounds (RE-nitrates to RE oxides) would occur readily within a reducing environment (i.e. vacuum or flowing nitrogen). Thus the time/temperature profile of a typical run included a calcining step. By taking the burn out phase from the powder handling to within the sintering phase of the processing contamination would be reduced.

The homogeneity of hot pressed samples was generally good. A few specific samples (mainly spinel) showed increased grain size at the edges in contact with the die walls or spacer, this was limited to within 1 mm of the sample edges. The prepress stage of the hot press run removed the vast majority of hard agglomerates that may have formed in previous steps and there is no evidence to suggest that the press was not uniform over the whole diameter. Any inhomogeneity in dopant distribution came from inadequate mixing, this was solved by increasing the mixing time of the powder slurry.

Run profiles

A typical runfile for the hot press was presented earlier. The heating rate, hold temperature and hold time were chosen either due to equipment restrictions or to maintain consistency with previous work. The heating rate of $10°\text{min}^{-1}$ was a limitation of the University of Warwick hot press as higher heating rates could not be controlled precisely. The applied pressure was limited by the strength of the graphite die, spacers and blocks.

Figure 4.1: *Selection of spinels showing sintering inhomogeneities and edge impurities.*

The temperature was measured with a platinum/rhodium thermocouple rather than an optical pyrometer as the thermocouple could be placed within the die, near to the sample itself so the measured temperature was indicative of the sample temperature rather than the die surface temperature.

Hot pressing of doped samples

It was not possible to use the previously succesful molybdenum disk spacers for hot pressing of rare earth dopants due to a reaction between the RE and a molybdenum oxide (MoO_3) layer. The reaction formed so called 'tungsten bronze' compound [93] leaching the RE from the samples. The molybdenum spacers were removed from the process to make the doped and undoped samples more comparable. A side effect of removing the Mo spacers was a discolouration of the sintered samples. Previous work by Komerek [94] and West [95] supports the idea that the graphite die and the reducing atmosphere leads to a reduction of oxides to carbides within the sample, thus the Mo spacers provide a barrier to this reaction and without them the discolouration takes places. It was decided that the slight discolouration was less important than the RE-Mo reaction thus carbon spacers were used. It will be shown that this affected the optical properties so that some of the doped optical samples were produced with spacers made of the undoped oxide.

4.1.2 Filter Pressed Ceramics

The filter press die

As mentioned in chapter 3.7.5, an Instron testing machine was used to apply the load to the filter press die. Initial attempts at filter pressing caused some problems. The steel die was simply not hard enough for the oxide powders, which were extremely abrasive. The resulting scratches along the length of the inside of the die led to uneven pressure applied to the powder and inhomogeneous green bodies. A hardened steel sleeve and plunger (sleeve inside diameter 25 mm) were made to solve this problem. Further green

bodies posessed greater green body strength (they could be handled after drying without crumbling).

Slurry variables

Throughout the processing stages the aim has been to reduce the number of processing steps and maintain the simplest route to the final sample. Thus it was hoped that succesful samples could be produced without the need for calcining powders, dispersants in the slurries, binders etc. The number of variables when trying to study colloidal processing is so large they require their own programs of work, thus only a small number of variables were used here.

Solids loading

No systematic solids loading was used as there was much variation in the literature and it was heavily dependent on the quality of the powder used. The spinel powder required more liquid to wet the solid fully, and maintained a different viscosity for a given solids loading. In general the solids loading was made either just enough to wet the powder or up to a cream/milk consistency.

Binder

In some slurries, a solution of PVA was used as a binder, where PVA "dust" was dissolved in distilled water to 1% total solids loading of the eventual slurry. Other slurries were left without binder.

Choice of solvent

The choice of PVA binder (due to availability) led the choice of solvent to be distilled and deionised water. This was due to the fact that the PVA would only dissolve in IPA at a higher temperature than the evaporation temperature (at standard pressure) of IPA. Thus the PVA solution was added to the deionised water prior to addition to

the slurry.
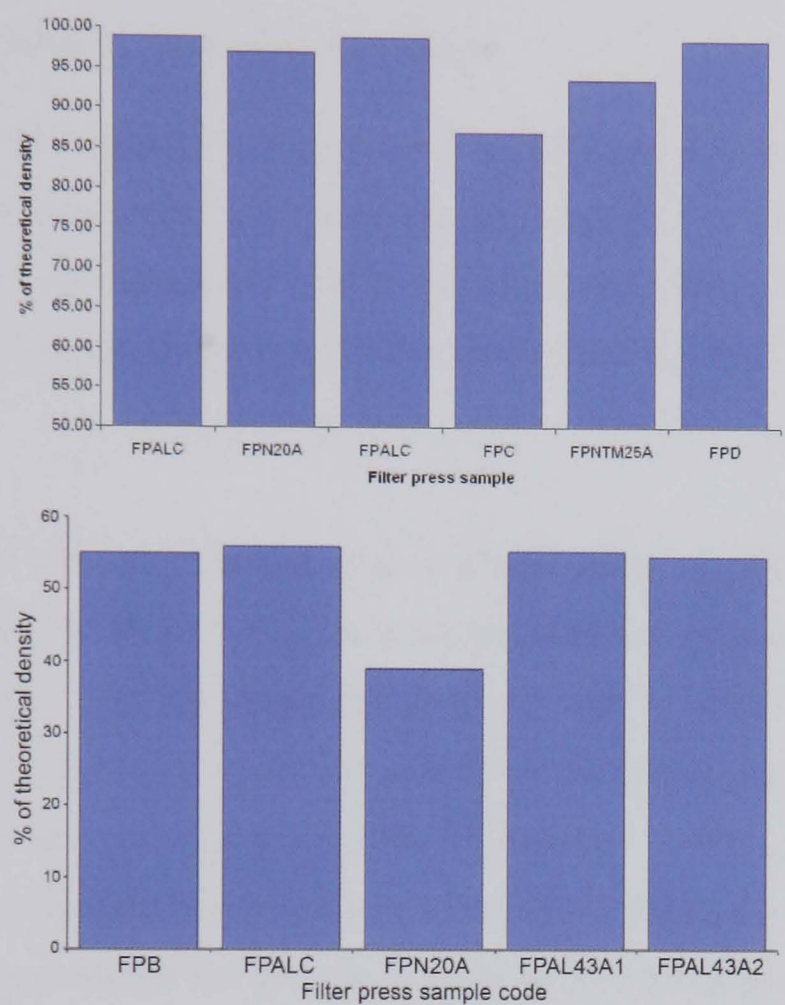
Figure 4.2: *Graphs of (top) density and (bottom) green density for filter pressed, pressureless sintered samples.*

Figure 4.2 shows the densities for various filter pressed samples as green body and sintered respectively. At each stage the spinel powder (FPN20A, FPNTM25A and FPN25A[1]) was processed and sintered to a lower density than the aluminas. This is due to the fact that the supplied Bakowski powder was extremely fine compared with the Taimicron alumina. The aluminas also showed no correlation with any of the above mentioned processing variables with all of the samples, yet all had green densities of

---

[1]The nomenclature for filter pressed samples is as follows, eg. FPNXA: FP = Filter Press, N = new Bakowski spinel powder batch, number X = solids loading percentage, A = sample number

approximately 55%. The sintered density for the aluminas was more varied, and no sample sintered to 'optical' quality, i.e. transparent.

4.1.3 Comparison of Sintering Methods

To compare the hot pressed and filter pressed samples was difficult as both methods required different heating rates and hold times to succesfully sinter the sample. For example, an alumina tube furnace was used for sintering of the filter pressed green bodies. Thus a maximum heating rate of $3°$ min^{-1} was used compared with $10°$ min^{-1} in the hot press.

There has been an increasing interest in spark plasma sintering (SPS) in an apparatus similar to a hot press where an ac current is applied and where exceedingly high heating rates are used[96, 97, 98]. SPS has been compared with hot pressing [99]. However, the conclusions do not fully consider the differences in heating rate and applied pressure, therefore it must not be used as a direct comparison of the sintering process but of technique. A similar situation arises here where the pressureless sintered filter press samples are compared to the hot pressed samples only in terms of the technique used to produce the samples.

Microstructural comparison

Figures 4.3 and 4.4 show typical fracture sections from pressureless sintered (FP) and hot pressed samples (HP). The key difference aside from the grain size is the porosity. The FP samples show considerable intragranular porosity where the gas was unable to diffuse from the intergranular regions at the early stages of sintering and was subsequently trapped during the grain growth phase. The pores are widespread and also occur at grain boundaries, this suggests that the grain growth occurred at a high rate. Once again the comparison is not valid due to the differences in sintering times and heating rates. Ignoring the grain growth, the effect of pressure on the porosity is important and

impacts heavily on the mechanical and optical properties of these samples.

The large grain size of the FP samples is due to the sintering temperature and hold time (1675°C, 2 hours). This time/temperature was chosen so that the samples were as dense as possible so that they would be comparable to hot pressed samples, however even with this regimen the level of porosity was such that hardness/fracture toughness/optical properties would not form a useful comparison. Pressureless sintering is economically the favoured processing route but precursor steps such as pressure filtration must be optimised.

Sample homogeneity

By removing the ball-milling stage of processing there is the risk that hard agglomerates will not be removed. Without milling media, the mixing stage may not be as complete, thus the added dopants may become restricted within small areas of the sample. Certain samples were found to have precipitates at grain boundary triple points (possibly RE oxide). While the grain size distribution in the areas with the triple points was not obviously different to the surrounding area it is possible that the triple points formed due to the boundaries being oversaturated.

Figure 4.5 shows examples TM doped alumina that did not have sufficient milling time. Clusters of triple points indicated inhomogeneous mixing of the RE-nitrate solution.

No RE doped samples had regions where the RE was not present at the grain boundaries, this suggests that the segregation is at a very low level (confirmed in chapter 5.3). There was an expected increase in the size of triple points for large grain samples as the total surface area of grain boundary was reduced. The particular imaging technique used can lead to confusion in terms of whether the candidate structure is indeed a second phase RE-oxide triple point or simply an imaging artefact due to the contrast from several
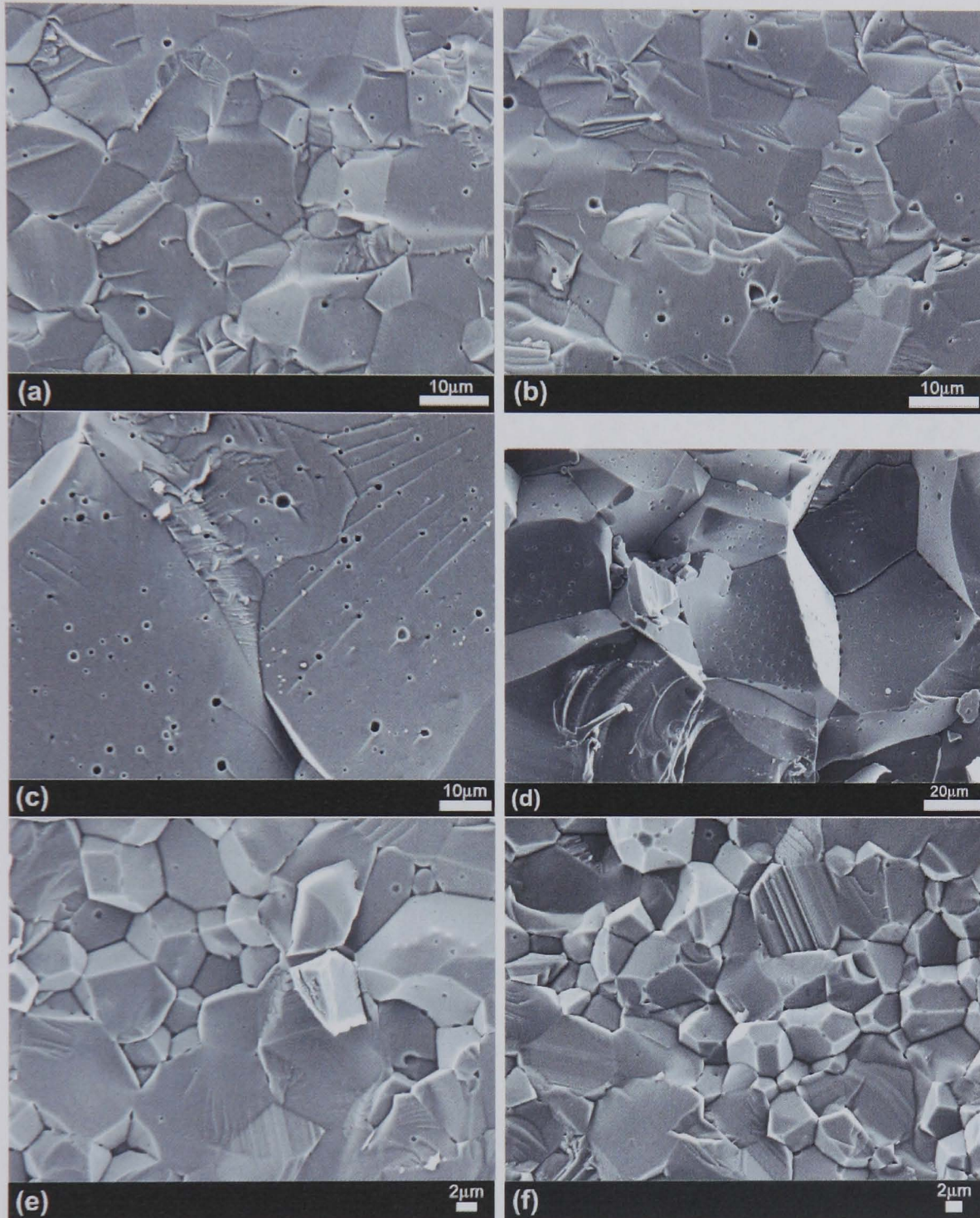
Figure 4.3: *Selection of samples filter pressed then pressureless sintered, all at 1675° C. a & b; alumina 25% slurry solids loading, c & d; Eu doped alumina 43% solids loading, e & f; Tm doped spinel 25% solids loading.*
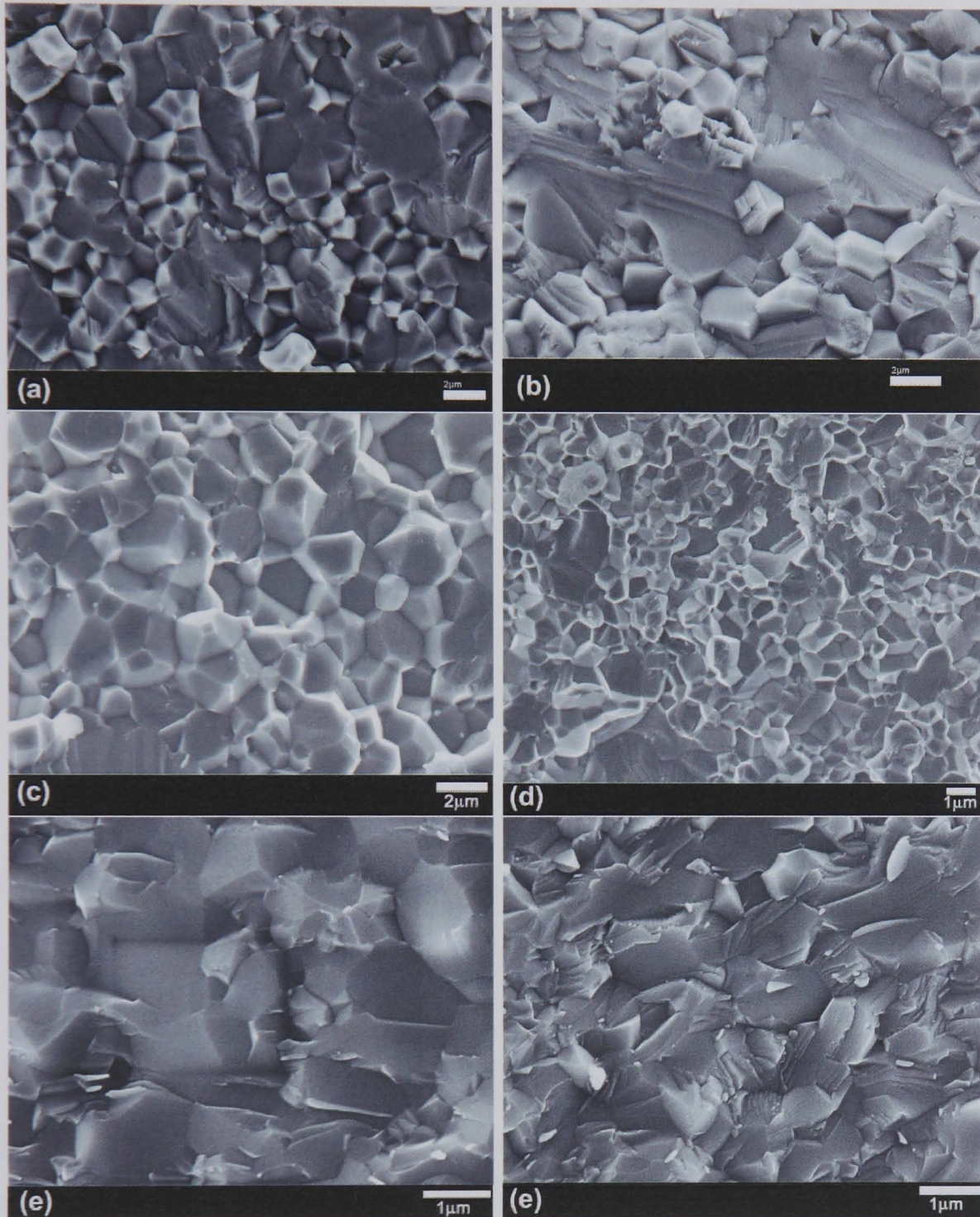
Figure 4.4: *Selection of samples hot pressed at various temperatures. a & b; undoped alumina 1450° C, c; Yb doped alumina 1600° C, d; Tm doped alumina 1500° C, e & f; undoped spinel 1500° C.*
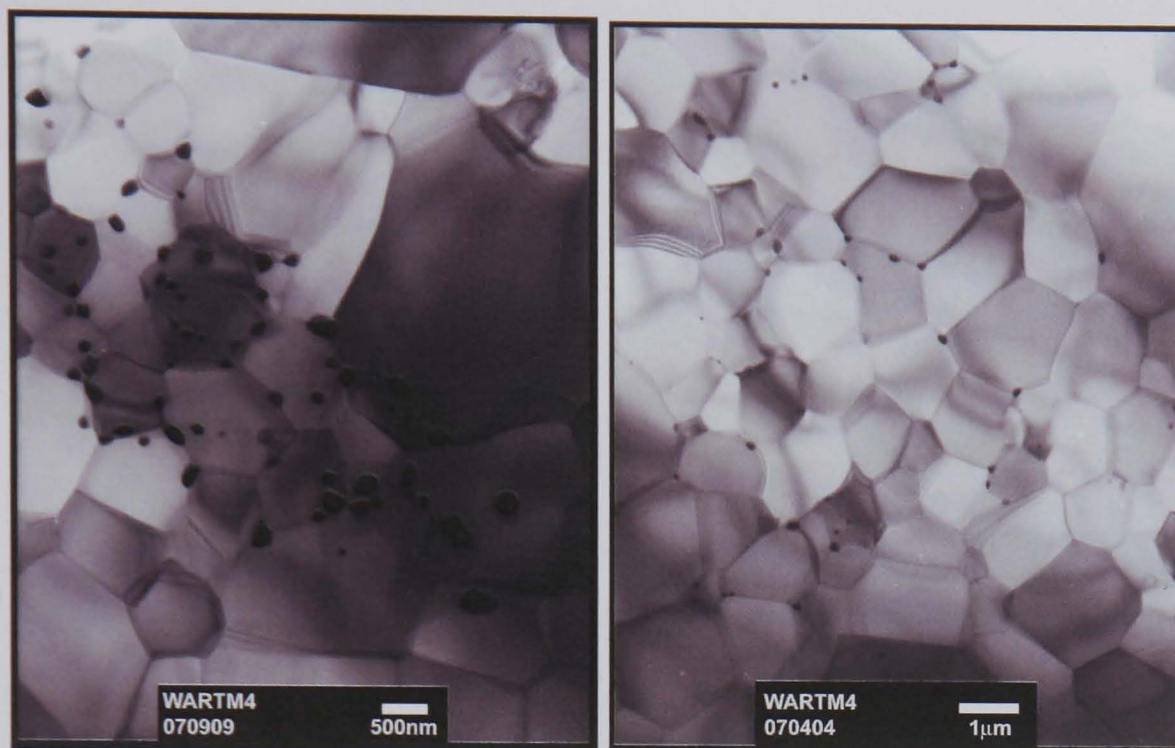
Figure 4.5: *TEM images of RE doped alumina. Area of inhomogeneity indicated by triple point precipitation of RE-oxide.*

boundaries meeting.

4.1.4 Effect of Dopants on Processing and Microstructure

The effect of dopants on the microstructure of ceramics has been well documented; from Coble's addition of MgO to aid the sintering of alumina[100, 101] to the balance of LiF content in spinel affecting its transparency [102]. Here, the use of new dopants, europium and thulium are considered, as well as the anion dopant sulphur, whose effects as an impurity may be similar to those of the RE for some properties, due to segregation to grain boundaries and the possible restriction of boundary mobility.

Effect of dopants on grain size

Figure 4.6 shows the average grain size for samples produced at various termperatures. The error in the graph comes from the variability of the thermocouple measuring the

temperature in the hot press die, as towards the end of a thermocouple's life it rapidly deteriorates in measuring accuracy. It is shown that for alumina the grain size is affected by the presence of rare earth dopants. The trend, as expected is for higher temperatures there is an increased grain size. This is due to increased time at the sintering temperature such that densification has been achieved and grain growth processes become dominant.
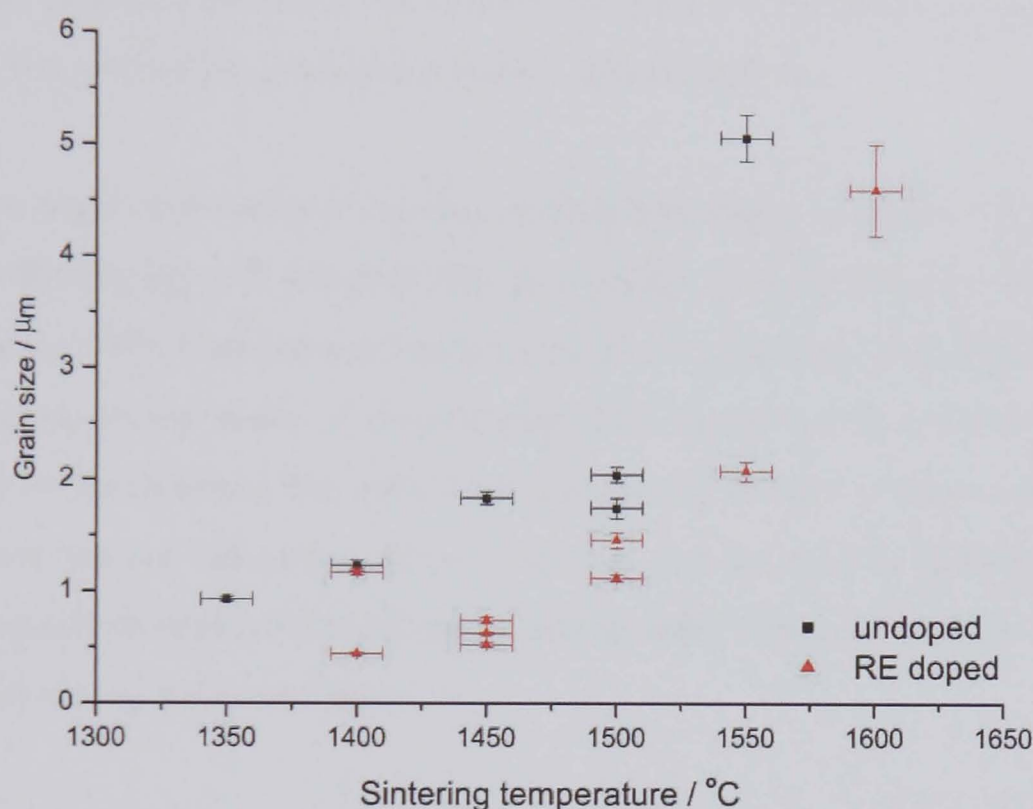
Figure 4.6: *Grain size against sintering temperature for RE doped and undoped alumina samples.*

For spinel, the relationship is not as obvious, with a less coherent correlation between the dopant and the grain growth. This is possibly due to anion impurities being present in the undoped spinel powders that cause similar grain growth restrictions at hot pressing temperatures to the rare earth. One suggestion is that sulphur impurities (present at a high level as shown in the powder table, chapter 3.7.5) may also restrict the grain

72

growth[103].

Sulphur contamination and doping

The doped spinel and undoped spinel show a similar grain size - temperature relation, however, microstructural analysis has shown that the RE segregates similarly in spinel as in alumina (see following chapter). It was suggested[103] that the sulphur impurity in the Bakowski powder was also segregating to the grain boundaries in spinel and re-stricting the boundary diffusion. The existence of sulphur in the spinel powder is directly related to the method by which the powder is synthesised[70].

To test the origin of the sulphur content, ammonium sulphate solution was added to a Taimicron alumina slurry at a level of 500 ppm (anion ratio) to artificially create sulphur contamination. Initial attempts at hot pressing the dried sulphur doped alumina led to a soot coating on the inside of the hot press, this caused an RF (inductive heating) breakdown in the chamber that shut down the heating process. A burn out cycle was added where the die was placed within a vacuum furnace prior to loading in the hot press. Succesful samples were produced by adding solid 'flowers of sulphur' in with the powder and mixing for several hours.

Two sulphur doped alumina samples (1450°C and 1650°C) and one Tm doped alumina sample (1550°C) were prepared for SIMS to compare the amount of sulphur present after a sintering run. The results are shown in figure 4.7. The amount of sulphur was not related to the sample used but to the sintering temperature. This may be expected for samples doped with such an impurity if the burn out phase of the sintering run is working correctly for the following reasons. During burn out of the ammonium sulphate derived 'sulphur doped' alumina the inside of the hot press was becoming coated with soot, suggesting that the doping compound was being burned out. The solid sulphur derived powder may also have burned out in this initial phase, but as sintering tempera-

ture was reached further sulphur may have leached in to the sample from the die walls.
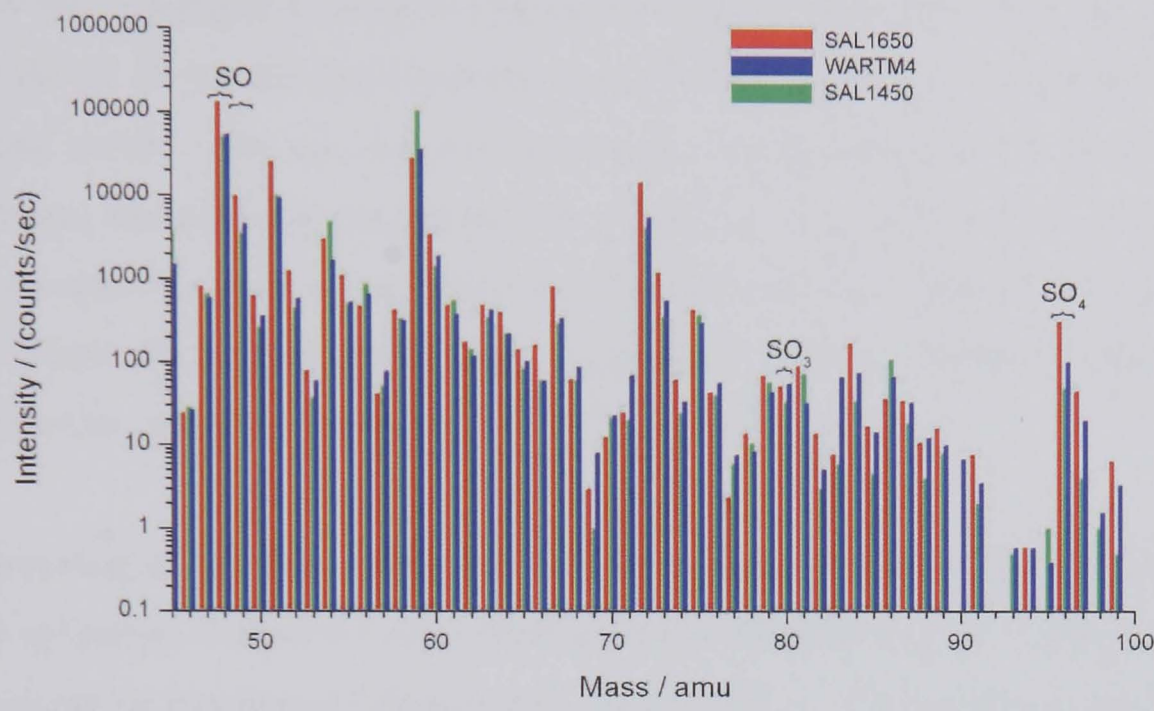
Figure 4.7: *Negative ion SIMS data from three samples sintered at different temperatures; SAL1650 (1650° C), Wartm4 (1550° C) and SAL1450 (1450° C), the main S and SOx peaks are indicated.*

Alumina does not have the inherent sulphur content within the powder grains like spinel and yet there existed some sulphur content. The spinel powder may burn out the inherent sulphur content but again, sulphur from the hot press die may leach in. If indeed the sulphur (whatever its origin) is then segregating to the grain boundaries then this will affect the RE segregation. Microscopic analysis of sulphur content by EDS analysis is discussed in section 5.3.

4.1.5 Optimisation of Processing

While the effect of impurities such as sulphur are currently inconclusive there is an argument that impurities may be leaching in from the hot press die. For most samples used in this investigation graphite spacers were placed above and below the powder within the die for the RE doped samples since the Mo spacers reacted with the RE (as described earlier). The use of spacers previously sintered using the relavent precursor powder was deemed to be the optimum procedure for impurity reduction. The use of precursor spacers was extremely time consuming and wasteful as the spacers had to be removed from the samples by diamond cutting, often resulting in fracture of the spacers such that they could not be reused.

The removing of the ball milling and calcining stages has had no detrimental effect on the properties, indeed the removal of expensive, high purity, high hardness milling media would be economically beneficial to a manufacturer. The calcining stage is effectively repeated in the burn out phase of the hot press run so it was decided it was not required as a separate processing step.

4.1.6 Comparison of Sintering Behaviour for RE Doped and Undoped Powders

The sintering behaviour of the two materials is determined by grain boundary migration (during grain growth) and material transport via grain boundaries. Concentrating on the area around the boundary, i.e. within a few monolayers, the existence of dopants will affect a number of things; The size and electronic structure, will be different to the basic state of the matrix cations. Whether this is at the boundary or within the grain will determine whether it has an effect on grain boundary migration (blocking of dislocations in the grain boundary region) or whether it has an effect on transport along a boundary (blocking grain boundary migration). The size of the segregated region will also affect these properties.

Clearly there is a difference between alumina and spinel in the grain growth mechanics as the spinel was not affected by the addition of RE dopants in the same way as alumina. Either the structure of the boundary is insensitive to the presence of the RE or it is complementary to existing growth suppressing processes. Further work is requiered to determine which of these hypotheses is correct.

4.1.7 Texture Analysis of Doped and Undoped Alumina and Spinel

The use of RE dopants to maintain microstructural control and the improvement of properties previouly mentioned requires that the homogeneity of microstructure must be maintained even with the applied uniaxial pressure during hot pressing. This includes the grain shape and texture. EBSD provides a quick technique to measure the texture of samples.

Figures 4.8 and 4.9 show EBSD maps for RE doped spinel and alumina respectively. As with the fracture sections, the EBSD maps were taken from randomly selected regions all over the sample. All the samples posessed random grain orientation and grain boundary misorientation distributions.

The examples shown demonstrate a number of aspects of EBSD of fine grained ceramics. The pole figures for both the alumina and spinel show that the orientation of the grains with respect to each other are random. The two different maps in figure 4.9 are from (a) a bulk sample surface and (b) a TEM thin foil. The spinel sample in figure 4.8 was from a TEM sample as the grains were too small to index in the bulk succesfully. This is due to the fact that the interaction volume that the EBSD signal that is generated from within the specimen comes from more than one grain in fine grained samples because the interaction volume is larger than a single grain. The use of TEM samples minimises the signal from grains beneath the surface grain.
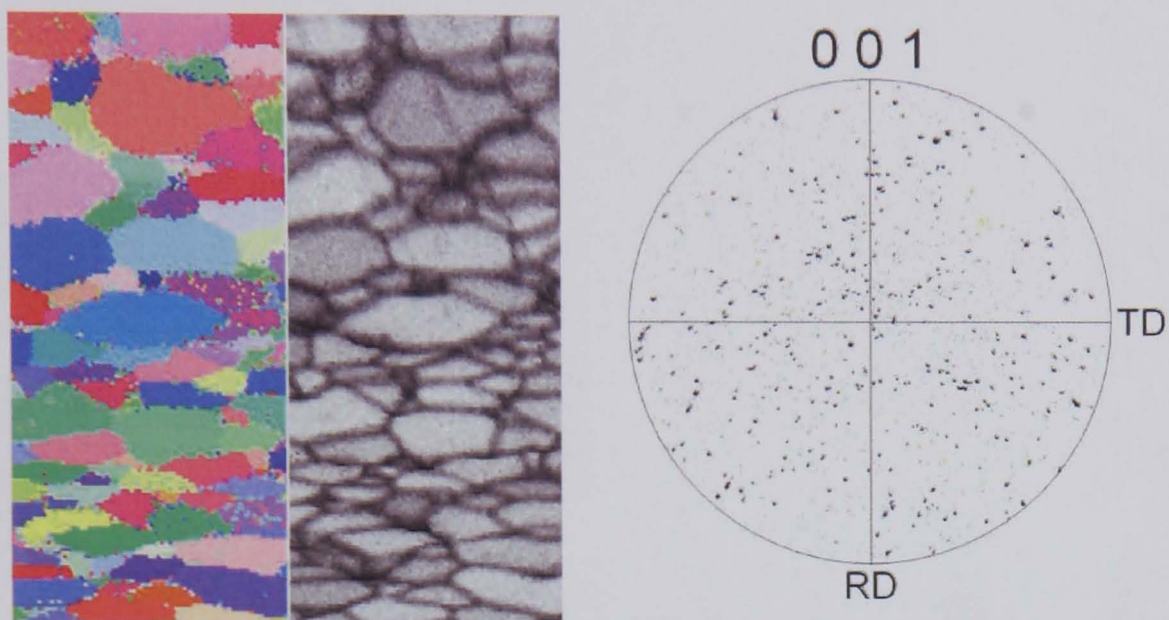
Figure 4.8: *EBSD map of a TEM foil of Yb doped spinel showing (from the left) orientation map, image quality map and pole figure.*
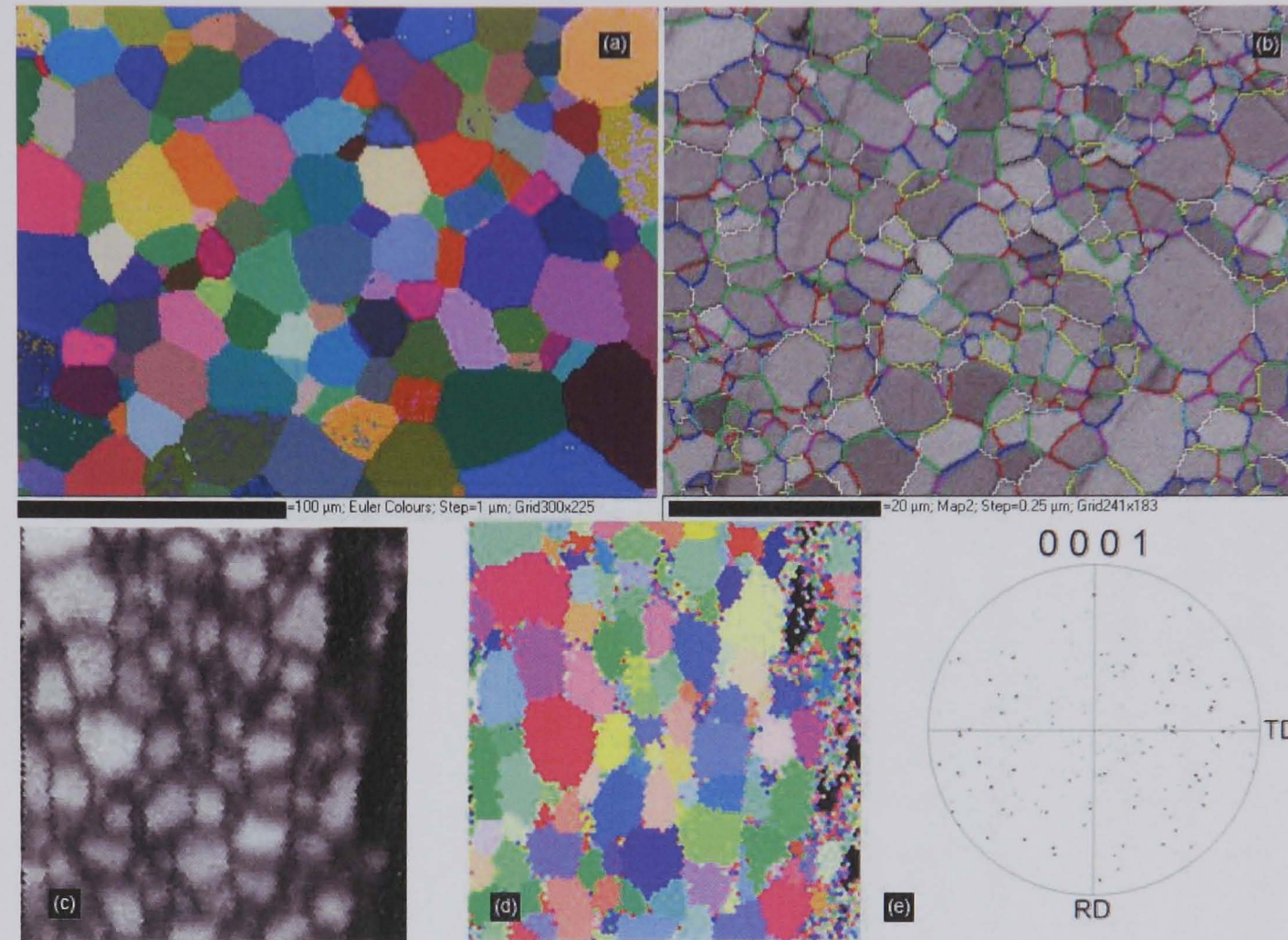
Figure 4.9: *EBSD analysis of (a & b) Gd, and (c, d & e) Tm doped alumina. (a) Map of Euler angles representing the orientation of each grain, (b) the angular misorientation with different colours representing different sets of angles, (c) an image quality map of a TEM specimen (bright = high confidence of succesful index, dark = low confidence), (d) Orientation map of the image quality map region, (e) pole figure showing random orientation of grains in (c)*

4.1.8 EBSD of TEM Sections

EBSD image quality maps show the confidence of the software in the results it displays in any other map of the region. The dark regions in these maps represent the areas where the indexing was poor or the software could not distinguish between patterns, for example on a grain boundary. As grain size is reduced the average depth of grain beneath the sample surface becomes smaller. The proportion of the signal from grain boundary regions and multiple grains for a single pixel position increases.

Microscope parameters can be used to improve the image quality by using a smaller aperture or lower accelerating voltage to both reduce the probe size and/or the interaction volume from which the backscattered electrons can be generated. However, there is still the problem of the depth of the smaller grains being less than the depth of the interaction volume.

A possible slolution to the second problem is to use thin sections. An ideal thin section is a TEM specimen. Figure 4.10 shows a TEM image of a section of Yb doped spinel along with the succesful orientation mapping of the same region.

This result benefits the TEM operator in that well aligned boundaries and/or grains can be identified quickly in the SEM prior to observation in the TEM. For every TEM, there is a lower limit to the size of lattice spacing that can be imaged. Different crystal orientations have varying sized lattice spacings, thus the technique could be used to identify the appropriate orientation for high resolution imaging and analysis. In most high resolution TEMs (for example the SuperSTEM), the extent to which the sample can be moved and tilted is limited so the ability to find a particular region with grains of certain orientation is important.

EBSD of TEM specimens has the potential to combine the analytical aspects of SEM

and TEM based techniques, careful sample preparation is required such that there is minimal topography due to ion beam thinning. One advantage of being able to find the orientations of thin regions is to find orientations that are close (i.e. can be easily oriented) to a strongly diffracting condition. Also, the grains with specific misorientations or grain boundaries between two well oriented grains can be found.
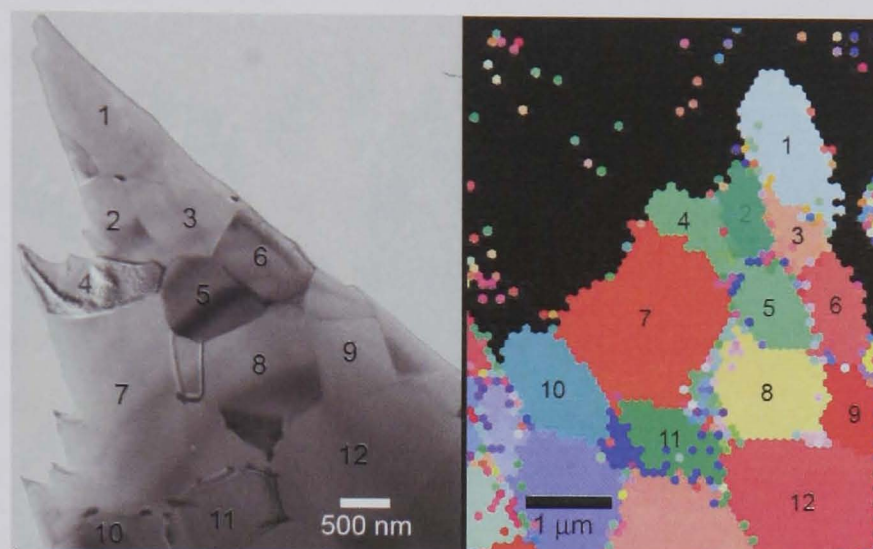
Figure 4.10: *Two images of the same region in a Yb doped spinel, left; CTEM and right; EBSD SEM image.*

4.2 Chapter Conclusions

The optimisation of the processing of oxides has benefited from the careful handling of high purity powders and removal of processes thought to introduce impurities into the system. Only the sulphur content is questionable, with the suggestion that sulphur may originate from the hot press graphite die itself. Commercial use of milling media and calcining will increase the impurity content, for example from the milling media itself (generally not manufactured from ultra high-purity powder).

The comparison between hot pressing and filter pressing has shown that, for ease of

processing and consistency of sample, the hot press is the favoured manufacturing technique. Colloidal processing of ceramics is expanding but the variables involved in simply producing the green body as well as the variations at the sintering stage went beyond the scope of this project. Pressureless sintering, while economically favourable as a commercial technique, proved insufficient in terms of density of sintered samples and sintering time. As such, hot pressing was used throughout to produce the samples subsequently studied. Hot pressed samples had the benefit of consistent microstructures and quicker production times.

The addition of newly studied RE dopants (Eu and Tm) to the oxide powders prior to sintering has proved succesful in maintaining a random grain shape and homogeneous grain size distribution throughout the samples. In the case of alumina, the RE restricted the grain growth for a given sintering temperature similarly to previous studies of Yb, La, and Gd dopants. The effect of RE dopants on the evolution of spinel grain size with sintering temperature remains unresolved as there appears to be a lack of increased grain growth of undoped spinel with increasing sintering temperature.

EBSD has provided information on the orientation and texture of hot pressed samples. The results show that the samples are not textured by the hot pressing process. EBSD has been conducted on TEM samples previously, or subsequently imaged in the TEM. This is useful for quickly identifying regions in which the orientation of boundaries or grains are of interest.

Chapter 5

Microscopic Analysis of Rare Earth Segregation

5.1 Introduction

TEM based techniques provide the best method for studying the grain boundary with their combined imaging and analysis capabilities. Well established techniques such as EDS and high resolution imaging have been used to probe grain boundary structures and chemistry. STEM is an important feature of the TEM analysis as the Z contrast imaging allows the RE segregates to be clearly located.

The most recent advance in TEM is the spherical aberration correction demonstrated in a small number of microscopes around the world. Chapter 6 will be dedicated to this technique as it is a significant step forward for electron microscopy.

5.2 Transmission Electron Microscopy

5.2.1 Sample Preparation

Important considerations for the study of grain boundaries are the homogeneity of the sample with respect to the dopant content and the alignment of the grain boundaries with respect to the imaging/spectroscopic probe. Adequate mixing or milling of the doped powders (see chapter 2) is essential to ensure a homogeneous distribution so that the microstructure is representitive of the bulk. For the grain boundary alignment, polycrystalline samples are an advantage as a large number of grains may be present in the electron transparent region. Therefore, there is a greater chance of finding a well aligned boundary. Figure 5.1 shows a well prepared Eu doped spinel sample with many grains in the electron transparent region.

It has been shown that alumina and spinel are prone to damage and contamination under the intense electron beams of TEMs[104]. To help solve these problems, TEM specimens are all plasma cleaned prior to analysis, those that have been imaged in the SuperSTEM were also heated to 200°C to remove contamination.

5.2.2 TEM Techniques

There have been a number of groups working on the detection of grain boundary segregation with existing techniques such as Auger [38, 39], EDS[79], EELS[78], SIMS[83, 84, 85] and STEM[78]. All techniques have their strengths, however, a common weakness is the spatial resolution available which leads to problems in quantitative analysis and structure determination. The TEM remains the most viable tool for probing structure with sub nanometre resolution.
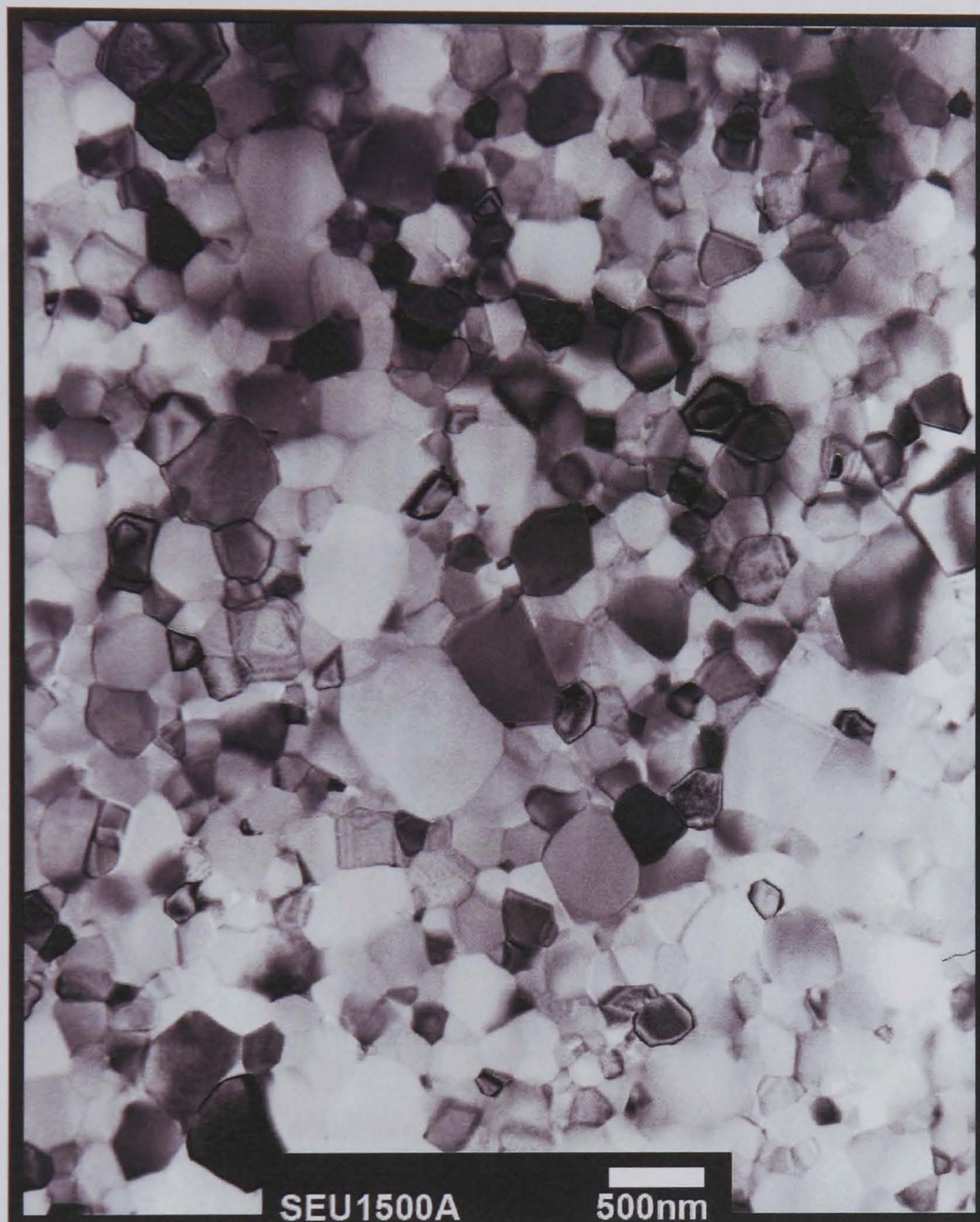
Figure 5.1: *Example of hot pressed spinel.*

Bright Field Imaging

BF images were used throughout for positioning the sample and searching for well thinned regions and aligned grain boundaries. Figure 5.2 shows a thulium doped alumina sample. The dark spots are triple points containing the thulium (possibly as thulium oxide), this was confirmed by analysis using EDS (figure 5.3).

High angle annular dark field imaging

Where possible, both bright field and HAADF images were aquired from the same region. Figure 5.4 shows the same area of a Yb doped spinel. Bright lines in the HAADF image clearly correspond to the grain boundaries in the bright field image. This is directly due to the heavy element (Yb) present at the boundaries. It can be seen that the poorly aligned boundaries produce a wide diffuse bright boundary in the HAADF image, whereas the well aligned boundaries give a sharp intense line. All RE dopants studied (Eu, Tm, La, Yb, Gd) in both alumina and spinel have produced bright contrast at boundaries in the HAADF images. For comparison, figure 5.4 also shows an undoped spinel. The contrast features in this image arise from mass-thickness contrast (similar to the other HAADF images) and dark regions where grains have pulled out during TEM sample preparation. There is no bright line along the boundaries, this can be seen by looking at the edges of the pores.

5.2.3 Determination of Grain Boundary Width

HAADF STEM is conducted with the microscope in diffraction mode, this allows the collection angle of the HAADF detector to be adjusted by altering the camera length. While the contrast mode is essentially atomic number related (from Rutherford scattering), there is also an element of diffraction contrast that remains. Some thickness contrast appears simply because of the increased propensity for scatter in the thicker areas. A pure HAADF image should contain only Z contrast. As discussed in the exper-
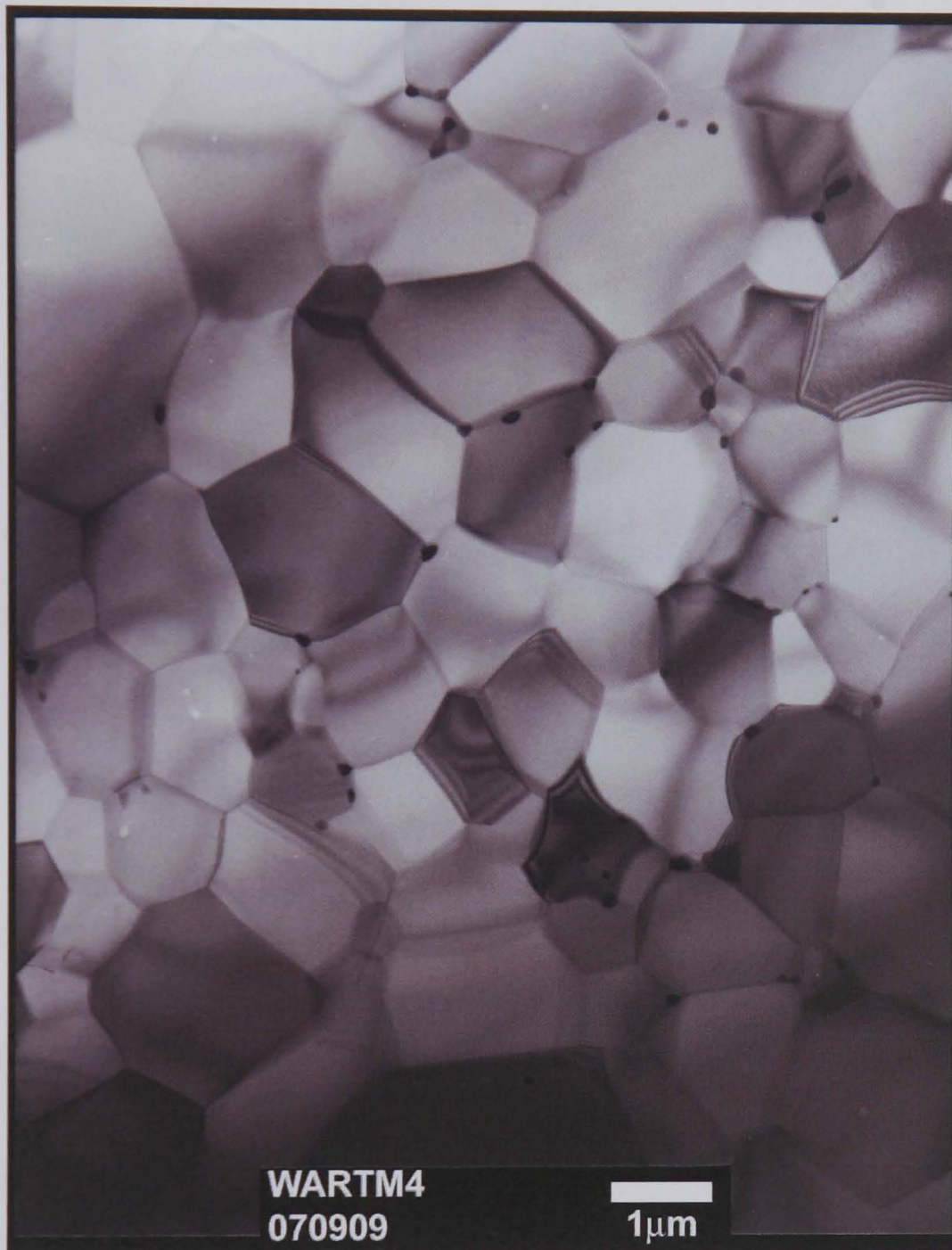
Figure 5.2: *TEM image of thulium doped alumina, showing clearly dark spots at triple points, these are thulium oxide precipitates.*
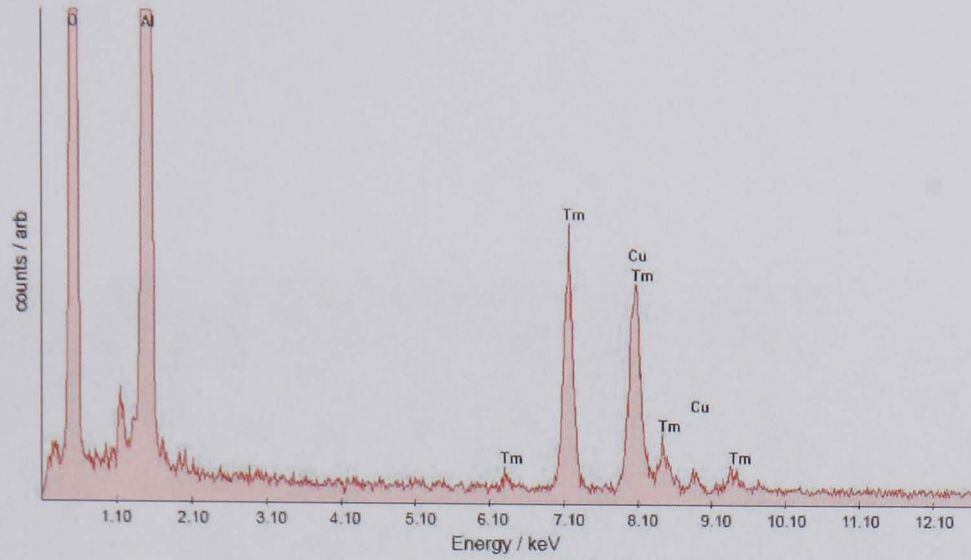
Figure 5.3: *EDS analysis of triple point in figure 5.2.*

imental details, the HAADF signal has collection angles of >50 mrad. Image intensity comes from the differential Rutherford cross section $d\sigma/dcos\theta$.

$$\left(\frac{d\sigma}{dcos\theta}\right)_R = \frac{\pi}{2}Z^2\alpha^2\left(\frac{\hbar c}{K_e}\right)^2 \frac{1}{(1-cos\theta)^2} \tag{5.1}$$

where Z = atomic number, $\alpha = 1/137$, $\hbar = h/2\pi$, c = velocity of light, K_e = Kinetic energy of incident electron, θ = scattering angle.

Thus, the scattering intensity is proportional to Z^2, hence there is strong contrast between RE elements and the bulk material, be it alumina or spinel. With even the well aligned boundaries there is usually some element of twist or tilt such that only a very small section is aligned perfectly. This can be seen when viewing HAADF images at high magnification. Also, the nature of grain growth often leaves curved boundaries. These features will be discussed further in the SuperSTEM section.

The HAADF images give a good indication in themselves of how well inclined individual boundaries are thus it becomes straightforward to choose a boundary for further analy-

87
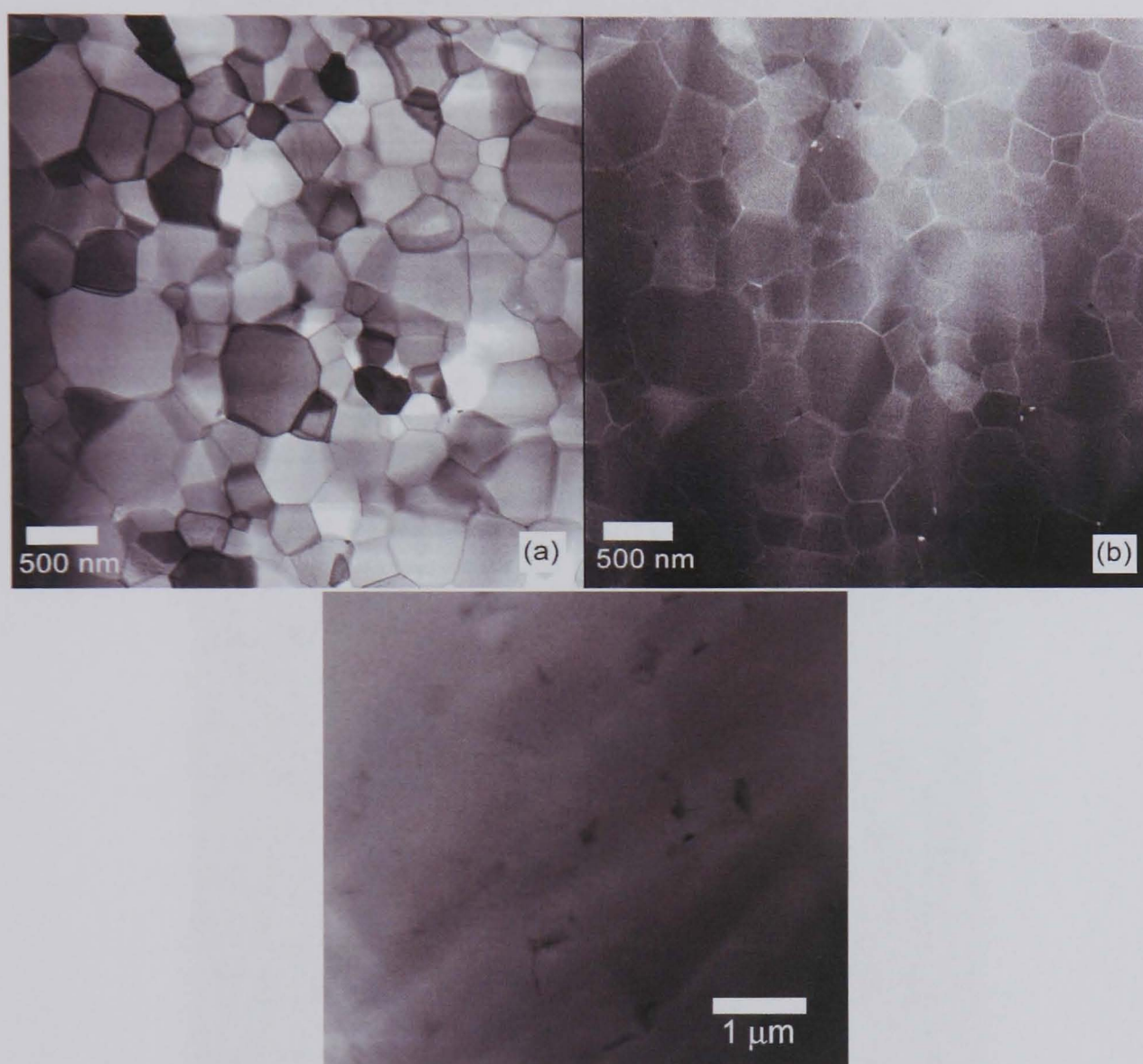
Figure 5.4: *a) BF TEM image of Yb doped spinel, b) the same region as in (a) imaged using the HAADF detector, clearly showing the RE at grain boundaries. Below is a HAADF image of an undoped spinel sample.*
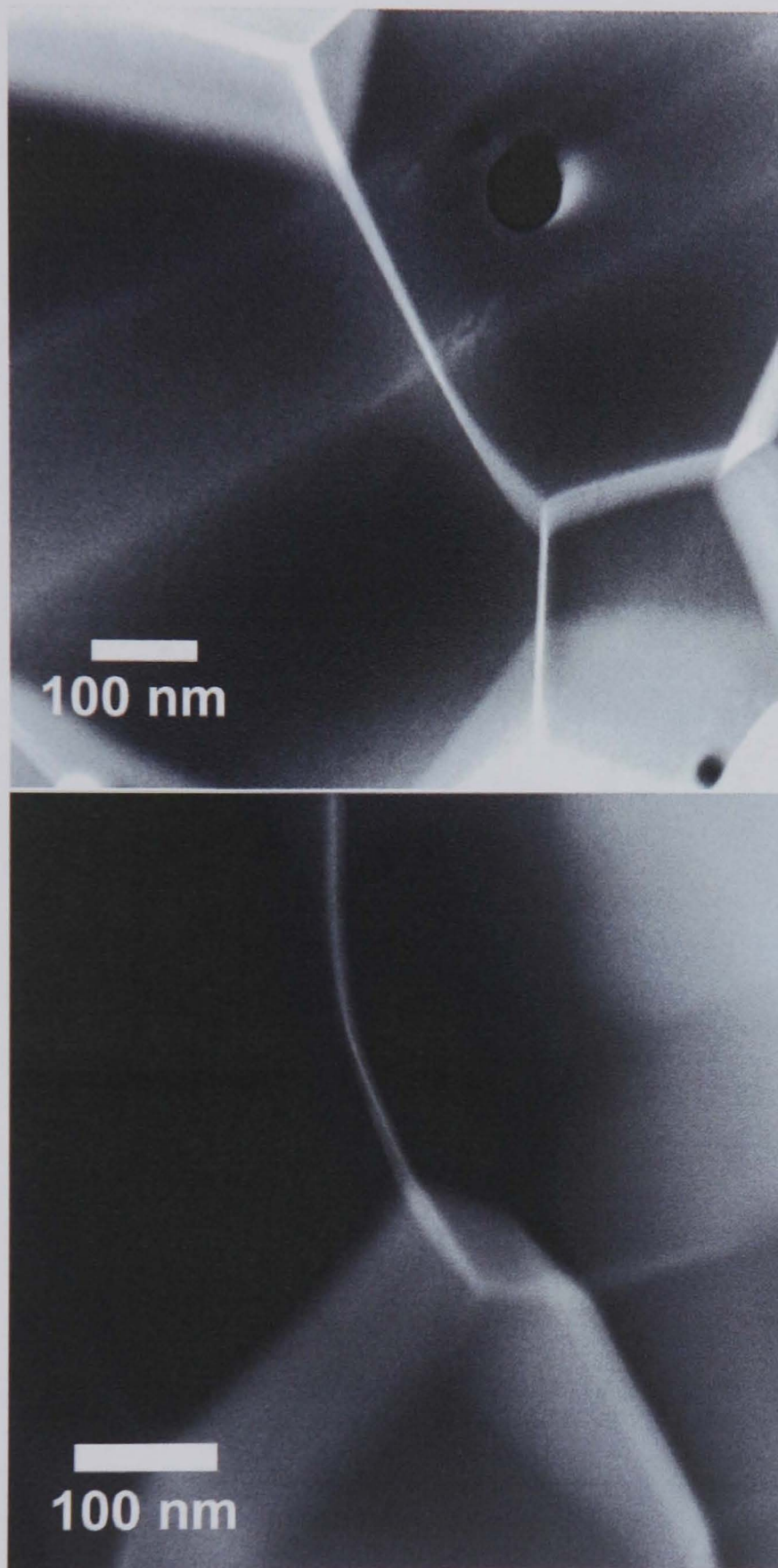
Figure 5.5: *STEM image of twisted and curved boundaries in a Tm doped alumina.*

sis. An intensity profile is then plotted to provide an estimation of the boundary width, this is done by plotting the image brightness against distance along the line-scan. The FWHM of the intensity profile is a good indication of the maximum region in which the heavier element is present.

The following images (figures 5.6 and 5.7) show HAADF images with the line scan positions shown as a red line. The associated intensity profile is plotted to give the FWHM.
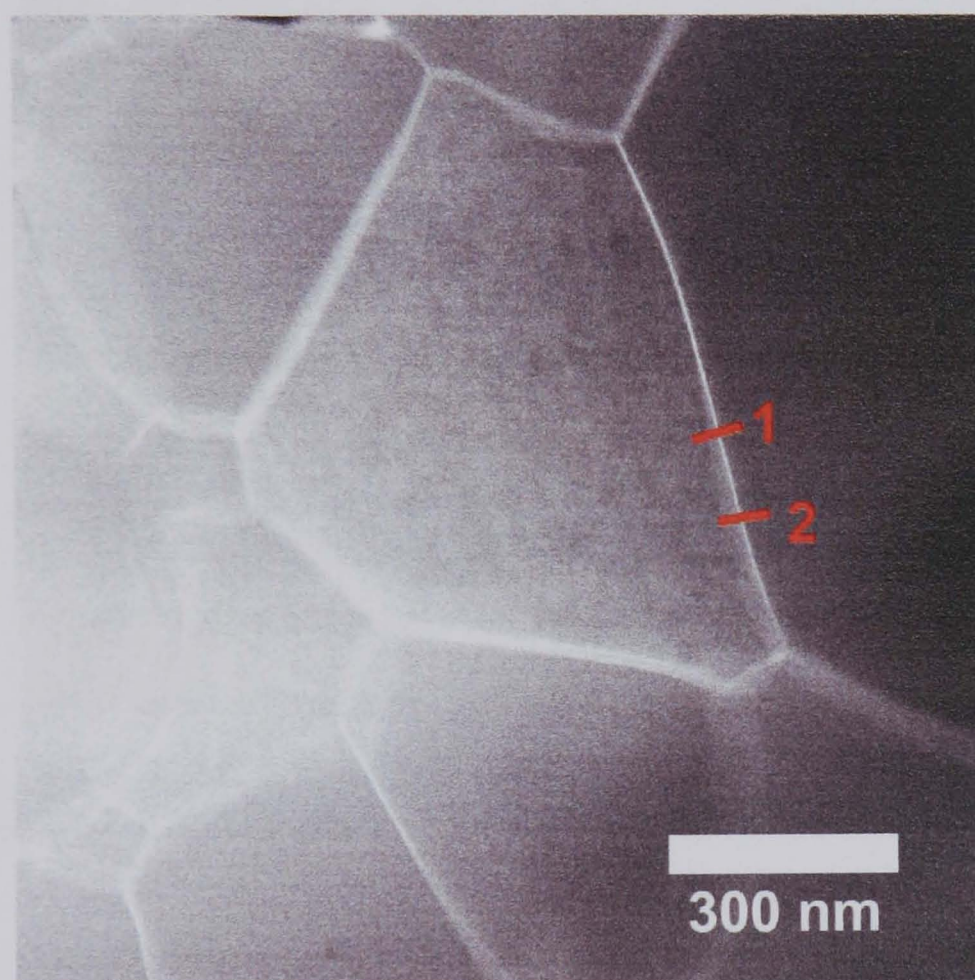
Figure 5.6: *HAADF image of a Yb doped spinel, showing the position of two intensity profiles, measured over a well oriented boundary.*

The FWHM of the Yb doped spinel peaks are 1.6 and 1.2 nm, and 1.1 and 1.1 nm for
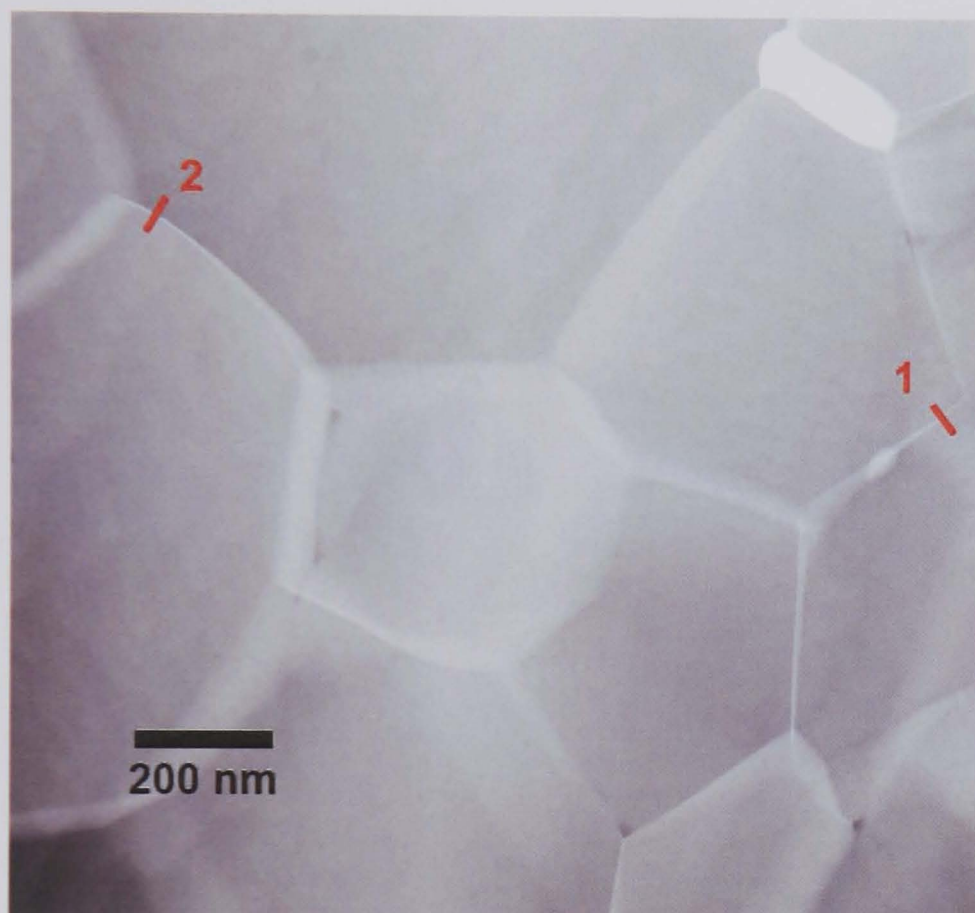
Figure 5.7: *HAADF image of a Tm doped alumina, showing the position of two intensity profiles, measured over a well oriented boundary.*
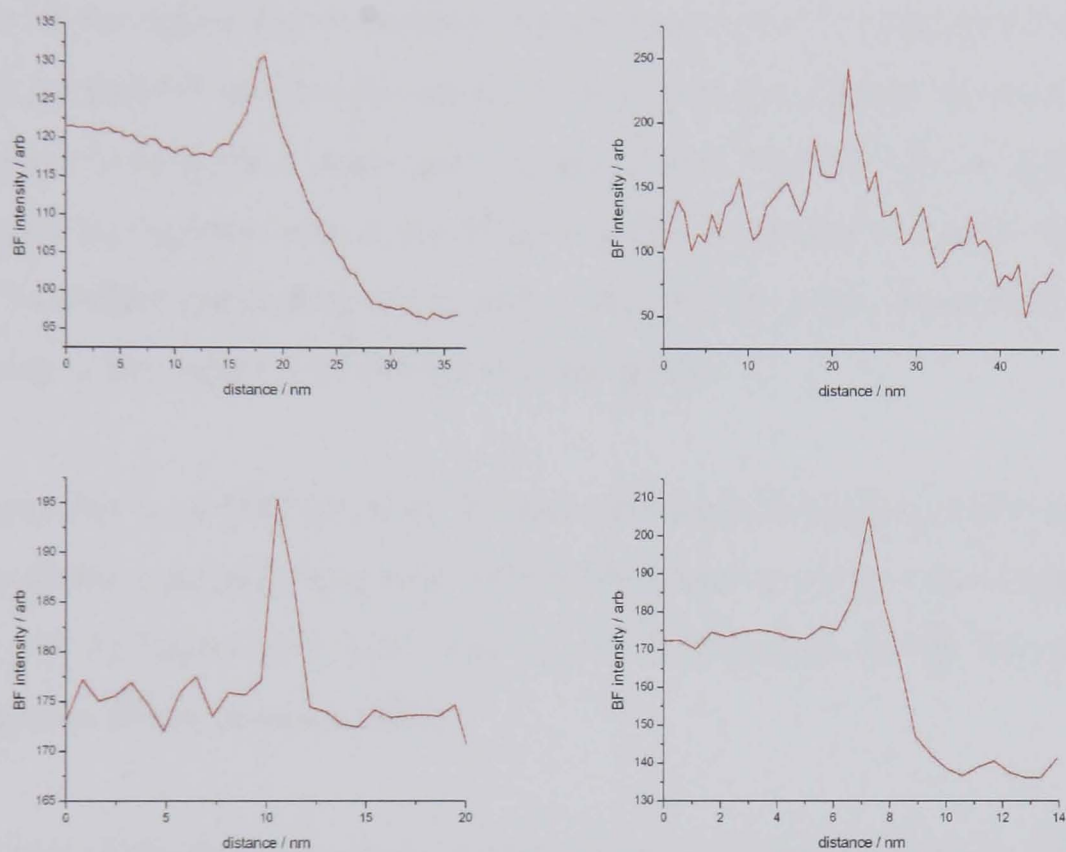
Figure 5.8: *BF intensity profiles from (top) positions 1 and 2 in figure 5.6 the Yb doped spinel, and (bottom) positions 1 and 2 in the Tm doped alumina.*

the Tm doped alumina. This suggests that the segregation is restricted within 1 nm of the grain boundary position.

The confirmation that the brightness is due to the segregant and not impurities or imaging artefacts comes from EDS analysis. An example spectrum from two positions, a) on the grain boundary and b) within a grain are shown in figure 5.9. The two spectra were taken from the same region of TEM sample so that the drift, charging and thickness of the region was comparable for each spectrum. A small spotsize was used in figures 5.6 and 5.7 as this was only for imaging and not analysis. In order to aquire a large enough x-ray signal a larger spot size was needed for the EDS line scans. For the imaging and (to a greater extent) the EDS line scans the sample was prone to drift which resulted in a slight broadening of the peak. Thus the line scans shown here provide an upper limit to the region in which the RE segregated.

When extended to an EDS line scan, the peak indicates the position of the dopant. The intensity profile is plotted along with the EDS linescans for each of the images in figures 5.10 to 5.12 in figures 5.14, 5.13, and 5.15 to confirm that the BF intensity peak is representative of the presence of RE.

The position of the RE peak clearly corresponds to the BF intensity peak. EDS requires a larger spot size such that statistical accuracy can be achieved, this leads to an increase in the FWHM of the BF intensity profile.

To obtain the concentration of dopant at the grain boundary the Cliff-Lorimer equation is used [80], however, it requires precise knowledge of the probe shape and size plus perfect alignment of the grain boundary with respect to the incident beam. This was attempted, however there are problems. Damage to the sample, specifically the boundary region, causes a broadening of the RE segregation, this is due to the fact that the
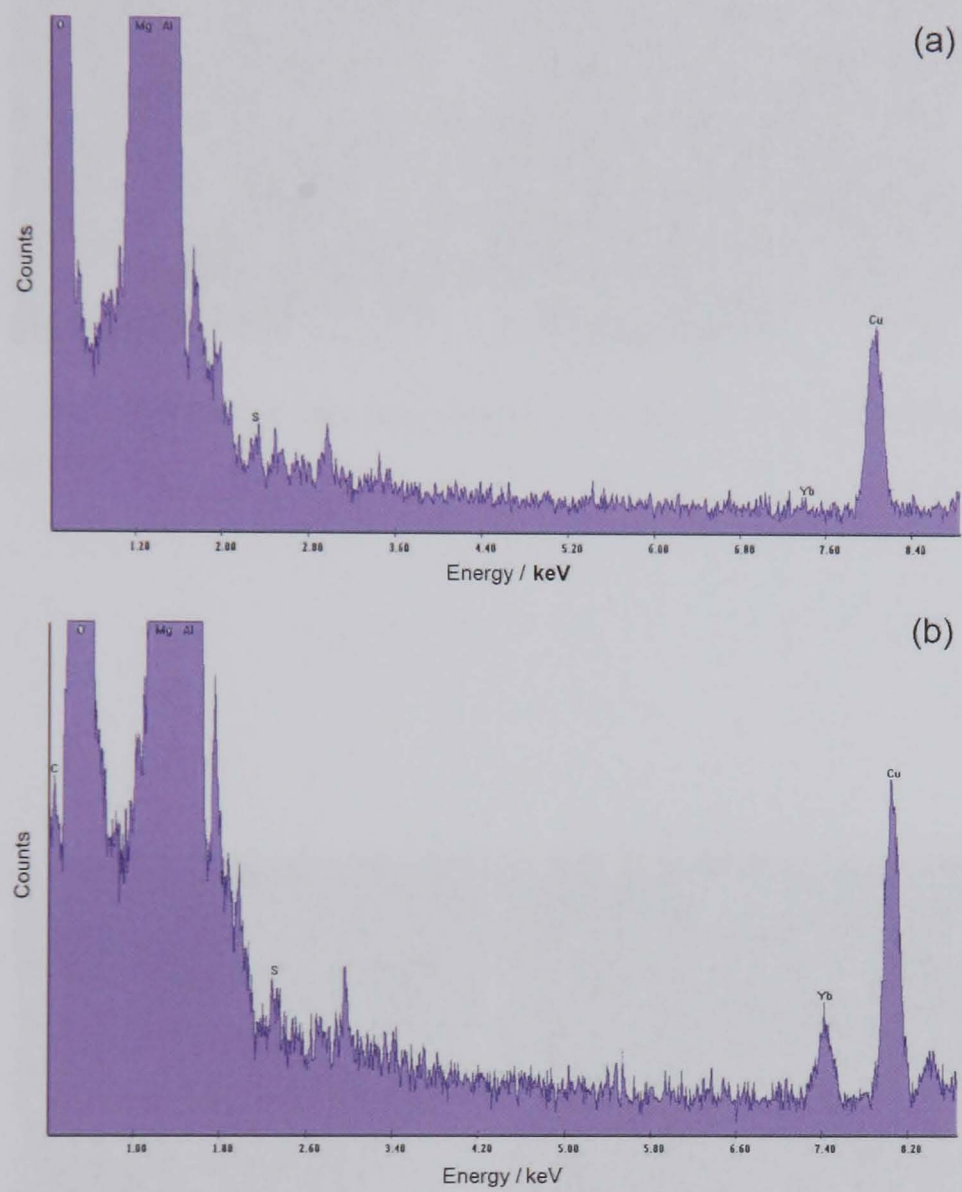
Figure 5.9: *EDS spectra from (a) grain centre and (b) grain boundary of Yb doped spinel.*
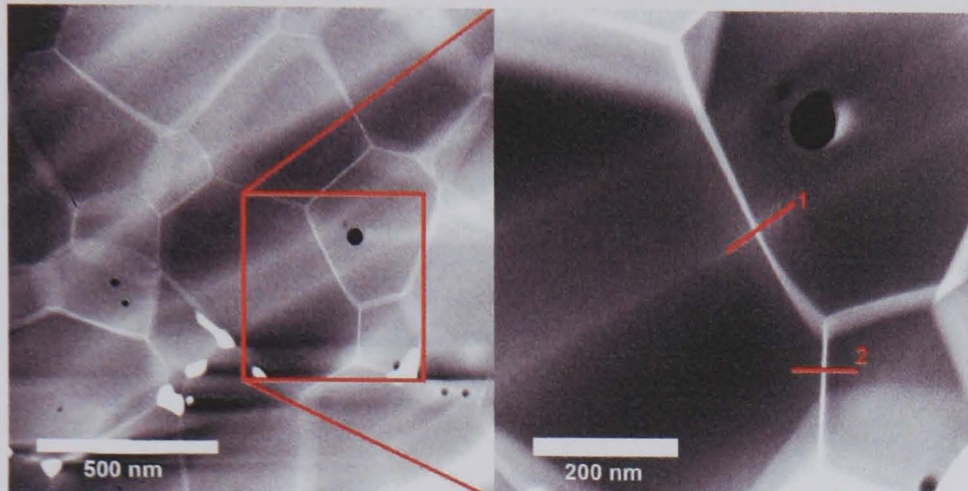
Figure 5.10: *HAADF image showing position of bright field intensity profile for a Tm doped alumina.*
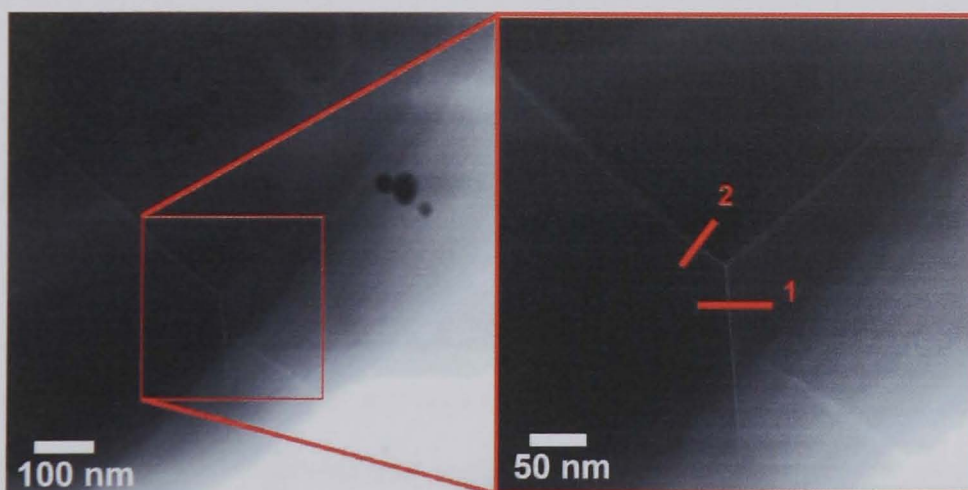
Figure 5.11: *HAADF image showing position of bright field intensity profile for a Eu doped alumina.*
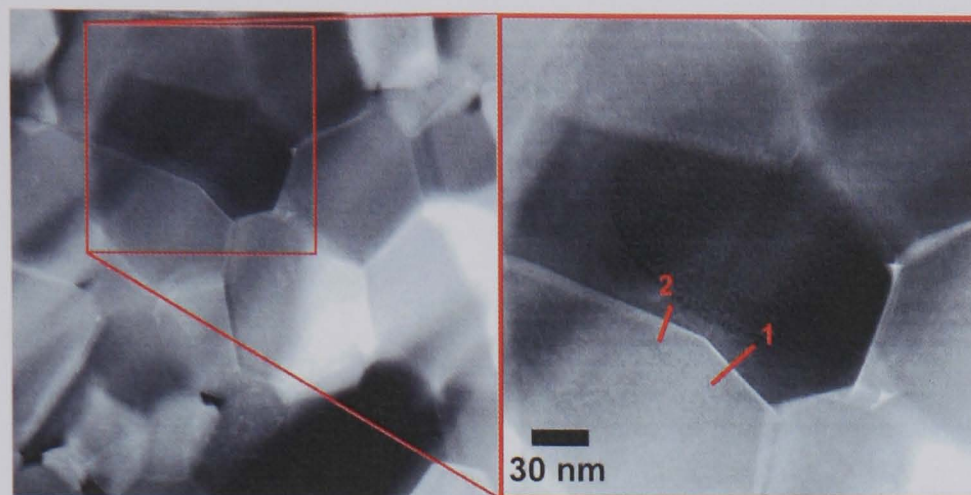
Figure 5.12: *HAADF image showing position of bright field intensity profile for a Eu doped spinel.*

samples are highly electronically and thermally insulating. Without suggesting specific processes, there may be some amorphisation at the boundary where the intense electron beam is incident, this may or may not be combined with the breaking of bonds allowing the RE to diffuse to the sample surface. When using finer probes for EDS, there was a low count rate which meant the aquisition times had to be increased, which led to problems with sample drift, hence for EDS acquisition larger spot sizes were used.

The value for grain boundary width found from the intensity profile plots was used in combination with the EDS results to calculate the segregant concentration at the boundaries. The fraction of the beam centred on the segregate layer $= \frac{2tr}{\pi r^2} = \frac{2t}{\pi r}$ which holds when $2r >> t$; Where $2r =$ probe diameter and $t =$ width of segregated region. Using 0.53 as the RE:Al sensitivity factor (for all RE used here) determined from LaAlO$_3$ powder and assuming the segregated region is smaller than the probe size used for the EDS line scan (which is found by taking the FWHM of an HAADF image formed with the larger probe) the RE/cation ratios for the samples are given in table 5.1.
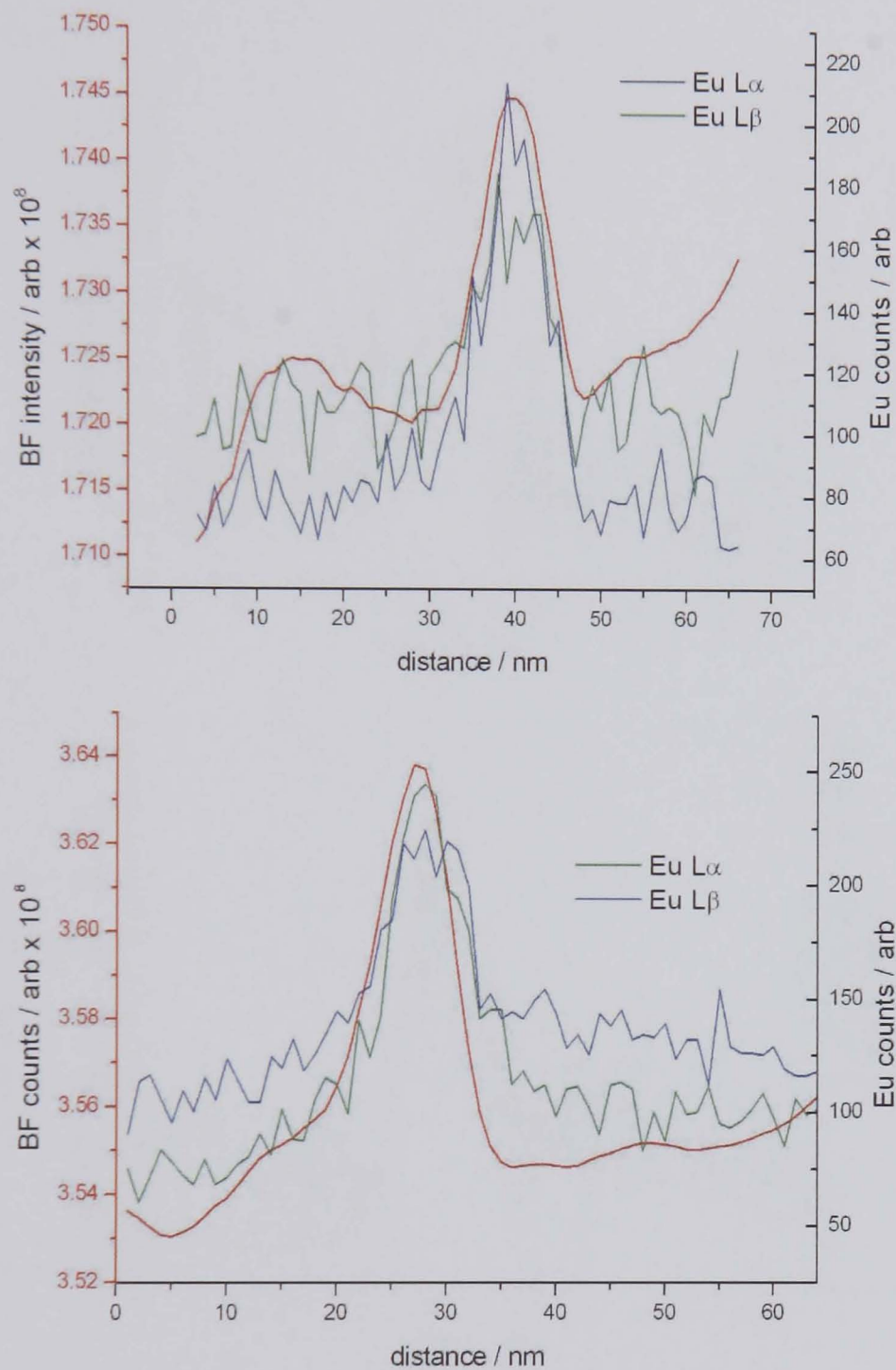
Figure 5.13: *Combined plot of bright field intensity and EDS counts for Eu across the line scan indicated in figure 5.11. Red line = BF intensity, Green and blue lines = Eu ESD signal for Lα and Lβ respectively.*
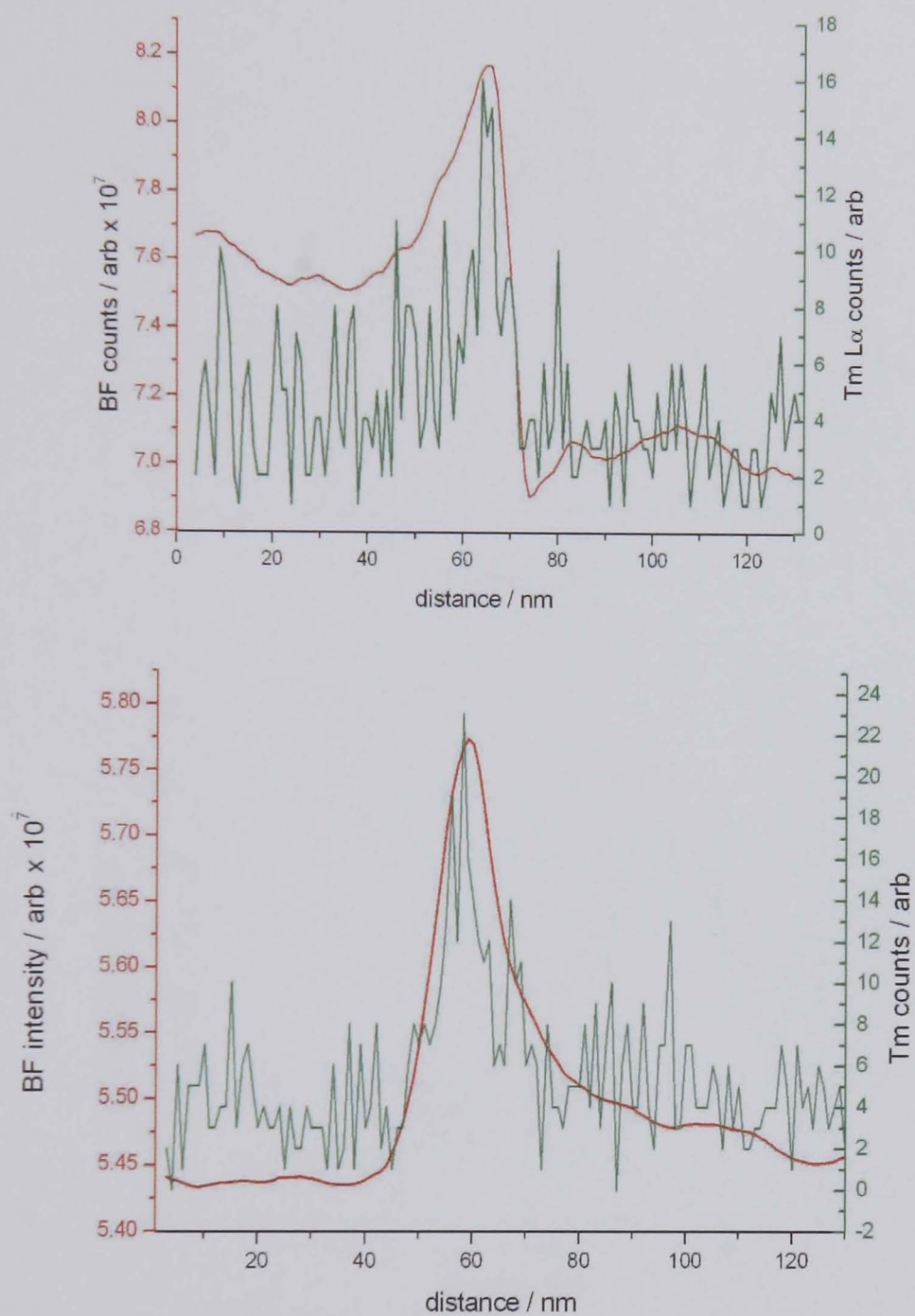
Figure 5.14: *Combined plot of bright field intensity and EDS counts for Tm across the line scan indicated in figure 5.10. Red line = BF intensity, Green line = Tm EDS signal.*
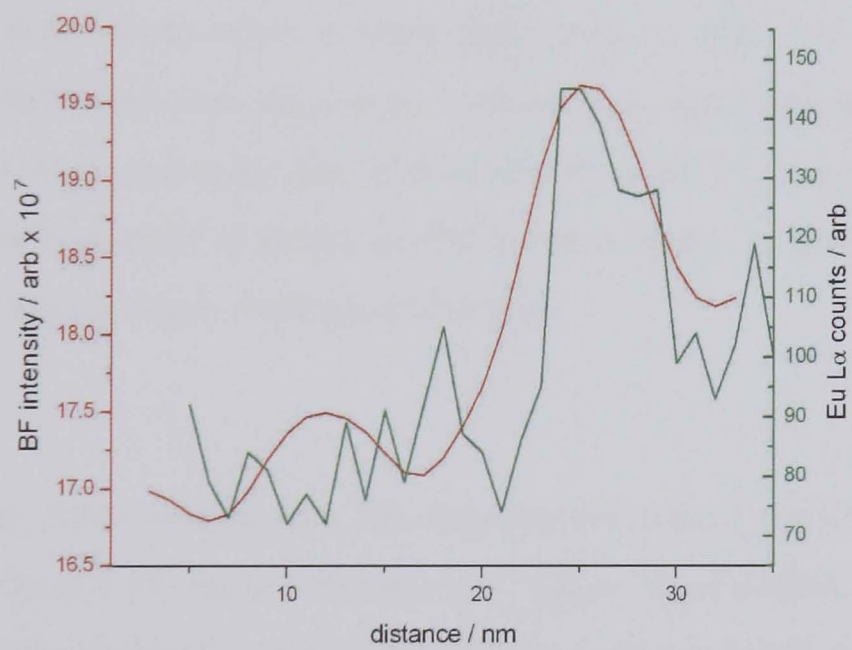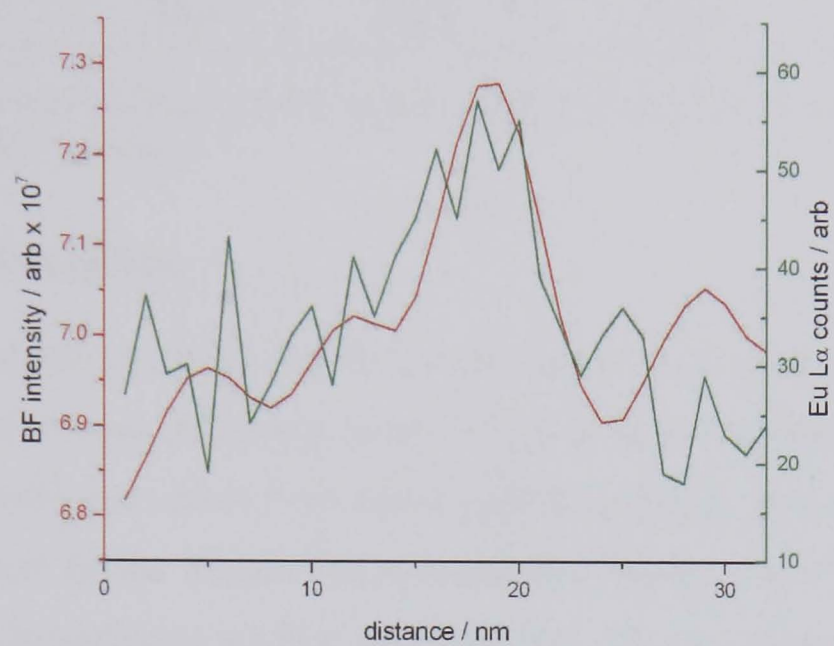
Figure 5.15: *Combined plot of bright field intensity and EDS counts for Eu across the line scan indicated in figure 5.12. Red line = BF intensity, Green line = Eu EDS signal.*

Material and dopant	RE counts	Cation counts	Probe size / nm	RE:cation ratio
Eu alumina	216	20505	10	0.11 ± 0.02
Tm alumina	45.5	3549	10.5	0.09 ± 0.02

Table 5.1: *The concentration of RE cations within 1 nm of the boundary position determined by EDS analysis.*

5.2.4 Anion Impurities

It has been suggested that there may be some influence from anion impurities segregating to grain boundaries. Returning to the Yb doped spinel from figures 5.4 and 5.6, a set of EDS spectra were taken from various positions chosen at random within the electron transparent region. Figure 5.16 indicates that in only one of the selected positions that there is significant sulphur contamination. This was taken at a large triple point and some segregation to the triple point may suggest general sulphur segregation. The fact that it is not found either in other triple points or grain boundary (although microscope conditions such as probe size etc. may not have been optimised) means that the segregation is at an extremely low level as the Yb peaks are large in comparison. The peak at 2.9 keV observed in all the spectra is due to argon contamination from the PIPS ion beam thinning stage of sample preparation.

Figure 5.18 shows similar analysis of a Tm doped spinel. One of the triple points analysed is shown in figure 5.17, marked by the arrow. Again, there is some sulphur content at the triple point but along the grain boundary there is evidence of Tm but no sulphur. The analysis at a grain centre is shown for comparison.

A study by West[103] on a similar Yb doped sample showed one spectrum that indicated the presence of sulphur. This was found using EDS analysis at a grain boundary on a Yb doped spinel. There were sulphur counts both on the boundary and close to the grain
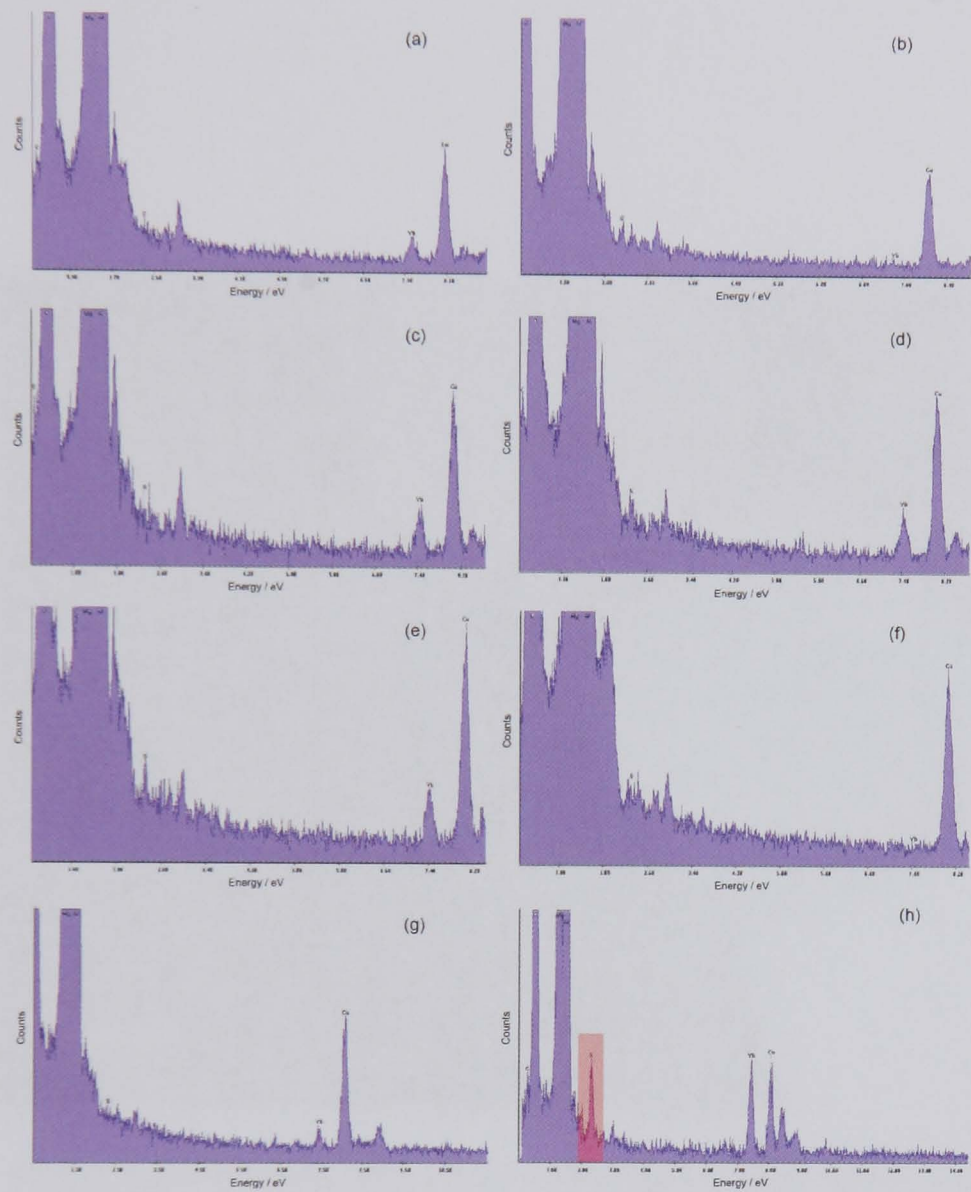
Figure 5.16: *Several EDS spectra from Yb doped spinel. Spectra taken from a variety of positions within the microstructure. Position of sulphur peak is indicated, and further highlighted in (i). Probe positions as follows; (a) triple point (non precipitate), (b) grain centre, (c) triple point (possibly precipitate), (d) triple point (possibly precipitate), (e) triple point (non precipitate), (f) grain centre, (g) grain boundary, (h) triple point (precipitate).*
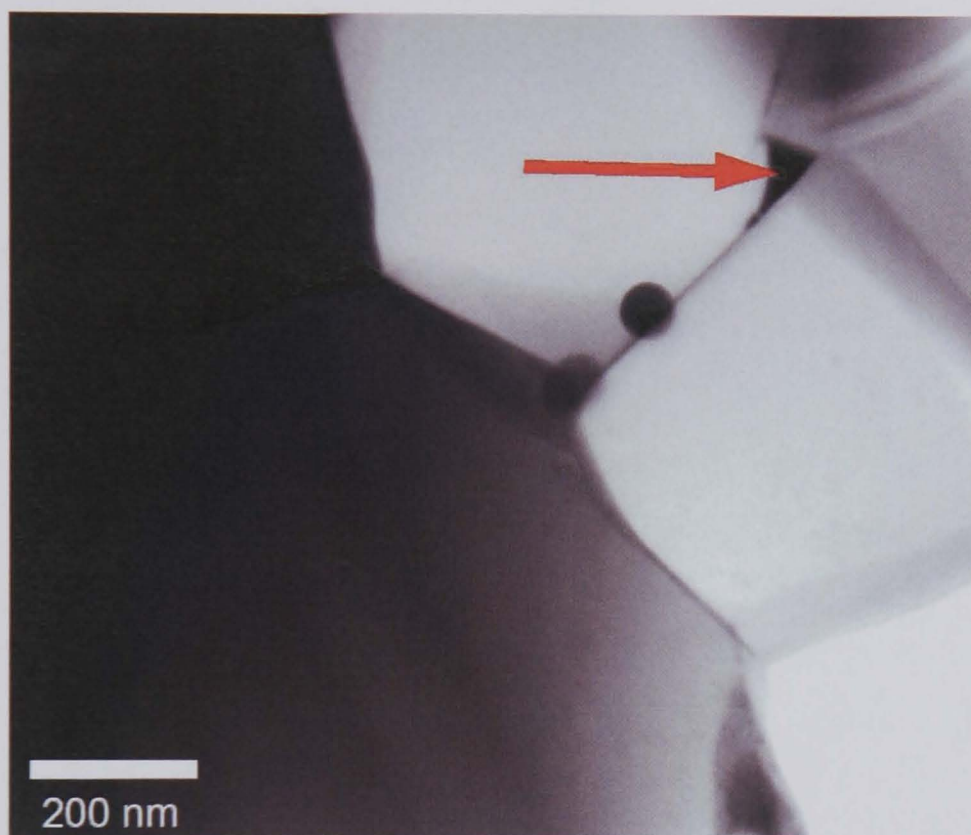
Figure 5.17: *TEM image showing one of the triple points from which the analysis in figure 5.18 comes.*
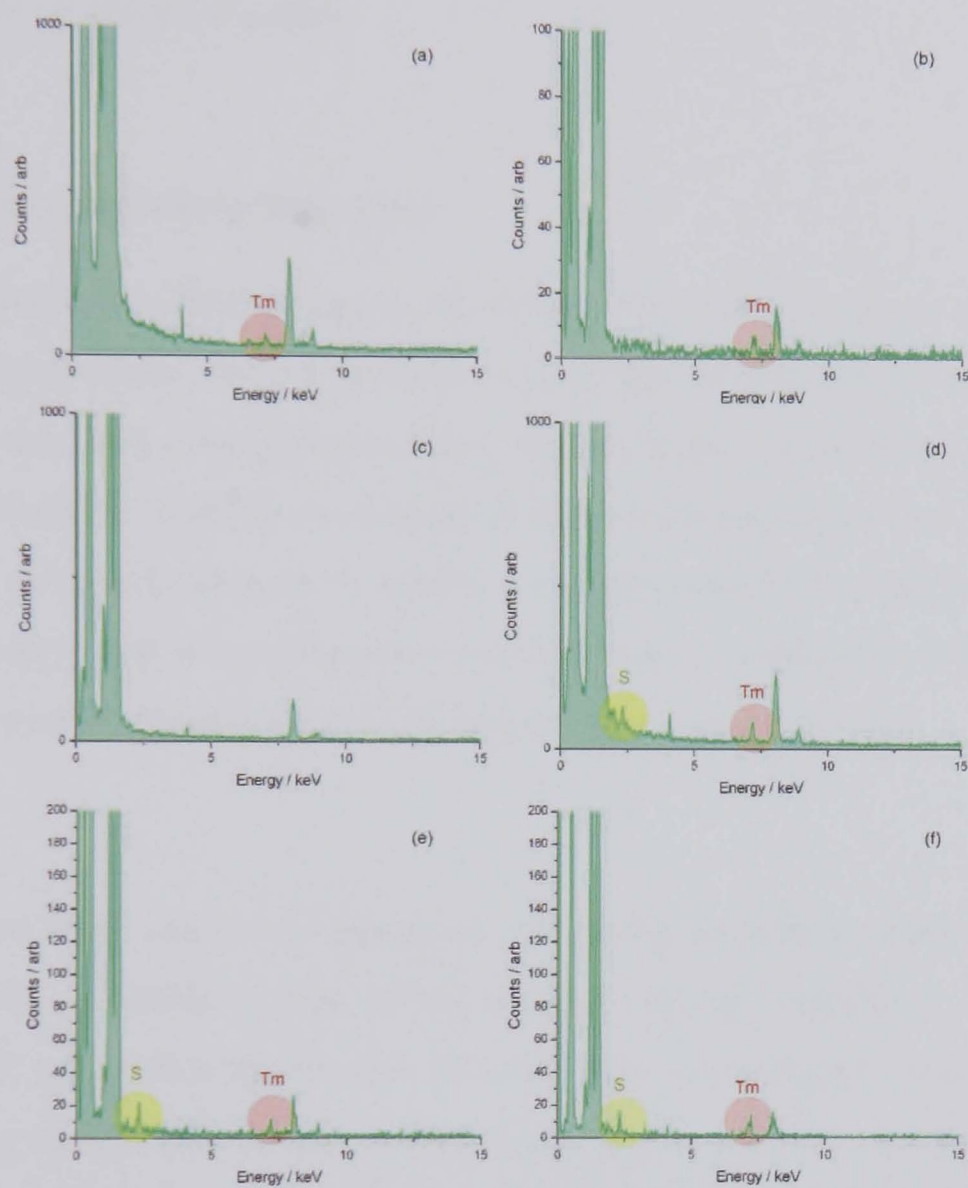
Figure 5.18: *Several EDS spectra from Tm doped spinel. Spectra taken from a variety of positions within the microstructure. (a) grain boundary, (b) grain boundary, (c) grain centre, (d) triple point, (e) triple point and (f) triple point.*

boundary but the total counts for the spectrum was higher than that aquired here.

For the Tm doped spinel, the presence of sulphur was confirmed at selected triple points, however, the low concentration in all other regions means that the effect is not as widespread as previously stated.

5.2.5 Grain Boundary Structure

The bright field and HAADF images in themselves do not show whether a second phase or indeed a glassy phase is actually present, for this, high resolution TEM was required to observe the character of the grain boundary. Figures 5.19 and 5.20 shows a selection of boundaries in spinel. These are boundaries chosen simply because of their alignment to the beam at the time of analysis. It is difficult to make any complicated tilt adjustments due to the rapid onset of contamination and/or damage. A well-thinned sample usually has many grains in a homogeneously thin region from which to choose.

It can be seen that there is no evidence of any second amorphous glassy phase at the boundary. The crystalline nature of the material remains throughout. It is unclear where the RE segregation fits into the structure from these images. Any brightness at the boundary cannot be attributed to the dopant atoms as it is an artefact caused by the imaging where the grain boundary structure leads to a contrast change due to a difference in the effective inner potential experienced by the electron beam[105]. Therefore, while the dopant atoms may well affect the local structure, the lattice potential has already been altered due to the presence of the boundary itself.

Figure 5.21 shows a twin boundary in a Eu doped spinel; As defocus is adjusted the
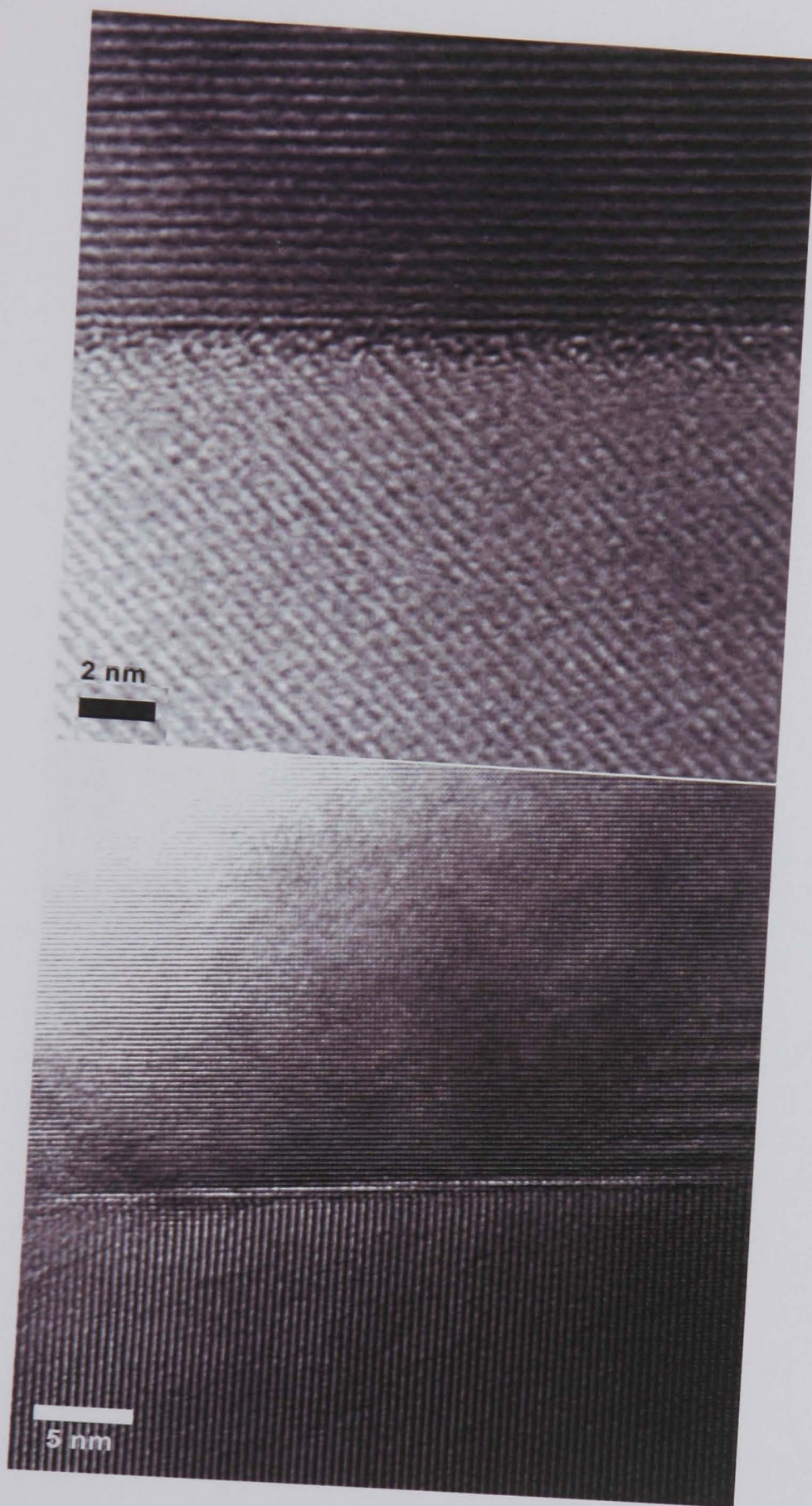
Figure 5.19: *HRTEM images of grain boundaries in Eu doped spinel.*
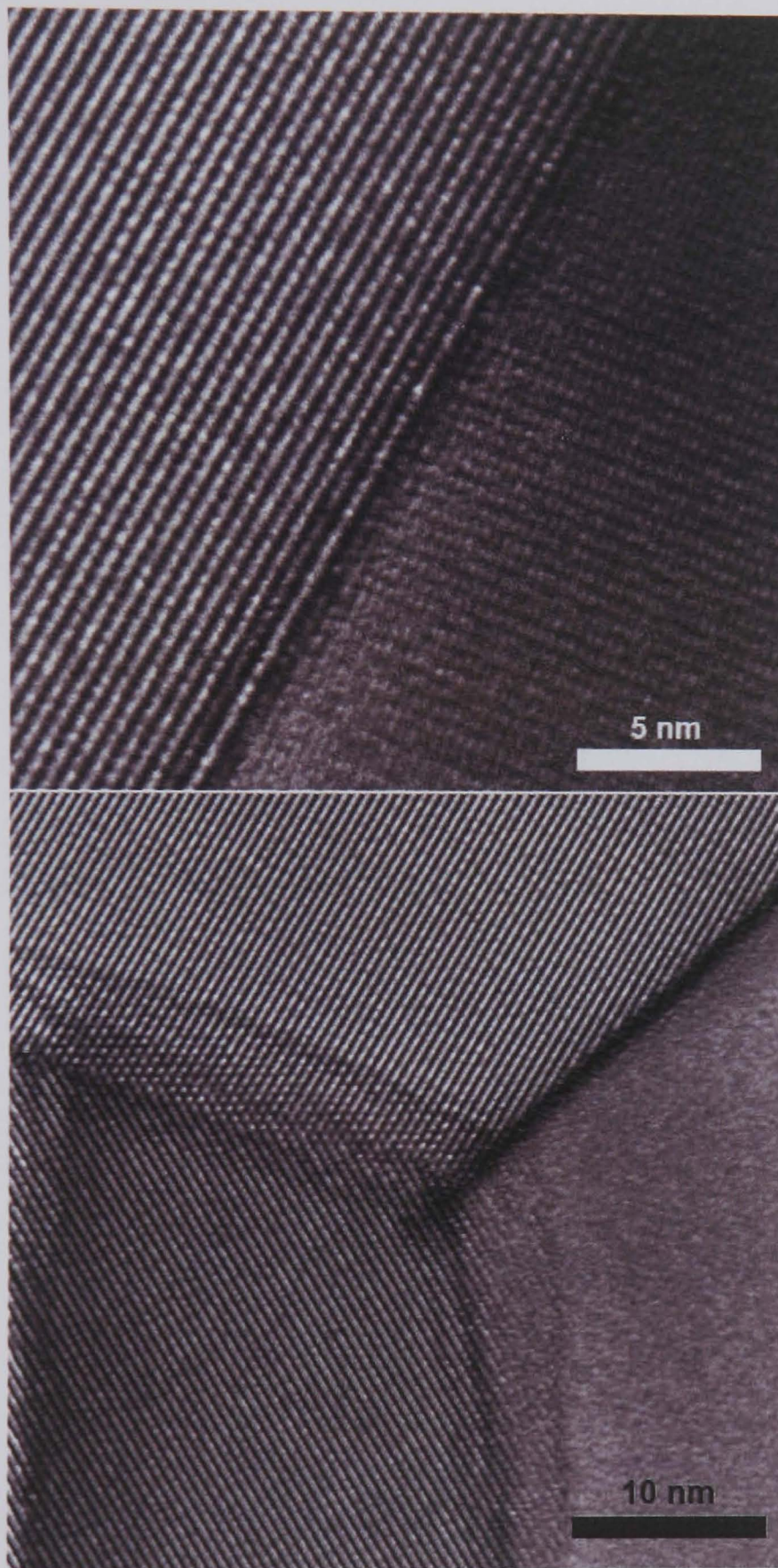
Figure 5.20: *HRTEM images of grain boundaries in Gd doped spinel.*
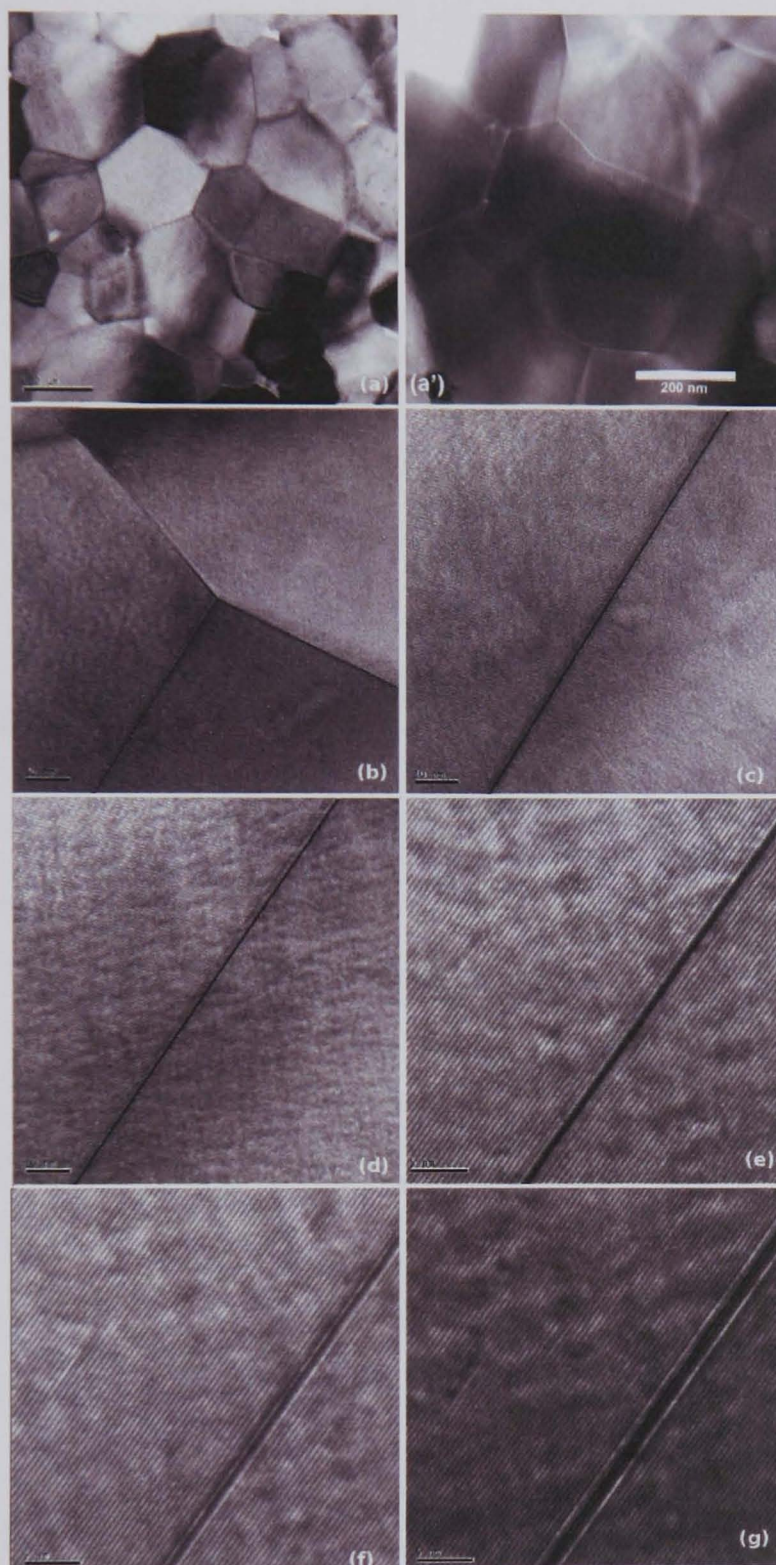
Figure 5.21: *HRTEM images of Eu doped spinel special boundary. a) BF image of region around grain. a') HAADF image of grain, showing damage due to imaging at higher magnification b) Grain containing twin boundary. c - g) HRTEM images of twin boundary imaged at different defocus positions.*

contrast at the boundary is altered. This is a method by which any structure in the boundary region can be identified. The through focus images show the fringes to be symmetrical about the boundary suggesting that the beam is well aligned with respect to the boundary, but also the fringes do not spread far either side of the central line. The associated HAADF image does show a small contrast change along the grain boundary suggesting segregation, however, this may simply be an anomalous contrast feature as coherent twin boundaries have a minimal structure difference from the perfect crystal. The differences in segregation depending on boundary type have been discussed in section 2.3.2, the HAADF images show a relatively homogeneous segregation.

5.3 Chapter Conclusions

The aim of the microscopic analysis is to find greater detail regarding the nature of RE doping in the oxides studied. Previous results have shown evidence of segregation to within 1 nm of the grain bounary for Y, La and Gd in alumina.

The TEM analysis of the Eu and Tm doped spinel and alumina has successfully identified the fact that the RE dopants are located within 1 nm of the centre of a grain boundary in all cases and that there is certainly no amorphous phase present (as would be expected if a large amount of silica or other liquid phase sintering compounds were used). The grain boundary is a crystalline region, within which the RE ions have segregated.

The use of conventional HRTEM does have the problem that imaging artefacts may occur producing misleading analysis. An example is that of the special boundary. While there is a contrast feature in the HAADF image, it is not conclusive evidence for RE segregation. Further investigation into the nature of the segregation follows in the succeeding chapter.

The importance of homogeneously thinned regions containing a large number of grains has been highlighted, this is central to all TEM imaging, not least the aberration corrected STEM in the following chapter.

Chapter 6

Aberration Corrected Scanning Transmission Electron Microscopy of Rare Earth Segregation

6.1 Introduction.

"The sub-Å regime has been succesfully achieved in the [aberration cor-
rected](sic) STEM, which as of today holds the record in spatial resolution
for a direct image of a crystal lattice. More importantly, the combina-
tion of atomic-resolution Z-contrast STEM and EELS represents a powerful
method to link the atomic and electronic structure of solids to their macro-
scopic properties, which allows the properties of the materials, nanoscale
systems, and interfaces to be probed in unprecedented detail." (*M. Varela et
al, 2005*)[106]

6.1.1 Review of Aberration Correction in the STEM

The idea of resolution is based on the ability to distinguish if an image feature is one or two different objects. The Rayleigh criterion[107] states the case where two sources of light are distinguishable. This is analagous to microscopy in that the resolution represents the ability to distinguish between two objects within an image. The goal of microscopists has long been to reach and surpass the limit whereby individual atoms can be distinguished.

In the electron microscopy field, the highest resolutions can be achieved in TEM. In a well oriented sample, electron beams may interact strongly with a crystal to form multiply diffracted beams which are then brought together in the objective lens such that the interference creates an image. The image is a direct depiction of the atom columns as the interference is that of the direct and diffracted (by the column) beams[108].

There are two modes of TEM operation. Conventional transmission electron microscopy (CTEM) is where the thin specimen is illuminated by a broad beam of electrons and post-sample optics focus the image on to a screen. Scanning TEM (STEM) works such that the electron optics focus a probe onto the surface of the TEM specimen (analagous to SEM) and images are produced using a variety of detectors. An important similarity arises due to the principle of reciprocity in optics; the optical rays (electron beams) may be switched to run in the opposite direction. This is equivalent to interchanging the object (source) with the image. Theoretically the two modes should produce identical information[109].

The resolution of an instrument is ultimately dependent on the wavelength of the incident radiation (photons for conventional optics, and electrons for TEM), however this assumes perfect lenses. All lenses manifest a degree of aberration (i.e. imperfection), and reduce the attainable resolution of the microscope, thus a combination of improve-

ments to the manufacture/control of lenses or correction of the aberrations is required. This is possible in light optics, however Sherzer[110] proved that electron optics will always suffer from spherical and chromatic aberrations (C_s and C_c respectively) if the following conditions exist: the optical system is rotationally symmetric, a real image of the object is produced, the lens fields do not vary with time and there is no charge on the axis.

Chromatic aberration may be reduced significantly by use of an energy filter to provide a monochromated beam, current systems employing spherical aberration correctors have well-controlled monochromated beams and/or energy filter systems so C_c will not be considered here.

Figure 6.1 shows the ray diagrams for both perfect and aberrated lenses. Higher angle rays come to focus before lower angle rays such that a disc of least confusion rather than an infinitesimal point is produced in the image plane.

The C_s was found by Sherzer[110] to be;

$$d_x = 0.64 C_s^{\frac{1}{4}} \lambda^{\frac{3}{4}} \tag{6.1}$$

Where d_x = the native (or Sherzer) resolution limit of an uncorrected electron microscope and λ = the electron wavelength. By increasing the accelerating voltage of the electron beam (i.e. reducing the wavelength) the resolution may be improved, however, this results in a number of other practical difficulties (including cost!)[108].

The resolution limit resides with the spherical aberrations, and therefore, a method for reducing these is the most practical way of improving the modern TEM. There are a number of approaches to dealing with spherical aberrations; image processing[111], super-resolution[112] and hardware correction[113]. Here, we deal with the hardware correction, specifically the SuperSTEM facility at Daresbury laboratories, Cheshire, UK.
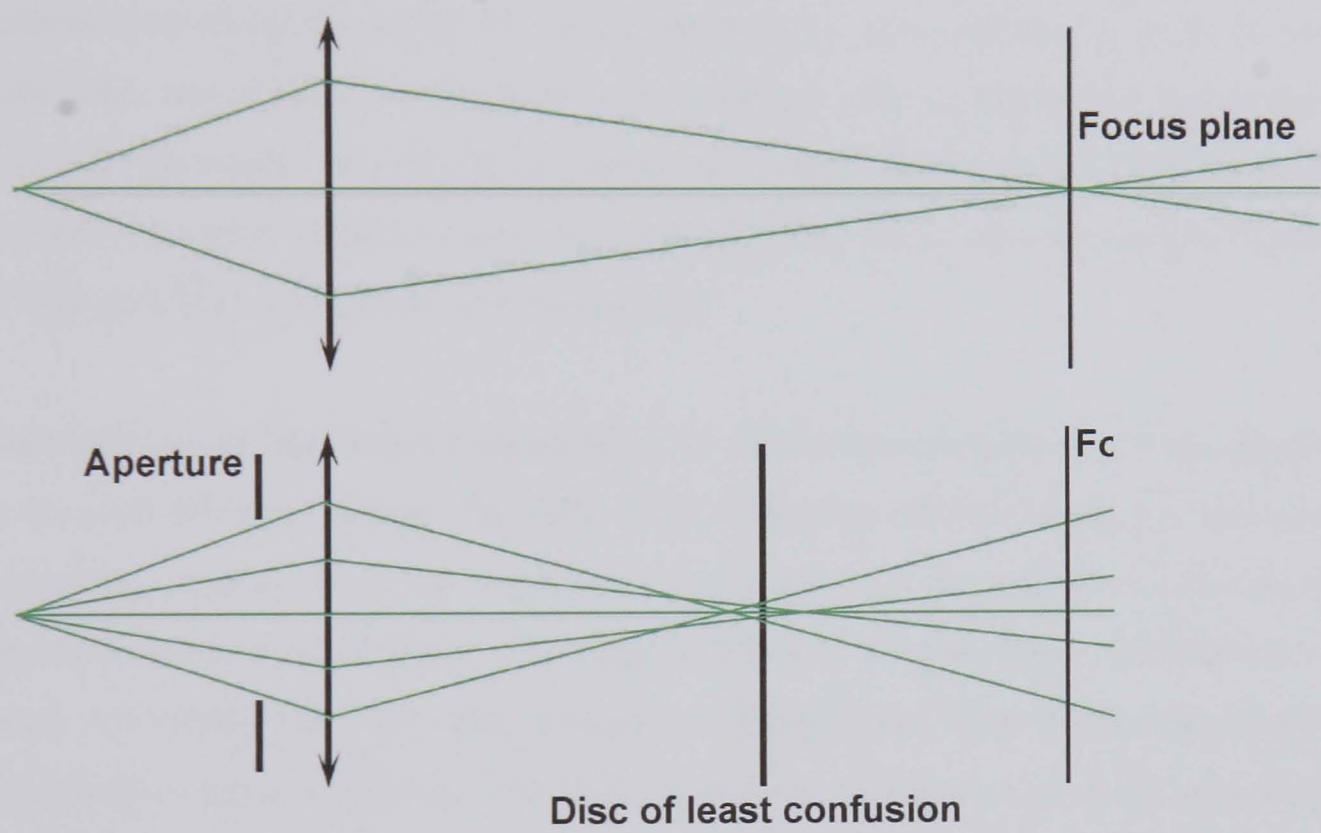
Figure 6.1: *Schematic diagram of rays through perfect and spherically aberrated lenses respectively.*

113

6.1.2 The Aberration Corrector

The probe size in a TEM is determined by the range of angles which contribute to the maximum in the probe intensity profile. The useful angular range is restricted to small angles in conventional round electron lenses thus creating a probe size of $\sim 100\lambda_e$[113]. For many years, there was no useful development in aberration correction, the recent advances owe much to the increase in computing power now available. Correction methods rely on constructing a device to create negative aberrations to compensate for the positive aberrations created by the lenses. Returning to the conditions in which aberrations arise, one of these conditions must be broken to remove aberrations (real image, rotational symmetry, time invarience and on-axis charge). A real image is still required, therefore the other conditions must be examined[109]. For a full mathematical review of each condition see Hawkes and Kasper[114].

Practically, it has been found that breaking the rotational symmetry of the lens system is the most effective method. By 1999, there were three different designs of corrector succesfully installed in various instruments based on either a quadrupole-octupole or hexapole combination of lenses. The SuperSTEM and the Oak Ridge National Laboratory, US facility[109, 113] have conventional (dedicated) STEM columns fitted with quadrupole-octupole correctors. The Q-O corrector was designed specifically to produce a fine and highly intense electron beam for use with HAADF imaging and EELS analysis. Figure 6.2 shows a schematic arrangement of the poles in the multipole lenses, and figure 6.3 shows the path of electrons through the aberration correction system within the STEM column along with an exagerrated representation of the shape of the beam normal to the column axis.

The actual lens aberrations are described as "the surface whose value is the distance between where the wavefront is and where it would be for an ideal lens" (*Bleloch and Lupini*[109]), represented by a polynomial expansion, where the low order terms are the
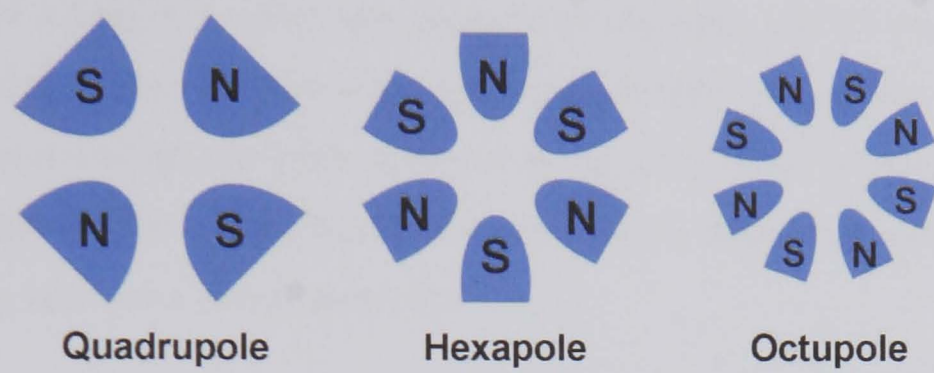
Figure 6.2: *Schematic of the multipole lenses used in aberration correctors.*
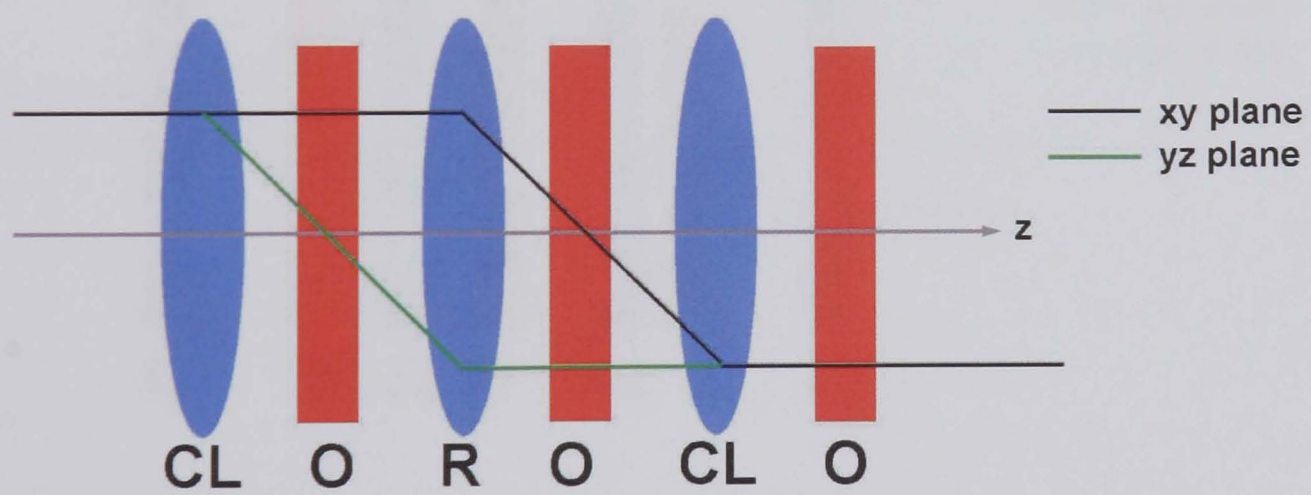
Figure 6.3: *Electron path through the aberration corrector.*

115

easiest to correct and higher order terms progressively more difficult. Spherical aberration is a 3rd order effect, which increases with the cube of the angular deviation. The multipole lenses (Q-O corrector) acts by distorting the roundness of the beam. The octupoles have a field that varies with distance off the optic axis (in the same way as spherical aberration) but has four-fold rotational symmetry (about the column axis). The beam passes through the series of correctors (figure 6.3) and is distorted such that it acquires negative spherical aberration from the octupole lenses then emerges from the corrector once again as a round beam[106].

The SuperSTEM-1 corrector (at the time of writing, the second microscope with new modular lens column was being installed) varies slightly from figure 6.3 and has a different arrangement of quad and octupole lenses removing the original round and cylinder lenses from the corrector (figure 6.4)[109]. Results shown in this thesis were obtained in the SuperSTEM-1 column. Figure 6.5 shows a schematic of the SuperSTEM column.
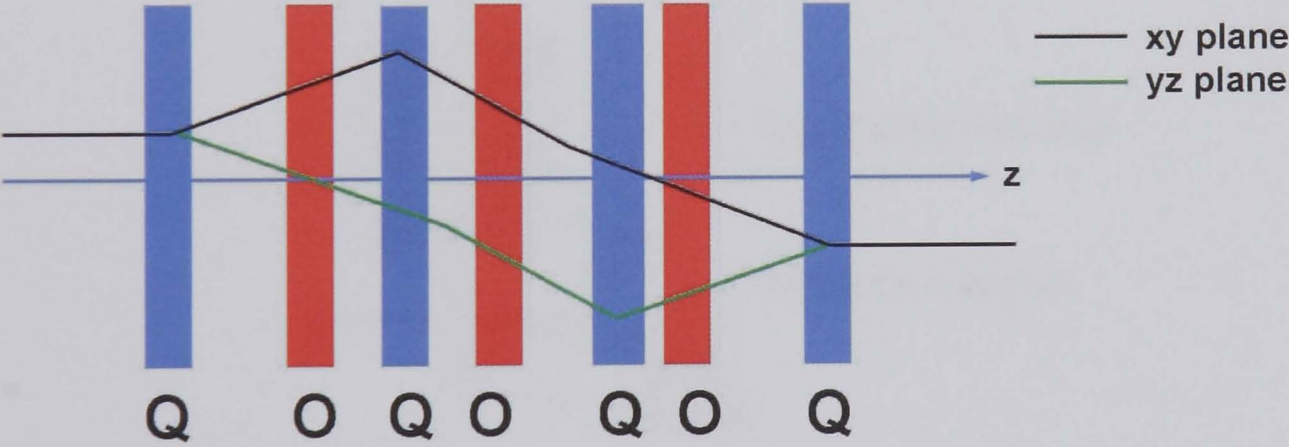
Figure 6.4: *Electron path through the SuperSTEM aberration corrector.*
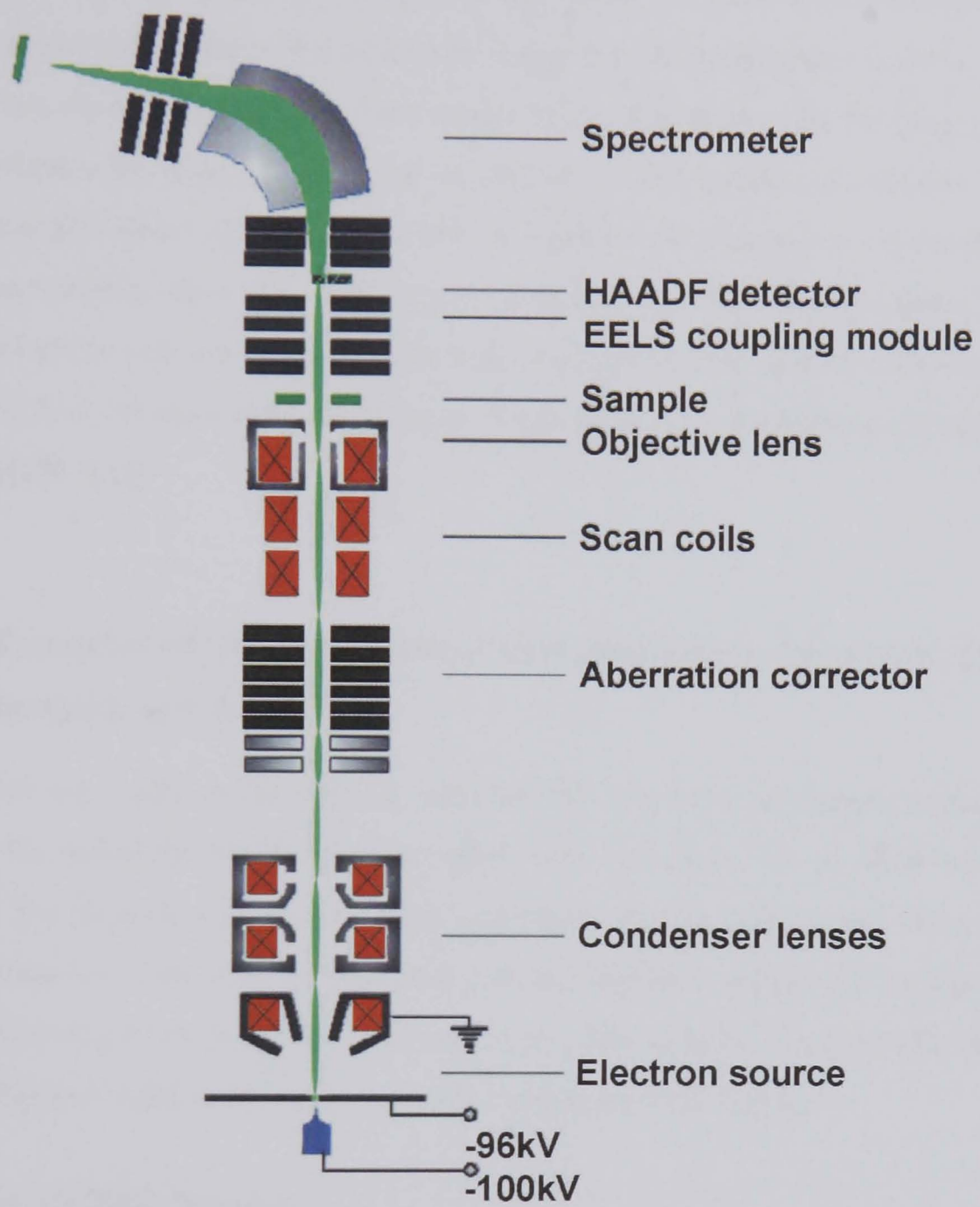
Figure 6.5: *Schematic of the SuperSTEM microscope column showing the main features including the positions of the EEL spectrometer and aberration corrector.*

6.1.3 Aberration Correction and Diagnosis

It has been mentioned that the advances over the last 5 - 10 years regarding aberration correction in the TEM has been accelerated due to the increases in computing power. This has allowed the methods for aberration correction to become semi automated. To measure the aberrations a Ronchigram image must be aquired. The Ronchigram is a far-field shadow BF image (in the case of aligned crystal samples, a coherent, large-angle convergent beam diffraction pattern). A number of Ronchigrams are recorded by a CCD, each with a slight shift from certain corrector coils. The expected shifts due to the control of the coils are compared with measured shifts (from unshifted Ronchigram) in order to find the aberration coefficients. From these, the aberrations are corrected iteratively[109, 113].

6.1.4 Examples of Recent Results from Aberration Corrected STEM Imaging and Analysis

While there are many varied possible uses for the aberration corrected microscope, currently the published work has dealt mainly with interfaces. In all TEM work the quality of the sample is paramount, and a guide to sample preparation follows that samples should be less than 20 nm thick (in the analysis region) and be free from damage induced by the preparation process itself. The samples must also be cleaned prior to insertion, again similarly to any well maintained TEM facility.

Example 1: Si/NiSi$_2$ interface

One of the key initial results from the newly built SuperSTEM facility was that of the interface structure of Si/NiSi$_2$. Interfaces of such structures are of interest to the semiconductor industry and therefore of vital importance. A model of the interface structure was constructed directly from the Z contrast STEM images at the SuperSTEM, rather than by simulation of the expected structure or a heavily processed image. This model,

constructed from the SuperSTEM images correlated well with a recently proposed model of the interface structure that did not comply with previous ideas. This was a perfect example of the potential influence of aberration corrected Z contrast imaging[115].

Example 2: segregation to interfaces of silicon nitride ceramics

Silicon nitride ceramics have similar problems to the oxide ceramics dealt with in this thesis. Changes to properties can be affected by the addition of dopants, for example the seeding of high aspect ratio grain structures to improve the fracture toughness and reduce the brittleness. This anisotropic grain growth is known to be increased with the addition of metal oxides and, with the greatest effect, the RE oxides. The Si_3N_4 ceramics are fabricated through liquid phase sintering, where amorphous intergranular films of oxynitride are formed at the boundary within a region of $\sim$2 nm. Shibita et al have used aberration corrected STEM to discover where within the grain boundary amorphous phase the RE were placed, i.e. within the glassy phase or along the crystal lattice at the boundary[116]. Preferential segregation to certain boundary types was found to be the reason behind the anisotropic grain growth[106] due to the RE ions residing in cation sites normally occupied by Si at grain surfaces whereby hindering the Si attatchment required for grain growth[116].

6.2 SuperSTEM Results

Aberration corrected imaging has allowed unambiguous analysis of grain boundaries to be performed where previously phase contrast imaging artefacts made contrast features at boundaries difficult to understand and resolution limits of HAADF imaging in the FEGTEM limiting the size of structures that may be observed. More recent advances at the SuperSTEM, such as the parallel bright field imaging capability, have led to an increased understanding of the grain boundary region. Figure 6.6 previews the potential of parallel HAADF and BF imaging of a spinel lattice in a well oriented grain in the

SuperSTEM. Further images of this sample appear later.

6.2.1 Sample Damage in the SuperSTEM

The same problems regarding damage in the FEG TEM are exacerbated by the greater energy density of the aberration corrected beam. However, it has been possible to image spinel samples prior to damage at atomic resolution. Attempts to image alumina were mostly unsuccesful because of sample drift and instability due to charging. Damage was a big problem with alumina samples, as such the bulk of the following results are from spinel samples. Spinel was also prone to damage, however was more stable in the column and was therefore less likely to drift during image aquisition/focussing. This may be due to the slightly different band gap energies in the two systems. In order to dissipate charge the electrons in the spinel may be excited to the valence band more easily than alumina. The difference between the two is small but may be enough to explain the difference in behaviour within the TEM. As far as possible, identical sample preparation was performed for both alumina and spinel, however, alumina was certainly more susceptable to sample damage.

Figure 6.7 shows the damage caused upon multiple raster scans of a grain boundary region in a Eu doped spinel. The bright, Eu rich, boundary becomes broadened and spread, suggesting diffusion of the Eu atoms either from the boundary on to the surface or to vacancies within the adjacent grains. This has proved the biggest problem in terms of imaging grain boundary regions owing to the low concentrations of dopant ions in the first place. Figure 6.7 shows damage after 1, 3 and 6 scans over the region.

Figure 6.8 shows a single grain boundary in a Tm doped alumina before and after a PEELS line scan. It is clear that the damage is significant in this particular sample and thus higher magnification or analysis work could not be achieved.

120
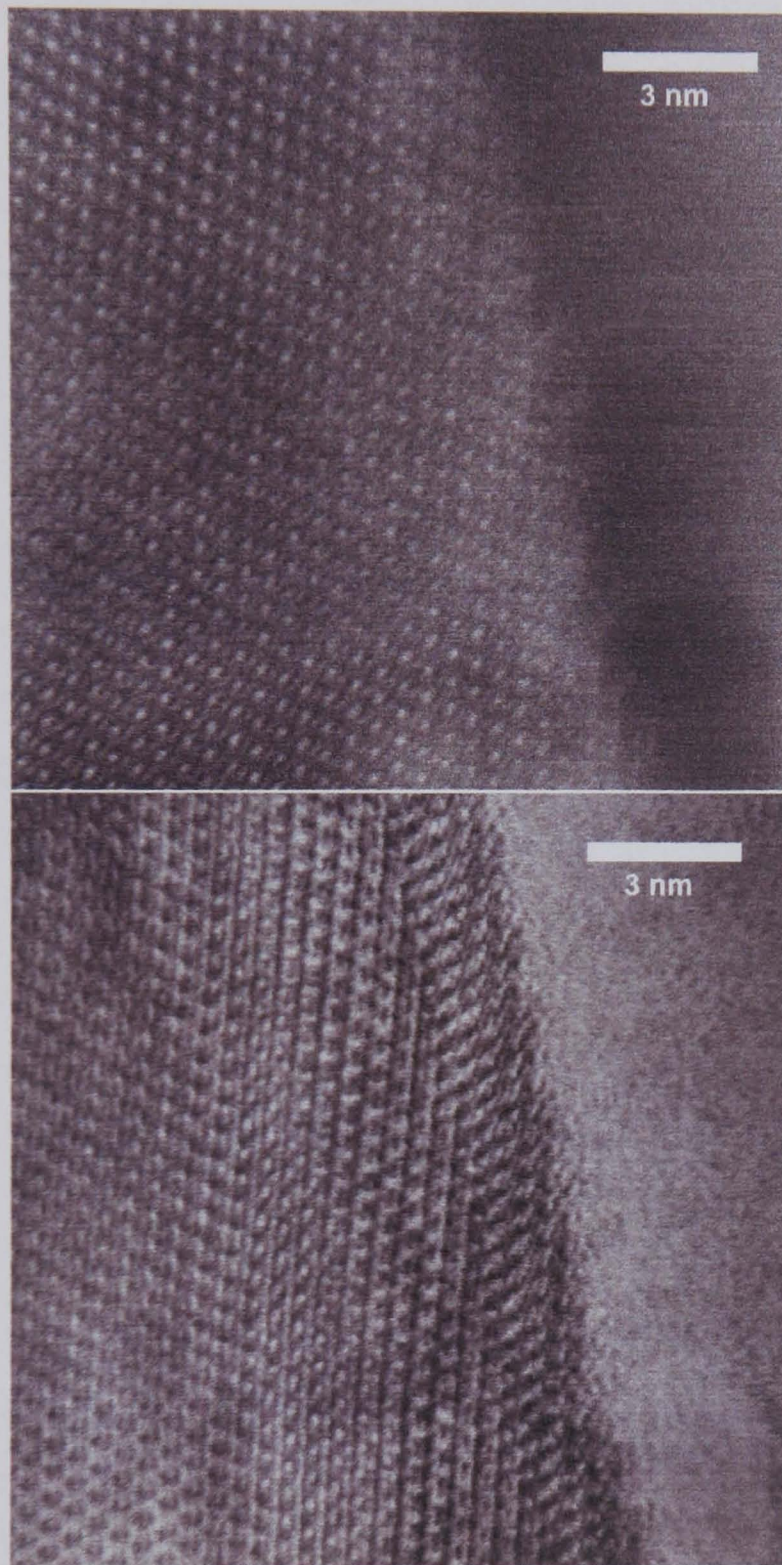
Figure 6.6: *(above) HAADF, and (below) BF images of a well oriented grain.*
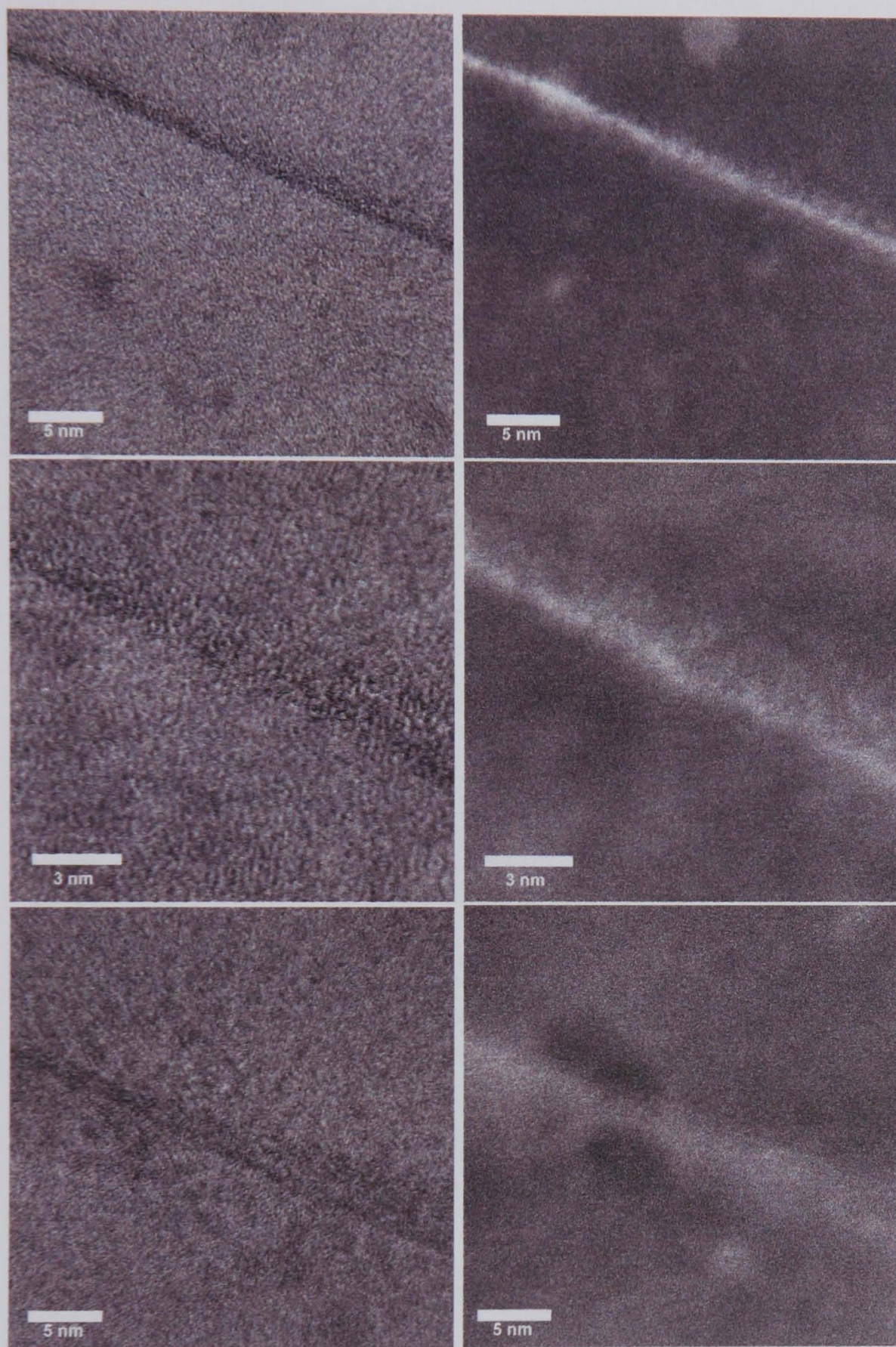
Figure 6.7: *Subsequent raster scans of the same region in a Eu doped spinel (HAADF on left and BF on right).*

122
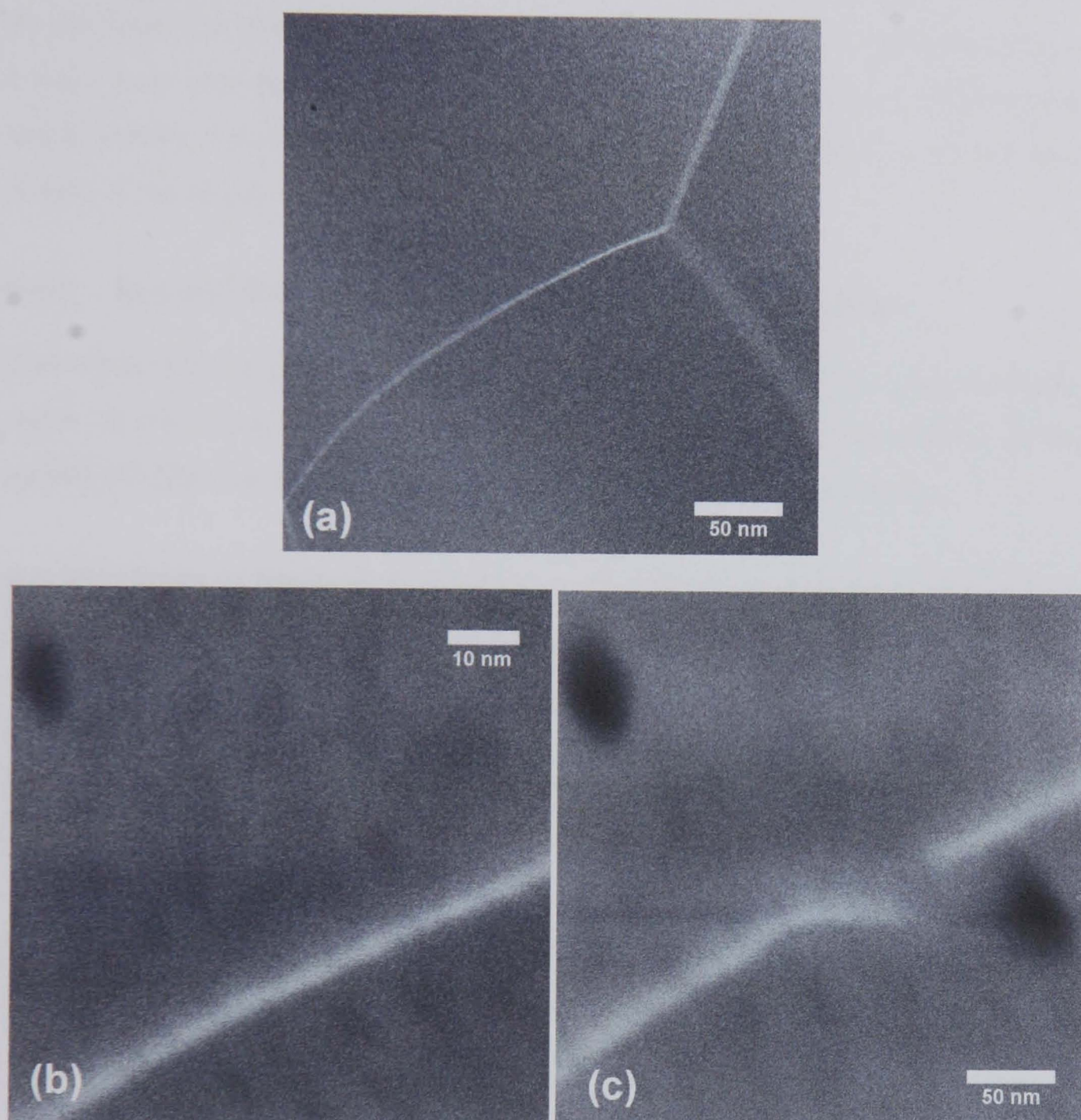
Figure 6.8: *Example of sample damage in a Tm doped alumina sample imaged in the SuperSTEM. a) Region of grain boundary, b) HAADF image before line scan, c) HAADF image after line scan.*

Several methods have been used to try to minimise charging and contamination problems. The samples analysed in this section of the thesis were all subject to plasma cleaning (as described in the experimental details section) and the Eu doped spinel sample was heated to 200° for 30 mins within the SuperSTEM column itself. Charging is a major issue with these insulating samples, they are relatively stable if left overnight before analysis, however a 100 μm copper mesh grid was positioned on the entrance surface of the sample within the holder.

6.2.2 SuperSTEM Analysis of Grain Boundary Composition

Two different Eu doped spinel samples were used to characterise the grain boundary region. Unfortunately the first of the samples was imaged prior to installation of the parallel BF detection system, hence purely HAADF images were obtainable.
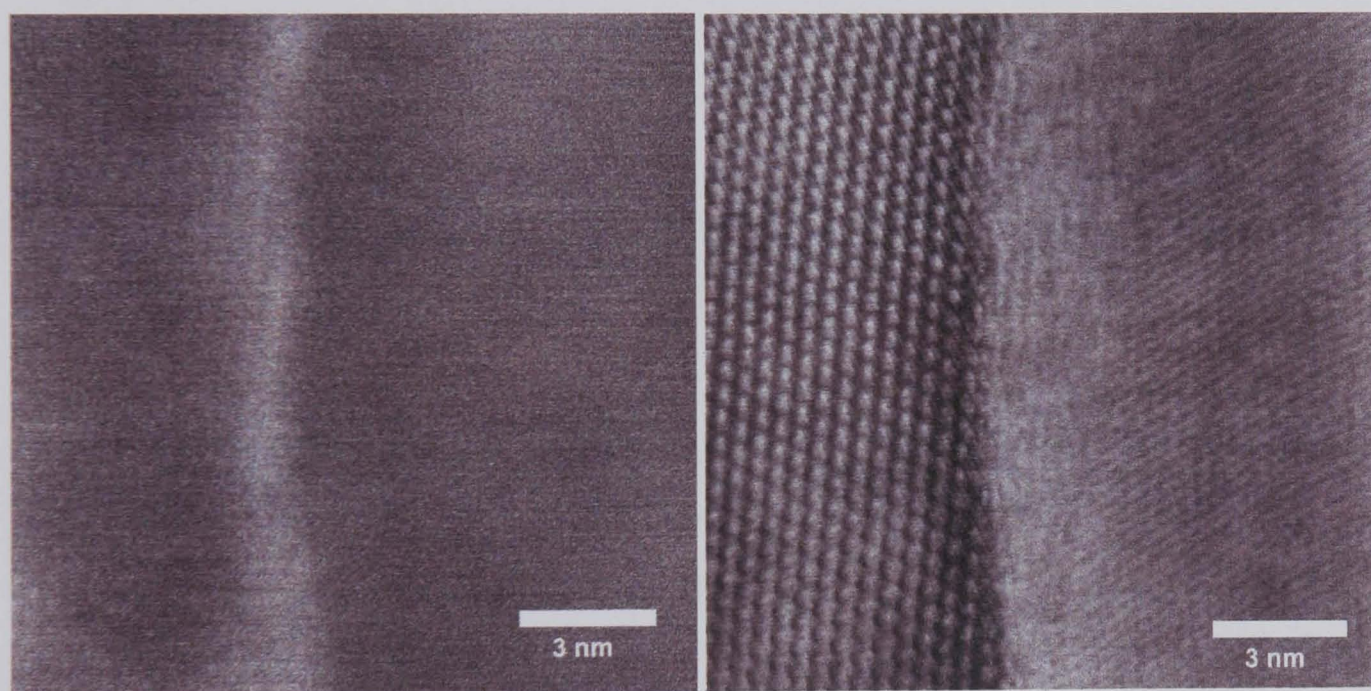
Figure 6.9: *Well oriented grain adjacent to poorly oriented grain, Eu doped spinel.*

Figure 6.9 shows a well-oriented grain next to a poorly oriented grain. Importantly, the boundary is curving as the lattice shows. This is matched exactly by the bright signal in the HAADF image. There is some evidence of structure in the HAADF image but

124

importantly (from intensity profile) the width of the bright (RE rich) region is <0.4 nm.
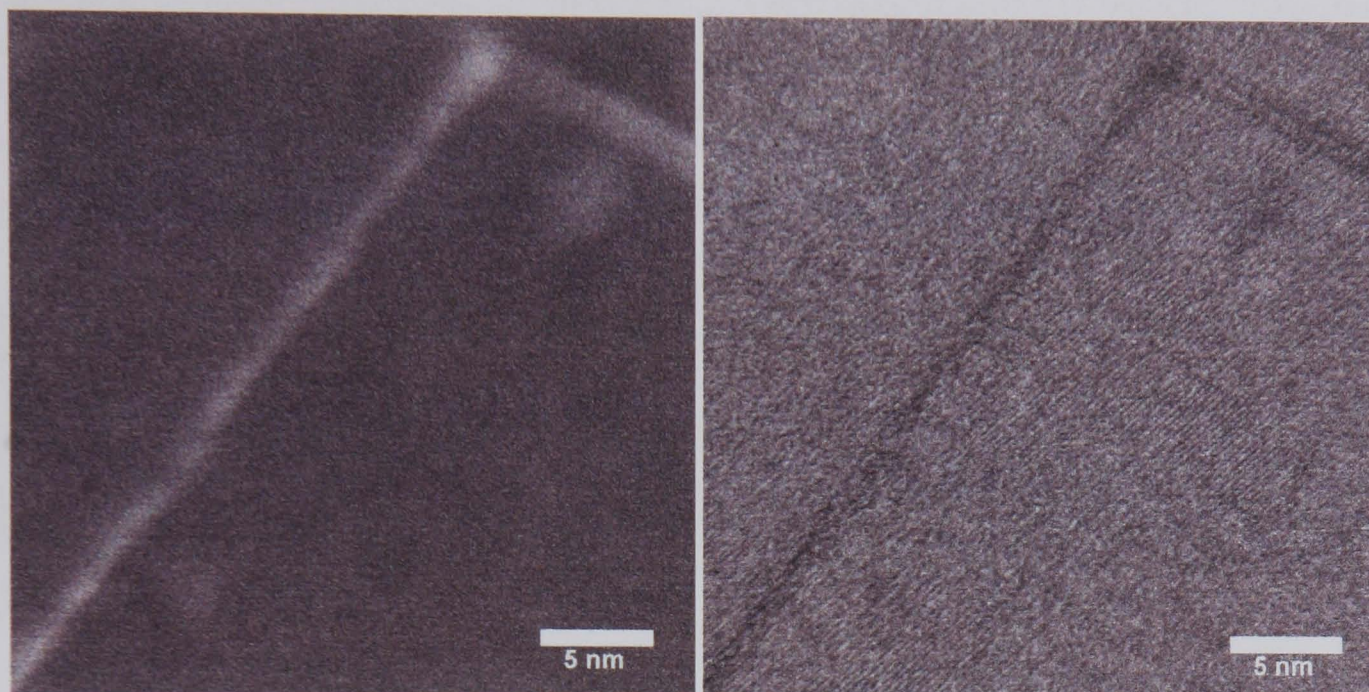
Figure 6.10: *SuperSTEM image of Eu doped spinel, HAADF and BF image pair.*

For figures 6.9, 6.10 and 6.11, the grains either side of the well aligned boundary are not parallel to a rational orientation and, therefore, are not in the beam chanelling condition (except the lh grain in figure 6.9.) This has serious implications for the estimation of the size of the RE containing region given above. When oriented in a channelling condition the beam couples with the atomic column producing a fine gaussian peak at the image plane. In a non channeling condition the beam does not couple and therefore spreads after the cross over (focus) position. The focus may not be precisely at the surface and so there is some uncertainty associated with the beam diameter. This is shown schematically in figure 6.12.

The following calculation provides an upper limit for the width of the bright region in an image of monolayer segregation in a non chanelling condition, i.e. assuming monolayer segregation, the eidth of the bright region can be no larger than the diameter of the beam at the exit surface. Using figure 6.12 as a model for the non-chanelling situation:
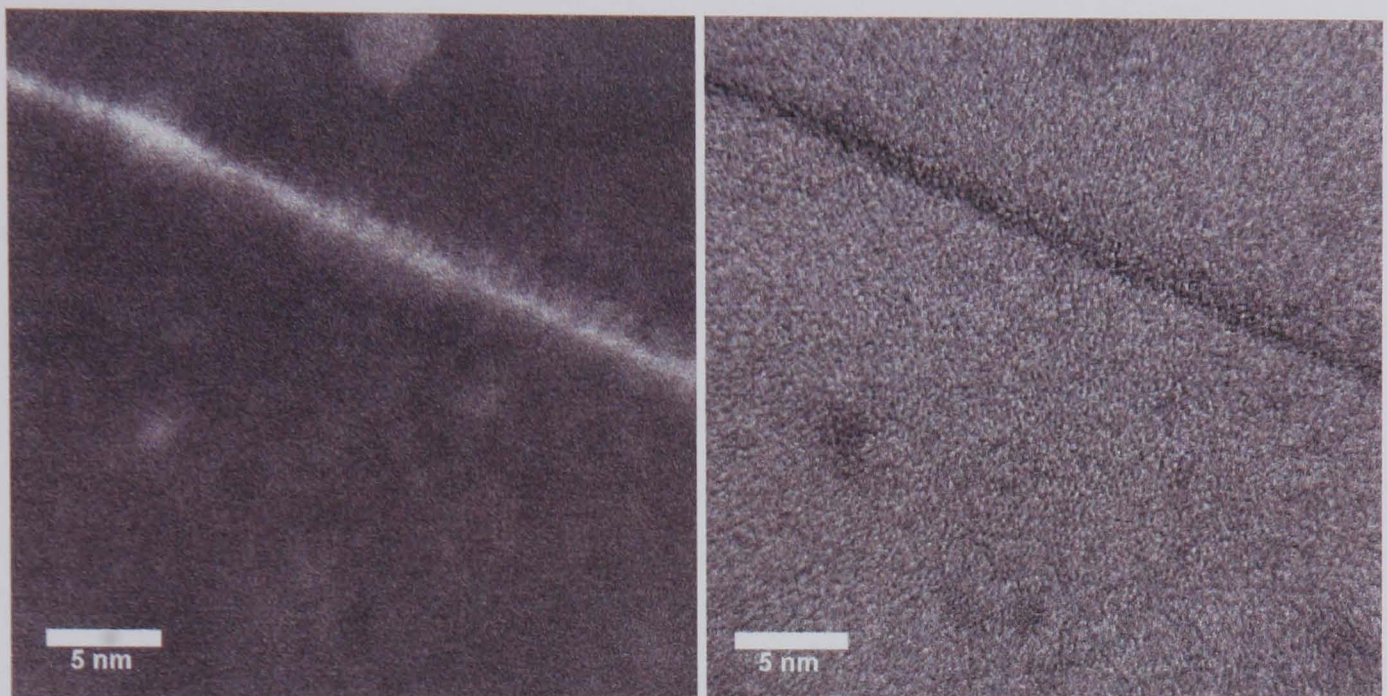
Figure 6.11: *SuperSTEM image of Eu doped spinel, HAADF and BF image pair.*
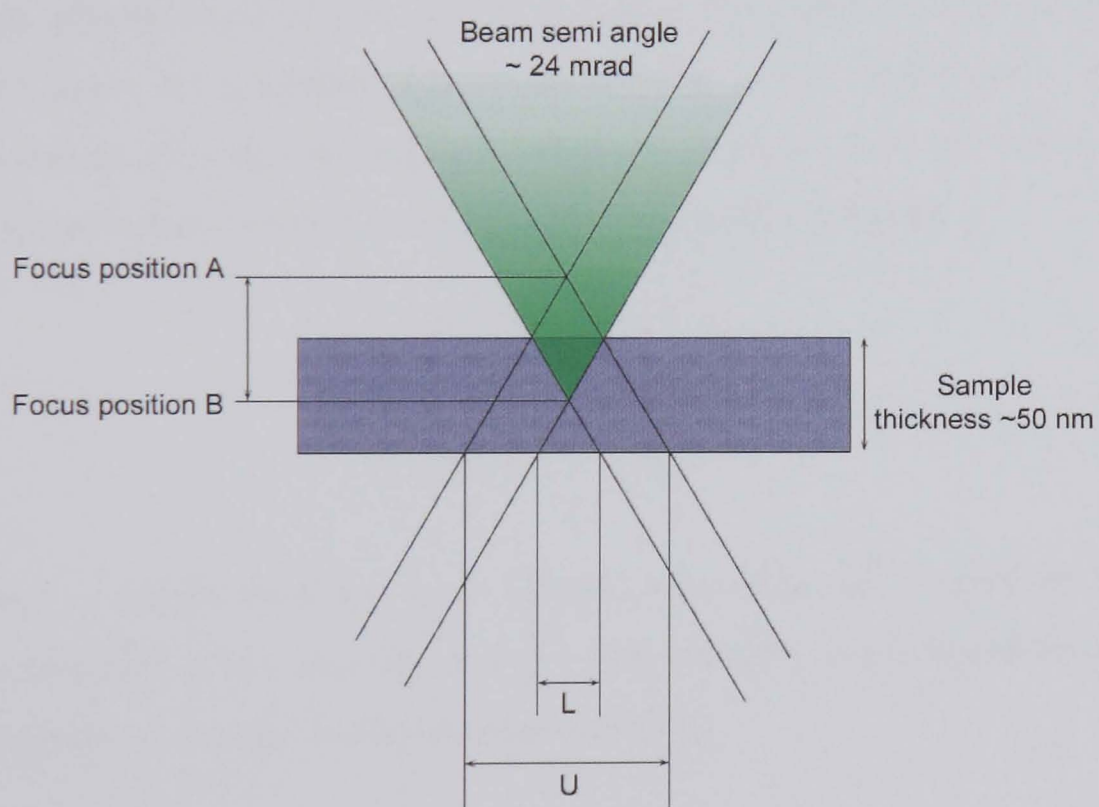
Figure 6.12: *Demonstration of the maximum size of a feature for a known beam semi angle and sample thickness. Labels L and U refer to the lower and upper limits to the beam size at the exit surface of the sample.*

$$b_{above} \times (t + (t \div 2)) = d_{above} b_{below} \times (t - (t \div 2)) = d_{below} \qquad (6.2)$$

Where b = beam semiangle at entrance surface assuming focus is $t \div 2$ above/below entrance surface (arbitrarily large error in order to provide upper limit to estimate), t = average thickness of region and d = diameter of beam at exit surface.

The thickness is derived from an EELS relative thickness map of a region around the boundary. Figure 6.13 shows a map of relative inelastic mean free path for an area close to the boundary images. The inelastic mean free path of the electrons directly relates to the thickness of the specimen at that point, therefore mapping a reagion can provide information about the average thickness. The thickness map was aquired with a 4 kV beam, 0.1 s integration time per pixel on a 19 x 32 pixel box. Each of the pixels contain data representing an entire EELS spectrum from that point from which the relative inelastic mean free path is calculated (and displayed);

$$t = \lambda_p \frac{I_p}{I_o} \qquad (6.3)$$

Where t = sample thickness, λ_p = plasmon mean free path (essentially the inelastic mean free path of the material) and $\frac{I_p}{I_o}$ = the intensity in the first plasmon peak and the intensity in the zero loss peak respectively[?].

The average thickness in the areas studied was found to be approximately 50 nm.

The beam semi angle is estimated as 24 mrad [117]. This is the semi angle spread of the beam at the sample position within the microscope column.

127
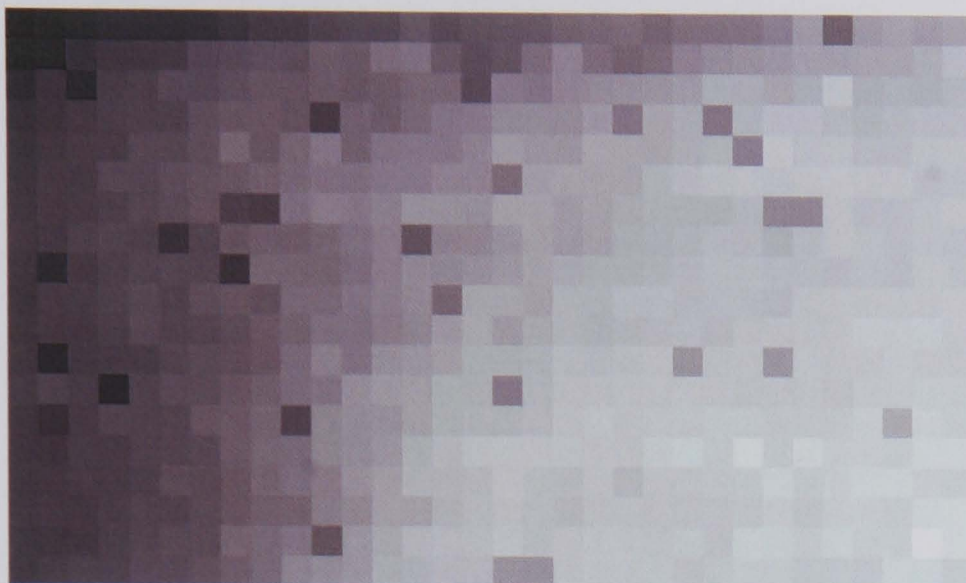
Figure 6.13: *Map from EELS data of the relative inelastic mean free path, this directly corresponds to the relative thickness of the sample in the region shown. Thicker regions are brighter.*

Assuming error in focus such that the focus is positioned $t \div 2$ above or below the sample entrance surface, 50 nm thick region and 24 mrad beam gives the upper limit to the diameter of the broadened beam at the exit surface of 2.5 nm. Therefore, due to the fact that the beam will continue to broaden as in figure 6.12 rather than chanelling, the width of the boundary in the HAADF image in figure 6.14 must be smaller than the width calculated from the FWHM intensity profile peak.

Remaining with figure 6.14, there is further evidence for nanometre scale boundaries. An integrated intensity profile taken from both the HAADF and BF images (the average linescan across the boundary integrated over a number of scans within the region) indicated gives the FWHM of <0.6 nm. Example linescans are shown in figure 6.15.

Figure 6.16 shows three boundary linescan positions in a Yb doped spinel. Associated intensity profiles for these boundaries are shown in figure 6.17. The FWHM of the
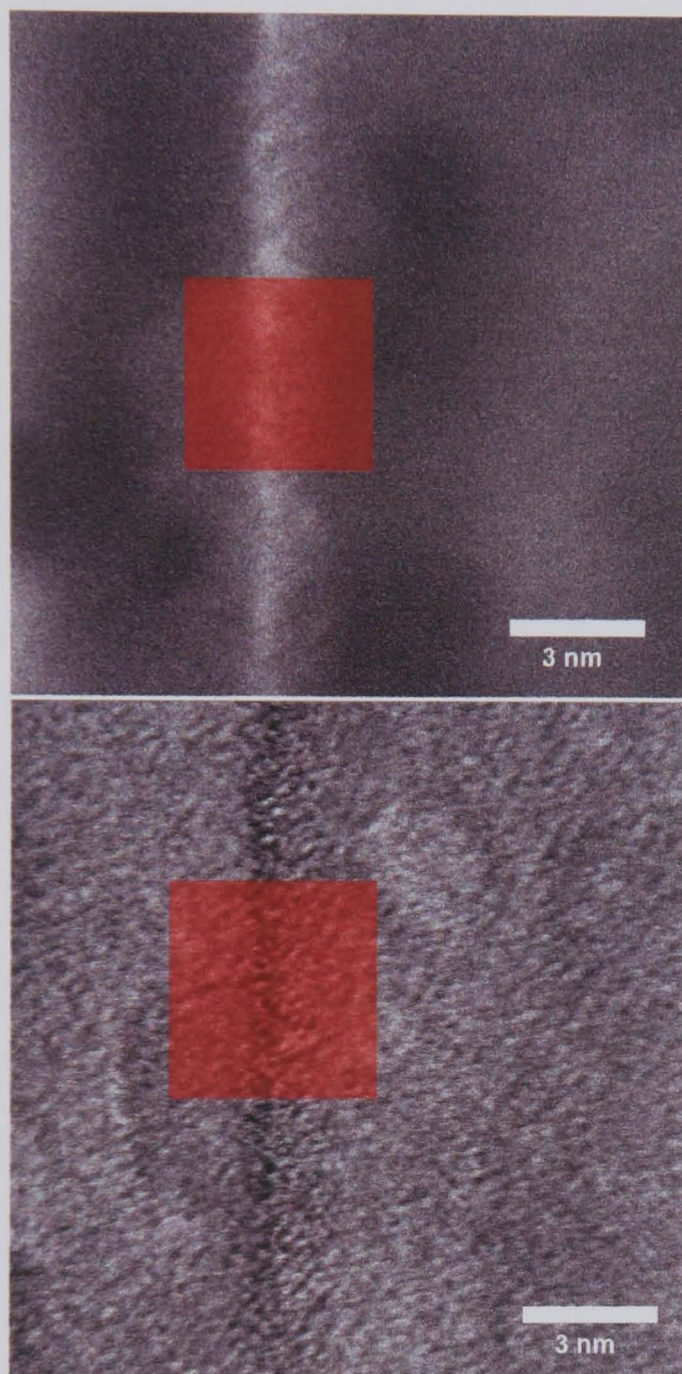
Figure 6.14: *HAADF and BF images of Eu doped spinel with linescan position indicated.*
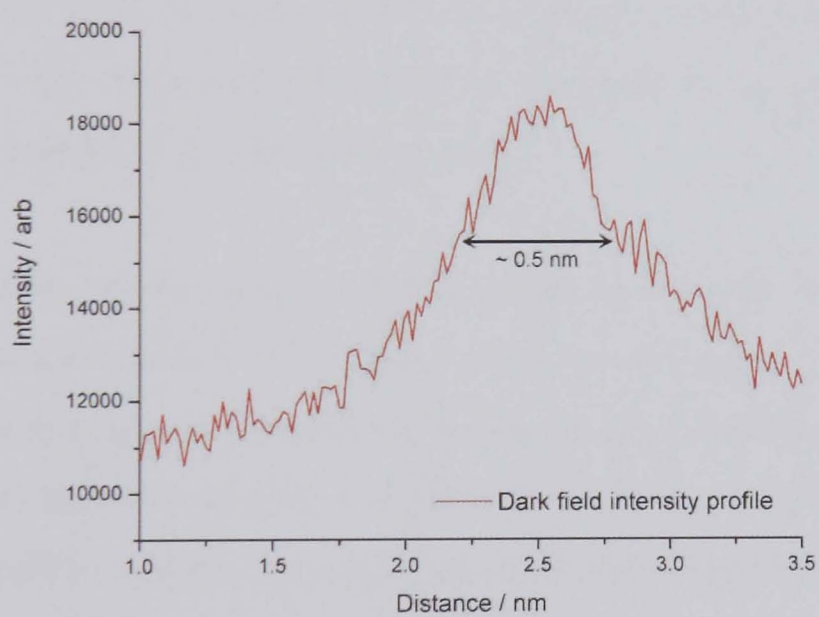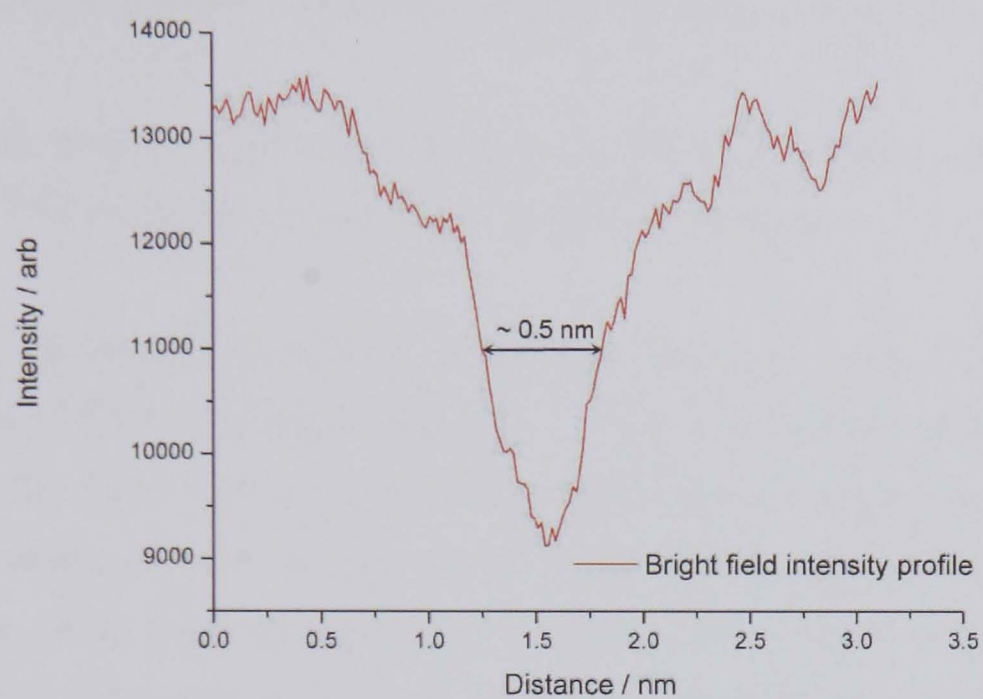
Figure 6.15: *BF and HAADF intensity profiles for figure 6.14*

boundaries are 0.31, 0.58 and 0.48 nm respectively.

Figure 6.18 shows a tilted grain boundary with the grains either side near a zone axis. The spread in the brightness across the boundary is indicative of a tilted boundary.

There is some evidence of periodicity along the boundary within which the RE ions are positioned. This periodicity is supported in the following images.

While there are images and intensity profiles that indicated sub-nanometer segregation, there is evidence for monolayer segregation. This comes from the perfectly aligned boundary in figure 6.19. While only the left side grain is close to a zone axis, the boundary itself is clearly well oriented with respect to the electron beam as there is virtually no broadening of the bright RE signal. It is possible to make out spots corresponding to atomic columns, again periodic in nature. Clearly with suspected monolayer segregation, the concentration of the RE is low, hence the level of contrast between the boundary and the bulk. This image was not altered or processed in any way (apart from line integration to smooth the lateral scanning noise).

Confirmation of the presence of Eu at the boundary comes from the EELS analysis. A line scan was performed with a 2 Å probe across the boundary. This was correlated with a BF intensity profile. Figure 6.20 shows the position of the line scan. Figure 6.21 shows the Eu/Al edge height ratio at each point along the line scan with the bright field intensity profile overlaid. Figure 6.22 shows the EELS spectra from the two points indicated in figure 6.20.

The Al and Eu ELNES edges in the EELS spectra overlap at around 125 and 145 eV, but the size and shape differ with the higher energy edge comprising a combination of the two. To unambiguously distinguish between Eu and Al in a line scan a ratio of the
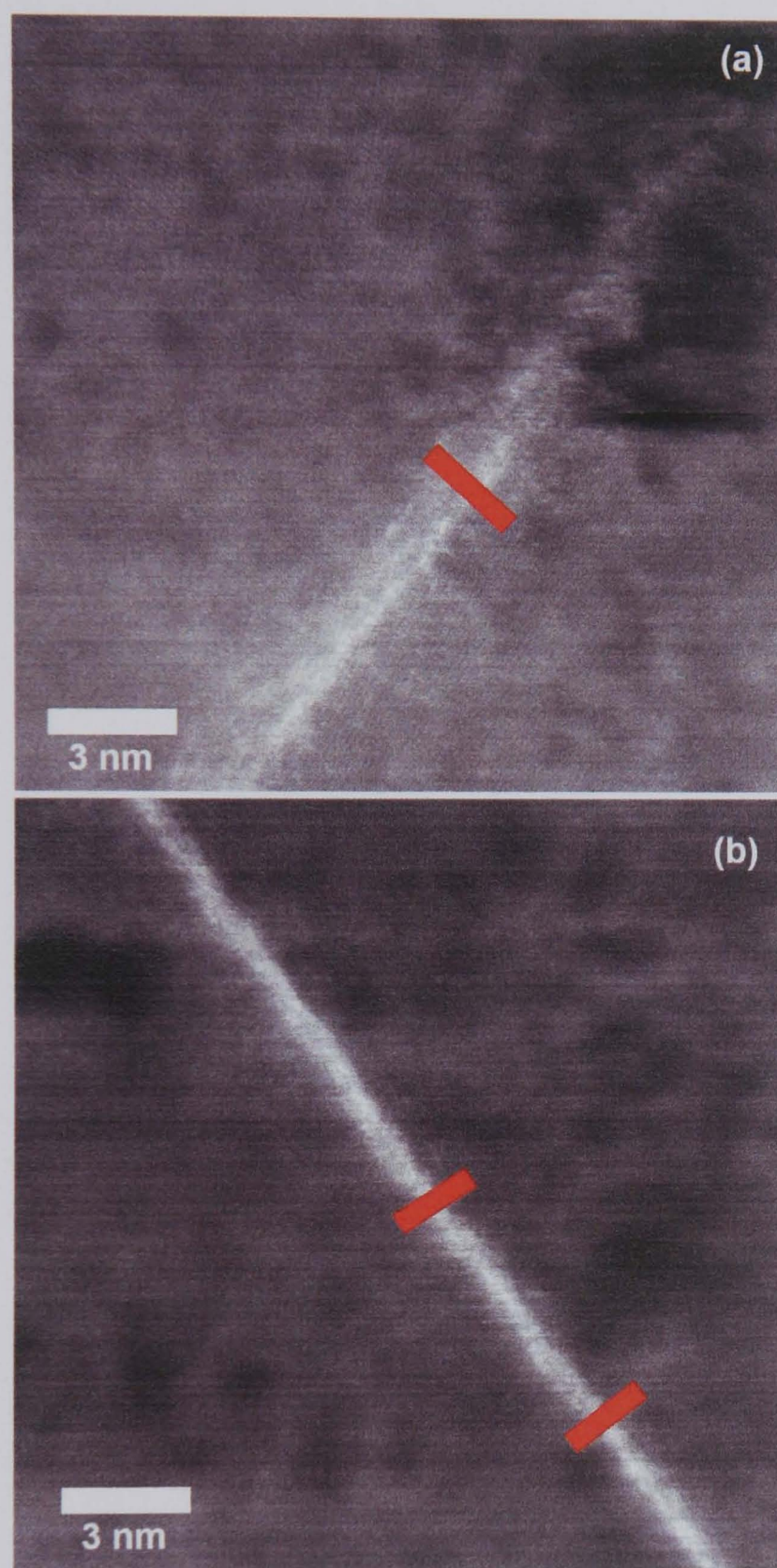
Figure 6.16: *Two HAADF images of a Yb doped spinel with BF intensity profile positions indicated.*
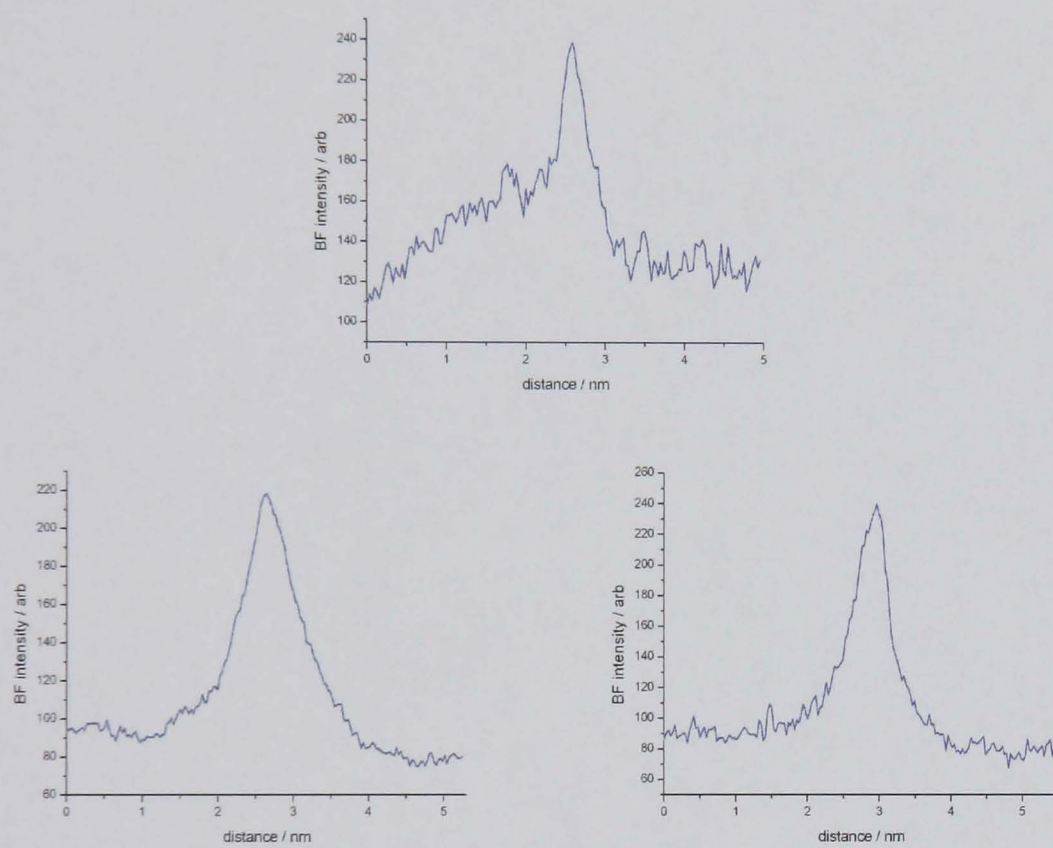
Figure 6.17: *BF intensity profiles from the positions marked in figure 6.16.*
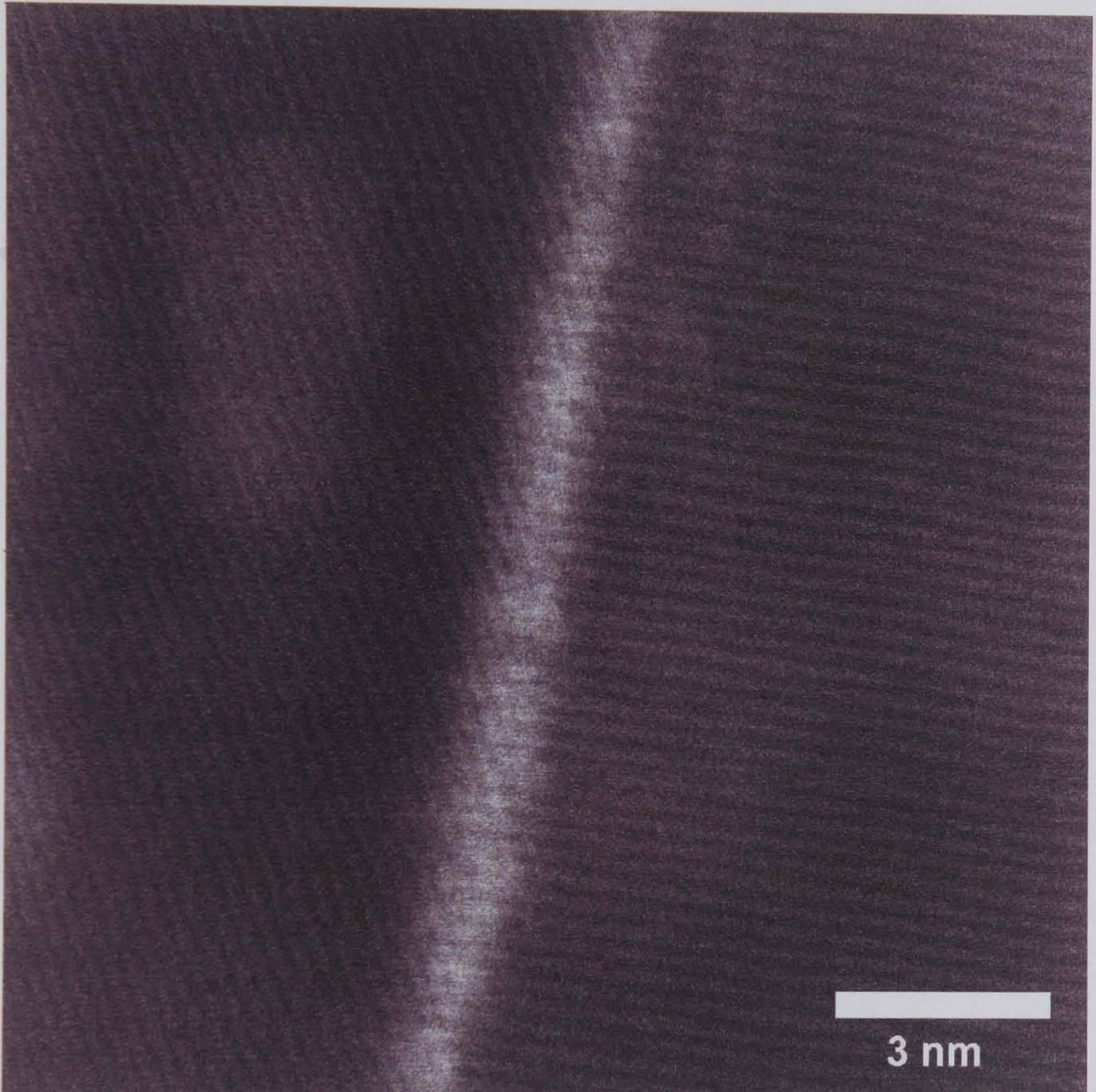
Figure 6.18: *Tilted grain boundary between well aligned grains in Eu doped spinel.*
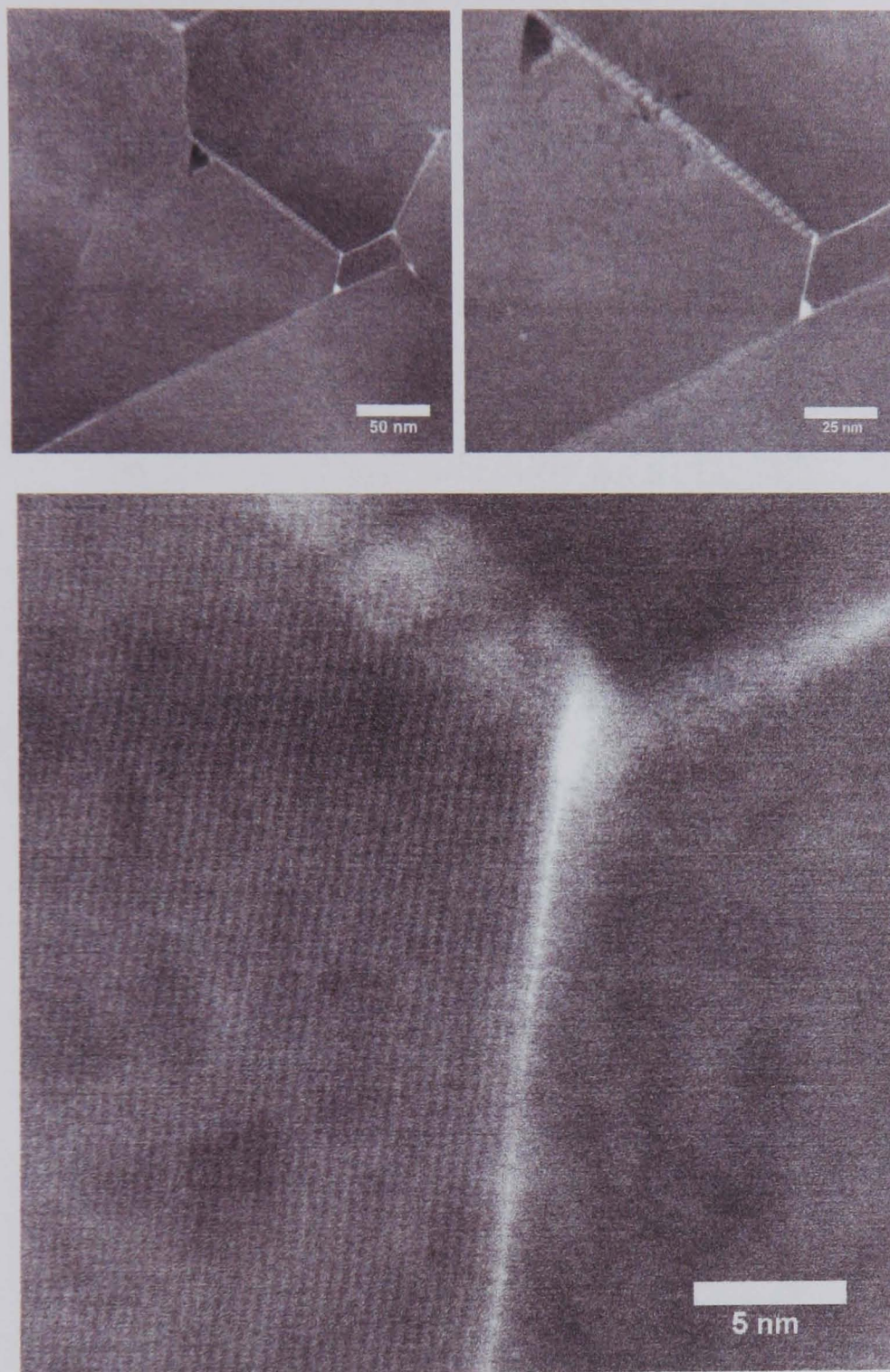
Figure 6.19: *Increasing magnification HAADF images of an oriented boundary in Eu doped spinel suggesting monolayer segregation of Eu along the boundary.*
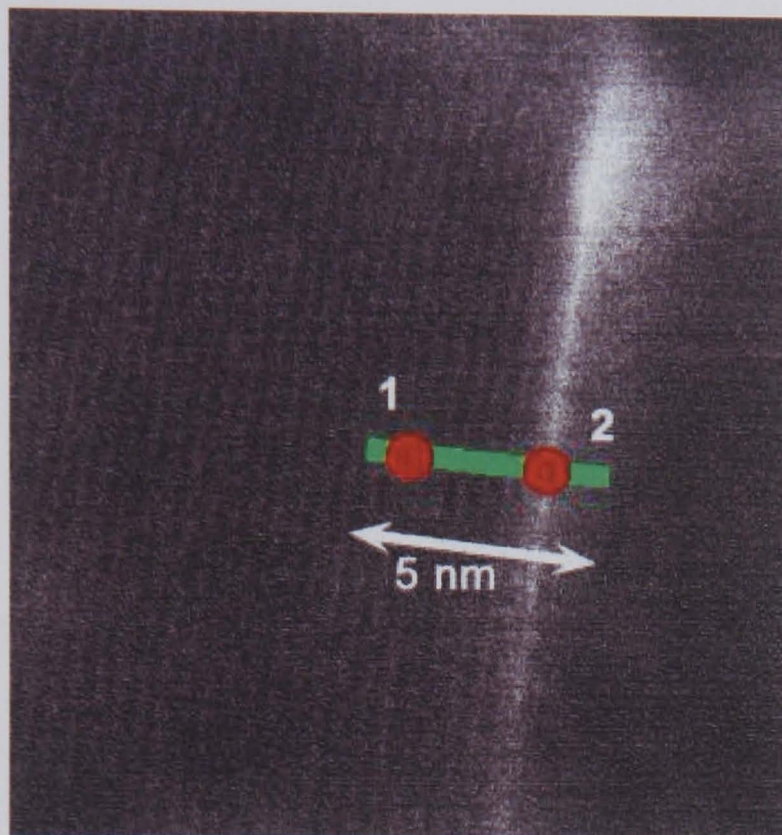
Figure 6.20: *Position of the analysis line scan over the boundary, also indicating the two points from which the spectra in figure 6.22 were taken.*
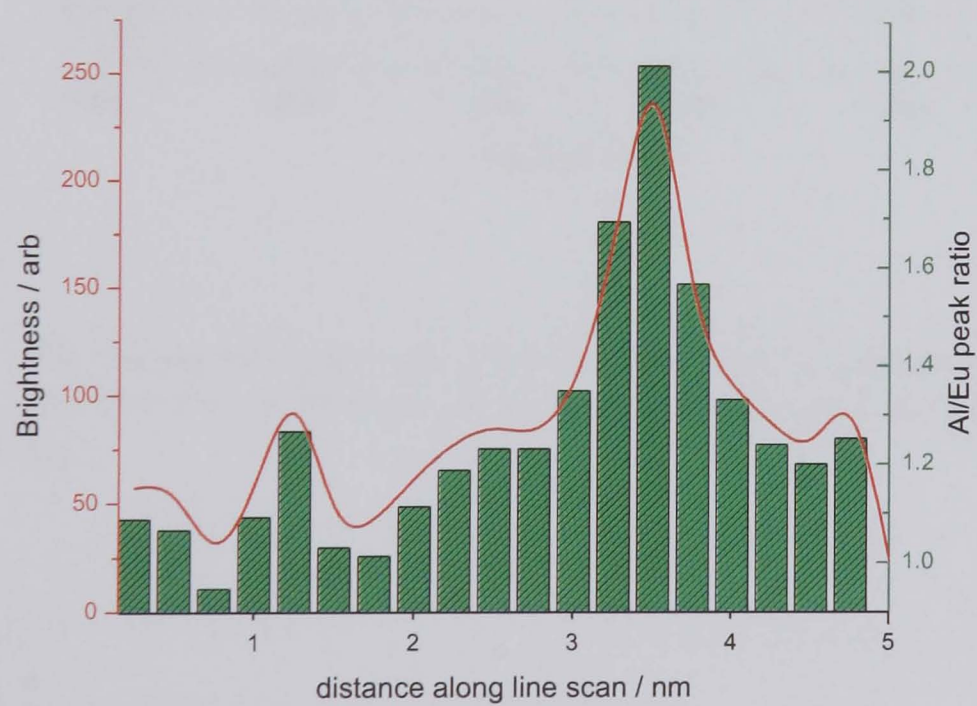
Figure 6.21: *Graph showing Eu/Al edge ratio at each 2 Å position with the bright field intensity profile overlaid.*

136
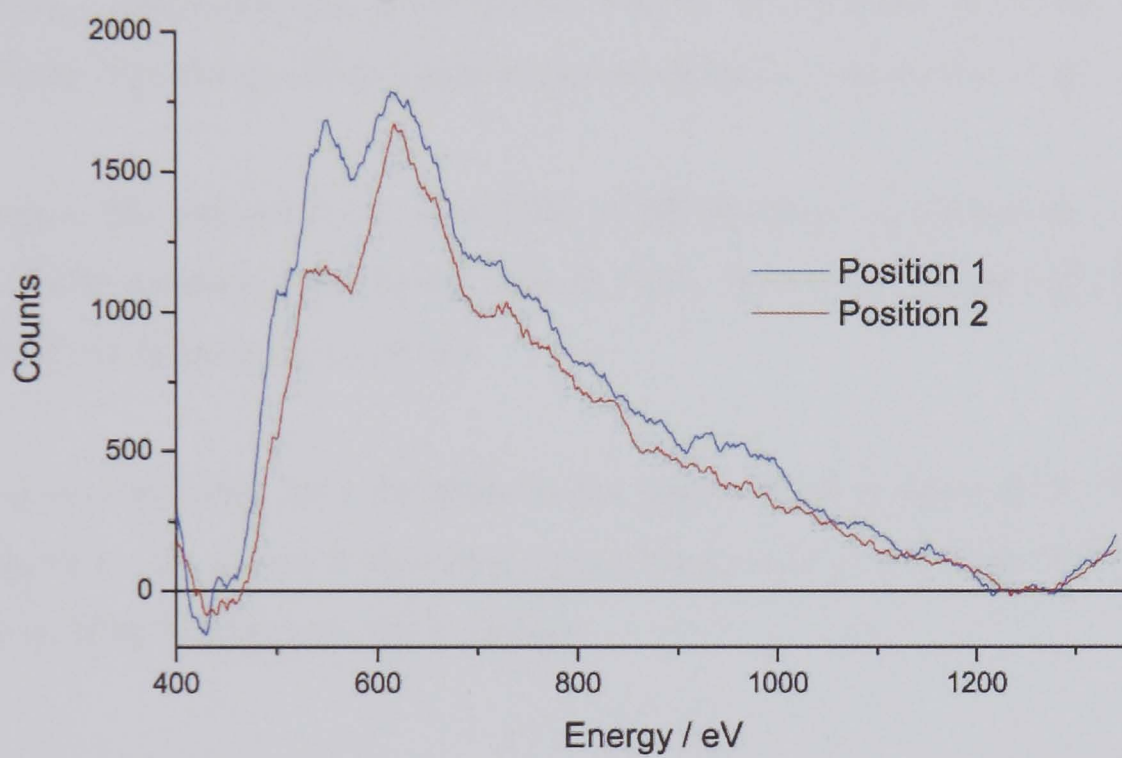
Figure 6.22: *The energy loss near edge structure (ELNES) at positions 1 and 2 in figure 6.20. The blue line is from the Al L_1 and the larger peak on the red line is from the Eu $N_{4,5}$*

edge intensities between 140 - 150 eV was plotted. Positions '1' and '2' are marked on the image and on the ratio plot, with the Eu rich region lying directly on the boundary with a FWHM of the peak $\sim$ 0.5 nm. The geometry of the sample and the fact that even with a s åprobe there is influence of the surrounding area on the energy loss spectrum means that the ELNES of the boundary will always contain information from the surroundings, i.e. the aluminium. This is why the ratio of edges is the only way to identify the positions where the the Eu edge appears. The edges detected are the Al L_1 and Eu $N_{4,5}$, these arise due to excitations from 2s and 4p states of the two elements respectively. The energy of the onset of the two edges is characteristic of the species.

Once again, the analysis (be it from EDS or EELS) shows unambiguously the segregation of RE matching with the BF intensity plot. In this case figure 6.21 shows the FWHM of the intensity as $\leq$ 0.4 nm.

A set of spectra taken from the linescan has been plotted in figure 6.23, this shows the edge ratios for several 2 åpositions across the boundary. It is clear that there is a change in ELNES shape over the boundary.

The lower magnification image (figure 6.19) also shows another boundary displaying distinct periodicity, this boundary is tilted and suggests some segregation to ledges along a boundary.

6.3   SuperSTEM Analysis of Grain Boundary Structure

While figure 6.19 shows clearly the monolayer segregation, further proof of monolayer segregation at other boundary types was required. Several images have been obtained (shown below) from a ytterbium (Yb) doped spinel sample. The preparation was key
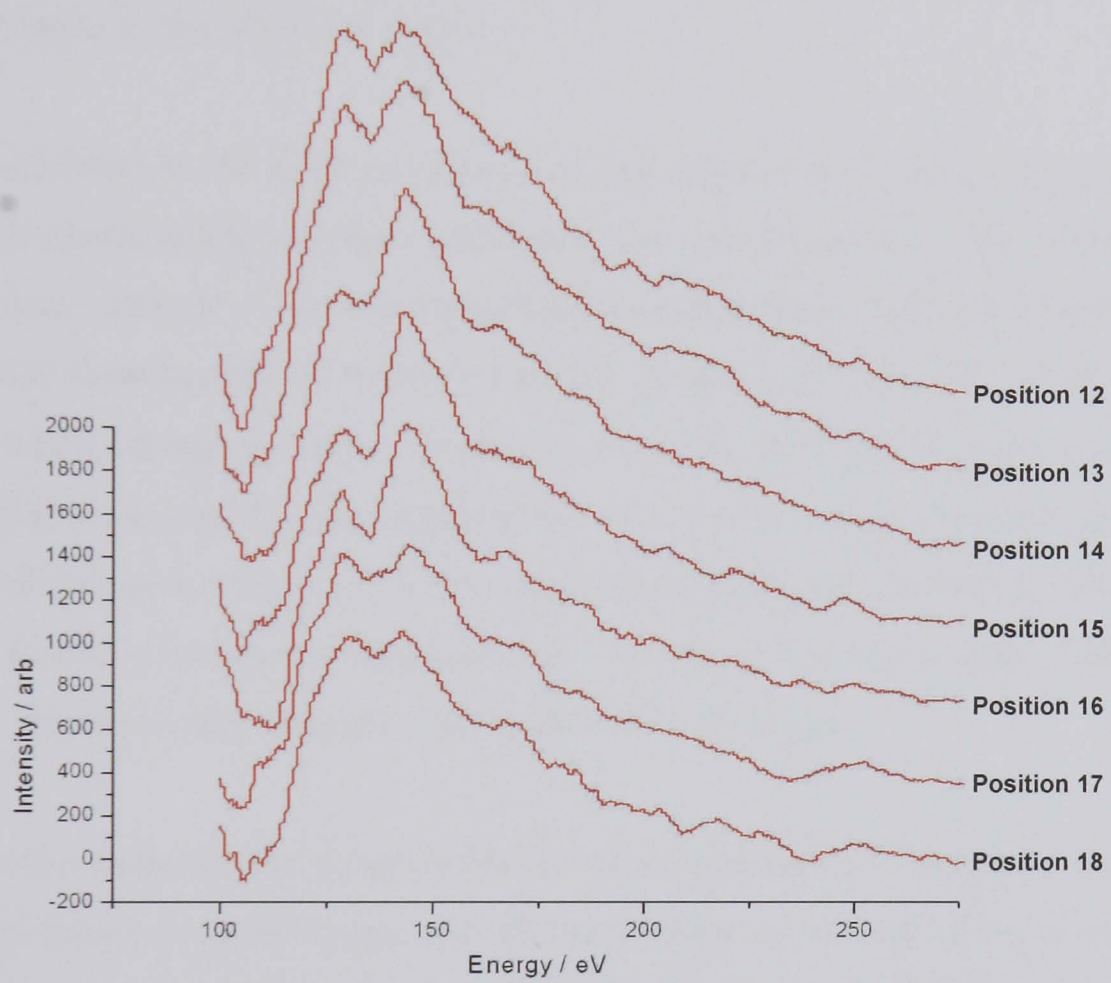
Figure 6.23: *The energy loss near edge structure (ELNES) from point positions in the linescan indicated in figure 6.20.*

to its success as a superSTEM sample. Figure 6.24 shows the region in which SuperSTEM DF images were obtained, demonstrating the number of grains within the homogeneously thinned area.

Subsequent imaging of a Yb doped spinel sample gives futher indication of the segregation of cations to the spinel lattice. Figures 6.25, 6.26 and 6.27 show three different boundaries in the Yb doped spinel.

The contrast at the grain boundary, i.e. the bright line of spots, shows the columns of RE atoms sitting at cation lattice positions unambiguously. The unoriented grains also have contrast at the boundaries with some structure showing as bright streaks. All three of these boundaries maintain a similar occupancy of RE atoms. With the charging and beam damage problems common to insulating oxide ceramics there was a limited number of scans that could be performed, thus the DF images were focussed within the grains that were on a pole (i.e. axis well oriented to the electron beam) then the sample was moved to image the boundary itself. The BF images had a slightly different focus and, therefore, were of poorer quality than the DF images.

A further indication of structure within certain boundaries is suggested in figure 6.25. While hidden in the BF image, the DF image shows an inclined boundary with 'stepped' segregation, suggesting a faceted boundary. This nano-faceted boundary meets the other grain in a region that would normally be imaged as a triple point. The orientation of such a boundary leads to increased contrast within this region thereby suggesting a separate phase when imaged in a lower resolution instrument. This is also evident in the low magnification image of the Eu doped monolayer segregation image (figure 6.19). Figures 6.28 and 6.29 indicate tilted and twisted boundaries and a triple point region manifesting some of the above mentioned structure.
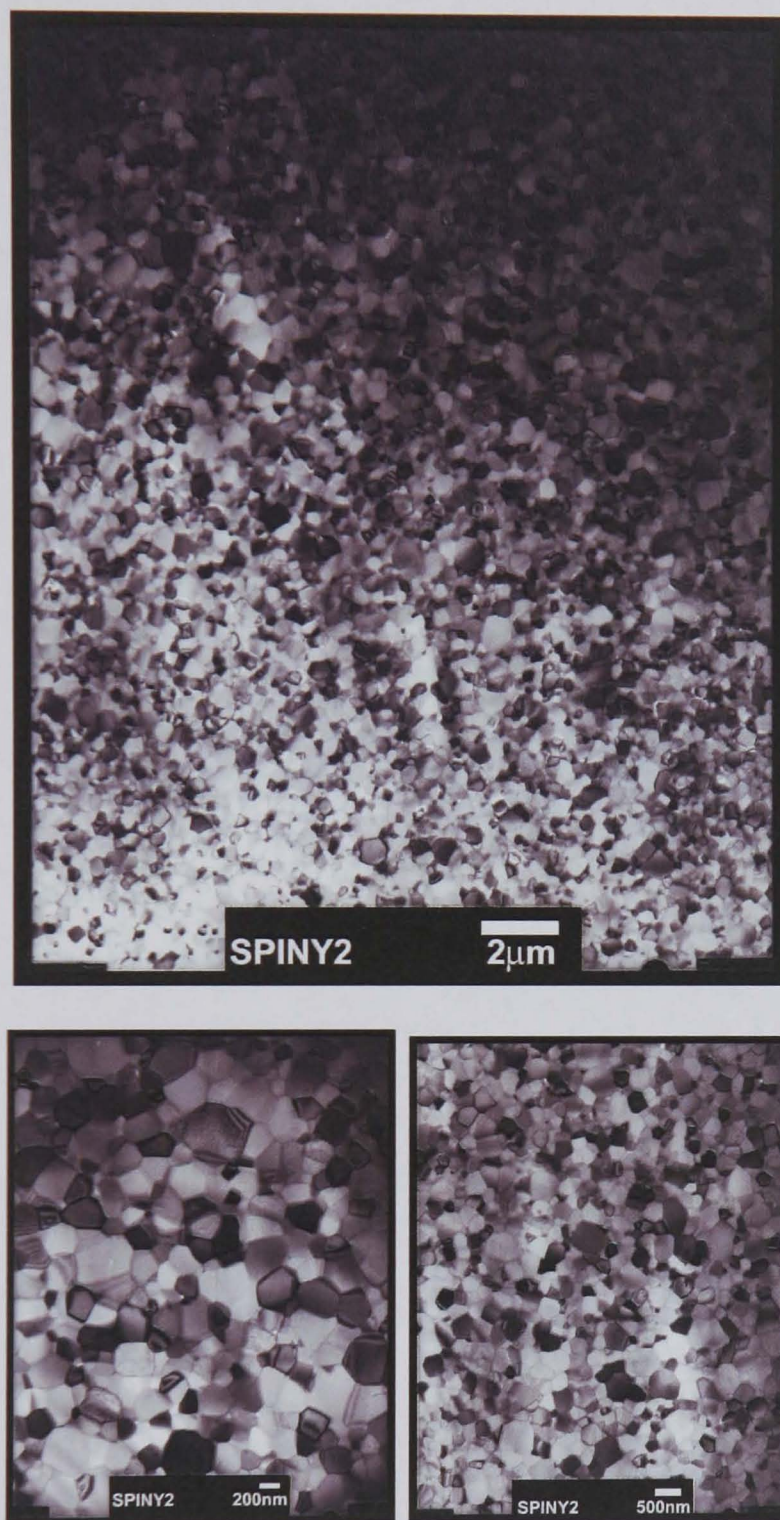
Figure 6.24: *Various conventional TEM images of large homogeneously thinned region in Yb doped spinel.*
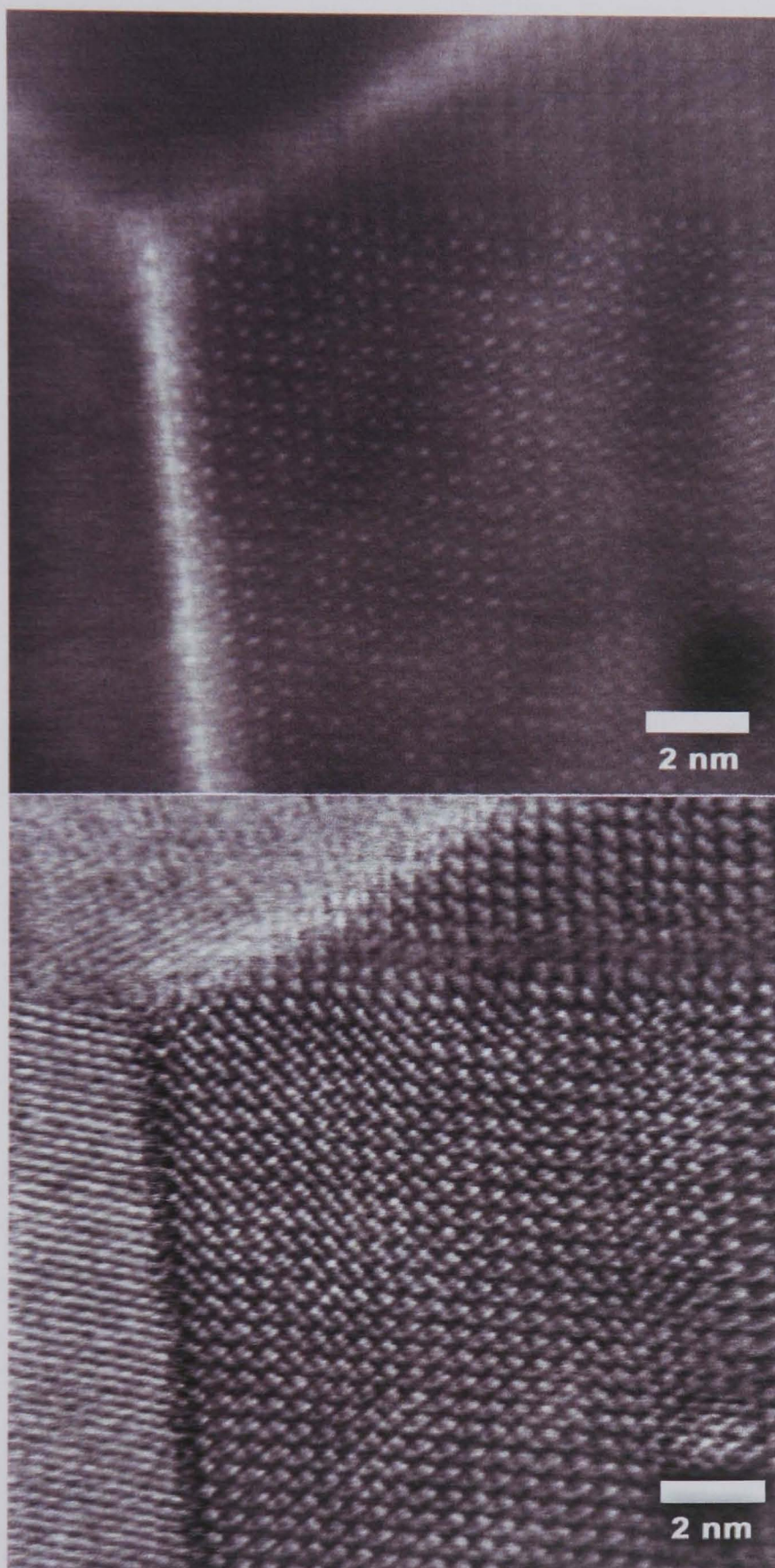
Figure 6.25: *HAADF (top) and BF (bottom) SuperSTEM images of Yb doped spinel boundary.*

142
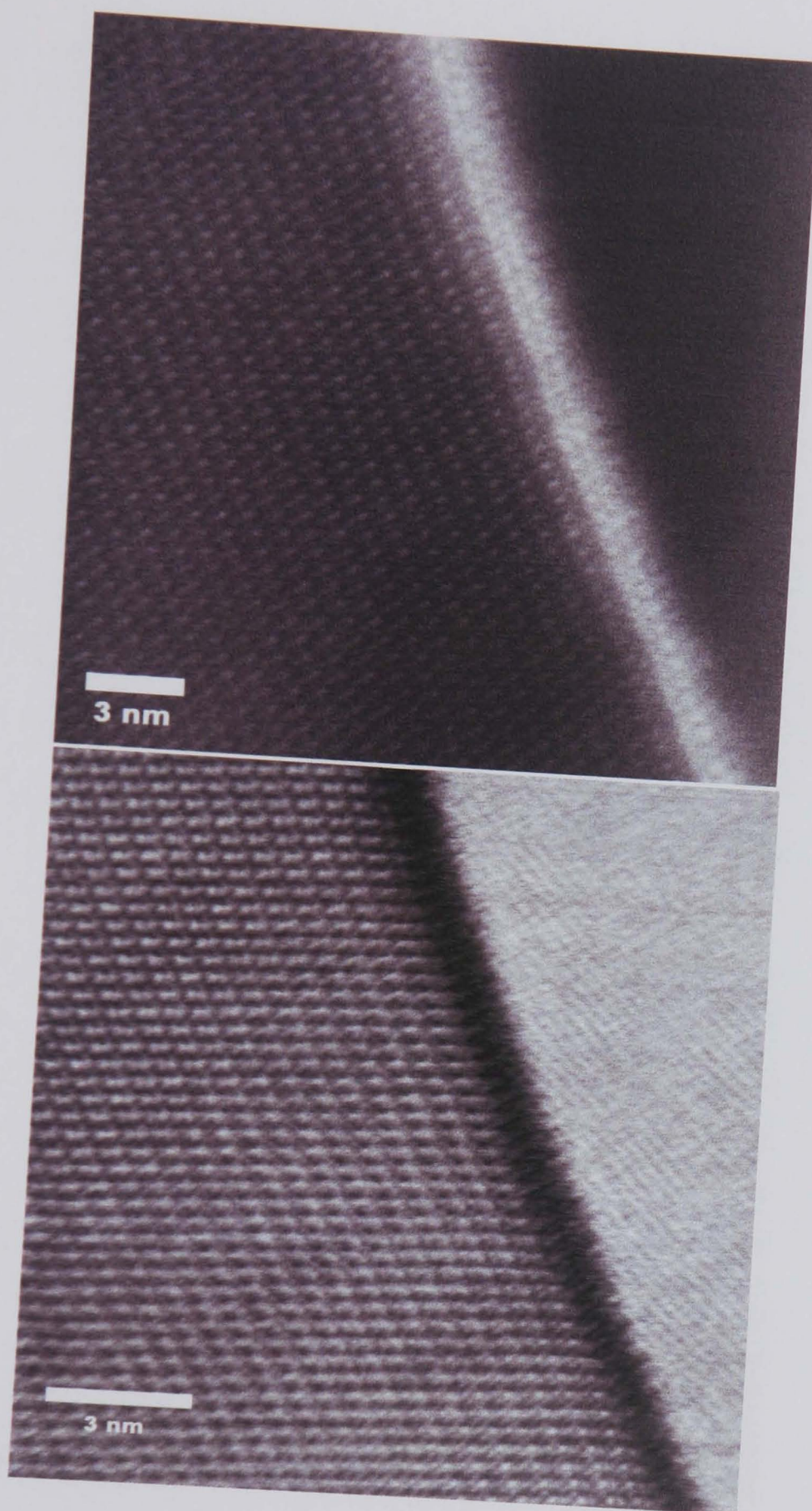
Figure 6.26: *HAADF (top) and BF (bottom) SuperSTEM images of Yb doped spinel boundary.*

143
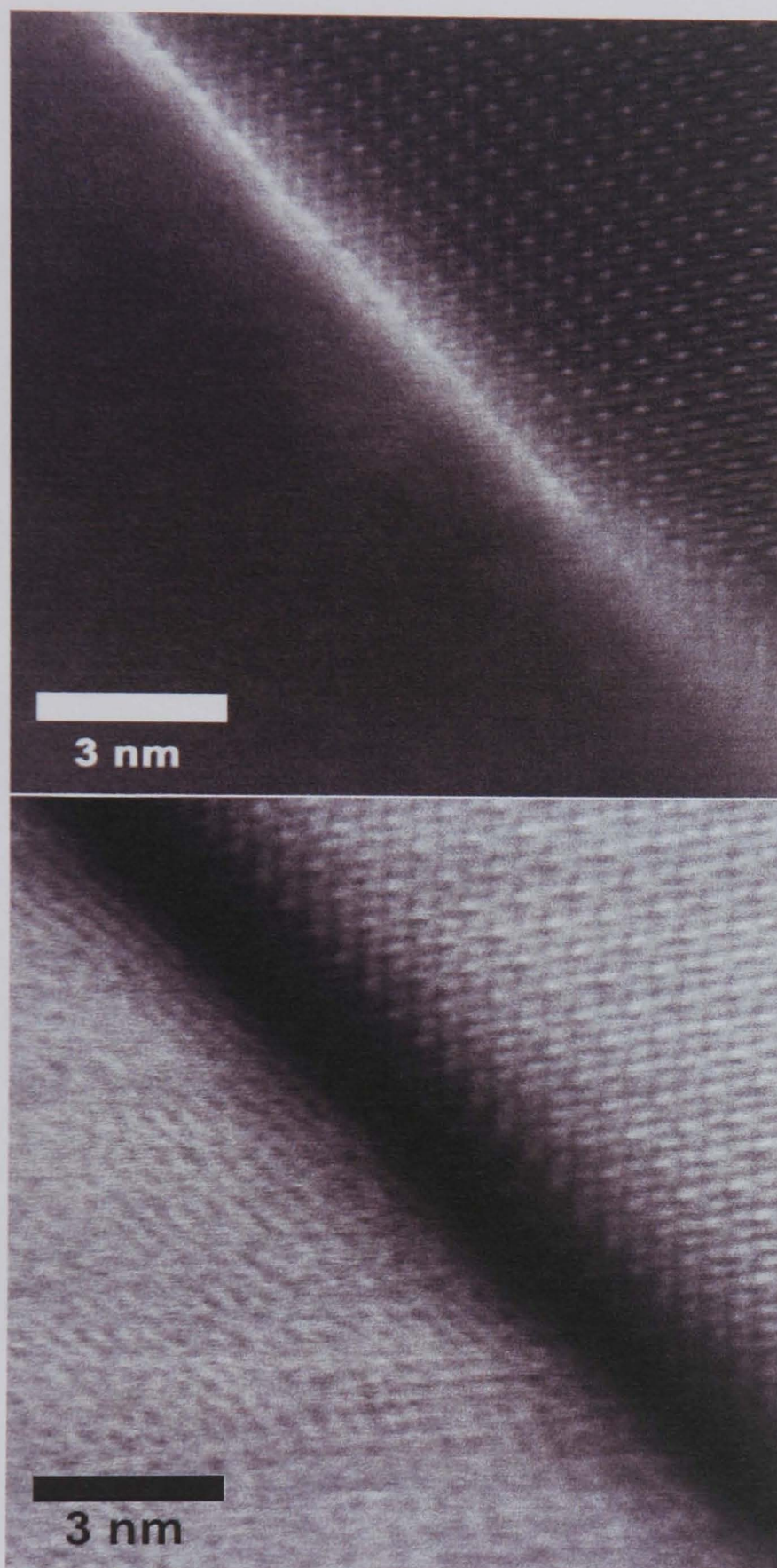
Figure 6.27: *HAADF (top) and BF (bottom) SuperSTEM images of Yb doped spinel boundary.*
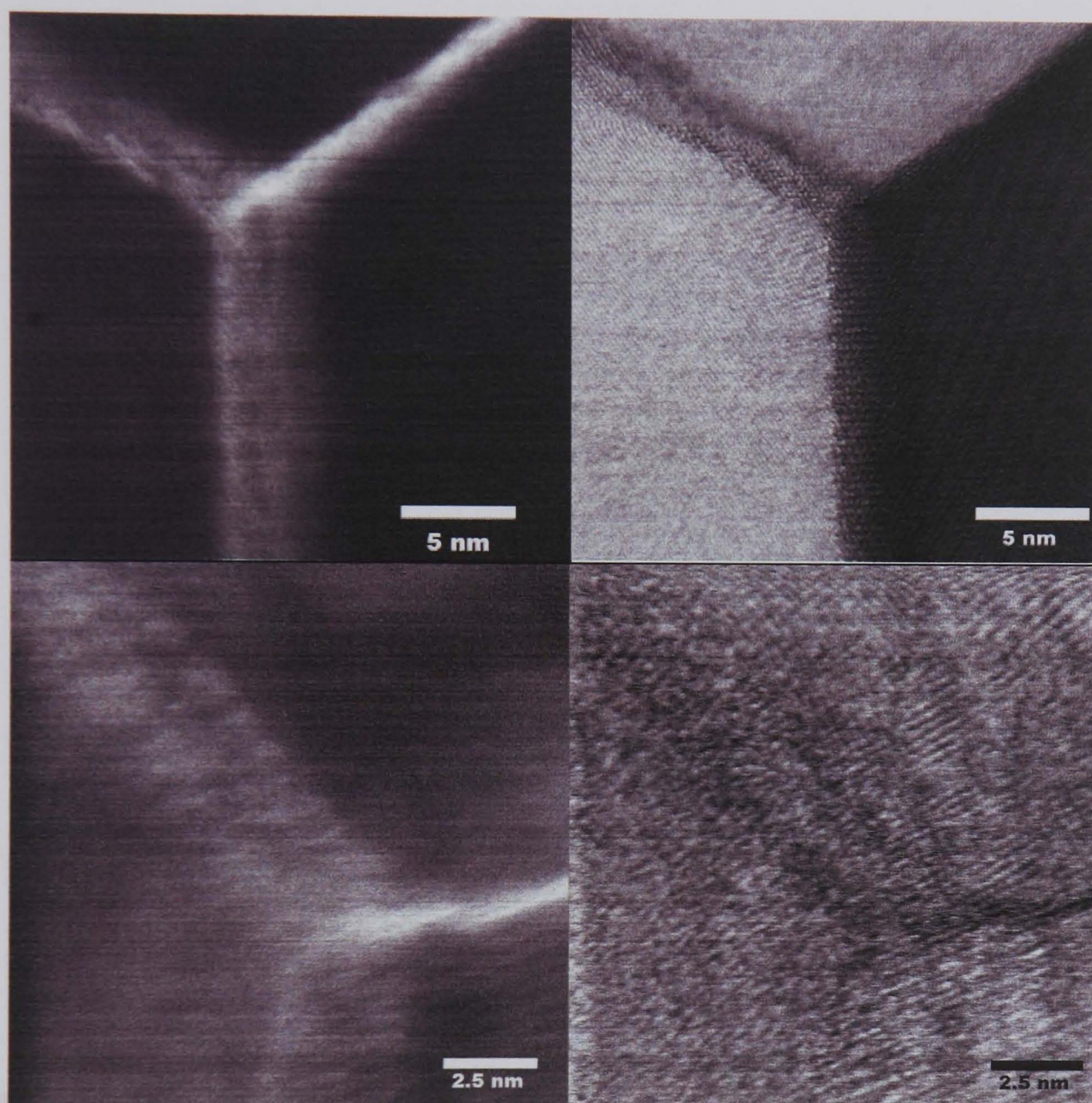
Figure 6.28: *SuperSTEM BF and HAADF pair images showing (top) region of a triple point, (bottom) same triple point at higher magnification suggesting 'faceting boundary' structure; 'nano-facets'.*
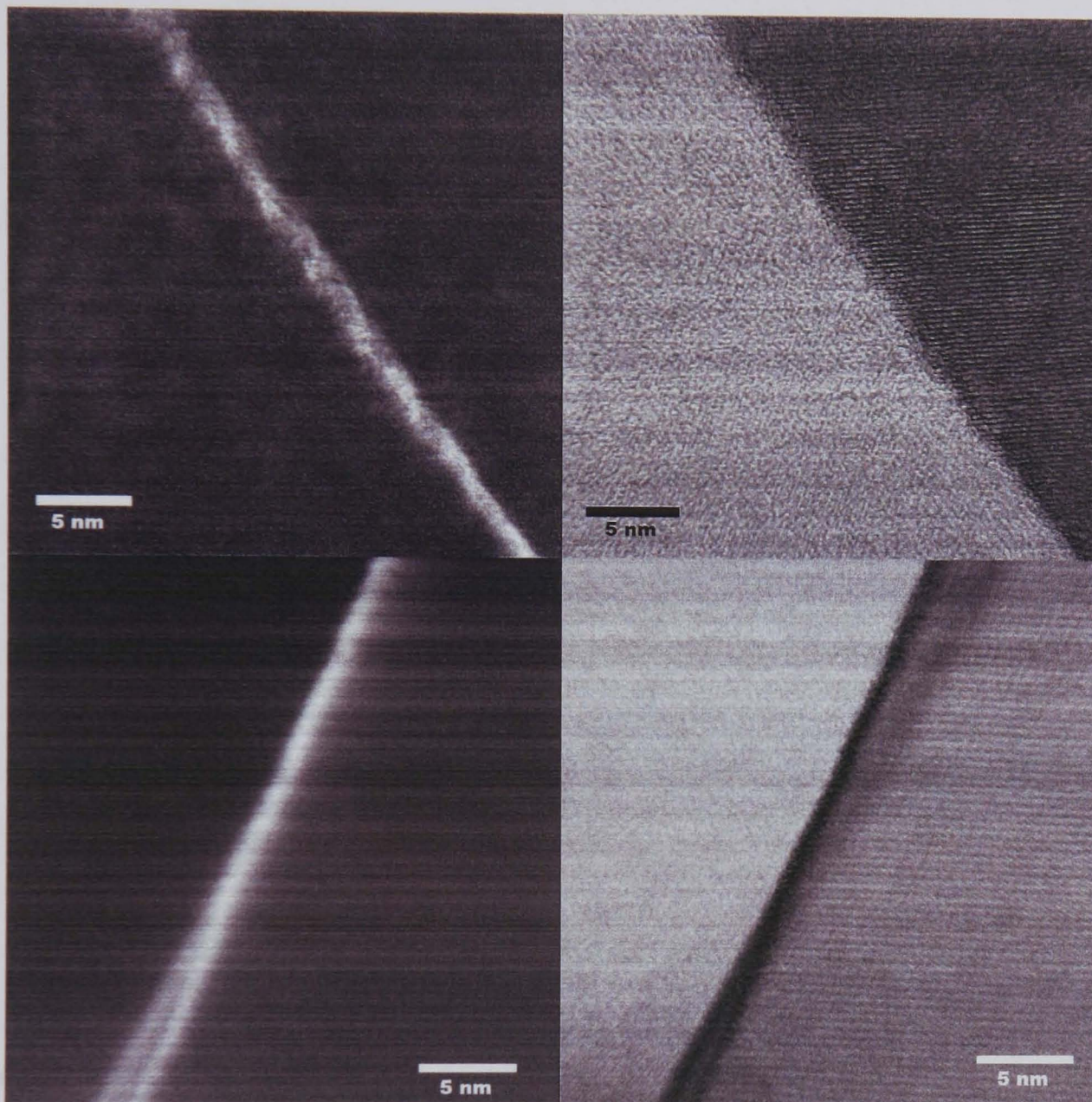
Figure 6.29: *SuperSTEM BF and HAADF image pairs showing (top) boundary with 'nano-facet' structure, and (bottom) a twisting boundary.*

146

6.3.1 Modelling Grain Boundary Structure

The SuperSTEM images are striking in terms of the clarity of the monolayer segregation. The effect of this on the properties is discussed further in the following chapter, however, the importance of such a feature must be emphasized. Recent work concerning the embrittlement of copper by grain boundary segregation of bismuth has shown that, given a monolayer segregation (the likelihood of segregation modelled in itself separately), the grain boundary structure is altered from that of an undoped polycrystalline sample. The nature of the segregation was originally thought to be an electronic effect where local electrons are attracted towards the impurity ion thus altering the local structure and bonding. More recently, a theory based on the modelling of segregation in metals has suggested an ionic size effect[118] where the segregating ion pushes the surrounding grains apart slightly along the region of the grain boundary. This parallels the hypothesis concerning boundary segregation in oxides, whereby the segregating ion sits on boundary cation sites and restricting the mobility of other atoms due to its large size.

In order to find the structure of the segregated boundaries, many candidate boundary configurations must be used. The segregation may take a number of forms, similar to the different forms of segregation proposed for equilibrium, saturated and supersaturated boundaries. "Working out a particular grain boundary structure is non-trivial" [119], and will not be discussed here, however, alongside solving the imaging conditions for alumina it should form the basis of future work.

Other information regarding the structure may be obtained from these images. The region in which the lattice has any perturbation from the undoped grain boundary structure is restricted to a region no greater than one monolayer. This suggests that the interactions between the RE cations and matrix cations, further towards the centre of the grains, are minimal. It also means that the pushing apart of the grains is restricted

147

to the segregated layer. In alumina this may contribute to the increased propensity for intergranular fracture (discussed in the next chapter), as the bonding between adjacent grains across the boundary becomes weaker.

Figure 6.30 demonstrates possible arrangements of RE atoms along the boundaries shown, assuming that the [111] crystallographic direction (into the page) is correct. The model is derived simply from the Z contrast image and assumes nothing about bond strength or interatomic interactions. In figure 6.30 the oxygen positions are not shown, however, there is a slight contrast feature in the original images that indicates the oxygen column positions. Recently published work concerning the segregation of Y in alumina has proposed that the Y segregation occurs at Al^{3+} sites at special boundaries. The report uses a special boundary to demonstrate the segregation to the site with lowest segregation energy, which was determined by static lattice calculations[120].

Extended to the general segregation of RE in oxides, it is possible that RE cations will segregate to low segregation energy cation sites in any type of boundary. Bruly et al[78] used ELNES of Y and La doped alumina boundaries to asses the effect of the dopants on the local bonding. While further work is required for the Eu, Tm and Yb systems studied here, there will be similarities in the data. Specifically: direct substitution of Al (or Mg) cations at the boundary (as suggested above) by RE. The possibility of sub-monolayer segregation where the segregated cation may not be able to form a complete unit cell, given the available sites that are energetically favourable to segregation. The segregation of the large RE cations to sites that will accomodate them i.e. expanding the cation-oxygen bond.

The effect of segregating ions on the oxygen bond remains unclear, with recent results indicating a strengthening of grain boundaries due to segregation[120], where the cation-oxygen bonds are strengthened when the cation is substituted with the dopant

RE. Once again the study focussed on special boundaries and further modelling of other boundary types is required.

6.3.2 Differences in Analysis Between Alumina and Spinel

The obvious difference when analysing the two materials is the susceptibility to damage in all forms of TEM instrument. The spinel allows more time for a given technique in any particular region before alteration of the lattice due to beam damage. Contamination and charging are more related to sample preparation, however, for identically prepared samples (wartm3_B, alumina and SEU1500A, spinel) the charging was notably worse and was much harder to stabilise in the SuperSTEM.

It is clear that RE dopants have a propensity to segregate to the grain boundaries of both materials to form monolayer periodic boundary structures. The inability to confirm a similar result for alumina is due to the aforementioned problems, however, the earlier images of HRTEM work do suggest that there is a similar boundary structure because of the absence of a glassy or crystalline second phase.

6.3.3 Influence of Sulphur as an Impurity

It has been suggested in previous work that sulphur segregates to the boundaries of the RE doped spinel[103]. The evidence presented earlier in section 5.2.4 demonstrates that the EDS analysis is difficult and sometimes inconclusive, however, there remains the possibility that the anion segregation of such a species does indeed occur. It is possible that the sulphur would appear at oxygen sites in the lattice but because its ionic radius (for identical coordination number) is bigger than that of oxygen (sulphur = 1.84, oxygen = 1.4[27, 121]) it may be concentrated within one or two monolayers of the boundary.

149
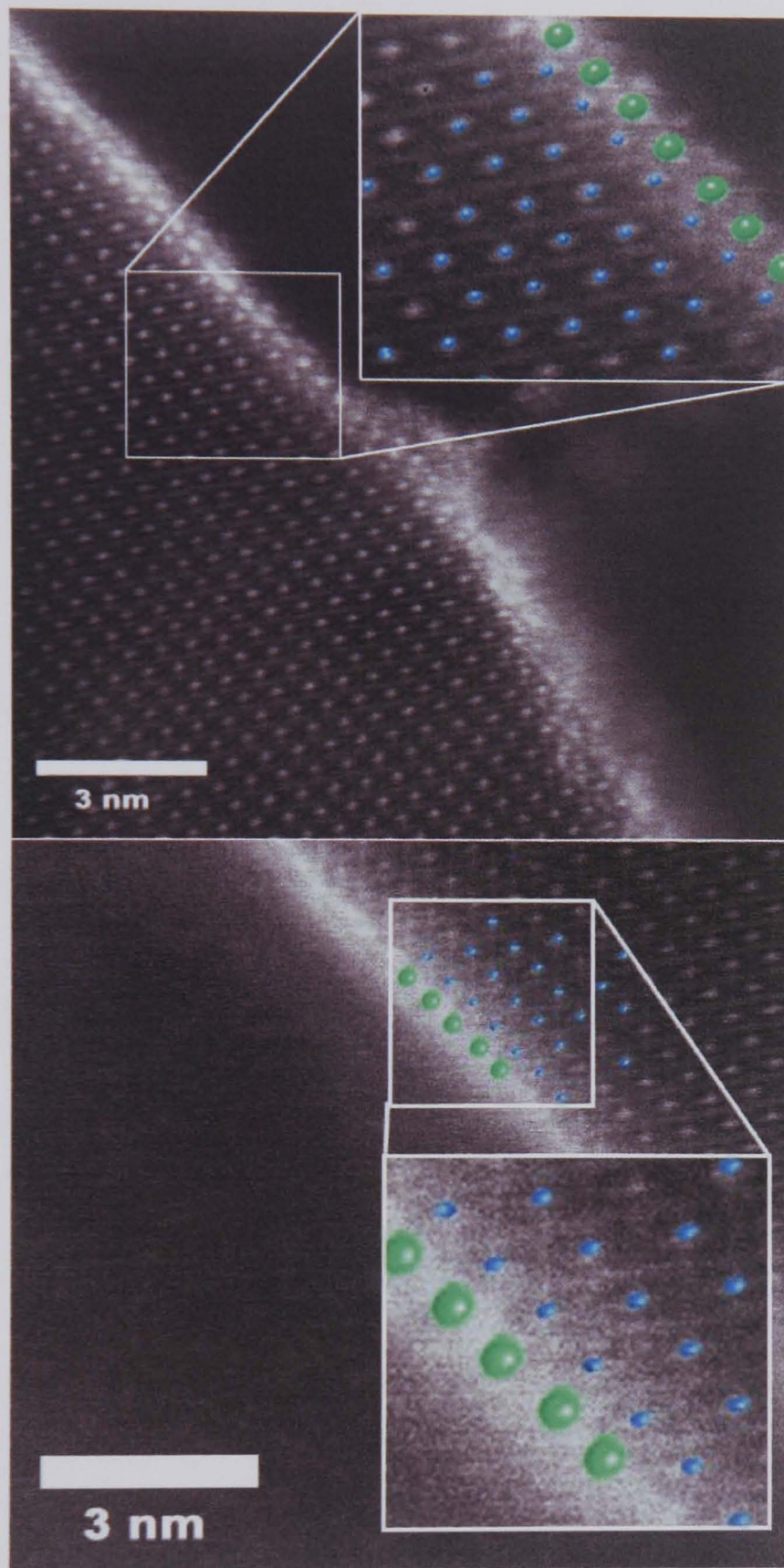
Figure 6.30: *Crystal model overlaid on HAADF SuperSTEM images of Yb doped spinel. Green spheres represent Yb cations, blue spheres show approximate matrix cation positions. Oxygen positions are not shown.*

150

Further study is required as the possible effects of anion impurity segregation may include the various differences between alumina and spinel, discussed in chapter 7.4, that occur after doping with RE cations. Deliberate sulphur inclusion in alumina is discussed in section 4.1.4.

While the ionic size suggests possible segregation, effects of such segregation may not be obvious. For example, if sulphur were a co-dopant then the effects due to sulphur and the effects due to the RE may be indistinguishable. At the same time, the fact that grain growth inhibition on sintering and a lack of increased intergranular fracture (see mechanical properties chapter) suggest a possible inhibition of expected properties due to the RE segregation.

There is now a question to be answered with respect to the actual role of sulphur impurities within the spinel structure and it is certainly a candidate for further study.

6.4 Chapter Conclusions

Aberration corrected STEM has allowed the unambiguous imaging and analysis of different boundaries in spinel indicating monolayer segregation of RE cations. While not as clear, the RE segregation in alumina has been confirmed to within <0.5 nm of the boundary. The aberration corrector has removed many of the imaging features that can alter the appearance of high resolution images and the use of high resolution annular DF imaging is a breakthrough for the combination of atomic scale structural analysis.

The structure of the spinel has confirmed the previously suggested equilibrium grain boundary concentration, as the existance of triple points removes excess dopant that would be present in supersaturated boundaries. SuperSTEM has proved a vital tool for imaging at the atomic scale even with hard to prepare insulating samples. Further inves-

tigation is required to ensure that sample damage can be prevented. Trials of coatings and TEM grid mounting methods are required.

Once again, the importance of well prepared, homogeneously thin regions of sample has been demonstrated. Large, fine grained regions are vital such that the availability of well aligned grains and grain boundaries is good, both for the probability of finding such grains and the variation in boundary type.

There is clearly now a question to be answered with respect to the actual role of sulphur impurities within the spinel structure. Further study should probe the extent of sulphur segregation and assess whether the removal of sulphur as an impurity would allow RE ions to produce some of the same property changes in spinel as those in alumina.

The SuperSTEM work has opened up a number of avenues for further research, not least the modelling of grain boundary structures to include possible effects of 'co-doping' with sulphur impurities.

Chapter 7

Mechanical Properties of Rare Earth Doped Oxide Ceramics

7.1 Introduction

This chapter summarises results from comparative studies of RE doped alumina and spinel, along with their undoped counterparts.

The literature mentions the changes such as hardness, high temperature creep, resistance to wear and fracture toughness, owing to the addition of low solublity dopants that segregate to grain boundaries. In order to provide an unbiased study, all of the results in this chapter were carried out with blind tests, i.e. the labelling of the samples and the mounting did not provide any clue as to whether the sample was doped, undoped, spinel or alumina.

7.1.1 Hardness

Previous studies of hardness have been, in general, subject to much variation in quoted results. The study by Rice et al [122] proved that while the trends in hardness for

ceramics remained similar (approximate Hall-Petch behaviour for grain sizes below that of the indenter), there is much variation due to factors such as porosity, measurement technique, surface finish and indentor load. Here, results are presented as a comparative study between samples of varying composition, while attempting to verify the trend associated with grain size.
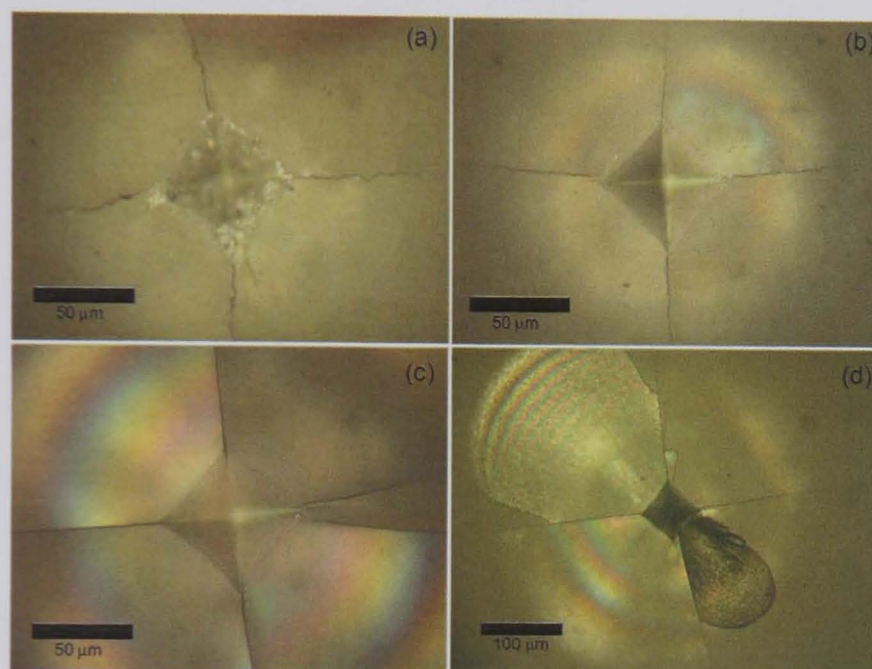
Figure 7.1: *Four examples of Vickers indents. a) undoped alumina, b) Gd doped alumina, c) Gd doped spinel and d) example of spallation in undoped spinel.*

A Vickers geometry was used for all hardness and fracture toughness indentation, since it is widely used as a hardness measurement standard and because the previous work by West[97] also used employed this method.

Two sets of five indents were made, with each indent spaced approximately 1.5 mm from the next. The sets of indents were 3 mm apart and each set had a different indentation load. Once the set load was reached on the indenter it was held for a number of seconds before being removed from the surface. Five indents per given load was chosen to reduce the error due to possible microstructural inhomogeneity and to minimise the

154

statistical effect of crack paths or indent damage due to spallation or other associated phenomena.

The existence of spallation increased with increasing grain size (as expected from the literature[123]) but was also more apparent in spinel than alumina. Figure 7.1 shows a case of spallation in a spinel indent. Sub surface lateral cracks led to a loss of material along a side of the surface cracks, rendering measurement of surface cracks impossible.

Fine grained samples showed less of the spallation problems associated with the coarse grain samples, however, the surface crack path was particularly difficult to follow. The ends of the cracks were found using an oblique illumination of the sample in the optical microscope, carefully observing the crack tip through focus positions to find the true tip end. In coarser grained samples the crack tip was easier to observe as it usually ended at an obvious boundary, occasionally passing around a bridging grain.

Figure 7.2 shows a set of data from various doped and undoped alumina samples. There is an indication of the increased hardness for smaller grain sizes, and also a suggestion of further correlation between RE doping and some extra increase in hardness.

There is a correlation between hardness and grain size in metallics known as the Hall-Petch relation, described by the following equation;

$$H_V = H_0 + kg^{-0.5} \qquad (7.1)$$

Where H_0 is a reference hardness, g is grain size and k is a constant of proportionality. Figures 7.3 and 7.4 show the Hall-Petch relation plotted for alumina. For the undoped alumina $H_0 = 1.40 \pm 6.88$ and $k = 6.056 \pm 9.8 \times 10^9$, for the doped aluminas H_{0d}

155
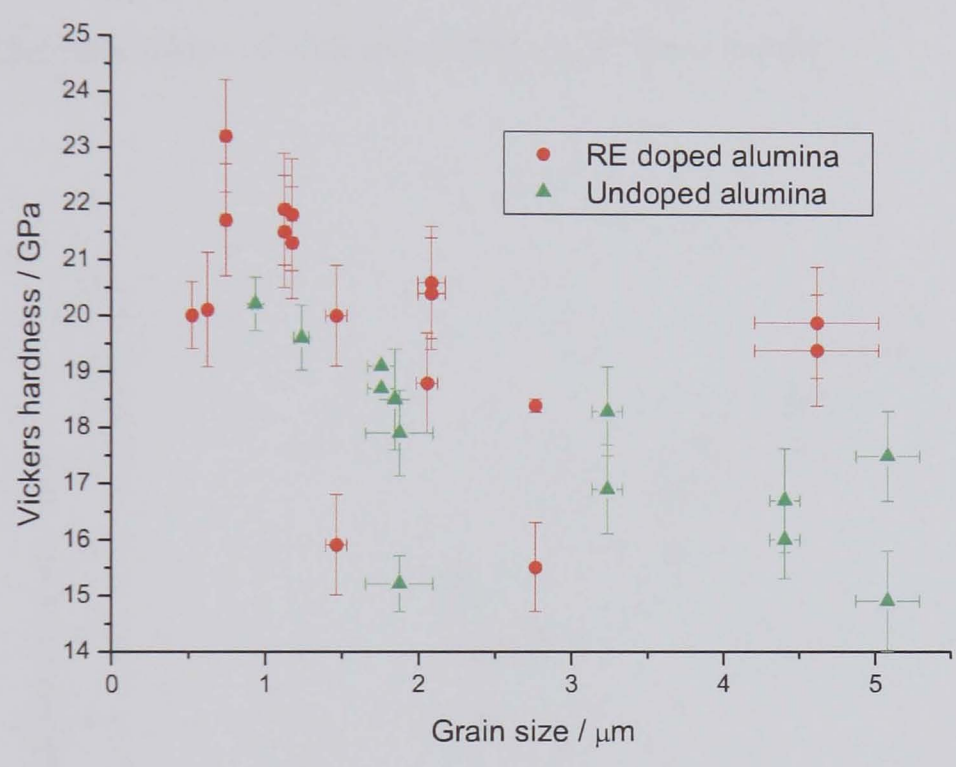
Figure 7.2: *Vickers hardness against grain size for a selection of RE doped and undoped alumina samples.*

= 1.61 ± 7.05 and k_d = 5.73 ± 8.12 x 10^9. These values are comparable to previous studies of the hardness relation in ceramics[124, 125]. The proportionality constant is dependent on the resistance provided by grain boundaries to dislocation movement which is related to the number of slip systems. The greater the number of slip systems the lower the proportionality constant. The slight difference between the doped and undoped alumina results may suggest an additional effect due to the grain boundary structure in the doped system. A change in grain boundary structure will alter the energy of the boundary, especially with the presence of large RE cations and it is possible that this affects the extent of dislocation pile up at the boundary.
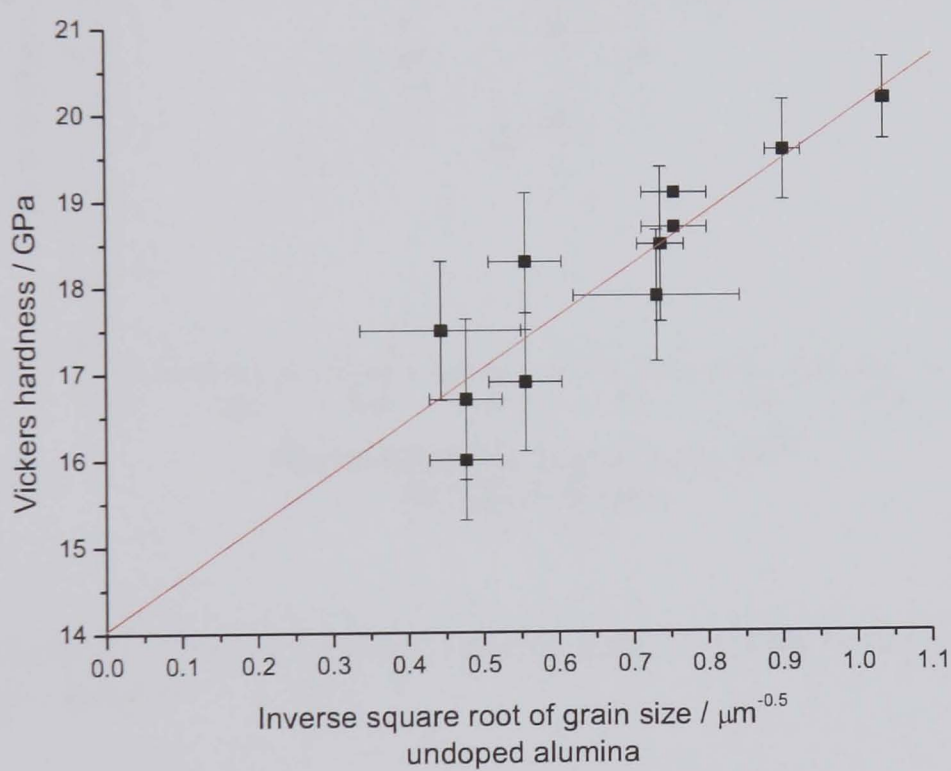
Figure 7.3: *Graph of Vickers hardness against inverse square root of grain size for undoped alumina samples.*

Spinel does not show a strong Hall-Petch type relationship, in fact there is no evidence for the increase in hardness for smaller grain sizes, as expected from the literature[122, 125].
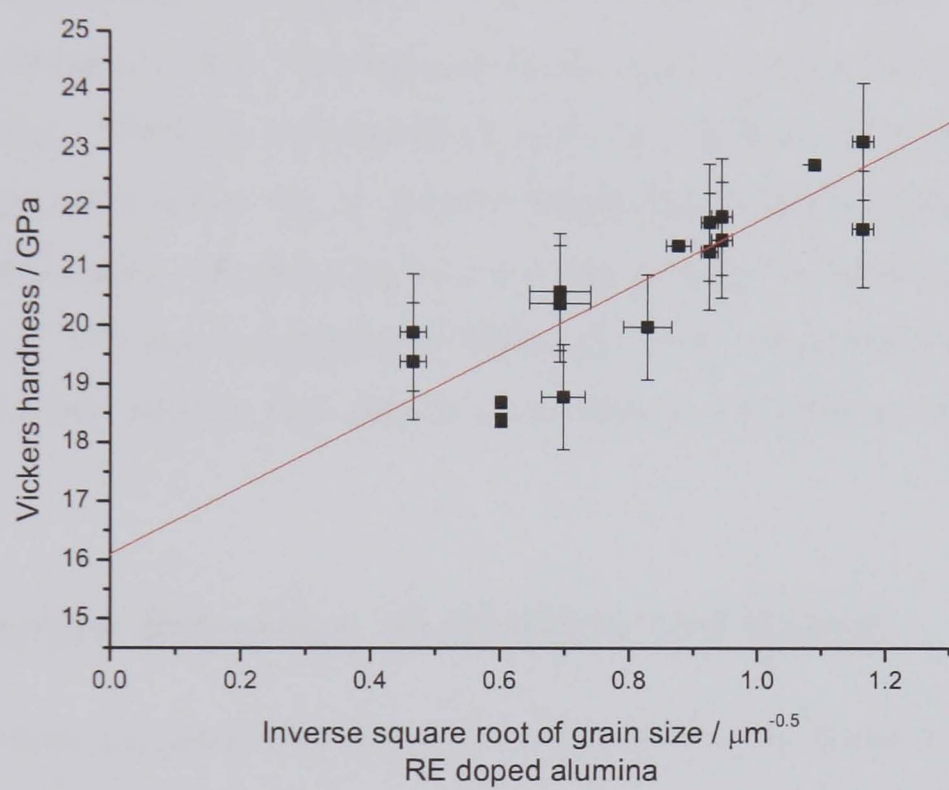
Figure 7.4: *Graph of Vickers hardness against inverse square root of grain size for doped alumina samples.*

Figure 7.5 shows the hardness of a number of spinels sintered at various temperatures. As expected, the hardness distribution is unchanging with temperature, however, there is some systematic difference between the doped and undoped samples. The spinel crystallography has many more slip systems than alumina and will, therefore, be unable to prevent dislocation movement at boundaries. There are two major possibilities for this data. It is possible that this is a genuine effect of doping, i.e. the presence of the RE ions at the boundaries is having some effect on the dislocation movement across the boundary. There is already a suggestion that the boundaries behave differently to the alumina counterparts in that there appears not to be the same effect on grain growth during sintering. There are some problems with this, however, since the data set of doped samples and the data set of undoped samples were taken at different times. It has been pointed out in the past that there is a large variation in methodology of indent measurement. This was highlighted by West[125], after comparing results from the same sample blind tested by four different researchers at four different laboratories.

7.2 Fracture Behaviour of Alumina and Spinel

It has so far been suggested here and in the literature that the presence of RE cations at grain boundaries in the oxides has an effect on the grain growth kinetics and densification, thus producing different microstructures for a given sintering temperature than undoped materials. As such, it is expected that other properties, such as fracture, will be directly effected by grain boundary cohesion and indirectly by grain size effects. Previous studies [54] concerned with fracture energy and strength have suggested that the segregation of RE dopants actually increases the grain boundary cohesion. This would result in increased transgranular fracture compared with undoped samples for a given sintering temperature.

The fracture behaviour of the two oxides has been studied using two methods. Firstly

159
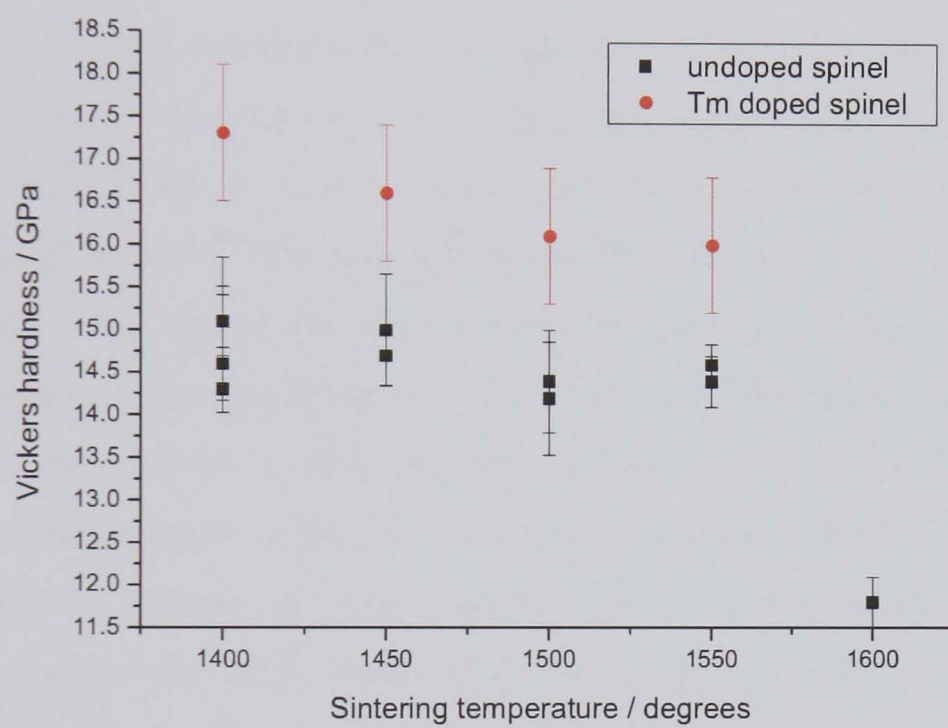
Figure 7.5: *Graph of Vickers hardness against sintering temperature for spinel samples.*

the fracture toughness of the samples was determined alongside the hardness using the Vickers indent method: for all indents with succesful and undamaged indents the surface cracks were measured. The second approach involved simply breaking small bars of the sample to provide a fracture cross section. These sections were observed in the SEM and subsequently analysed using the image-J program[91] to measure the extent of trans-granular fracture.

7.2.1 Effect of Dopants on Mode of Fracture

The effect of adding RE dopants to grain boundaries in ceramics was previously thought to be the increase in the grain boundary cohesion[54] (unlike grain boundary segregation in metallics). There are several problems with previous studies which also affect other aspects of ceramic mechanical and optical properties, that of residual porosity and grain size. It has already been demonstrated that the use of RE dopants restricts the grain growth and thus grain size for a given sintering temperature. Porosity is also tremendously important for samples that are not >99% dense (for this study, samples with density >99% were all translucent, so opaque samples were deemed too porous for fracture study). For alumina, the reduction of grain size also has the effect of changing the size and shape of the grains which influences the residual stress anisotropy. However, the shorter time at sintering temperature for the very fine grain samples may cause incomplete densification, hence a greater probability of inter-granular fracture.

The images below show the fracture surfaces of a selection of samples, both alumina and spinel, doped and undoped. To unambigously define a particular area as trans or inter-granular fracture proved difficult and time consuming. Images acquired in the SEM were used to highlight areas of transgranular fracture by identifying features such as cleavage through more than one grain, curved boundary edges, stepped fracture paths etc. In order to provide statistically relevant results at least six regions within a sample were imaged at random with sample codes unrelated to the sample manufacturing charac-

teristics. Figure 7.6 shows a SEM image of a fracture section with the transgranular component removed. The image was then processed using the image-J software to find the percentage of the image remaining (i.e. the inter-granular fracture component). The imaging conditions in the SEM were set such that the features described above representing transgranular fracture could be identified clearly. The images here are displayed so that there are approximately the same number of grains in each image, this means that the magnifications of the images are different, however, it shows instantly the differences between predominantly inter/transgranular fracture samples.
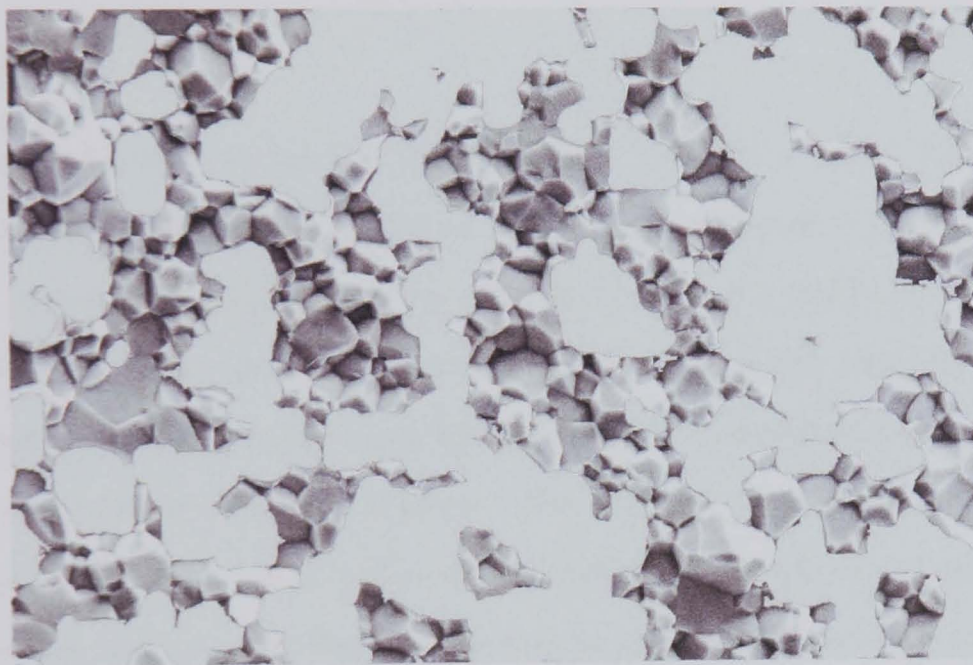
Figure 7.6: *SEM image showing the fracture surface of an undoped alumina sample. The micron bar and image border are not included as the software would interpret these features as part of the highlighted section. The image 'threshold' level was altered so that the intergranular fracture was black and the transgranular was white, then the software was able to calculate the percentage black region, i.e. percentage intergranular fracture.*

Fracture mode in alumina

Figure 7.7 shows a selection of typical doped and undoped alumina fracture images.

Figure 7.8 shows a separation in percentage transgranular fracture (PTF) between the doped and the undoped samples.

This result represents a clear difference between the RE doped and undoped alumina samples. There are a number of factors that need to be considered to explain the phenomenon.

Undoped alumina

The points representing undoped alumina in figure 7.8 show a mixed mode of fracture in all the samples. The undoped sample with grain size below 1 μm was sintered at 1350°and is thought to contain a larger amount of residual porosity as it was the most opaque sample that was used in the fracture study. The slight trend in reduced PTF with increased grain size may be explained by the thermal expansion anisotropy present due to the non cubic structure of alumina. The thermal expansion anisotropy leads to microstresses between grains of different orientation promoting intergranular fracture. With large grains this may manifest itself as spontaneous grain boundary cracking. Such effects are reduced with smaller grain sizes as suggested by the graph.

While this graph shows a slight trend, often the mode of fracture is dominated by other factors such as the impurity content and the level of porosity[126, 127]. Both use of a high purity powder and translucent samples minimised any effects due to impurities and porosity except for the sample sintered at 1350°.

163
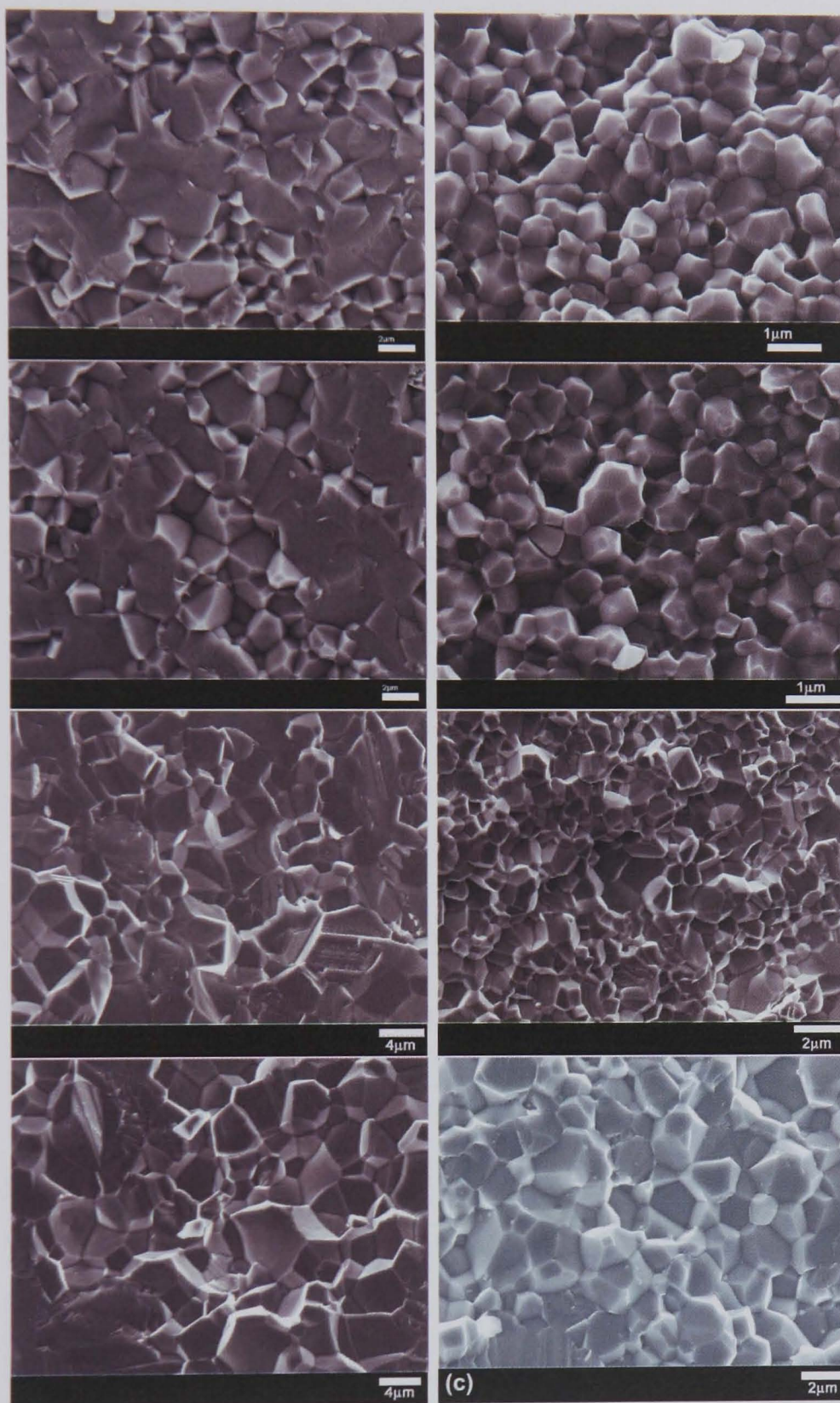
Figure 7.7: *Example SEM images of alumina fracture. Four pairs of (left) undoped and (right) doped '1 of equal sintering temperature: 1450° undoped/La doped, 1500° undoped/La doped, 1550° undoped/Tm doped and 1600° undoped/Yb doped.*
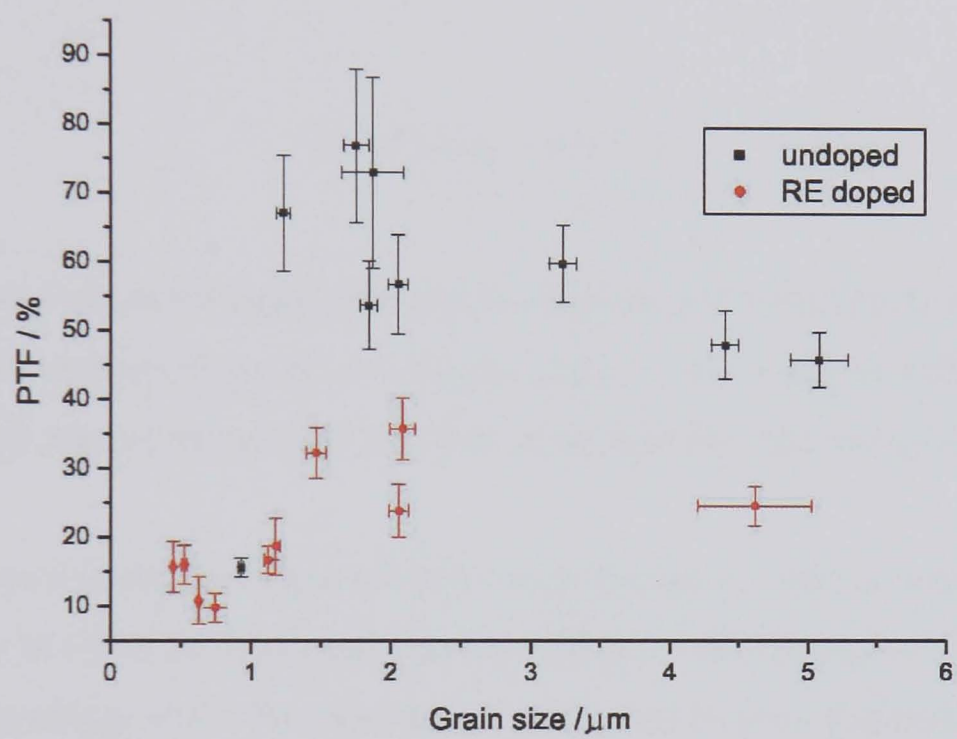
Figure 7.8: *Percentage transgranular fracture against grain size for doped and undoped alumina samples.*

RE doped alumina

The RE doped samples showed a much reduced PTF compared with their doped counterparts. This apparent reduction in PTF has implications regarding the strength and fracture toughness of RE doped aluminas compared with undoped. By using the Griffith energy balance model for brittle materials, the effect of RE doping on the fracture of alumina may be explained. Assuming two types of fracture, cleavage (transgranular - c) and grain boundary (intergranular - gb), and symmetrical fracture:

$$G_c = 2\gamma_c G_{gb} = 2\gamma_s - \gamma_b \qquad (7.2)$$

[19]

Where G_c and $G_g b$ are the work of fracture for cleavage and intergranular faliure respectively, γ_c is the surface energy of the cleavage plane, γ_s is the specific surface energy of each grain exposed by fracture and γ_b is the grain boundary free energy per unit area.

The undoped alumina points show mixed fracture throughout, thus G_c and $G_g b$ are similar, however, the PTF for RE doped alumina is biased such that $G_g b < G_c$. Therefore, as the surface energy of the cleavage plane is unaffected by grain boundary segregation, the RE dopants must cause a reduction in the work of fracture for intergranular failure. Reducing the work of fracture for intergranular failure, therefore, reduces grain boundary cohesion and consequently the strength of a material. This phenomenon is well documented in metal embrittlement studies; it is well known that impurity segregation causes a reduction in absolute surface free energies[128].

The previous chapter elucidated the fact that the segregation in alumina and spinels was thought to be submonolayer or monolayer. This means that upon fracture the segregant will be split between the two fresh surfaces, and each surface will have energy $< \gamma_s$ (non equilibrium surface segregation[19]). Also, $G_g b$ does not include the influence

166

of non-planar crack paths or grain boundary frictional sliding during crack propagation. The $2\gamma_s - \gamma_b$ energy balance is accepted, however, for multilayer segregation coupled with a symmetrical fracture path and there is the possibility that the presence of segregate atoms on the fracture surfaces may facilitate a relaxation of surface atoms, and a reduction of γ_s compared with the pure surface (i.e. no segregates).

Assuming the reduced grain boundary cohesion, the preferred fracture is therefore intergranular, however, there is an additional aspect which the graph suggests may be explained by a simple grain size effect. As described previously, the reduction in grain size for a given sintering temperature is another effect of RE doping, which is why there are a greater number of sub-micron grain size samples in this particular study. The sub-1.5 μm grains show a transition where the PTF is further reduced. As demonstrated in the Vickers indents, if a crack path can easily carry on without a large change in angle (i.e. following a grain boundary) it will do so, however, if a large grain is present then it may still be energetically more favourable to follow a transgranular path. Thus, for the fine grained samples the crack path may easily follow the intergranular route.

It should be considered that other effects such as porosity or the presence of impurities at grain boundaries will have an effect on the fracture properties. Where grain size effects are thought to be dominant it may be that significant levels of porosity alter the fracture behaviour[129]. This does not remove the fact that this is in contradiction with the literature regarding grain boundary properties, where it is suggested that RE segregation increases the grain boundary strength. Such studies are based on fracture energy[54] and strength[52] studies using large grain pressureless sintered samples with variable porosity.

Figure 7.9 shows the PTF plotted against sintering temperature and reinforces the clear difference in fracture type between the undoped and RE doped samples. While the liter-

167
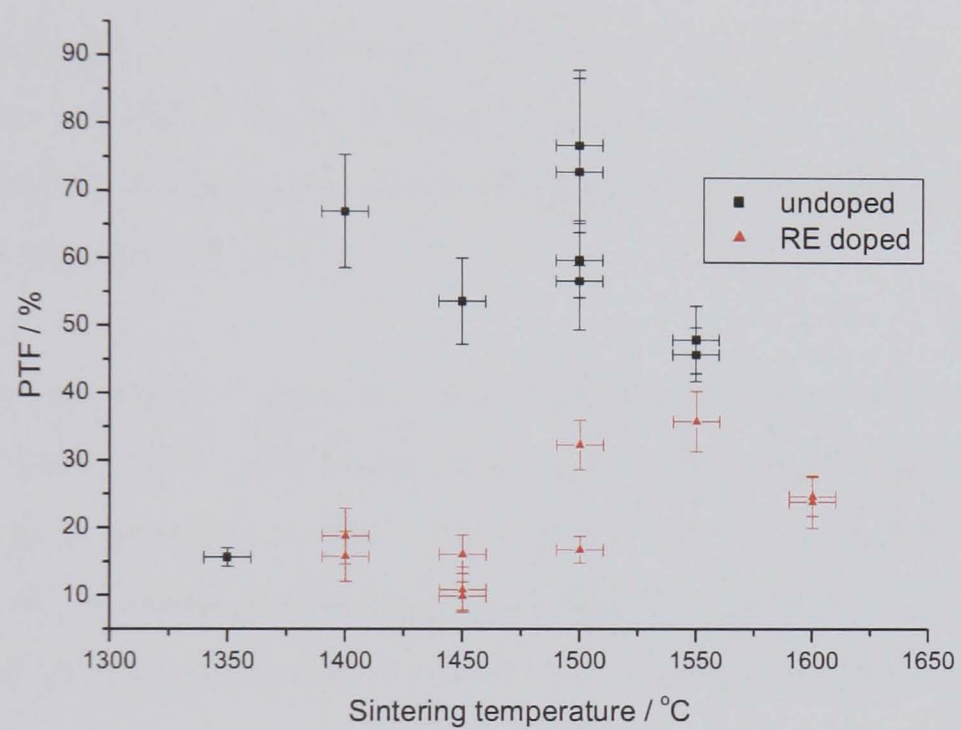
Figure 7.9: *Percentage Transgranular Fracture against sintering temperature for doped and undoped alumina samples.*

ature may contradict this result, there is evidence for indirect support. Lartigue-Korinek et al studied Y doped alumina and found increased grain boundary pull-out observed in wear tests, suggesting the reduced grain boundary cohesion[44]. Also, Deng et al attributed their increased intergranular fracture in RE doped alumina/SiC composites to the combined effects of a RE-Si composition at the boundaries[130].

Fracture Mode in Spinel

The fracture images of the spinel samples (figure 7.10) do not show the same effect of RE doping on the fracture mode as their alumina counterparts. The mode of fracture was predominantly transgranular irrespective of dopant or grain size. This is a major difference between the two oxides.

The intrinsic properties of spinel are likely to be the root cause of this difference in behaviour. Spinel has a cubic based structure and, similarly to MgO, has a greater number of slip systems than alumina (hexagonal structure) and a higher propensity for cleavage. Thus, even with RE segregation to the grain boundaries, there is unlikely to be a reduced grain boundary cohesion such that it dominates over the multiplicitous cleavage planes.

7.3 SIMS Analysis of RE Doped Alumina Surfaces

A pair of samples prepared from the same sintered pellet of Eu doped alumina were analysed using SIMS. Both were polished to a 1 μm mirror finish, then one was thermally etched at 1200°C for 2 hours. The SIMS was performed on a 0.5 x 0.5 mm section in the middle of each sample, with a sputtering depth of <100 nm such that only the top surface was analysed. The SIMS results are shown in figure 7.11. This spectrum was aquired by counting the negative ion yield for each mass unit, this ensures that peaks
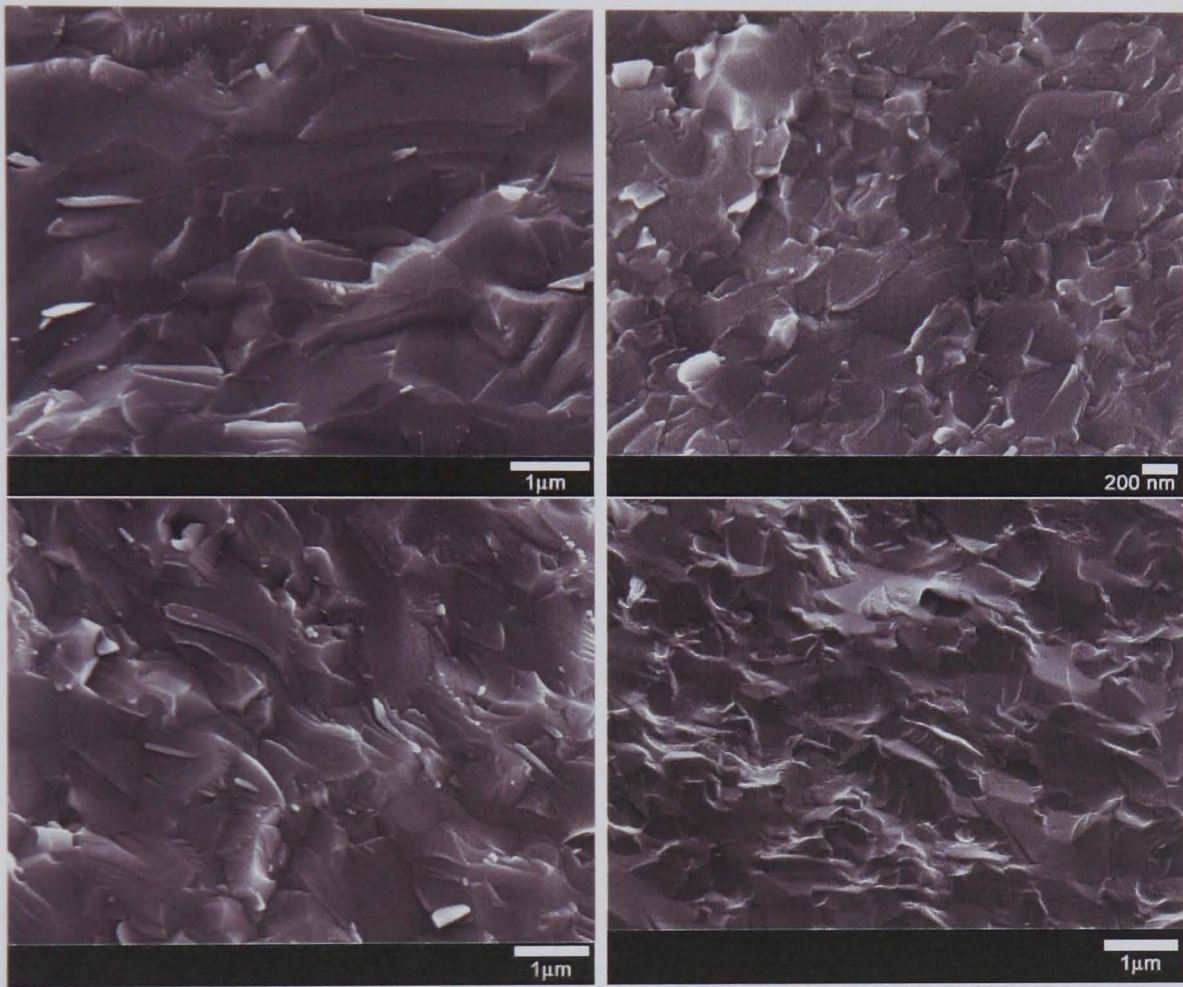
Figure 7.10: *Examples of SEM images of spinel fracture; top left undoped 1450°, top right Gd doped 1450°, bottom left undoped 1500°, bottom right Tm doped 1500°.*

are identified as SO_x are not O_y ions, e.g. SO not O_3. The Eu counts for the thermally etched sample are larger than the counts for the polished sample suggesting the Eu from the boundaries has transported to the surface.

This result has implications in terms of surface/boundary energy considerations, especially important for the fracture analysis shown previously. Currently, dihedral angle measurements are used to determine grain boundary/surface energy ratios. If the boundary segregant is removed, or moved via the boundary to the surface then both the boundary energy and the surface free energy will be altered, so simply measuring the dihedral angle will provide an incorrect result.

In terms of fracture processes, it is not the absolute grain boundary or surface energies that are important, it is the relative energy. Thus, if the relative surface/boundary energy is lowered significantly via segregation to a free surface then there is an increased likelihood of grain boundary fracture.

7.4 Chapter Conclusions

It was expected that the addition of RE dopants to alumina would have similar effects to the RE doping of spinel. While the segregation of RE cations to grain boundaries is similar (if not identical) in the two materials, the effect of such segregation on mechanical properties is not. There are two main effects of RE doping that have been identified; the effect of doping on sintering behaviour (mentioned in chapter 3.7.5), and the effect of doping on the grain boundary properties.

The major similarity between the two systems is the fact that the RE dopants segregate to grain boundaries. All other changes in terms of mechanical effects are limited to alumina. This is purely due to differences between the alumina and spinel crystallog-
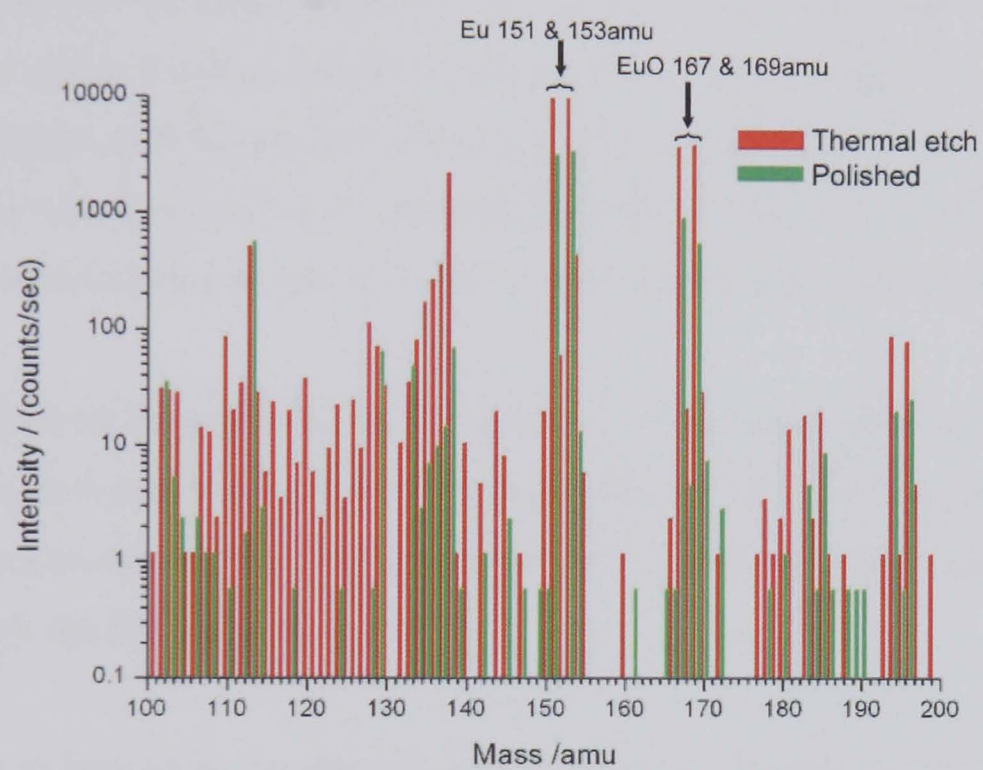
Figure 7.11: *Negative ion SIMS spectrum of thermally etched and polished Eu doped alumina samples, with the Eu and EuO peaks indicated.*

raphy.

An extremely important result is the change in fracture mode for RE doped alumina. There is clear evidence for a change from mixed fracture (inter and transgranular crack paths) to predominantly intergranular fracture when comparing undoped with doped alumina. SIMS data has shown that RE dopants segregate to the sample surface during annealing therefore altering the surface energy. It can be assumed that, upon fracture, RE will remain on the newly fractured surfaces which therefore have different surface energy to the undoped surface. Cohesion is based on the relative energies between surface and grain boundaries, therefore the intergranular fracture may not necessarily represent an absolute reduction in cohesion. Instead there may be a reduction in the ratio of grain boundary to free surface energy, as the free surface may be altered by the presence of RE.

This phenomenon has not been found in spinel as the slip systems in the spinel structure lead to a much increased propensity for transgranular fracture. Another important factor in the intergranular fracture phenomenon is that it is insensitive to dopant concentration, dopant identity and grain size.

There was an increase in hardness for a given sintering temperature for both RE doped alumina and RE doped spinel. In alumina this was due to the control of grain growth leading to reduced grain size for a given sintering temperature, however, there was also evidence of an increase in hardness in addition to the purely grain size effect. There was no trend in the hardness increase with grain size for the spinel, however, there was evidence for a general increase in hardness for Tm doped samples. Hardness is a difficult property to measure reliably and reproducibly hence the large error bars in the measurements. In general, spinel was found to have a hardness 2 - 4 Gpa less than the respective doped or undoped aluminas of similar sintering temperature.

Chapter 8

Optical Properties of Rare Earth Doped Oxide Ceramics

8.1 Introduction

One goal of materials scientists is the production of transparent materials for advanced components such as armour or advanced electromagnetic windows. Oxide ceramics are good candidates for this due to the high hardness, high temperature stability, strength and corrosion resistance. Materials including AlON, YAG and single crystals of alumina (sapphire) are commonly used for such applications. Polycrystalline alumina and spinel have shown potential for optical materials. Previous barriers to the development of optical polycrystalline alumina have included the fact that its non-cubic structure leads to birefringence. While this is true for coarse grain alumina, as the grain size approaches the wavelength of light the dominant scattering mechanism changes thus removing the birefringent element leaving a high quality optical material[63]. Spinel does not undergo any thermally induced phase changes and it has a more favourable transmission spectrum in the visible region than the widely used ALON[9], it also has a cubic structure. This chapter provides examples of fine grained alumina and spinel and discusses their potential for use as an optical material as well as assessing the effect of dopants on the optical

174

properties.

8.2 Modelling Light Scattering in Polycrystalline Ceramics

8.2.1 Measuring the Scattering of Visible Light

The optical quality of a sample is dependent on two factors; the quantity of transmitted light per unit thickness and the angular distribution of the transmitted light. The definition of transparency has been mentioned earlier (section 2.3.2), figure 8.1 demonstrates schematically the difference between transparency and translucency. Traditional examples of the two are translucent polycrystalline alumina and transparent single crystal sapphire.
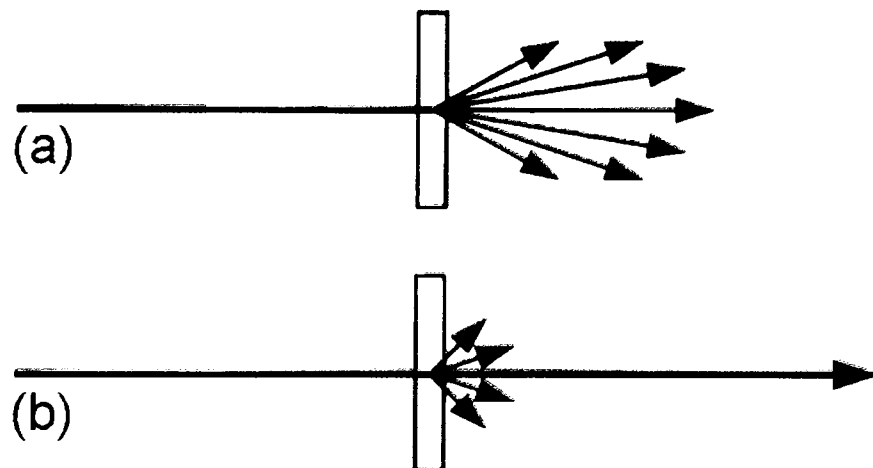
Figure 8.1: *Schematic of highly scattering and low scattering transmission through polycrystalline optical ceramic samples[131].*

A problem that exists in the literature is that the definition of transparency is used where translucency would be more appropriate, for example when spectrophotometers are used to measure transmitted light. A spectrophotometer collects light using a large collection angle (up to ~5°), thus components of low angle scatter and undeviated light

175

are both collected. Spectrophotometers are designed to measure the absorption rather than scatter of light from a material. The spectrophotometer measures light from a large collection angle but not the entire TFT. To extract the unscattered component, the undeviated beam (in general taken to be the transmitted light within ~0.5° is defined as the RIT and is accepted to be a true measure of transparency[63]. Thus by comparing the TFT with the RIT a true measure of transparency can be found.

The RIT is defined as:

$$RIT = (1 - R_s)exp(-\gamma d) \tag{8.1}$$

where R_s = the total reflectance, d = sample thickness and γ = total attenuation coefficient:

$$\gamma = \alpha + \gamma_t \tag{8.2}$$

where α = the absorption coefficient and γ_t = total scattering coefficient (made up of a number of components, discussed in turn shortly).

8.2.2 Absorption of Light

The absorption of ceramic materials has two components; intrinsic and extrinsic, where the intrinsic arises from the perfect crystal and extrinsic is due to dopants, impurities and defects. There is a large intrinsic absorption for alumina and spinel in the UV region of the spectrum. The UV cut off (Urbach tail) is caused by electronic transitions across the band gap, defined as λ_c (wavelength cut-off):

$$\lambda_c = \frac{hc}{E_g} \tag{8.3}$$

where h = Planck's constant, c = velocity of light in a vacuum and E_g = the band gap energy of the chosen material. The wavelength cut offs are 140 nm for alumina and 160 nm for spinel (band gap energies 8.8 eV and 7.8 eV respectively)[132].

The IR cut off is due to absorption by lattice vibration, which depends on bond length,

176

strength and atom sizes. Increasing IR transmission, therefore, affects the mechanical properties (except diamond, which possesses good transmission at wavelengths $>100 \mu$m due to its high symmetry which prevents vibrating atoms absorbing radiation).

Thus alumina and spinel allow minimal absorption of visible light and will be neglected ($\alpha = 0$).

8.2.3 Reflection of Light

There are two components of reflection; diffuse (surface) and specular (where angle of incidence = angle of reflection). Diffuse reflections may be reduced or eliminated by careful preparation of the incident surface.
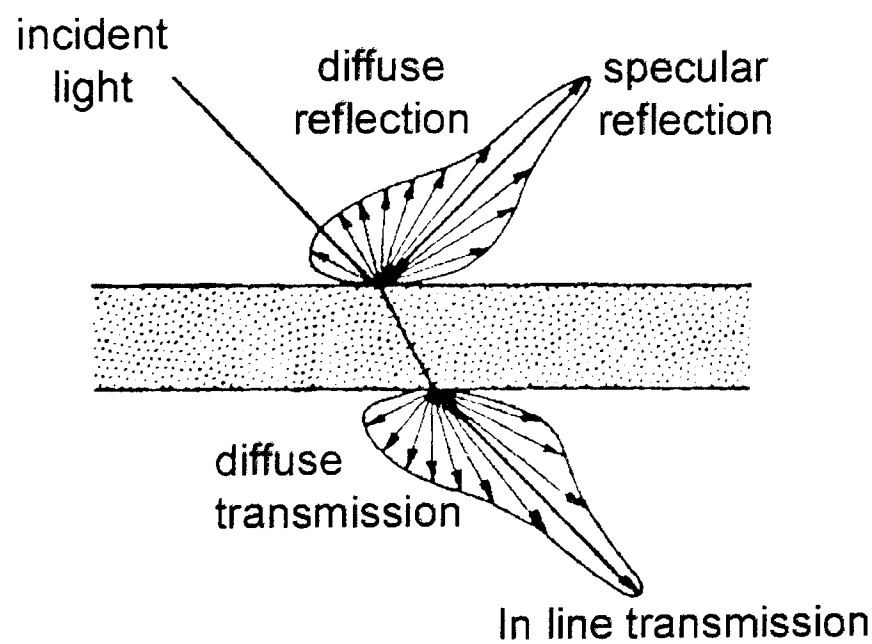
Figure 8.2: *Components of absorption and reflection in a polycrystalline ceramic sample[62].*

The incident air/crystal surface may be carefully prepared by polishing such that the

roughness and/or undulations of the surface are less than $1/10\lambda_{vis}$[133]. For specular reflections the following model can be derived. For normal incidence reflections occur at entrance and exit surfaces such that reflection, R is calculated by considering refractive indices;

$$R = \left(\frac{n_1 - n_2}{n_1 + n_2}\right)^2 \tag{8.4}$$

at the surfaces, s, of the material, $n_1 = $ air $= 1$, crystal $n_2 = n$, so;

$$R = \left(\frac{1-n}{1+n}\right)^2 \tag{8.5}$$

$$R_s = \frac{2R}{1+R} \tag{8.6}$$

such that $R_s = $ total reflection and $R = $ reflection from one surface.

The refractive indices of alumina and spinel vary depending on temperature of the sample and wavelength of light, however, for the visible region of the spectrum the variation is small. Further details of temperature and wavelength effects on refractive index are published elsewhere[71]. Alumina has different refractive indices in different crystallographic directions (cause of the birefringence mentioned earlier). While the refractive indices change slightly with wavelength and temperature, the difference between the minimum and maximum values do not.

Grain boundary reflection

The difference in refractive index depending on grain orientation in alumina mentioned above should lead to reflections at the grain boundaries themselves. The discontinuity at any given boundary will range between 0 and Δn. Using the equation for reflectivity perpendicular to the boundary:

$$R_\perp = \frac{(n_1 - n_2)^2}{(n_1 + n_2)^2} \tag{8.7}$$

where n_1 and n_2 are the refractive indices of the neighbouring grains. Light does not pass through all grains with a perpendicular incidence therefore Fresnel's laws must be

178

used to calculate general reflectivity at all angles[63]. Given that the largest difference in refractive index for alumina is 0.008 (extraordinary ray; parallel to c axis = 1.760, ordinary ray; perpendicular to c axis = 1.768[71]) then the maximum reflectivity is $\sim 5 \times 10^{-6}$. If it is assumed that all the incident rays enter a boundary at an angle of 90°, the total maximum reflectivity R_{max} for m grain boundaries is:

$$R_{max} \simeq 1 - (1 - R_\perp)^m \tag{8.8}$$

It can be seen that even for a thick sample with a large number of boundaries, the reflection contribution from grain boundaries given the difference in refractive index will be low and will be neglected here. As spinel has no direction dependence for refractive index it is also unaffected[63].

8.2.4 Refraction of Light

The total refraction of light within a polycrystalline sample is non trivial. The total scattering coefficient (γ_t) is made up of three main scattering processes:

$$\gamma_t = \gamma_p + \gamma_{gb} + \gamma_i \tag{8.9}$$

where γ_p, γ_{gb} and γ_i are the pore, grain boundary and impurity/inclusion/precipitate scattering coefficients, respectively[134]. The relative effect of each of these scattering centres depends on their size with respect to the wavelength of the incident radiation. A full mathematical treatment of light scattering theory is not included here and may be found elsewhere[62, 133, 135, 136].

Refraction from impurities and precipitates

For the materials studied here, the impurity content is extremely low and distributed across many grain boundaries within the sample. In addition, the precipitates have only formed as small grain boundary triple points distributed throughout the sample. These triple points and small areas of impurity generally have a very small difference

179

in refractive index from the bulk material and are weak scatterers as a result. The scattering from impurities and precipitates will therefore be neglected.

Scattering at grain boundaries

In alumina, the refractive index differences ensure that refraction is not negligible. There are two regimens to be considered, large and small grain systems. For grains much larger than the wavelength of light (strictly the condition is $G \triangle n > \frac{2\pi\lambda}{n}$), the deviation of light, from Snell's law:

$$n_1 sin\alpha_1 = n_2 sin\alpha_2 \tag{8.10}$$

where n_1 and n_2 represent the first and second grains in which the light travels, α_1 is the angle of incidence and α_2 is the angle of refraction at the boundary between the two grains. This model shows that refraction at grain boundaries has considerable effect, especially in a real sample where several boundaries are encountered for a given thickness. This model has been shown to be valid for grains $>40\mu$m.

Apetz and van Bruggen have recently applied the Mie theory to model scattering from grains <10 μm. Here, it is assumed that a matrix exists with dispersed particles of average size equal to the average grain size of a given fine grained alumina and refractive index differential $|\triangle n| = |n_2 - n_1|$ smaller than $\triangle n_{max}$. In alumina, if $\triangle n$ is averaged over all orientations (with isotropic distribution) it gives that $\triangle n = 2/3\triangle n_{max} \sim 0.005$.

The small refractive index differential and thus mainly single scattering events per boundary incidence gives the grain boundary scattering coefficient (γ_{gb}) as:

$$\gamma_{gb} = C_{scat}N \tag{8.11}$$

Where C_{scat} is the scattering cross section across a single sphere and N is the density of spheres. By implementing the Rayleigh-Gans-Debye theory (when the phase shift
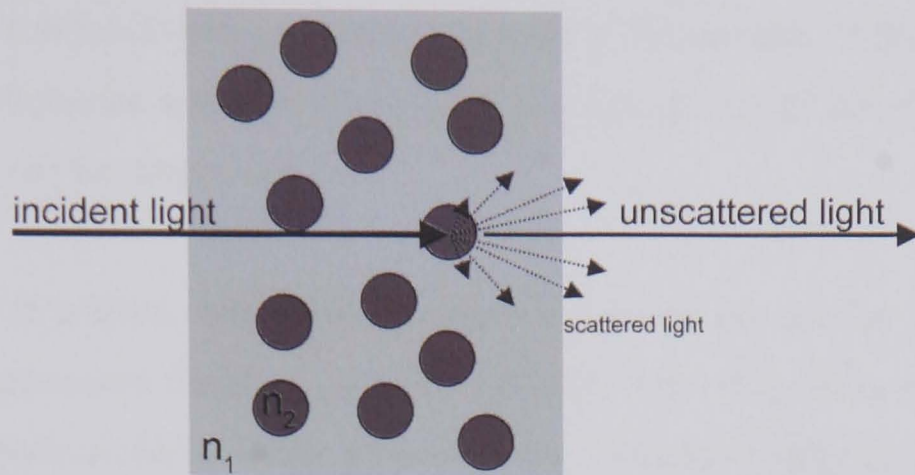
Figure 8.3: *Diagram demonstrating the approximation by Apetz and van Bruggen that a polycrystalline ceramic can be modelled by a matrix with dispersed particles.*

caused by scattering objects, i.e grains, is small)[135] the scattering cross section can be written as:

$$C_{scat} = (\frac{\pi^3 g^4}{\lambda_m^2})(\frac{\triangle n}{n})^2 \tag{8.12}$$

By substitution, the grain boundary scattering coefficient γ_{gb} is given by:

$$\gamma_{gb} = \frac{3\pi^2 g \triangle n^2}{8\lambda^2} \tag{8.13}$$

This model contains a number of assumptions (importantly the assumption that the grains are spheres and the grain size distribution is approximated by a mean grain size), however, it has been demonstrated that it is valid[63].

8.2.5 Magnesium Aluminate Spinel

The expected optical properties of spinel were theoretically good due to the cubic structure and high purity precursor powder, however, there was some variability in the trans-

parency of the samples produced. In general the hot pressed samples showed excellent transmission compared with pressureless sintered (PS) samples. Figure 8.4 shows a number of hot pressed spinel samples. By shining a laser through the samples the scattering profile can be determined.

A technique of pressure filtration was used to minimise the powder packing defects by colloidal processing the slurry with a dispersant. The FP green bodies were visibly more homogeneous than the cold pressed or dry uniaxially pressed samples but it was decided that hot pressing gave the highest density and most reproducable samples. Pressure filtration, and more general colloidal processing has been widely studied[137], yet the phase space for experiment variables is so large that further study within the time and scope of this project was deemed unworkable. Krell and coworkers have succesfully worked through the experimental problems to provide undoped polycrystalline spinel by colloidal processing in a commercial environment. A recent patent application has been published on this work[138].

8.2.6 Hot Pressed Spinel

The hot pressed spinel samples showed some variability in their optical characteristics, yet were generally of higher optical quality than the filter pressed samples. The large grain spinels most commonly studied in the literature arise due to the high temperatures used in sintering. Here, temperatures from 1350 to 1650°C were used with minimal hold time (10 mins) in the hot press. All hot pressed spinel samples showed a fine grained structure, notably those that were undoped showed no obvious differences to their doped counterparts.

To initially optically characterise the samples, the top and bottom surfaces of the hot pressed pellet were removed using a diamond grinding wheel. This simple process allows
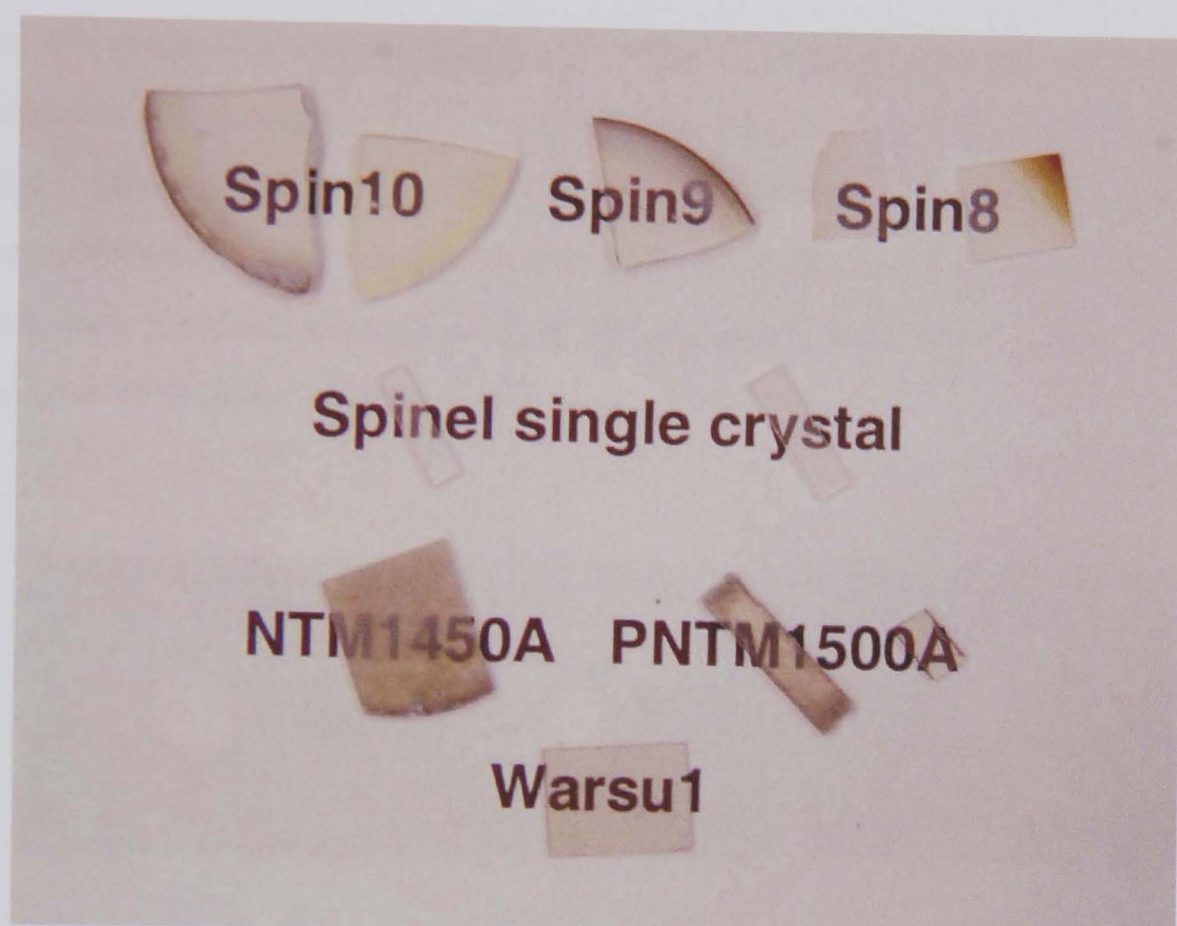
Figure 8.4: *Examples of optical spinel samples.*

a visual inspection of the translucency of the sample. The general rule was that if the sample was optically translucent at this stage, then the hot pressing to near theoretical density was succesful. If the sample was opaque then it was not processed any further for optical testing, the cause of opaque sample production was due to mechanical problems in most cases. The translucent samples underwent further preparation as detailed in section 3.7.5.

Figure 8.5 shows the image captured by a CCD array of a laser spot shone through two different spinels. Again, this is a good indication of the optical quality of the material and a demonstration that the filter pressed samples produced more scatter than the hot pressed samples. The fine-grained hot pressed sample shows a small amount of low angle scatter compared with the coarse-grained pressureless sintered sample. An image of the laser spot alone is given for reference.

Figure 8.5: *CCD images of 532 nm laser light shone through (from the left) uninterrupted beam, fine grained hot pressed spinel and large grain filter pressed spinel.*

There is a ceiling for the intensity as this is the point where the CCD saturates. However, the low angle scatter can be compared with the unobstructed laser. The similarity in scattering profiles from the unobstructed laser and the hot pressed spinel show that the fine grain structure has no detrimental effects on the low angle scattering profile, this manifests itself as high transparency.

184

A second set of images is shown in figure 8.6, where the laser light shone through a number of undoped spinel samples of various thicknesses is imaged. A radial plot of these images is given in figure 8.7.
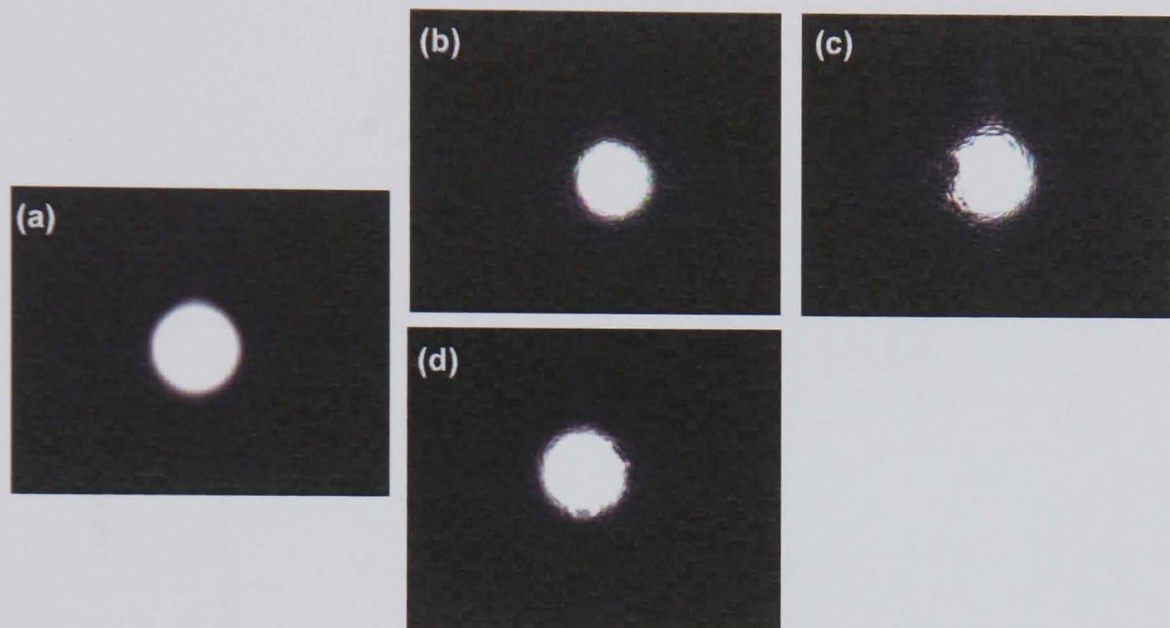
Figure 8.6: *CCD images of 532 nm laser light shone through undoped spinel samples of various thicknesses: (a) Unobstructed beam, (b) 1.56 mm (c) 1.07 mm and (d) 0.85 mm.*

While the low angle scatter component is similar for these thicknesses of sample, it can be seen that the thinnest sample has an intensity plot most similar to the unobstructed beam.

The wavelength dependence in the UV/visible/near IR range of the spinel transmission is shown in figure 8.8 for undoped and Tm doped samples. There are no obvious differences in the plots, indeed both sets of data show a characteristic feature at $\sim$800 nm and $\sim$540 nm. The reduced transmission in the 1600°C Tm doped sample may be due to an increase in impurity content from the hot press die as discussed earlier in section 4.2 leading to increased absorption.

185
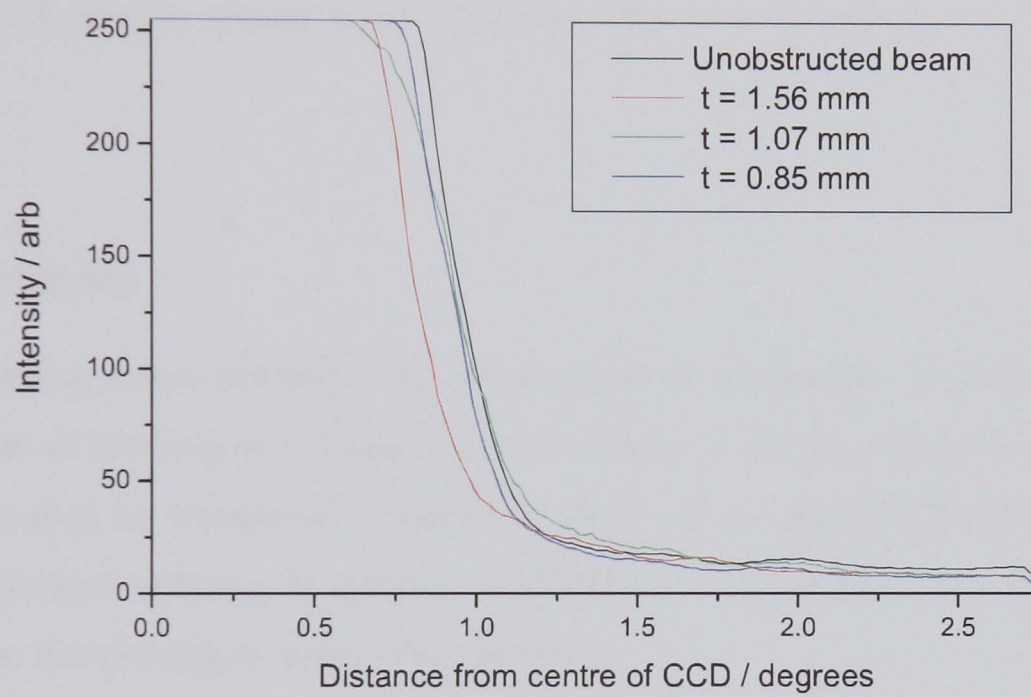
Figure 8.7: *Optical radial scatter profiles for a selection of undoped spinel samples of various thicknesses.*

The expected wavelength cut-off is 160 nm, however all of the transmission spectra show a cutoff between 250 and 400 nm. This may be due to the polycrystalline nature of the samples. Lower periodicity at grain boundaries results in localised energy states located within the band gap, which can absorb lower energy radiation. Also, the inclusion of impurities or dopants at boundaries alters the local bonds, further modifying the absorption.

IR transmission spectra are plotted in figure 8.9. There are no obvious absorption peaks and all samples showed good IR transparency with the cutoff at ~1500 - 1800 nm.

8.2.7 Alumina

The preceeding review demonstrated the potential of fine-grained alumina to remove the problem of birefringence. Considering this, there are few reports of the use of fine-grained alumina for transparent materials in the literature, importantly only using hot isostatic pressure sintering to achieve full density for the fine grain size materials[60] rather than hot pressing or pressureless sintering.

RE doped alumina

Doping with RE elements has been shown to reduce the grain growth on sintering and has been used here to minimise the grain size with the aim of producing better optical properties. Due to reasons described earlier (section 3.7.5), Mo spacers were not used in the hot press die when sintering the RE doped alumina powder. This produced an unexpected side effect in the transmission spectra of the alumina samples, i.e. extra absorption peaks, and is thought to be due to impurities leaching from the die itself, possibly the graphite. This manifests itself visibly as slight colouration, or darkening of
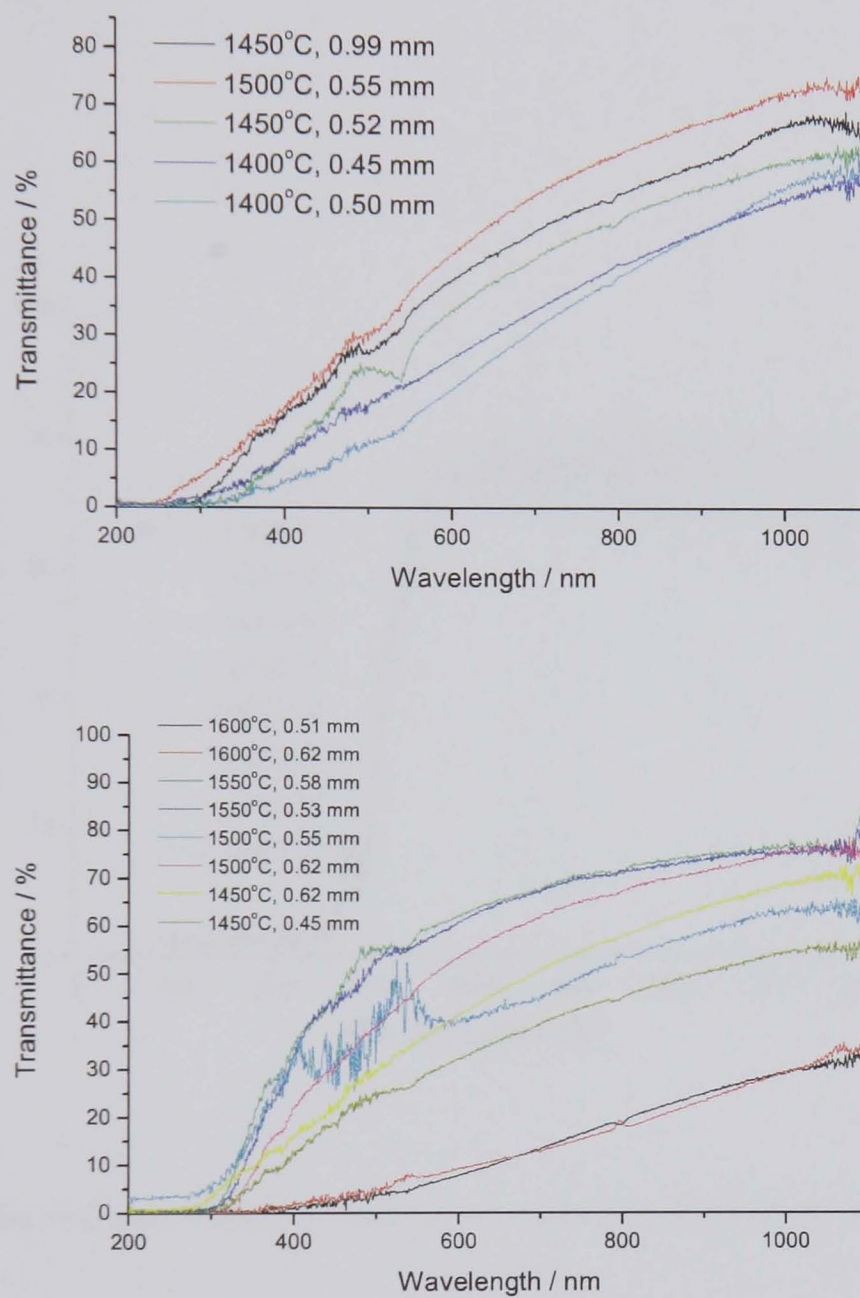
Figure 8.8: *Optical transmission spectra for selection of (top) undoped and (bottom) Tm doped spinel samples.*
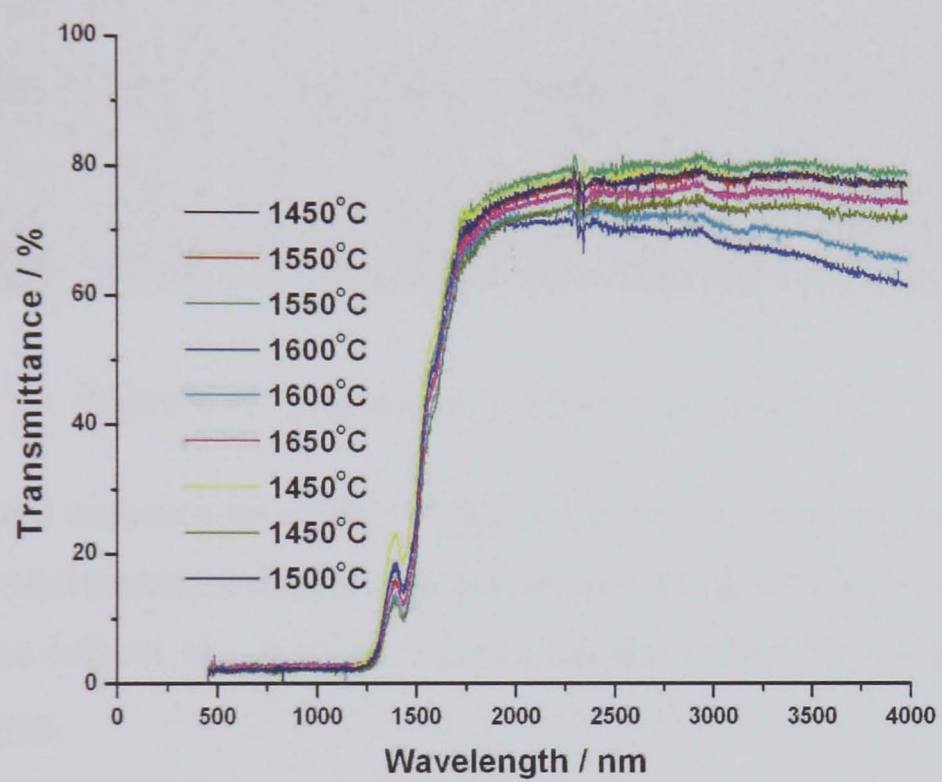
Figure 8.9: *Infra red transmission spectra for selection of Thulium doped spinel samples.*
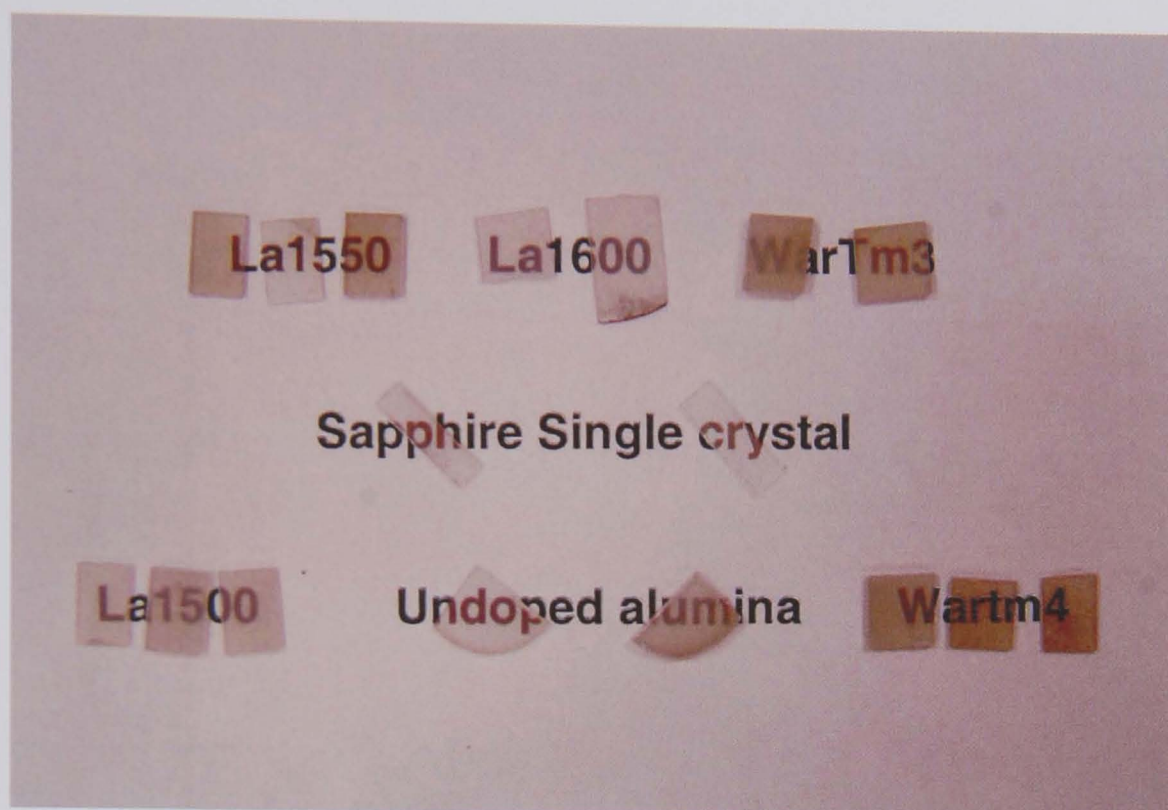
Figure 8.10: *Selection of optical alumina samples.*

the sample and occured with all the RE dopants used, thus reducing the total forward transmission of the material slightly. The undoped samples also showed some colouration when sintered without Mo or parent material spacers, suggesting the die may be the impurity source.

Advantages of fine-grained alumina

Figure 8.11 shows a scattering profile of two alumina samples, one fine-grained and one coarse-grained. There was a large difference between the RIT (low angle component $<0.5°$) of the two samples, however the total forward transmission was found to be almost identical ($\sim$55%). The RIT is the component that determines transparency, and it is clear that the fine-grained sample has a higher transmitted transparent component than the coarse-grained sample, due to the much reduced grain boundary scatter. The scattering mechanism is different in the two samples, the fine-grained is predomanently pore-induced scatter, and the coarse-grained is predominantly grain boundary scatter.

190
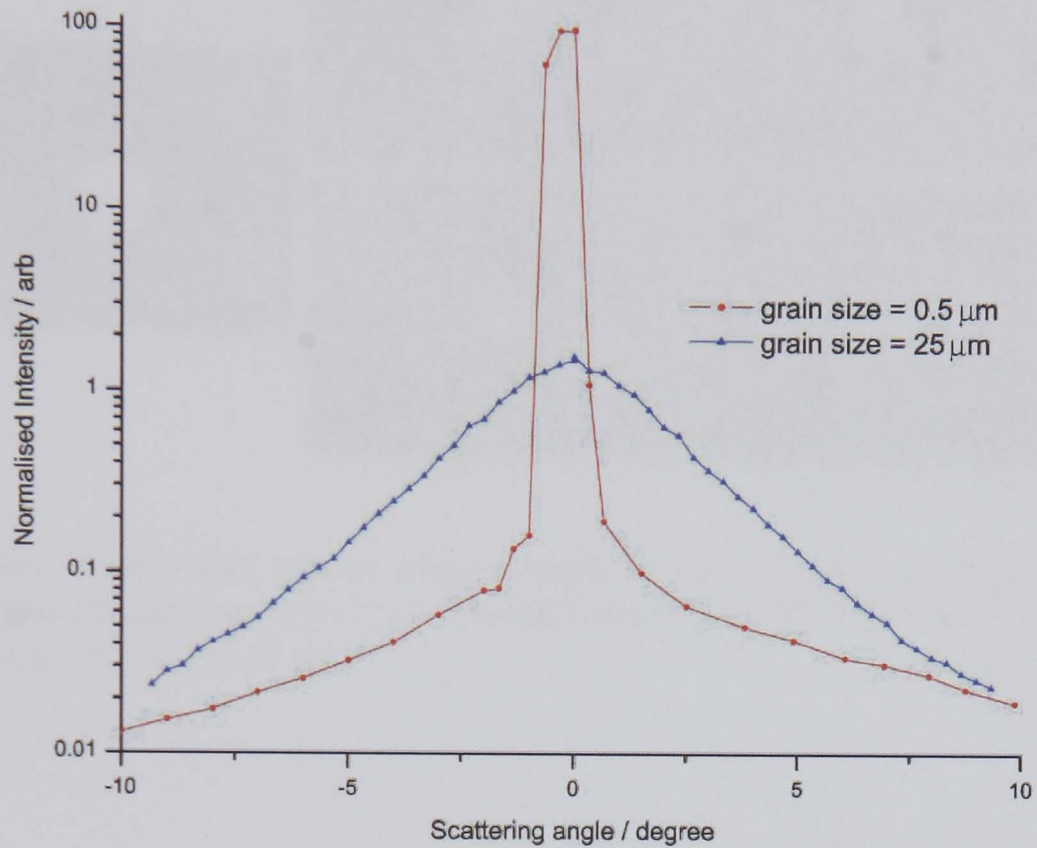
Figure 8.11: *Graph of angular dependence on scatter for fine grained (~ 0.5 μm) and coarse grained (~ 25 μm) undoped alumina samples.*

A similar set of images to figure 8.6 using the CCD camera were taken for a selection of alumina samples (figures 8.12 and 8.14) plotted as angular intensity profiles (figures 8.13 and 8.15). These plots show the relationship between grain size and low angle scatter, where the fine grained samples have a smoother profile. This can be compared with the thickness plot where there are similarities between the profiles. The plots could not be used as a quantitative tool as the ccd saturated when intensity was too high and automatically altered the gain when the range of intensies was too large.

Figure 8.16 shows the CCD image of a defect in a filter pressed alumina. This is thought
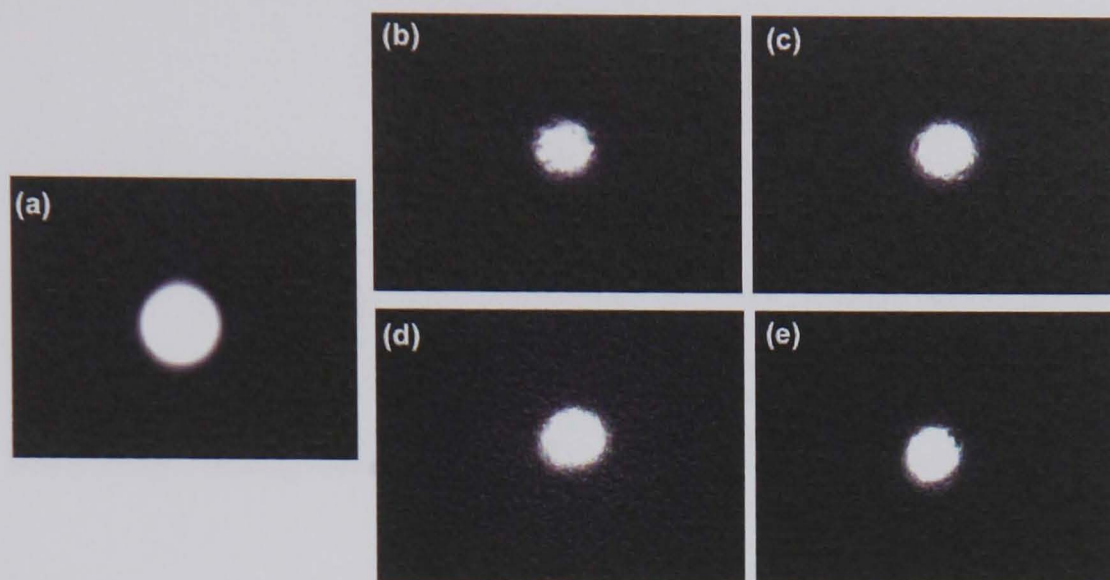
Figure 8.12: *Visible light scatter images captured on a CCD of various thicknesses of Tm doped alumina samples. (a) Unobstructed beam, (b) 0.85 mm, (c) 0.83 mm, (d) 0.76 mm and (e) 0.55 mm.*
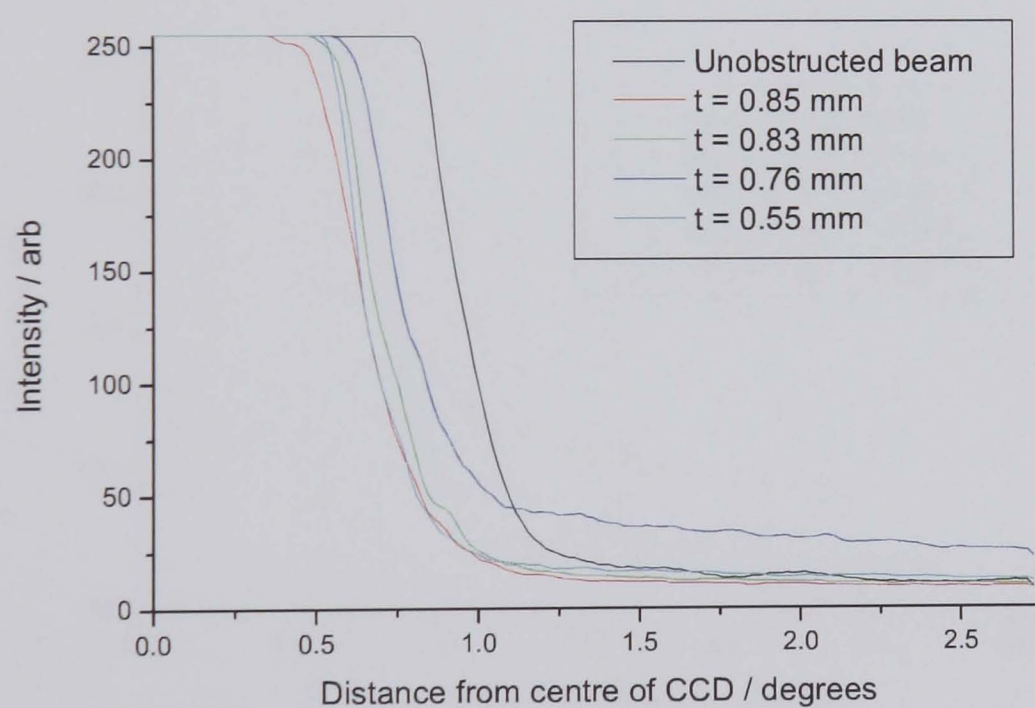
Figure 8.13: *Optical radial scatter profiles for various thicknesses of a single Tm doped alumina sample (G = 2.08 µm).*

192
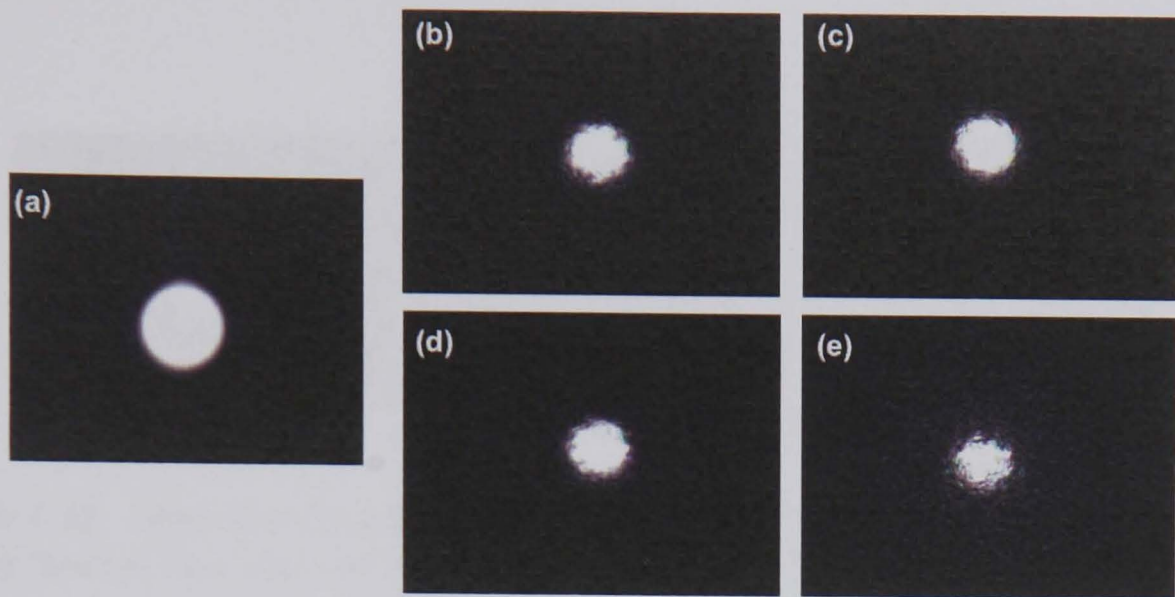
Figure 8.14: *Visible light scatter images captured on a CCD of various grain size Tm doped alumina samples: (a) Unobstructed beam, (b) 0.74 μm, (c) 1.12 μ, (d) 2.08 μ and (e) 4.61 μm.*
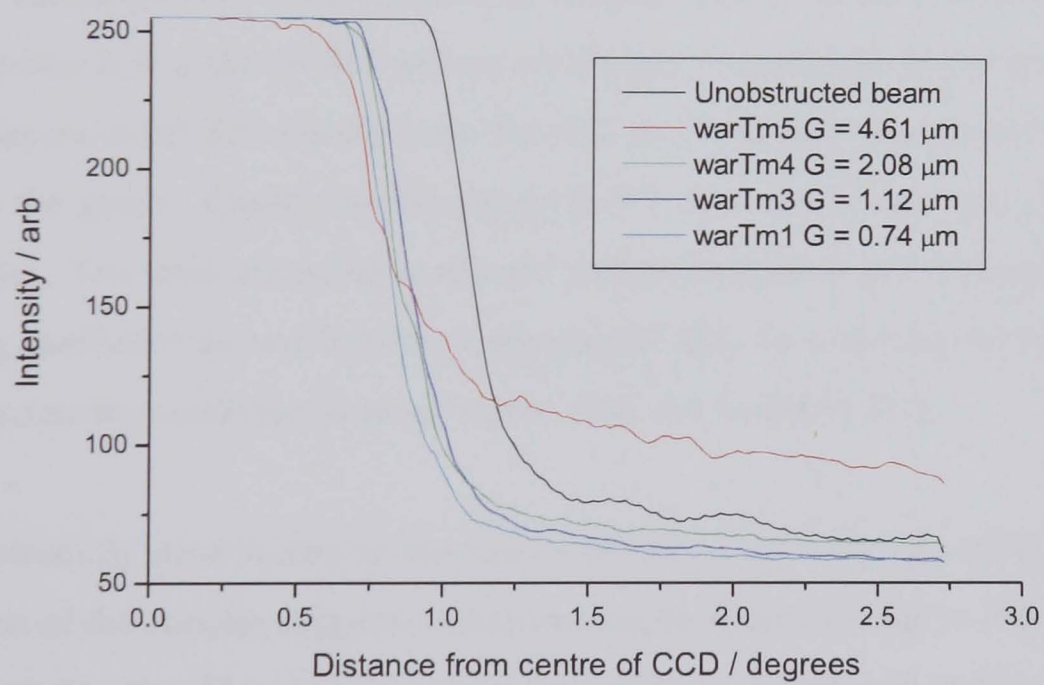
Figure 8.15: *Optical radial scatter profiles for a selection of Tm doped aluminas of various grain sizes.*

193

to be due to a powder packing defect.

Figure 8.16: *Sintering defects from poor powder processing imaged by 532 nm laser shone through thin alumina sample onto CCD.*

8.2.8 Real In-Line Transmission of Alumina

While the photos in figure 8.10 show the alumina samples to have clear optical potential, the quality of the RIT is important. Figures 8.17 and 8.18 provide some idea of the problems associated with these hot pressed samples. From the RGD model, mentioned earlier (section 8.3) a plot of RIT against wavelength for particular grain sizes has been made. Experimental RIT results from the 532 nm YAG laser experiment have been added to the graph. Clearly the experimental RIT is far lower than the expected for the samples. The total scattering coefficient was also modelled and compared with the scattering coefficient derived from the experimental RIT. As expected, for a given grain size the scattering coefficient is much higher than the modelled data.

There is obviously some scattering mechanism unnacounted for in the model. The slight colouration of the samples suggests that there may be absorption due to impurities from the hot pressing die. The samples were produced using an identical method to the un-doped and doped spinel samples which did not show a large reduction in transmission upon adding the Tm. There is no specific absorption peak in the transmission spectra so the slight colouration will not have affected the overall transmission. The TEM images

194
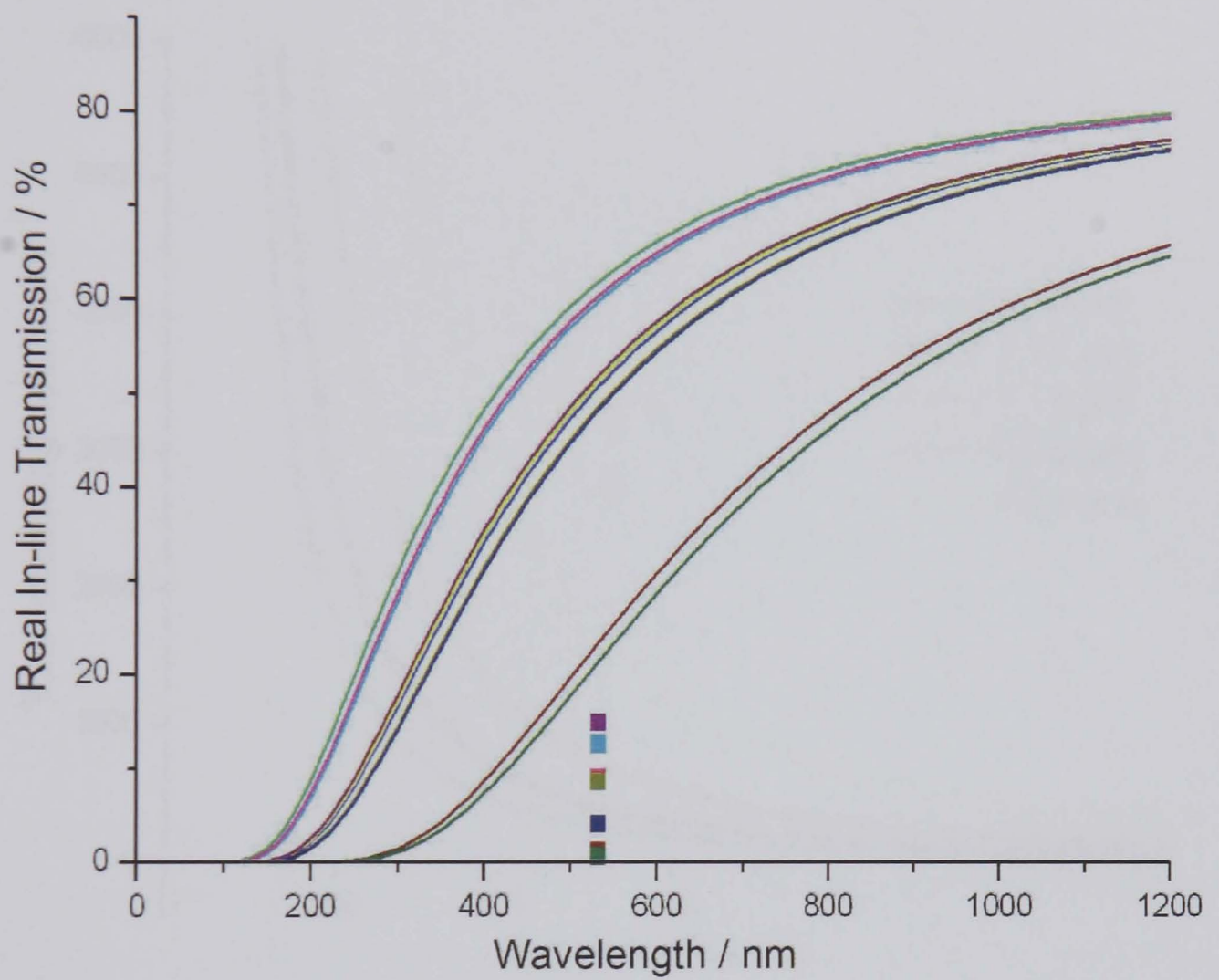
Figure 8.17: *Plot of wavelength against RIT for a set of Tm doped aluminas, with model data shown as a solid line and experimental results shown as individual points.*

195
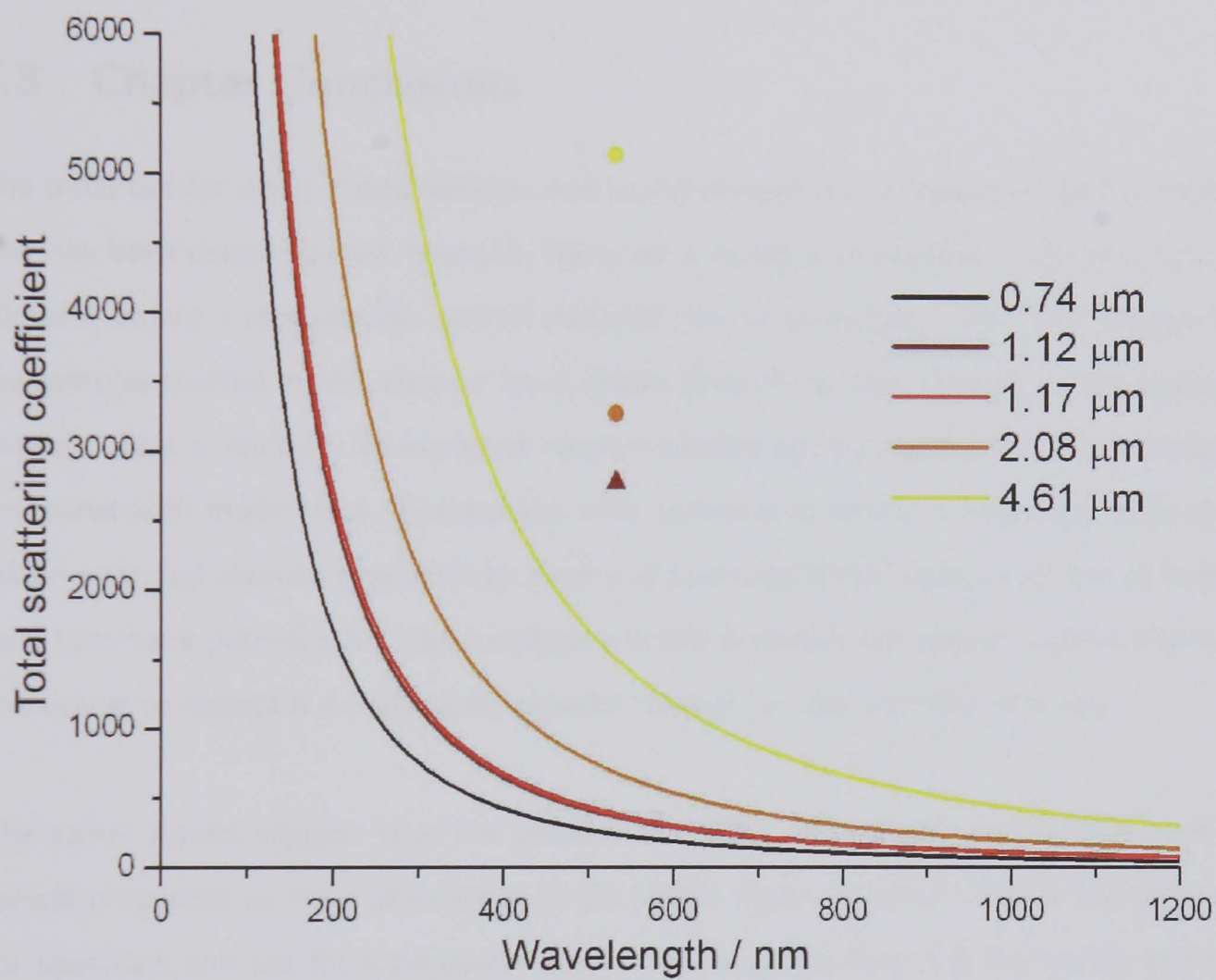
Figure 8.18: *Plot of wavelength against total scattering coefficient for set of Tm doped alumina samples, model data shown as solid line, experimental data as individual points.*

do not show significant porosity of the scale that would either cause major scattering, i.e. reducing RIT, or indeed affect fracture properties. The phenomenon of intergranular fracture in alumina would not occur if there was a large amount of residual porosity within grains as this would increase the amount of trans-granular fracture.

8.3 Chapter Conclusions

The potential for using doped alumina and spinel samples for transparent optical materials has been demonstrated, however, there are a number of problems that need to be adressed before a reproducible optical material can be produced. The TEM images of the samples studied in this chapter have shown little or no pore content in the regions imaged. This is contrary to expected results considering the much lower transmission compared with model data. Comparison with commercial optical transparent polycrystalline undoped alumina produced by Krell and co-workers[139] shows that the samples used here have potential for high hardness window materials but require careful powder processing to maintain a high purity powder throughout the sintering process.

The spinel results suggest that the process of doping the powder directly affects the optical properties as the transmission in the visible region is lower. This is throughout the spectrum and not for a particular peak which suggests that it is not purely due to the addition of RE. The alumina results showed a reduction in low angle scatter for fine grain sizes compared with coarse grained samples. The transmission, however, was lower than predicted by the RGD model. While the minimal porosity in these samples is assumed (from the TEM images), it is still possible that changes in structure at grain boundaries as well as scattering from existing triple points and pores may contribute more to scatter than the model predicts.

The reduction in low angle scatter for reduced grain size is consistent with the RGD

197

model. If the absorption mechanism that is reducing the overall transmission can be identified, the use of the RE to restrict grain growth in alumina will provide better optical properties alongside the marked changes in mechanical properties highlighted in the previous chapter.

Chapter 9

Final Conclusions

The atomic scale segregation of RE cations to the boundaries in magnesium aluminate spinel has been succesfully imaged using aberration corrected STEM. The confirmation of monolayer segregation is an important step forward in terms of understanding the role of dopants with respect to mechanical and optical properties of these materials. For RE cations in alumina, evidence strongly suggests monolayer segregation and through HAADF STEM imaging has been confirmed to within 0.5 nm of the boundary region. The damage from the intense eletron beams in FEGTEMs and the SuperSTEM have limited the atomic resolution. Accompanying the imaging, EDS has confirmed that RE cations are present within 1 nm and PEELS confirmed the monolayer segregation (FEGTEM and SuperSTEM results respectively).

The addition of RE to alumina has been shown to reduce the grain growth upon sintering. This has been explained by the mechanism of blocking grain boundary diffusion. In addition, the segregation of RE cations in alumina has led to a marked change from mixed to predominantly intergranular fracture. The RE segregation enhances intergranular fracture which suggests a reduction in grain boundary cohesion or a reduction in the ratio of grain boundary to surface free energy. The hardness of doped alumina and spinel is increased compared with undoped samples produced using an identical sintering

time and temperature. The addition of RE dopants in spinel has not shown the marked differences as in alumina, however, the hardness of Tm doped spinel was higher than its undoped counterpart for samples produced under the same conditions.

Improvements in optical quality have been shown for both RE doped alumina and spinel. The reduction in low angle scatter, thus improving the transparency or RIT, has been achieved due to the restriction of grain growth. Sub-micron grains remove the problem of birefringence associated with non-cubic materials, i.e. alumina.

The aim of further work should follow a number of strands. An obvious starting point would be to obtain the same quality images of segregation in alumina as in spinel. This requires the problems of drift and damage to be overcome, much of which should be explored as a TEM sample preparation investigation. As well as imaging, the high resolution analysis should follow with further work on both alumina and spinel samples specifically to probe the nature of the bonding at the boundary. This will certainly involve further EELS analysis and STEM imaging in order to provide more clues as to the real structure of the boundary. From this, it may be possible to model selected boundaries then calculate the EELS spectrum using a commonly used density of states code such as WIEN2k. The absolute aim would be to identify the preferred boundary structures and ultimately relate such structures to the mechanical and optical properties of the doped samples.

From a processing point of view, the improvement of optical samples and optimisation of production methods should remain a priority, with further investigation of the variables involved in producing reliable and fully dense FP/pressureless sintered samples. The increased use of spark plasma sintering would provide a faster production method for sintering ceramic samples. Further investigations involving reproducability, amount of dopant, and sintering time/temperature variables requires careful planning

as the number of variables is so large. These are variables that, like the fracture analysis presented here, require statistically meaningful results as small changes in impurity/pore content and or processing methods may produce anomolous data.

Bibliography

[1] M. Shimada, T. Endo, T. Saito, and T. Sato. Fabrication of transparent spinel polycrystalline materials. *Materials letters*, 28:413–415, 1996.

[2] Transparent alumina and method of preparation, 1962. U.S. patent 3,026,210.

[3] R. Nathan Katz. Advanced ceramics: At the cutting edge, ceramics in the cutting tool market, 2000.

[4] G. Brandt. Ceramic Cutting Tools. *Industrial ceramics*, 21(3):169–172, 2001.

[5] R. S. Dobedoe, G. D. West, and M. H. Lewis. Wear performance of fine grained alumina produced during the sparkciba project. unpublished, 2002.

[6] A. Faulkner. Effectiveness of hip prostheses in primary total hip replacement: A critical review of evidence and an economical model. *Health technology assessment*, 2, 1998.

[7] Engineering our future through ceramics, Report of the Advanced Ceramics Task Force, 2002.

[8] Andreas Krell, Paul Blank, Hongwei Ma, Thomas Hutzler, and Manfred Nebelung. Processing of High Density Submicrometer Al2O3 for New Applictions. *J. Am. Ceram. Soc.*, 86(4):546–53, 2003.

[9] Gary Gilde, Parimal Patel, Philip Paterson, David Blodgett, Donald Duncan, and Daniel Hahn. Evaluation of Hot Isostatic Pressing Parameters on the optical properties of spinel. *J. Am. Ceram. Soc.*, 88(10):2747–2751, 2005.

[10] G C Wei. Transparent ceramic lamp envelope materials. 38:3057–3065, 2005.

[11] Adebayo Y. Badmos and Douglas G. Ivey. Characterization of structural alumina ceramics used in ballistic amour and wear applications. *J. mat. sci.*, 36:4995–5005, 2001.

[12] Parimal J. Patel, Gary A. Gilde, Peter G. Dehmer, and James W. McCauley. The amptiac newsletter. *AMPTIAC*, 4(3):1–6, 2000.

[13] Ceramic industry magazie, online content. industry news, nov 2005.

[14] University of the West Indies, Chemistry homepage., nov 2002.

[15] Nist property data summaries, feb 2001.

[16] D. McLean. *Grain Boundaries in Metals*. Oxford, 1957. pp 116 - 122.

[17] J. W. Gibbs. *The Collected works, vol 1*. Longmans, Green & Co, 1906.

[18] W. C. Johnson and J. M. Blakeley. *Interfacial Segregation*. American Society for Metals, 1977. pp 213 - 220.

[19] M. P. Seah. *Interface adsorption, embrittlement and fracture in metallurgy*, volume 53. Surface Science, 1975. pp 168 - 212.

[20] Stephen J. Bennison and Martin P. Harmer. Grain-growth kinetics for alumina in the absence of a liquid phase. *J. Am. Ceram. Soc.*, 68(1):c22–c24, 1985.

[21] A. Morcellin and W. D. Kingery. Microstructural changes during heat treatment of sintered alumina. *J. Am. Ceram. Soc.*, 56(6):309–14, 1973.

[22] http://www.geolite.com/.

[23] A. Maun. Microstructural changes during heat treatment of sintered alumina. *Am. J. Sci.*, 56(6):309–314, 1973.

[24] D. M. Roy and R. E. Barks. Subsolidus phase equilibriums in aluminium oxide-chromium (III) oxide. *nature*, 235(58):118–9, 1972.

203

[25] G. Petot-Ervas, B. Saadi, C. Petot, and M. Loudjani. Transport properties of titanium-doped alpha-alumina: experimental results. *J. Eu. Ceram. Soc.*, 17:943–950, 1996.

[26] S. K. Roy and R. L. Coble. Solubilities of Magnesia, Titania and Magnesium Titanate in Aluminium Oxide. *J. Am. Ceram. Soc.*, 51:1–6, 1968.

[27] R. D. Shannon. Revised Effective Ionic Radii and Systematic Studies of Interatomic Distances in Halides and Chalcogenides. *Acta Crystallographica.*, A32:751–767, 1976.

[28] Christian Elsasser and Traude Elsasser. Codoping and Grain-Boundary Cosegregation of Substitutional Cations in alpha-alumina: A Density-Functional-Theory Study. *J. Am. Ceram. Soc*, 88(1):1–14, 2005.

[29] C. M. Wang, G. S. Cargill III, H. M. Chan, and M. P. Harmer. Structural Features of Y-Saturated and Supersaturated Grain Boundaries in Alumina. *Acta. Mater.*, 48:2579–2591, 2000.

[30] S. Fabris and C. Elsasser. First-principles analysis of cation segregation at grain boundaries in alpha-alumina. *Acta. Mater.*, 51:71–86, 2003.

[31] R. C. McCune, W. T. Donlon, and R. C. Ku. Yttrium Segregation and YAG Precipitation at Surfaces of Yttrium-Doped alpha Al

2O

3. *J. Am. Ceram. Soc.*, 69(8):196–199, 1986.

[32] D. Bouchet, F. Dupau, and S. Lartigue-Korinek. Structure and Chemistry of Grain Boundaries in Yttria-Doped Aluminas. *Mater. Sci. Forum.*, 207–209:205–208, 1996.

[33] J. Cho, H. M. Chan, M. P. Harmer, and J. M. Rickman. Influence of Yttrium Doping on Grain Misorientation in Aluminium Oxide. *J. Am. Ceram. Soc.*, 81(11):3001–3004, 1998.

[34] Jean-Yves Laval, Cecil Cabanel, and Marie-Hélène Berger. Local Electrical Behavior, Crystallography, and Chemistry of Grain Boundaries in Mn-Zn Ferrites. *J. Am. Ceram. Soc.*, 1998.

[35] Mehmet A. Gulgun, Valery Putlayev, and Menfred Ruhle. Effects of Yttrium Doping alpha-Alumina: 1, Microstructure and Microchemistry. *J. Am. Ceram. Soc*, 82(7):1849–56, 1999.

[36] Giulio Rossi and Joseph E. Burke. Influence of Additives on the Microstructure of Sintered Al2O3. *J. Am. Ceram. Soc.*, 56(12):654–659, 1973.

[37] W. C. Johnson and R. L. Coble. A Test of the Second-Phase and Ipurity-Segregation Models for MgO-Enhanced Densification of Sintered Alumina. *J. Am. Ceram. Soc.*, 61(3):110–114, 1978.

[38] H. L. Marcus and M. E. Fine. Grain-Boundary Segregation in MgO-Doped Al2O3. *J. Am. Ceram. Soc.*, 55(11):568–70, 1972.

[39] R. I. Taylor, J. P. Coad, and R. J. Brook. Grain-Boundary Segregation in Al2O3. *J. Am. Ceram. Soc.*, 57(12):539–40, 1974.

[40] P. J. Jorgensen and J. H. Westbrook. Role of Solute Segregation at Grain Boundaries During Final-Stage Sintering of Alumina. *J. Am. Ceram. Soc.*, 47(7):332–338, 1964.

[41] C. A. Handwerker, J. M. Dynys, R. M. Cannon, and R. L. Coble. Dihedral angles in magnesia and alumina: Distribution from surface thermal grooves. *J. Am. Ceram. Soc.*, 73(5):1371–77, 1990.

[42] K. L. Gavrilov, S. J. Bennison, K. R. Mikeska, and R. Levi Setti. Role of magnesia and silica in alumina microstructure evolution. *J. Mat. Sci.*, 38:3965–3972, 2003.

[43] Alumina ceramic, 1968. U.S. patent 3,377,176.

[44] S. Lartigue-Korinek. Multiscale aspects of the influence of Yttrium on microstructure, sintering and creep of alumina. *J. Eu. Ceram. Soc.*, 22:1525–41, 2002.

[45] C. M. Wang, J. Cho, H. M. Chan, M. P. Harmer, and J. M. Rickman. Influence of dopant concentration on creep properties of Nd2O3-doped alumina. *J. Am. Ceram. Soc.*, 84(5):1010–16, 2001.

[46] J. Cho, C. M. Wang, H. M. Chan, J. M. Rickman, and M. P. Harmer. Role of segregating dopants on the improved creep resistance of aluminium oxide. *Acta. mater.*, 47(15):4197–4207, 1999.

[47] H. Yoshida, Y. Ikuhura, and T. Sakuma. High-temperature creep resistance in rare-earth-doped fine-grained alumina. *J. Mater. Res.*, 13:2597–2601, 1998.

[48] Yuichi Ikuhara, Hidehiro Yoshida, and Taketo Sakuma. Impurity effects on grain boundary strength in structural ceramics. *Mat. Sci. Eng. A.*, A319–321:24–30, 2001.

[49] H. Yoshida, Y. Ikuhura, and T. Sakuma. Role of segregating dopants on the improved creep resistance of aluminium oxide. *Acta. mater.*, 50:2955–2966, 2002.

[50] J. Cho, C. M. Wang, H. M. Chan, J. M. Rickman, and M. P. Harmer. A study of grain-boundary structure in rare-earth doped aluminas using an EBSD technique. *J. Mat. Sci.*, 37(1):59–64, 2002.

[51] M. P. Seah. Interface adsorption, embrittlement and fracture in metallurgy. *Surface Science.*, 53:168–212, 1975.

[52] D. Amutha Rani, Y. Yoshizawa, K. Hirao, and Y. Yamauchi. Effect of Rare-Earth Dopants on Mechanical Properties of Alumina. *J. Am. Ceram. Soc*, 87(2):289, 2004.

[53] C Baudn and P Pena. Influence of stoichiometry on fracture behaviour of magnesium aluminate spinels at 1200C. *J. Eur. Ceram. Soc.*, 17(12):1501–1511, 1997.

[54] Y. Takigawa, Y. Ikuhara, and T. Sakuma. Grain boundary bonding state and

fracture energy in small amount of oxide-doped fine-grained Al2O3. *J. Mat. Sci.*, 34(9):1991–1997, 1999.

[55] G. D. West, J. M. Perkins, and M. H. Lewis. The effect of rare earth dopants on grain boundary cohesion in alumina. *in press*, 2005.

[56] Andreas Krell, Paul Blank, Hongwei Ma, and Thomas Hutzler. Evaluation of Hot Isostatic Pressing Parameters on the Optical Properties of Spinel. *J. Am. Ceram. Soc.*, 86(1):12–18, 2003.

[57] Transparent articles of aluminium oxide and methods of manufacturing said articles, 1973. U.S. patent 3,846,146.

[58] G. De With. Fracture of translucent alumina: temperature dependance and influence of CaO dope. *J. Mat. Sci.*, 19:2195–2202, 1984.

[59] Curtis Scott, Mary Kaliszewski, Charles Greskovich, and Lionel Levinson. Conversion of Polycrystalline Al2O3 into Single-Crystal Sapphire by Abnormal Grain Growth. *J. Am. Ceram. Soc.*, 85(5):1275–80, 2002.

[60] K. Hayashi, O. Kobayashi, S. Toyoda, and K. Morinaga. Transmission optical properties of polycrystalline alumina with submicron grains. *Mat. Trans*, 32(11):1034–29, 1991.

[61] J. G. J. Peelan. Transparent hot-pressed alumina, II: Transparent versus Translucent alumina. *Ceram. Int.*, 5(2):115–19, 1979.

[62] J. G. J. Peelan and R. Metselaar. Light scattering by pores in polycrystalline materials: Transmission properties of alumina. *J. App. Phys.*, 45(1):216–220, 1974.

[63] Rolf Apetz and Michel P. B. van Bruggen. Transparent alumina: A Light-Scattering Model. *J. Am. Ceram. Soc.*, 86(3):480–86, 2003.

[64] Dirk Godlinski, Meinhard Kuntz, and Georg Grathwohl. Transparent Alumina with Submicrometer Grains by Float Packing and Sintering. *J. Am. Ceram. Soc.*, 85(10):2449–2456, 2002.

[65] J. G. P. Binner. New Processing Techniques for Advanced Ceramics. *Proc. 2nd Int. Conf. on Shaping of Advanced Ceramics.*, pages 1–9, oct 2002.

[66] Wolfgang M. Sigmund, Nelson S. Bell, and Lennart Bergstrom. Novel Powder Processing Methods for Advanced Ceramics. *J. Am. Ceram. Soc.*, 83(7):1557–74, 2000.

[67] Jian-Lin Shi and J. D. Zhang. Compaction and Sintering Behaviour of Bimodal Alumina Powder Suspensions by Pressure Filtration. *J. Am. Ceram. Soc.*, 83(4):737–42, 2000.

[68] Mark C. L. Patterson, Jenni E. Caiazza, and Don W. Roy. Transparent Spinel Development. *Proceedings of SPIE*, 4102:59–68, 2000.

[69] A. F. Dericioglu and Y. Kagawa. Effect of Grain Boundary Microcracking on the light transmittance of sintered transparent mgal2o4. *J. European. Ceram. Soc.*, 23:951–959, 2003.

[70] Ji-Guang Li, Takayasu Ikegami, Jong-Heun Lee, and Toshiyuki Mori. Fabrication of Translucent Magnesium Aluminate Spinel Ceramics. *J. Am. Ceram. Soc.*, 83(11):2866–68, 2000.

[71] T. M. Hartnett, S. D. Bernstein, E. A. Maguire, and R. W. Tustison. Optical properties of ALON (aluminium oxynitride). *Infra-red Phys. and Tech.*, 39:203–211, 1998.

[72] S. Ramanathan, S. K. Roy, and Y. J. Bhat. Transparent YAG from powder prepared by homogeneous precipitation reaction - $Al(NO_3)_3$ + $Y(NO_3)_3$ + $(NH_4)_2SO_4$ + $CO(NH_2)_2$. *Mater. Sci. Lett.*, 20:2119–2121, 2001.

[73] Xinlu Su, Peiling Wang, Weiwu Chen, Bo Zhu, Yibing Chen, and Dongsheng Yan. Translucent (alpha)-sialon ceramics by hot pressing. *J. Am. Ceram. Soc.*, 87(4):730–32, 2004.

[74] Mark I. Jones, Hideo Hyuga, Kiyoshi Hirao, and Yukihiko Yamauchi. Highly Transparent Lu-(alpha)-SiAlON. *J. Am. Ceram. Soc.*, 87(4):714–16, 2004.

[75] David B. Williams and C. Barry Carter. *Transmission Electron Microscopy, A Textbook for Materials Science.* Plenum, 1996. p 7.

[76] R. F. Egerton. *Electron Energy Loss Spectroscopy in the Electron Microscope.* Plenum, 1986.

[77] David B. Williams and C. Barry Carter. *Transmission Electron Microscopy, A Textbook for Materials Science.* Plenum, 1996. page 678.

[78] John Bruley, Junghyun Cho, Helen M Chan, Martin P Harmer, and Jeffrey M. Rickman. Scanning Transmission Electron Microscopy Analysis of Grain Boundaries in Creep-Resistant Yttrium and Lanthanum-Doped Alumina Microstructures. *J. Am. Ceram. Soc.*, 82(10):2865–70, 1999.

[79] C. M. Wang, G. Slade Cargill III, Helen M Chan, and Martin P Harmer. X-Ray Absorption Near-Edge Structure of Grain-Boundary-Segregated Y and Zr in Creep-Resistant Alumina. *J. Am. Ceram. Soc.*, 85(10):2492–98, 2002.

[80] G. Cliff and G. W. Lorimer. The quantitative analysis of thin specimens. *J. Micros.*, 103:203–207, 1975.

[81] Chong-Min Wang, Helen M Chan, and Martin P Harmer. Effect of nd2o3 Doping on the Densification and Abnormal Grain Growth behaviour of High-Purity Alumina. *J. Am. Ceram. Soc.*, 87(3):378–83, 2004.

[82] Hans-Joachim Kleebe. Comparison between SEM and TEM Imaging Techniques to Determine Grain-Boundary Wetting in Ceramic Polycrystals. *J. Am. Ceram. Soc.*, 85(1):43–48, 2002.

[83] A. Mark Thompson, Kamal K. Soni, Helen M. Chan, Martin P. Harmer, David B. Williams, Jan. M. Chabala, and Riccardo Levi-Setti. Dopant Distributions in Rare-Earth-Doped Alumina. *J. Am. Ceram. Soc.*, 80(2):373–76, 1997.

[84] K. K. Soni, A. M. Thompson, M. P. Harmer, D. B. Williams, J. M. Chabala, and R. Levi-Setti. Solute segregation to grain boundaries in mgo-doped alumina. *Appl. Phys. Lett.*, 66(21):2795–2797, 1995.

[85] Konstantin L. Gavrilov, Stephen J. Bennison, Kut R. Mikeska, Jan. M. Chabala, and Riccardo Levi-Setti. Silica and Magnesia Dopant Distribution in Alumina by High-Resolution Scanning Secondary Ion Mass Spectrometry. *J. Am. Ceram. Soc.*, 82(4):1001–8, 1999.

[86] G. D. West, J. M. Perkins, and M. H. Lewis. Transparent Fine-Grained Oxide Ceramics. *Key Eng. Mater.*, 264–268:801–804, 2004.

[87] D. W. Richerson. *Modern Ceramic Engineering*. Marcel Dekkar inc., 1992.

[88] G. R. Anstis, P. Chantikul, B. R. Lawn, and D. B. Marshall. A critical evaluation of indentation techniques for measuring fracture toughness: I, Direct crack measurements. *J. Am. Ceram. Soc.*, 64(9):533–38, 1981.

[89] M. G. Dowsett, N. S. Smith, R. Bridgeland, D. Richards, A. C. Lovejoy, , and P. Pedrick. *Secondary Ion Mass Spectrometry SIMS X*, page 367. Wiley, 1997.

[90] www.oed.com.

[91] Image j, Java image processing software.

[92] J. D. French, J. Zhao, M. P. Harmer, H. M. Chan, and G. A. Miller. Creep of Duplex Microstructures. *J. Am. Ceram. Soc.*, 77(11):2857–2865, 1994.

[93] M. Miyayama and K. Koumoto. *Engineered Materials Handbook volume 4 - Ceramics and Glasses: Engineering properties of single oxides*, pages 748–757. ASM international, 1991.

[94] K. L. Komerek, A. Coucoulas, and N. Klinger. Reactions between refractory oxides and graphite. *J. Electro. Chem.*, 110(7):783–791, 1963.

[95] G. D. West. *Microstructure-property relations in fine-grained oxide ceramics*. PhD thesis, University of Warwick, 2004. p95.

[96] Z. Shen, M. Johnsson, Z Zhao, and M Nygren. Spark plasma sintering of alumina. *J. Am. Ceram. Soc.*, 85(8):1921–1927, 2002.

[97] G. D. West. *Microstructure-property relations in fine-grained oxide ceramics.* PhD thesis, University of Warwick, 2004.

[98] L. Gao, Z. Shen, H. Miyamoto, and M. Nygren. Superfast densification of oxide/oxide ceramic composites. *J. Am. Ceram. Soc.*, 82(4):1061–63, 1999.

[99] R. S. Dobedoe, G. D. West, and M. H. Lewis. Spark plasma sintering of ceramics. *Bull. of ECerS.*, 1:19–24, 2003.

[100] R. L. Coble. Sintering Crystalline Solids. II. Experimental Test of Diffusion Models in Powder Compacts. *J. Mat. Sci*, 32:793–799, 1961.

[101] R. L. Coble. Sintering Crystalline Solids. I. Intermediate and Final State Diffusion Models. *J. Mat. Sci.*, 32:787–792, 1961.

[102] G. R. Villalobos, J. S. Sanghera, and I. D. Aggarwal. Degradation of magnesium aluminum spinel by lithium fluoride sintering aid. *J. Am. Ceram. Soc.*, 88(5):1321–1322, 2005.

[103] G. D. West. *Microstructure-property relations in fine-grained oxide ceramics.* PhD thesis, University of Warwick, 2004. p110.

[104] J. E. Bonavich and L. D. Marks. Electron radiation damage of alpha-alumina[2]. *Ultramicroscopy*, 35(2):161–166, 1991.

[105] David B. Williams and C. Barry Carter. *Transmission Electron Microscopy, A Textbook for Materials Science.* Plenum, 1996. pp 459 - 481.

[106] M. Varela, A. R. Lupini, K. can Benthem, A. Y. Borisevich, M. F. Chisholm, N. Shibata, E. Abe, and S. J. Pennycook. Materials Characterization in the Aberration-Corrected Scanning Transmission Electron Microscope. *Annu. Rev. Mater. Res.*, 35:539–69, 2005.

[107] Lord Rayleigh. *Phil. Mag.*, 47(310):81–93, 1874.

[108] M. A. O'Keefe. Sub-Angstrom Resolution with Aberration-Corrected TEM:

Present and Future. *Microscopy and Microanalysis*, 10(4), dec 2004. Aberration-free meeting, Savanna, Georgia.

[109] A. Bleloch and A. Lupini. Imaging at the picoscale. *Mats. today*, 7(12):42–48, 2004.

[110] O. Sherzer. The theoretical resolution limit of the electron microscope. *J. App. Phys.*, 20:20–29, 1949.

[111] A. I. Kirkland and W. O. Saxton. Cation segregation in $Nb_{16}W_{18}O_{94}$ using high angle annular dark field scanning transmission electron microscopy and image processing. *J. Microscopy*, 206(1):1–6, april 2002.

[112] C. Kiselowski, E. Principe, B. Feitag, and D. Hubert. Benefits of microscopy with super resolution. *Physica B*, 308-310:1090–1096, 2001.

[113] O. L. Krivanek, N. Dellby, and A. R. Lupini. Towards sub-angstrom electron beams. *Ultramicroscopy*, 78:1–11, 1999.

[114] P. W. Hawkes and E. Kasper. *Principles of electron microscopy*. Academic press, London, 1994.

[115] Uwe Falke, Andrew Bleloch, Meiken Falke, and Steffen Teichert. Atomic structure of a (2 x 1) Reconstructed $NiSi_2$/Si (001) Interface. *Physical Review Letters*, 92(11):116103-1–116103-4, 2004.

[116] Naoya Shibata, Stephen J. Pennycook, Tim R. Gosnell, Gayle S. Painter, William A. Shelton, and Paul D. Becher. Observation of rare-earth segregation in silicon nitride ceramics at subnanometre dimensions. *Nature*, 428(15):730–733, 2004.

[117] Personal correspondance with Dr Andrew Bleloch, UK SuperSTEM facility.

[118] R Schweinfest, A T Paxton, and M W Finnis. Bismuth embrittblement of copper is an atomic size effect. *nature*, 432:1008–1011, 2004.

[119] Personal correspondance with Dr M. Finnis, Department of Materials, Imperial College, London.

[120] J. P. Buban, K. Matsunaga, J. Chen, N. Shibata, W. Y. Ching, T. Yamamoto, and Y. Ikuhara. Grain Boundary Strengthening in Alumina by Rare Earth Impurities. *Science*, 311:212–215, 2006.

[121] L. Pauling. *The nature of the chemical bond*. Ithaca: Cornell University Press, 1961.

[122] R. W. Rice, C. Cm. Wu, and F Borchelt. Hardness-grain-size relations in ceramics. *J. Am. Ceram. Soc.*, 77(10):2539–2553, 1994.

[123] M. Li and M. J. Reece. Influence of grain size on the indentation-fatigue behavior of alumina. *J. Am. Ceram. Soc*, 83(4):967–70, 2000.

[124] S. R. Hah, T. E. Fischer, P. Gruffel, and C. Carry. Effect of grain boundary dopants and mean grain size on tribochemical behaviour og highly purified alpha-alumina in the mild wear regime. *Wear.*, 181–183:165–177, 1995.

[125] G. D. West. *Microstructure-property relations in fine-grained oxide ceramics*. PhD thesis, University of Warwick, 2004. p153.

[126] A Muchtar and L. C. Lim. Indentation Fracture Toughness of High Purity Sub-micron Alumina. *Acta. Mater.*, 46(5):1683–1690, 1998.

[127] G. Dewith. Fracture of tranlucent alumina - Temperature dependance and influence of CaO dope. *J. Mat. Sci.*, 19(7):2195–2202, 1984.

[128] S. F. Pugh. *An introduction to grain boundary fracture in metals*. The institute of metals, London, 1991.

[129] A Muchtar and L. C. Lim. Indentation fracture toughness of high purity submicron alumina. *Acta Mater.*, 46(5):1683–90, 1998.

[130] Z-Y Deng, Y Zhou, M. E. Brito, J-F Yang, and T Ohji. Fracture-mode change in

alumina-silicon carbide composites doped with rare-earth impurities. *J. Am. Ceram. Soc.*, 86(10):1789–1792, 2003.

[131] Rolf Apetz and Michael P. B. van Bruggen. Transparent Alumina: A Light-Scattering Model. *J. Am. Ceram. Soc.*, 86(3):480–86, 2003.

[132] G. D. West. *Microstructure-property relations in fine-grained oxide ceramics.* PhD thesis, University of Warwick, 2004. p178.

[133] J. H. Simmons and K. S. Potter. *Optical Materials.* Academic press, San Diego, 2000.

[134] G. D. West. *Microstructure-property relations in fine-grained oxide ceramics.* PhD thesis, University of Warwick, 2004. pp18 - 20.

[135] H. C. v. d. Hulst. *Light scattering by small particles.* Dover, New York, 1982.

[136] R. Tilley. *Colour and the optical properties of materials.* Wiley, Chichester, 2000.

[137] J. A. Lewis. Colloidal Processing of Ceramics. *J. Am. Ceram. Soc.*, 83(10):2341–59, 2000.

[138] Transparent polycrystalline sintered ceramic of cubic crystal structure, 2005. U.S. patent 2005/0164867.

[139] Fraunhofer IKTS, Dresden. http://www.ikts.fhg.de.